Analysis and Utilization of Reverse Power Flow of Wind Energy Source Using Multi-Port Power Electronic Transformer

Ereola Johnson Aladesanmi

217071301

A thesis submitted to the University of KwaZulu-Natal, College of Agriculture, Engineering and Science in fulfillment of the requirements for the degree of

Doctor of Philosophy

Supervisor: Professor David G. Dorrell

School of Engineering, Electrical Engineering

University of KwaZulu-Natal

December 2020

Copyright © 2020 Ereola Johnson Aladesanmi

All Rights Reserved

Declaration

I, Ereola Johnson Aladesanmi, declare that:

(i) The research reported in this dissertation, except where otherwise indicated, is my original research.

(ii) This thesis has not been submitted for any degree or examination at any other university.

(iii) This thesis does not contain other persons' data, pictures, graphs or other information, unless specifically acknowledged as being sourced from other persons.

(iv) This thesis does not contain other persons' writing, unless specifically acknowledged as being sourced from other researchers. Where other written sources have been quoted, then:

a) their words have been re-written but the general information attributed to them has been referenced:

b) where their exact words have been used, their writing has been placed inside quotation marks, and referenced.

(v) This thesis does not contain text, graphics or tables copied and pasted from the Internet, unless specifically acknowledged, and the source being detailed in the thesis and in the References sections.

Candidate: Ereola Johnson Aladesanmi

Signature :

As the candidate's supervisor I agree to the submission of this thesis for examination.

Supervisor: Professor David G. Dorrell

Signature:

ABSTRACT

Analysis and Utilization of Reverse Power Flow of Wind Energy Source Using Multi-Port Power Electronic Transformer

Ereola Johnson Aladesanmi

School of Engineering

Doctor of Philosophy

The recent liberalization of the electricity market and increased environmental concerns as well as an increase in energy demand across the globe have brought the use of renewable energy sources such as wind energy to the fore. Some of the potential benefits of renewable energy sources (RESs) are: localized generation, environmental-friendliness, generation of clean energy, reduction in greenhouse gas (GHG) emissions, increase in energy generation for increasing demand, and reduction in transmission losses. However, high penetration of RESs exposes power grids to several challenges. Some of these challenges for RESs are: increases in voltage profile level, high power losses, reverse power flow (RPF), protection and control issues. The main concern of this research work is RPF.

RPF is a situation whereby excess power generated on a grid as a result of high integration or penetration of RES is fed back to the source of generation. RPF exposes power grids to various challenges; aside from causing grid instability. RPF incurs additional losses on the grid, causing over-voltage and overloading of the connecting elements such as conductors and transformers. In recent times, various control strategies have been deployed to mitigate these effects on the grid. Energy management systems (EMSs) with energy storage devices (ESDs) are the most commonly applied strategies. However, intrusion into consumers' privacy and the high cost of energy storage devices poses a challenge to this approach. Voltage rise (VR) is one of the consequences of RPF. Line impedance reduction and reactive power compensation using flexible AC transmission system (FACTS) devices are some of the methods use for voltage rise control. On-load tap changer transformers (OLTCs), generation curtailment and reverse power relay are also deployed to control RPF. However, reactive power compensation and generation curtailment approaches lead to power losses and voltage instability respectively.

This thesis proposes a more secure method for utilising reverse power flow to supply power to modern electric vehicle (EV) charging stations through a multi-port power electronic transformer (MPPET). The proposed method consists of a RPF detection stage (RPFDS) electrically coupled to the point of common coupling (PCC), which discriminates between the total power

generated on the grid and the actual load demand. A smart circuit breaker operates as soon as it picks up signal from RPFDS. The MPPET receives power from RPF utilization substation which is then used for electric vehicle (EV) charging. The method was validated experimentally in the laboratory. The results of the research work proved the effectiveness of the MPPET in voltage regulation and in RPF utilisation.

PUBLICATIONS ARISING

Analysis and Utilization of Reverse Power Flow of Wind Energy Source Using Multi-Port Power Electronic Transformer

Ereola Johnson Aladesanmi

School of Engineering

Doctor of Philosophy

1. E J Aladesanmi and D G Dorrell, "Investigation and Assessment of the Impacts of Reverse Power Flow on Power System Network Loading under High Penetration of Wind Energy," Saupec, 2019.

ACKNOWLEDGMENTS

I sincerely acknowledge and appreciate the support of my supervisor Professor D. G. Dorrell for his support from the beginning of the work to the end. It has been a wonderful opportunity to work under your supervision to develop my research dexterity. My sincere appreciation also goes to Mr Greg Loubser and Dr Remmy Musumpuka for their support throughout the design and implementation of this project in the laboratory. I am sincerely grateful to Dr Musumpuka for help in developing several parts of this thesis

My appreciation also goes to my mother, Mrs. Aderomola Aladesanmi who taught me to be patient, persistent and courageous in any situation, may God Almighty give you long life. My special thanks go to my wife, Oluwatoyin Aladesanmi and my sons Eniola and Iyiola Aladesanmi for their understanding, support, prayers and patience throughout the journey of my studies. The motherly and friendly roles you played in my life throughout the course of my studies is highly appreciated,thank you very much. My appreciation also goes to my sister in-law Mrs Omowumi Ojo for her immeasurable support and care for my family during the course of my studies.

My special thanks go to ESKOM for the financial support and the opportunity given to me to work in the Smart Grid Centre.

Finally, and most importantly, my deepest appreciation and gratitude goes to God Almighty for His protection and unmerited favour bestowed on me to go this far in life, may His name be glorified.

Contents

1 Introduction **1**

1.1 Background . . . 1

1.2 Research Motivation . . . 2

1.3 Research Questions . . . 2

1.4 Research Aims and Objectives . . . 2

1.5 Research Methodology . . . 3

1.5.1 Phase A . . . 4

1.5.2 Phase B . . . 5

1.6 Research Contribution . . . 5

1.7 Scope and Limitations . . . 6

1.8 Structure of the Thesis . . . 7

2 Literature Review **9**

2.1 Structure of Electric Power Grid . . . 9

2.2 Global Installed Capacity of Wind Energy . . . 11

2.3 Wind Energy Conversion Systems . . . 13

2.3.1 Wind Turbine Technology and Application . . . 13

2.3.2 Applications of Wind Turbines . . . 14

2.4 Impacts of High Penetration of Wind Energy on Power Grid . . . 15

2.5 Reverse Power Flow and Mitigation Strategies . . . 15

2.5.1 Definition and Causes of Reverse Power Flow . . . 15

2.6 Overview of Excess Power Generated From Renewable Energy Sources . . . 16

2.7 Impacts of Reverse Power Flow on the Grid . . . 17

2.7.1 Reverse Power Flow and Voltage Profile . . . 17

2.7.2 Reverse Power Flow and Grid Protection . . . 17

2.7.3 Reverse Power Flow and Grid Loading . . . 18

2.7.4 Reverse Power Flow and Grid Congestion . . . 18

2.7.5 Reverse Power Flow and Power Losses . . . 19

2.7.6 Reverse Power Flow and Power Quality . . . 19

2.7.7 Reverse Power Flow and Grid Stability . . . 20

2.7.8 Reverse Power Flow and Islanding . . . 20

2.7.9 Reverse Power Flow and Total Harmonic Distortion . . . 20

2.8 Mathematical Analysis of Reverse Power Flow and Voltage Rise on the Grid . . . 21

2.8.1 Penetration Level . . . 24

2.9 Reverse Power Flow Mitigation Strategies 24
2.9.1 Energy Management Approach 24
2.9.2 Voltage Rise (VR) Control Approach 25
2.10 Recent Research Work on Reverse Power Flow Utilisation and Control Strategies 27
2.11 The Concept of Power Electronic Transformer and Electric Vehicle Charging Technology 29
2.12 Classification and Topology of PET 30
2.12.1 Classification of Power Electronic Transformer 31
2.12.2 Power Electronic Transformer Topology 31
2.13 Features of a Power Electronic Transformer (PET) 36
2.14 Comparison between a Power Electronic Transformer and a Traditional Line Frequency Transformer 37
2.15 Functions and Applications of a PET 37
2.15.1 Functions of Power Electronic Transformer 38
2.15.2 Applications of Power Electronics Transformers 38
2.16 Adoption of Power Electronic Transformers 42
2.17 PET and EV Charging Technology 42
2.17.1 Electric Vehicle and Charging Technology 42
2.17.2 Types of Electric Vehicle 43
2.17.3 Electric Vehicle Battery and Charging Technology 43
2.17.4 Electric Vehicle Charging Technology 44
2.17.5 Electric Vehicle Charging Power Level 45
2.18 Electric Vehicle Charger Technology 46
2.18.1 Electric Vehicle Charger Connectors 48
2.19 Electric Vehicle Charger Topologies 49
2.19.1 AC/DC and DC-DC Converter Topologies 49
2.19.2 AC/AC and AC/DC Converter Topologies 49
2.20 EV Charging Control Techniques 50
2.20.1 Constant Current Control 50
2.20.2 Constant Voltage Control 50
2.20.3 Advanced Control Technique (ACT) 51
2.21 Impacts of EV Charging on Electric Power Grid 52
2.21.1 Electric Vehicle Charging and Load Profile 52
2.21.2 Electric Vehicle Charging and Grid Connecting Elements 52

2.21.3 Electric Vehicle Charging and System Losses . . . 52
2.21.4 Electric Vehicle Charging and Grid Stability . . . 52
2.22 Electric Vehicle Battery Charging Stations . . . 52
2.22.1 Residential Charging Stations . . . 53
2.22.2 Private Charging Stations . . . 53
2.22.3 Public Charging Station . . . 53
2.23 Summary . . . 53

3 Investigation and Analysis of Reverse Power Flow Conditions of High Penetration of Wind Energy Source on Power System Network 55
3.1 Introduction . . . 55
3.2 System Description and Modelling . . . 55
3.2.1 Conductors . . . 57
3.2.2 Resistance . . . 57
3.2.3 Line Inductance . . . 57
3.2.4 Line Capacitance . . . 57
3.2.5 Wind Turbine and Wind Farm . . . 58
3.3 Simulation Scenarios . . . 60
3.4 Simulation Results Analysis and Discussions . . . 61
3.4.1 Voltage Profile Analysis . . . 61
3.5 Network Loading and Reverse Power Flow Analysis . . . 66
3.5.1 Transformer Loading . . . 66
3.6 Reverse Power Flow Analysis . . . 68
3.6.1 Transformer Losses Analysis . . . 71
3.7 Line Loading and Losses Analysis . . . 72
3.7.1 Total Power Losses . . . 75
3.7.2 Voltage Total Harmonic Distortion at Different Penetration Levels . . . 76
3.8 Summary . . . 81

4 Proposed Reverse Power Flow Utilisation Using Power Electronic Transformer 82
4.1 Introduction . . . 82
4.2 Methodology . . . 82
4.3 Utilisation Procedure . . . 83

4.3.1 Reverse Power Flow Detection Stage (RPFDS) . . . 83
4.3.2 Reverse Power flow Utilisation Substation (RPFUS) . . . 83
4.3.3 Multi-port Power Electronic Transformer . . . 83
4.3.4 Input Stage (AC-DC Converter) . . . 84
4.3.5 DC-AC Conversion Stage . . . 86
4.3.6 High Frequency Transformer . . . 88
4.3.7 AC-AC Conversion Stage . . . 88
4.3.8 Modulation Techniques for Matrix Converter . . . 90
4.3.9 Space Vector Pulse Modulation Techniques . . . 91
4.3.10 Input Filter . . . 91
4.3.11 Output Filter . . . 92
4.3.12 Charging Station Arrangement . . . 93
4.4 Utilisation Algorithm . . . 93
4.5 Simulation Scenarios . . . 94
4.5.1 Design and Simulation of Power Electronic Transformer for Voltage Control 95
4.5.2 Simulation Cases . . . 95
4.6 Simulation Results and Discussion . . . 97
4.6.1 Simulation Under Normal Conditions . . . 97
4.7 Simulation Results under Abnormal Conditions . . . 99
4.7.1 Voltage Sag . . . 99
4.7.2 Voltage Swell . . . 100
4.8 Variations in the Grid Loading System . . . 102
4.8.1 Reduction in the Grid Loading System . . . 102
4.8.2 Increase in the Grid Loading System . . . 103
4.9 Variation in Output of the Micro-generation . . . 104
4.10 Modeling and Simulation of the Proposed MPPET for Reverse Power Flow Utilisation . . . 106
4.10.1 Electric Vehicle Charging Station Design . . . 106
4.10.2 DC Bus Voltage and Capacitor . . . 107
4.10.3 Electric Vehicle Battery Selection and Modeling . . . 107
4.11 Proposed EV Charger and Control . . . 109
4.11.1 Proposed DC-DC Charger and Control System . . . 110
4.11.2 Proposed AC-DC Charger and Control System . . . 111
4.12 Proposed EV Charging Station Control . . . 112

4.13 Simulation Results Analysis and Discussion . . . 113
4.13.1 Impacts of the Proposed PET on RPF at Different Penetration Levels of Wind Energy Source . . . 113
4.14 Summary . . . 117

5 Implementation and Testing of the Proposed MPPET 118
5.1 Background . . . 118
5.2 Design Procedure . . . 119
5.2.1 System Requirements and Specifications . . . 119
5.2.2 Components Selection . . . 119
5.2.3 Heat Sink Design and Analysis . . . 122
5.2.4 IGBT Gate Driver Design . . . 123
5.2.5 High Frequency Transformer Design . . . 124
5.2.6 System Control and Switching Programming . . . 129
5.2.7 System Assembling and Testing . . . 131
5.3 Case Studies and Implementation Results Analysis . . . 134
5.3.1 Implementation Scenarios . . . 134
5.3.2 Experimental Results . . . 134
5.4 Summary . . . 140

6 Conclusions and Recommendations for Further Work 141
6.1 Conclusions . . . 141
6.2 Recommendation for Further Work . . . 142

References 143

A MATLAB/Simulink Models 159

B DC-AC Converter Switching Code 165

C Programming Code for Matrix Converter Switching 169

List of Figures

1.1 Research Methodology 3

2.1 Characteristics and Voltage Level of Electric Power Network 9
2.2 Power System Network with Renewable Energy Connected 11
2.3 Global Cumulative Installed Capacity of RES and Wind Energy from 2008-2018 11
2.4 Projected Global Cumulative Installed Capacity of Wind Energy 2020-2030 . . . 12
2.5 Wind Energy Conversion System 13
2.6 Wind Turbine [7] 13
2.7 Two-Bus System with Wind Energy Source Connected 22
2.8 Basic Structure of Power Electronic Transformer 30
2.9 Power Electronic Transformer Classification and Topology 30
2.10 Single-Stage without DC link 32
2.11 Single-phase to 3-phase matrix inverter [78] 32
2.12 3-phase to 3-phase matrix inverters - direct and indirect [84] 33
2.13 Structure of Two Stages PET with DC-link on the Secondary Side 34
2.14 Structure of Two Stages PET with DC-link on the Primary Side 34
2.15 Three Stage PET with DC-Link on both Secondary and Primary Sides 35
2.16 DC-DC Conversion Stage 35
2.17 Traction Locomotive Application of a PET 39
2.18 Power Electronic Transformer in Wind Energy Conversion 40
2.19 Power Electronic Transformer and Smart Grid System 40
2.20 Electric Vehicle Charging Technology 45
2.21 Constant Current Control Method 50
2.22 Constant Voltage Control Method 51
2.23 Advanced Charging Method 51

3.1 Single-Line Diagram of the Power System Network under Investigation 56
3.2 Wind turbine characteristic 59
3.3 Wind farm layout 60
3.4 Scope Display of the Network without Wind Farm Connected 62
3.5 Scope Display of the Network without Wind Farm Connected 62
3.6 Scope Display of the Network without Wind Farm Connected 63
3.7 Scope Display of the Network under Investigation without Integration of Wind Farm 63
3.8 Voltage Profile Analysis without Wind Farm 64

3.9 Penetration Effect of Wind Farm on Voltage Profile 65
3.10 Power Flow Through TR2 67
3.11 Power Flow Through TR3 67
3.12 Power Flow Through TR4 68
3.13 Active power flow without integration of wind farm 69
3.14 Reverse active power flow with 1.0 % penetration at transformer TR3 69
3.15 Reverse active power flow with 1.1 % penetration at transformer TR3 70
3.16 Reverse active power flow with 1.2 % penetration at transformer TR3 70
3.17 Transformer Losses at Different Penetration Level 71
3.18 Line loading at Different Penetration Levels 73
3.19 Line Losses at Different Penetration Levels 74
3.20 Line Losses at Different Penetration Level 76
3.21 Voltage Total Harmonic Distortion at NO WT and 0.1 % Penetration Levels . . 77
3.22 Harmonics at 0.2 and 0.3 % Penetration Levels 77
3.23 Voltage Total Harmonic Distortion at 0.4 and 0.5 % Penetration Levels 78
3.24 Voltage Total Harmonic Distortion at 0.6 and 0.7 % Penetration Levels 78
3.25 Voltage Total Harmonic Distortion at 0.8 and 1.0 % Penetration Levels 79
3.26 Voltage Total Harmonic Distortion at 1.1 and 1.2 % Penetration Levels 79
3.27 Voltage Total Harmonic Distortion (THD %) at the PCC 80

4.1 Single Line Diagram of the Proposed Method for Reverse Power Flow Utilisation 82
4.2 Single line Diagram of the Proposed Power Electronic Transformer 83
4.3 Basic Structure of AC-DC Converter with DC-link 84
4.4 Three level converter [138] 84
4.5 Input stage AC-DC control circuit 86
4.6 Basic Structure of DC-AC Inverter 86
4.7 Complete Control Circuit for DC-AC PET Conversion Stage 87
4.8 Basic Structure of Three-phase High Frequency Transformer 88
4.9 Basic Structure of Matrix Converter. v_{ABC} are three phase inputs and v_{abc} are three phase outputs of different frequency and magnitude; sw1 = S_{Aa}, sw2 = S_{Ab}, sw4 = S_{Ba}, etc. 89
4.10 Equivalent Circuit of LC Filter 91
4.11 Equivalent Circuit of Series LCL Filter 92
4.12 Single-Line Diagram of the Overall System Modelling 93

4.13 Proposed RPF Utilisation Flow Chart Algorithm 94
4.14 Single Line Diagram of Network under Investigations 95
4.15 PET Input Voltage and Current under Normal Condition 97
4.16 PET Output Voltage and Current under Normal Condition 98
4.17 HFT Primary and Secondary Voltage 98
4.18 PET Input Voltage and Current during Voltage Sag 99
4.19 PET Output Voltage and Current during Voltage Sags 100
4.20 PET Input Voltage and Current during Voltage Swell 101
4.21 PET Output Voltage and Current during Voltage Swell 102
4.22 PET Output Voltage and Current during Reduction in Load 103
4.23 PET Output Voltage and Current during Increase in Load 104
4.24 PET Output Voltage and Current during Reduction in Output Generation . . . 105
4.25 PET Output Voltage and Current during Increase in Output Generation 105
4.26 Schematic Diagram of the Proposed Utilisation System with Electric Vehicle Charging Station 106
4.27 Lithium-ion Battery Pack Equivalent Circuit Model 108
4.28 Basic Diagram of Buck Converter Circuit 110
4.29 Proposed DC-DC Charger Control Circuit 110
4.30 Proposed AC-DC Charger Topology 111
4.31 Proposed AC-DC Charger Control in Grid-to-Vehicle Operation Mode 111
4.32 Proposed Constant Voltage Electric Vehicle Battery Control 112
4.33 PI Controller Transfer Function Control Loop 113
4.34 Active power flow at 1.1 % penetration after utilization 114
4.35 DC Fast Charging Characteristics 115
4.36 AC Fast Charging Characteristics 116
4.37 Battery SOC during Fast Charging DC Charging 116
4.38 Battery SOC during Fast Charging AC Charging 117

5.1 Complete block diagram of the implementation prototype 118
5.2 MPPET Design and Implementation Procedures 119
5.3 IGBT Gate Driver 123
5.4 HFT Design and Implementation stages 125
5.5 High Frequency Transformer Winding 128
5.6 Block diagram of the proposed PET with control blocks 129

5.7 Controller Printed Circuit Board and Design Prototype Module 130
5.8 ChipKIT Max32 Micro-controller board. 131
5.9 Hardware Implementation of Diode Rectifier 132
5.10 Printed Circuit Board and Design Prototype Module of DC-AC Converter . . . 132
5.11 Printed Circuit Board and Design Prototype Module of Matrix Converter 133
5.12 Complete Assembly of the Designed Transformer Prototype 133
5.13 Transformer prototype design under Load Condition 134
5.14 Grid input line voltage (red - 100 V/div) and line current (blue - 2 A/div) waveforms under normal conditions - 50 Hz input 135
5.15 Input line-line voltage to HFT under normal conditions - V_{Line} = 44.5 V 136
5.16 Input current to HFT under normal conditions - I_{Line} = 1.5 A 136
5.17 Input power using to HFT under normal conditions measured using 2-Wattmeter method - total power = 97.7 W 136
5.18 Output line-line voltage to HFT under normal conditions - V_{Line} = 44.5 V . . . 137
5.19 Input current to HFT under normal conditions - I_{Line} = 0.883 A 137
5.20 Output power using to HFT under normal conditions measured using 2-Wattmeter method - total power = 93 W 137
5.21 Matrix converter output power to resistive load - black is phase voltage (V) and red is current (10 × A) 138
5.22 Grid input line voltage (red - 100 V/div) and line current (blue - 5 A/div) waveforms under 50 % increased conditions - 50 Hz input 139
5.23 Input and output voltage waveforms are 50 % loading 139

A.1 Network under Investigation Modelled in MATLAB/Simulink 159
A.2 Battery Equivalent Model in MATLAB/Simulink 159
A.3 MATLAB/Simulink Model of Electric Vehicle DC-Fast Charging Station 160
A.4 MATLAB/Simulink Model of Electric Vehicle AC-Fast Charging Station 160
A.5 Block Diagram Internal Structure of Three-Phase MC in MATLAB/Simulink . . 161
A.6 Internal Structure of MC Input Modulator in MATLAB /Simulink Model 161
A.7 Internal Structure of MC Switching in MATLAB/Simulink Model 162
A.8 Complete Structure of MC Switching in MATLAB/Simulink Model 162
A.9 Complete Model of Power Electronic Transformer in MATLAB/Simulink 163
A.10 Complete Model of the Proposed Utilisation Network in MATLAB/Simulink . . 164

List of Tables

2.1 Transmittable power and connection of wind turbines to different levels of the electrical network . . . 10
2.2 IEEE Standard 519-1992 Harmonic Voltage Distortion Limits . . . 21
2.3 Features of a Power Electronic Transformer . . . 36
2.4 Comparisons between Power Electronic Transformer and Traditional Line Frequency Transformer . . . 37
2.5 Challenges of Power Electronic Transformer . . . 42
2.6 Characteristics of Various Electric Vehicle Battery . . . 44
2.7 Comparison between Off-board and On-board Charging Technology . . . 47
2.8 Summary of DC Fast Charging Methods . . . 48

3.1 Network under Investigation Parameters . . . 56
3.2 Line Parameters . . . 58
3.3 Wind Turbine Parameters . . . 60
3.4 Per-unit Voltage Analysis of the Grid without Wind Farm Integration . . . 64
3.5 Bus Voltage Analysis with Wind Turbine Connected in per unit . . . 65
3.6 Transformer Loading . . . 66
3.7 Transformer Losses Analysis . . . 71
3.8 Line Loading Analysis . . . 72
3.9 Line Losses Analysis . . . 74
3.10 total Power Losses Analysis . . . 75
3.11 Voltage Total Harmonic Distortion Analysis . . . 80

4.1 Power Electronic Transformer and Grid Parameters . . . 96
4.2 Line Parameters . . . 96
4.3 Electric Vehicle Charging Station and Battery Parameters . . . 109

5.1 Electrical Characteristics of the Selected Diode @$T_A = 25^O$C . . . 120
5.2 IGBT Absolute Maximum Rating . . . 121
5.3 HFT Design Parameters . . . 128
5.4 HFT Measurement . . . 129
5.5 Summary of Micro-controller Characteristics . . . 131
5.6 MPPET Prototype Design Parameters . . . 131
5.7 Comparison of normal and increased loading on HFT . . . 139

List of Abbreviations

Abbreviation	Definition
AC	Alternating Current
ACCS	Advanced Charging Control
ACSR	Aluminium Conductor Steel Reinforcement
ANN	Artificial Neutral Network
AVC	Automatic Voltage Control
BEV	Battery Electric Vehicle
CCCS	Constant Current Control System
CVCS	Constant Voltage Control System
DC	Direct Current
DNOs	Distribution Network Operators
DR	Demand Response
DFIG	Doubly-Fed Inductor Generator
DSM	Demand Side Management
DSVPWM	Direct Space Vector Pulse Width Modulation
EBI	Energy Balance Index
EMS	Energy Management System
ESS	Energy Storage System
ET	Electronic Transformer
EV	Electric Vehicle
FACTS	Flexible Alternating Current Transmission System
FI	Feeding Index
FL	Fuzzy Logic
GA	Genetic Algorithm
GHG	Greenhouse Gas
GWEC	Global Wind Energy Conversion
G2V	Grid to Vehicle
HEV	Hybrid Electric Vehicle
HFT	High Frequency Transformer
HVDC	High Voltage Direct Current
IPPs	Independent Power Producers
ISVPWM	Indirect Space Vector Pulse Width Modulation
LVDC	Low Voltage Direct Current

LV	Low Voltage
MC	Matrix Converter
MPPET	Multi-port Power Electronic Transformer
MPPT	Maximum Power Point Tracking
MV	Medium Voltage
OLTC	On-Load Tap Changer
OPS	Over Current Protection System
PCC	Point of Common Coupling
PCB	Printed Circuit Board
PET	Power Electronic Transformer
PHEV	Plug-in Hybrid Electric Vehicle
PI	Proportional Integral
PL	Penetration Level
PLL	Phase Lock Loop
PWM	Pulse Width Modulation
RES	Renewable Energy Source
RPFDS	Reverse Power Flow Detection Stage
SAE	Society of Automotive Engineers
SCB	Smart Circuit Breaker
SST	Solid State Transformer
ST	Smart Transformer
STATCOM	static Synchronous Compensation
SVC	Static Var Compensation
SVPWM	Space Vector Pulse Width Modulation
SOC	State of Charge
TIC	Total Installed Capacity
TLD	Total Load Demand
TLFT	Traditional Line Frequency Transformer
TR	Transformer
V2G	Vehicle to Grid
VR	Voltage Rise
VSI	Voltage Source Inverter
VSR	Voltage Source Rectifier

WT	Wind Turbine

List of Symbols

Symbols	Meaning
T_{Los}	Transformer losses
C_{Los}	Conductor Losses
P_{Los}	Active Power Losses
Q_{Abs}	Reactive Power - Positive is Absorbing
V_R	Receiving End Voltage
ΔV_{ji}	PCC Voltage Variation
P_{TG}	Overload Power Generated
C_{Mx}	Maximum Capacitance of the Capacitor
L_{in}	Line Inductance
R_{d}	Damping Resistance
L_{Ei}	Interface Inductance
K_p	Proportional Constant
K_i	Integral Constant
Δ_{Max}	Maximum Peak to Peak current
C_{rated}	Charging Station Capacity
K_{Load}	Charging Station Over Load Factor
$V_{Min(bat)}$	Battery Minimum Voltage
M_{Min}	Charger Minimum Modulation Index
t	Period of AC Voltage Wave
ΔP	Change in DC Power
V_{dc}	DC Voltage
C_{cb}	Bulk Capacitance
C_{cs}	surface capacitance
R_1	Battery Internal Resistance
R_2	Battery polarization Resistance
V_{cb}	Voltages Across the Bulk Capacitor
V_{cb}	Surface Capacitor
V_0	Battery Pack Terminal Voltage
I_0	Battery Pack Terminal Current
D	Duty Cycle
V_S	Input Voltage
V_O	Output Voltage

I_{Out}	Output Current
ΔI_L	Inductor Current Ripple
ΔV_{Out}	Output Voltage Ripple
P_{out}	Output Power
i_{E1}	Converter Input Line Current
V_{E1}	Input Voltage
ω	Angular Velocity
V_0	Voltage Drop
R_d	Virtual Impedance Resistor
i_d	Inverter Output Current
V_{ref}	Voltage Reference
$C_{\max}$	Maximum Capacitance of the Capacitor
$I_{\min}$	Transformer Minimum Current
$Q_{\max}$	Phase Shift between the Input and the Output Current
V_c	capacitor voltage
ω_{cin}	Cut-off Angular Frequency of the Filter
C_{in}	Input Capacitor
L_1	Inverter Side Inductor
L_2	Grid Side Inductor
V_{DC}	DC-link voltage
f_S	Switching Frequency
$\Delta I_{L\max}$	Maximum Peak to Peak Current Ripple
P_{ratad}	Rated Active Power
p	inductance Ratio at the Inverter Side to the Inductance at the Grid Side
V_{ph}	Phase Voltage
Z_b	Base Impedance
C_b	Base Capacitance
V_{RMS}	Line-line RMS Voltage
ω_g	Grid Angular Frequency
P_{SW}	Switching Power losses
E_{SW}	Total Energy Losses
$E_{SW(on)}$	Energy Losses during IGBT Turn on

$E_{SW(off)}$	Energy Losses during IGBT Turn off
$P_{SW(on)}$	Total Power Dissipated during Turn-on
$P_{SW(off)}$	Total Power Dissipated during Turn-off
$I_{c-\text{tail}}$	Collector Current Tail
T_J	IGBT Junction Temperature during Normal Operation
R_{SA}	Heat Sink to Ambient Thermal Resistance
θ_{JC}	junction-to-case Thermal Resistance
θ_{CS}	Case to Heat Sink Thermal Resistance
P_{tot}	Total Power Dissipation
T_c	Case Temperature
ΔT	Change in Temperature
$T_j - T_C$	Case Temperature
$I_{CE(\text{ ave })}$	Collector Current
I_{gate}	Gate Current
P_E	Emitter Power
I_F	Forward Input Current
V_F	Forward Input Voltage
V_p	Transformer Primary Voltage
V_s	Transformer Secondary Voltage
N_1	Number of Turns on the Primary Side of the Transformer
N_2	Number of Turns on the Secondary Side of the Transformer
B_{max}	Maximum Flux Density
A_c	Transformer Area of the Core
K_f	Square Wave Excitation
f_s	Transformer Switching Frequency
A_{min}	Minimum Cross Sectional Area of the Core
T	Transformer Period of Operation
I_{RMS}	RMS Current
A_{wire}	Area of the Wire
d_{wire}	Diameter of the Wire
S	Current Carrying Capacity of the Wire
$V_{L(RMS)}$	Line -line RMS Voltage

Chapter 1

Introduction

1.1 Background

In recent times, the use of renewable energy systems (RESs) such as wind farms has increased globally due to the numerous benefits associated with such energy sources. Aside from being environmentally-friendly, renewable energy sources alleviate energy losses and the cost of power generation, transmission and distribution due to their proximity to end-users. In addition, RESs enhance grid stability, generate clean energy and reduce greenhouse gas emissions [1]. However, their high penetration can be detrimental to normal operation of the grid. According to [2] and [3], high penetration of RESs has a negative influence on voltage profile levels and thus can reverse the direction of power flow on the grid. The reversal in the direction of power flow on the grid is called reverse power flow (RPF). RPF is a situation whereby the excess power generated in the grid due to high penetration of RESs is fed back to the source of generation. RPF occurs when the total power generated is more than the total power demand. RPF is more prevalent from renewable energy sources with intermittent power generating capacity, such as wind and solar energy. RPF impacts negatively on power system networks. It can violate the thermal capacity of the connecting elements due to overloading, increasing fault current level, malfunction of the voltage control system, protection systems and increased grid losses. Therefore, recently, this issue has led to extensive research by academia and utility companies. Nevertheless, more research needs to be done in order to come up with more effective ways of utilizing the excess power generated rather than controlling the situation which may create additional issues in the grid. Among the utilization strategies, energy management systems (EMSs) with energy storage devices and generation curtailment through total disconnection of the connected renewable energy source are widely deployed by distribution network operators (DNOs). However, privacy intrusion to the customers' domains, high cost of energy storage devices and grid instability due to sudden disconnection of renewable energy sources are some of the drawbacks to these strategies. Furthermore, the disconnection of renewable energy sources from the grid has adverse effects on the income of independent power producers (IPP) and the grid operator. Thus, aside from the enhancement of the generation and penetration level, the utilisation technique proposed in this work does not negatively affect the IPP.

1.2 Research Motivation

According to [4],[5], the world net electricity generation is anticipated to increase by 92.5 % by the year 2030, with undoubtedly, a large percentage coming from RESs such as wind energy. The intermittent nature of wind energy makes output generation unpredictable. Wind energy production is higher at night [6]. This may seem counter-intuitive because at night the earth cools causing more stable air at ground level. However, this allows the prevailing wind to flow without turbulence which gives steadier wind which is more harvestable. The demand for power is also substantially less, hence the issue of excess power generation and thus reverse power flow cannot be avoided when dealing with renewable energy sources that are stochastic in-nature. Grid component overloading, unintentional islanding, sympathetic tripping of the protection devices and over-voltage are some of the challenges confronting DNOs due to RPF. To overcome these challenges and ensure the reliability and sustainability of the grid, attention must be given to the issue of RPF particularly in the low distribution network which is directly connected to the end-user. In reality, there are still no standard means of preventing RPF on power system networks, with most of the techniques deployed only to keep the situation under control which at times may impacts negatively on IPPs that own the renewable generation companies. Therefore, there is a need to develop a more effective means of utilising RPF instead of controlling or preventing the situation.

1.3 Research Questions

The research study attempted to answer three principal questions:

(i) What level of wind energy penetration causes RPF on the investigated power system network?

(ii) What impact does RPF have on the entire power grid?

(iii) How can RPF be effectively utilised instead of merely controlling or preventing it?

Thus, this work proposes a novel method of utilizing reverse power flow (the excess power generated) for supplying power to a modern-day electric vehicle (EV) charging station.

1.4 Research Aims and Objectives

The research work aims to investigate and examine the issue of RPF on a power system network and provide an efficient way of utilising the surplus power generated. The primary aims of the research are as follows:

1. To investigate the possible penetration level of wind energy sources that can cause RPF on the investigated power system network;

2. To investigate and examine the impacts of RPF on the entire power system network in relation to the following conditions:

   - Power system losses on the entire grid;
   - Transformer loading system and losses;
   - Conductor loading system and losses; and

3. To investigate and analyse the effectiveness of a proposed power electronic transformer in voltage rise mitigation under different scenarios such as:

   - Voltage sag;
   - Voltage swell;
   - Variation in grid loading system;
   - Variation in the total power generated by the integrated wind farm; and

4. To develop effective and efficient means of utilizing the excess power generated on the grid using a multi-port power electronic transformer (MPPET) to supply power to an EV charging station.

1.5 Research Methodology

Fig. 1.1 shows the approach adopted to achieve the aims and objectives of the research work.

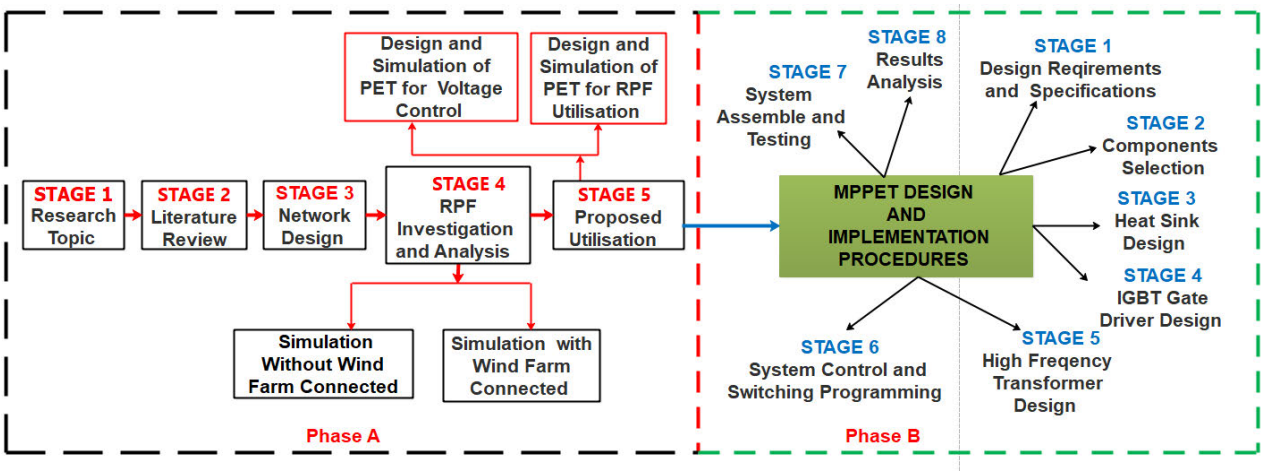

Figure 1.1: Research Methodology

1.5.1 Phase A

This phase presents the literature review and software simulation. Details are given below.

- **Literature Review**

  A comprehensive literature review was conducted on the current concept of the topic. The main focus of the review was on the concept of wind energy sources and the impact of wind energy on power system networks, focusing mainly on the issue of voltage rise and RPF. In the area of RPF, the causes and the impact on the grid was thoroughly reviewed. Furthermore, a review of the possible control and utilisation techniques was conducted. The concept of a power electronic transformer (PET) and EV charging technology was also reviewed.

- **Power System Network Configuration**

  For proper and efficient investigation and analysis of RPF, a complete power system network was designed and modelled using MATLAB/Simulink.

- **Reverse Power Flow Investigation**

  To investigate and analyse the impacts of RPF, the following conditions were considered. The network was simulated without a wind farm connected to ascertain that the power network worked according to the required standards. Voltage at each bus bar was measured and plotted so that comparison could be made when the wind farm is connected. The wind farm was then connected to the grid and the performance of the grid at different penetration levels was examined. To achieve this the output generation of the wind farm was continuously increased while all other parameters on the grid remained constant. This continued until RPF occurred on the grid.

- **Analysis of Reverse Power Flow**

  After the simulation of the network with and without wind farm, the result of the simulation was analysed and plotted. At this point, the percentage penetration level that resulted in RPF was determined. Furthermore, different impacts of RPF on the grid such as the impact on power losses, loading condition and connecting elements was analysed.

- **Proposed Reverse Power Flow Utilisation**

  After the investigation and analysis, the proposed utilisation technique was implemented using MPPET. For effective understanding of the proposed method, this stage was further grouped into two sections.

1. **Design and Simulation of PET for Effective Voltage Control**
   Over-voltage is one of the main effects of RPF and a PET is considered to be effective in mitigating the voltage rise on the grid, thus this section demonstrated the effectiveness of PET in voltage rise regulation on the grid.
2. **Design and Simulation of MPPET for Reverse Power Flow Utilisation**
   This section presents the simulation of a MPPET for supplying excess power generated on the grid to the proposed EV charging station. The design comprises both off-board and on-board charging stations.

1.5.2 Phase B

This phase presented the design and implementation of the proposed PET. The Phase consisted of eight stages as shown in Fig. 1.1 above. These stages are listed below.

- **Stage 1:** PET design requirement and specification;
- **Stage 2:** Component selection;
- **Stage 3:** Heat sink design and implementation;
- **Stage 4:** IGBT gate drive design and implementation;
- **Stage 5:** High frequency transformer (HFT) design and implementation;
- **Stage 6:** System control and programming implementation;
- **Stage 7:** System Assembly and testing; and
- **Stage 8:** Implementation results analysis.

1.6 Research Contribution

There has been rapid growth in the use of renewable energy sources in generating electricity; however, there are negative impacts, in particular of RPF, on the grid. This area of study is of significant value to DNOs and enables sufficient planning, monitoring and controlling of power system networks for effective integration of renewable energy sources in the future. The contributions of this research work are:

1. This research works provides a platform for investigating the possible penetration level of wind energy that causes RPF on the power system. To achieve this, the network under investigation is simulated without and with a wind farm connected. The level of

penetration that causes RPF is determined by continuously increasing the total output power generated by the connected wind farm until the grid is overloaded and RPF sets in. The total active power flow was measured at the PCC of the wind farm and also at the transformer TR3.

2. The research work provides a framework for analysing the impact of RPF on the entire power system network. In this case, the effects of RPF on power system losses and the effects on the connecting elements such as conductors and transformers are investigated and analysed.

3. The research work contributes significantly to knowledge by effectively investigating and analysing the effectiveness of a PET for effective voltage control under different situations on the grid. To achieve this, the work considers the impact of a PET on the grid during voltage sag, swell variation in grid loading systems, and output generation of the connected wind farm.

4. The work develops an effective means of utilising RPF without energy storage devices through a MPPET rather than controlling or preventing the occurrence of the situation on the grid. The research uses the excess power generated to supply power to an EV charging station instead of building additional generation for public charging stations.

5. The proposed MPPET can successfully accommodate both off-board and on-board charging techniques, thus the name multi-port power electronic transformer.

6. The proposed method can enhance improved integration of renewable energy sources. Also, it can be used with energy storage systems (ESSs).

1.7 Scope and Limitations

The research work investigated, analysed and provided an effective means of utilising RPF in a power system network. The analysis is based only on zone A of the network under investigation. The effectiveness of a MPPET in reverse power utilisation and in voltage rise mitigation was also examined. The investigation was limited to the use of wind sources of energy only in grid connected mode and to supply the excess power generated to an EV charging station only. Furthermore, the work considered only a grid to vehicle (G2V) system and the constant current EV charging method.

1.8 Structure of the Thesis

- **Chapter 1:** This chapter presents a general introduction to the research work. Research background, motivation, aims and objectives, methodology, contribution of the research, scope and limitation of the research as well as general arrangements of the thesis are presented.

- **Chapter 2:** This chapter presents the literature review of the research work. The general concept of power system networks, global installed capacity of renewable energy and wind power are discussed. The chapter also discusses future projection of the wind energy market status globally, wind energy conversion systems, wind turbine applications both in offshore and onshore modes. The impact of high penetration of wind energy sources on the power system network are also reviewed. Furthermore, the chapter gives an extensive review on RPF and its causes, impacts and the mitigation strategies of RPF. The chapter discusses the general concept of PET and EV charging technology. Classification, features, functionality and differences between a PET and a traditional line frequency transformer (TLFT) are presented. The concept of EV charging technology, types of EV, and EV battery charging technology are presented. Furthermore, EV battery charger technology, charging power levels, and comparison between on-board and off-board charging technologies are discussed. Finally, control strategies such as constant voltage control (CVCS) and constant current control (CCC) and advanced charging controlling (DCCS) are described.

- **Chapter 3:** This chapter presents investigation and analysis of RPF conditions under high penetration of wind energy sources. The penetration level of wind energy source that leads to RPF are determined. RPF at the PCC are investigated and analysed. Furthermore, the impacts of RPF on the power system connecting elements such as transformers and conductors are also investigated and analysed. In addition, the impact of RPF on power system, transformer and conductor losses are investigated and analysed.

- **Chapter 4:** The proposed RPF utilisation using a MPPET is presented in this chapter. For better understanding and analysis of the effectiveness of a PET in RPF utilisation, two stages of simulation scenarios are considered. The stages are:

  (i) Design and simulation of a PET for effective voltage rise mitigation since reverse flow accompanies voltage rise. In this section, normal and abnormal conditions on the grid are considered for simulation scenarios. The abnormal simulation scenarios

included: sudden changes in the system loading, voltage swells and dips and sudden disconnection of a connected renewable energy source.

(ii) Design and simulation of an MPPET for effective utilisation of RPF. This section presents active power flow monitoring at the PCC during RPF utilisation. Different characteristics of EV batteries are examined during this process.

- **Chapter 5:** This chapter presents experimental implementation and testing of the designed MPPET for validating the effectiveness of the MPPET in voltage rise mitigation and thus RPF under different loading conditions. The experimental set-up results are analysed and discussed.

- **Chapter 6:** This chapter presents the conclusion and recommendations for future work.

Chapter 2

Literature Review

2.1 Structure of Electric Power Grid

An electric power grid is an interconnection of networks for transporting electricity from the point of generation to end users. It consists of a generating station, a transmission network and a distribution network. The power generated from the generating station is transmitted at high voltage via long distance transmission lines to the distribution network, which delivers the power to the end users at the required voltage levels. The distribution network is made up of medium-voltage (MV) and low-voltage (LV) networks. Medium-voltage networks usually operate with a voltage level ranging from 11 kV to 22 kV. Low-voltage distribution networks are the part of the distribution network that directly connects electricity to residential users through distribution transformers. In some countries like America, low-voltage distribution networks operate at a voltage level range from 120 V to 240 V at 60 Hz frequency, while in Europe and Africa low voltage distribution networks operate at 220 V to 240 V at 50 Hz frequency. Fig. 2.1 shows the characteristics and voltage levels of an electric power network.

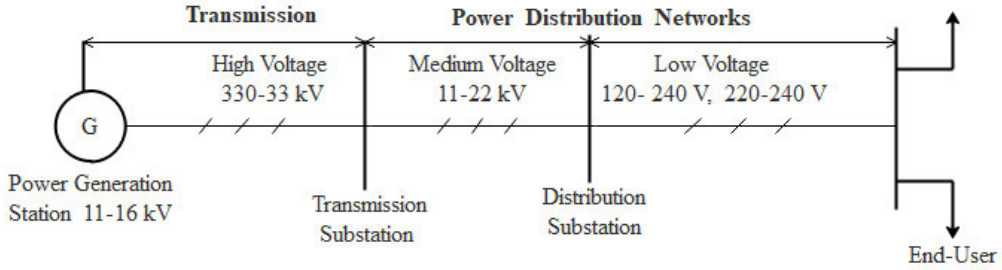

Figure 2.1: Characteristics and Voltage Level of Electric Power Network

Due to the liberalization of the energy market and demand for clean energy and contamination free environments, renewable energy sources are being integrated into distribution networks, changing the power generation system from a centralised generation system to decentralized generation system. Integration of renewable energy sources such as wind energy reduces transmission and distribution losses and improves the voltage profile level on the grid among other aspects. Nevertheless, high integration makes the grid more complex and prone to various challenges. Wind turbines can be connected to electrical power supply system grid at different voltages; i.e., low voltage, medium voltage, and high voltage as well as to the extra-high voltage system. While most of the wind turbines are connected to medium voltage (1 kV

- 35 kV) systems, future large offshore wind farms will be connected to the high and extra-high voltage level [7], [8], [9]. Table 2.1 shows the voltage system, size of wind farm and level of transmittable power to different levels of the electrical network.

Table 2.1: Transmittable power and connection of wind turbines to different levels of the electrical network

Network Voltage System	**Size of Wind Turbine or Wind Farm**	**Transmittable Power**
Low voltage system	Small to medium wind turbines	up to 300 kW
Medium voltage system	Medium to large wind turbines and small wind farms	up to 2 – 5 MW
Medium voltage system, at transformer substation to high voltage	Medium to large onshore wind farms	up to 10 – 40 MW
High voltage system	Clusters of large onshore wind farms	up to 100 MW
Extra high voltage system	Large offshore wind farms	> 0.5 GW

In [10], a wind farm is connected to a high voltage (HV) transmission system (35 kV - 230 kV). The authors present a novel solution algorithm for connecting the internal grid of a wind farm based on a combination between generic algorithm and a specific algorithm. Furthermore, [11], investigated the potential challenges of the wind farm, on voltage fluctuations, zone substation, and distribution transformer loading, power flow characteristics, and harmonic emissions with the integration of wind energy into both the high voltage (HV) and low voltage (LV) distribution network (DN). While in [12], the authors discussed the technical and economic assessment of a wind farm connected to 33 kV and 66 kV respectively. [13] discussed the connection of a wind farm to 132 kV and 400 kV transmission lines respectively in the Laingsburg and Karoo areas, Western Cape, South Africa. An electric power grid with integration of renewable energy sources such as wind and solar energy is shown in Fig. 2.2

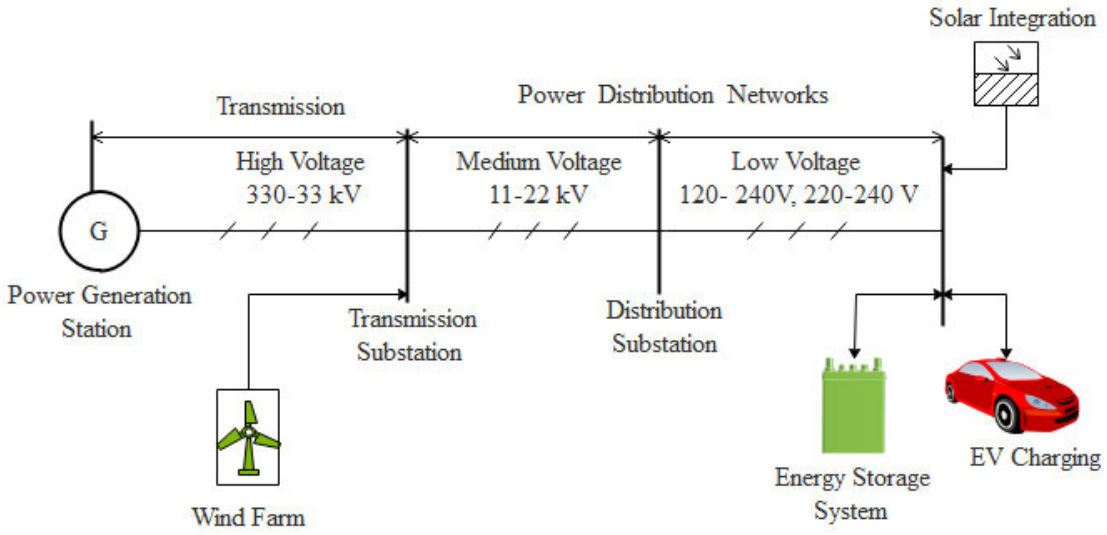

Figure 2.2: Power System Network with Renewable Energy Connected

2.2 Global Installed Capacity of Wind Energy

Wind energy has gained popularity among all renewable energy sources owning to its availability and environmentally-friendly features. Fig. 2.3 shows the cumulative installed capacity globally of renewable energy sources and wind energy [14],[15].

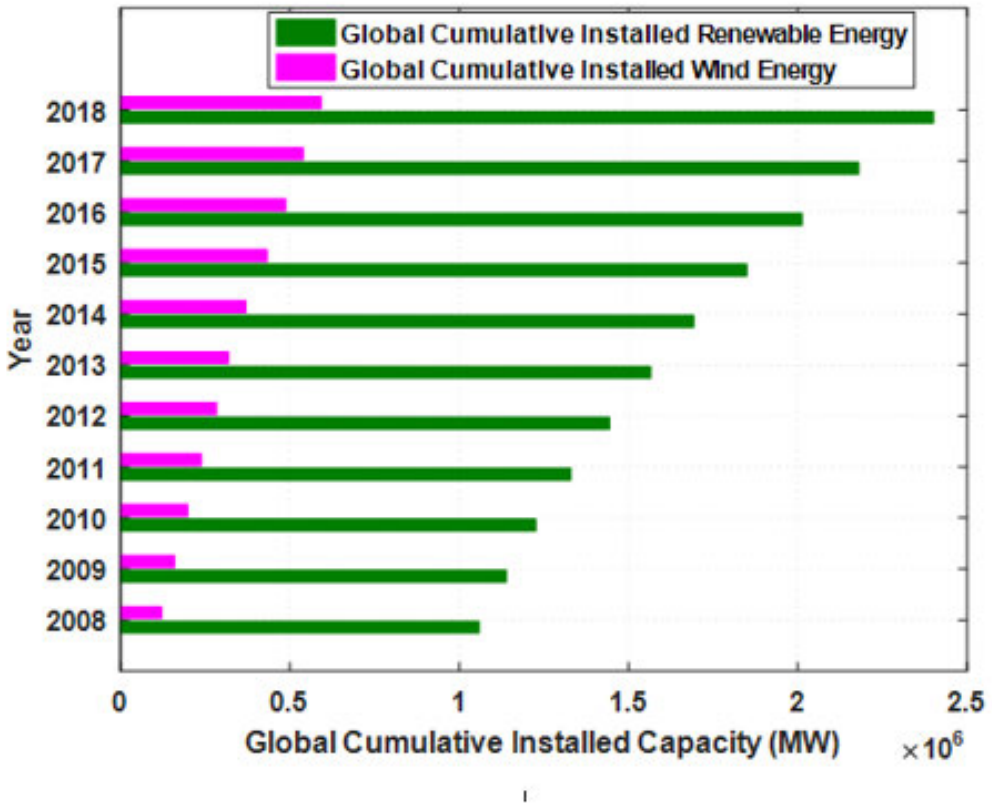

Figure 2.3: Global Cumulative Installed Capacity of RES and Wind Energy from 2008-2018

From Fig. 2.3 it is evident that the global wind energy market is increasing rapidly. The analysis is based on the total cumulative installed capacity globally of renewable energy and wind energy from 2008-2018. In 2008 there was 1,057,962 MW of installed renewable energy of which wind energy was 120,696 MW (11.41 %). The total installed renewable energy generation in 2018 was 2,400,000 MW, of which wind energy was 592,000 MW (24.67 %). Hence, installed Wind energy generation over 11 years (2008 to 2018) was estimated to be around 20.89 % of the total installed renewable energy generation. Fig. 2.4 shows the predicted cumulative installed capacity of wind energy for the period of 2020 to 2050.

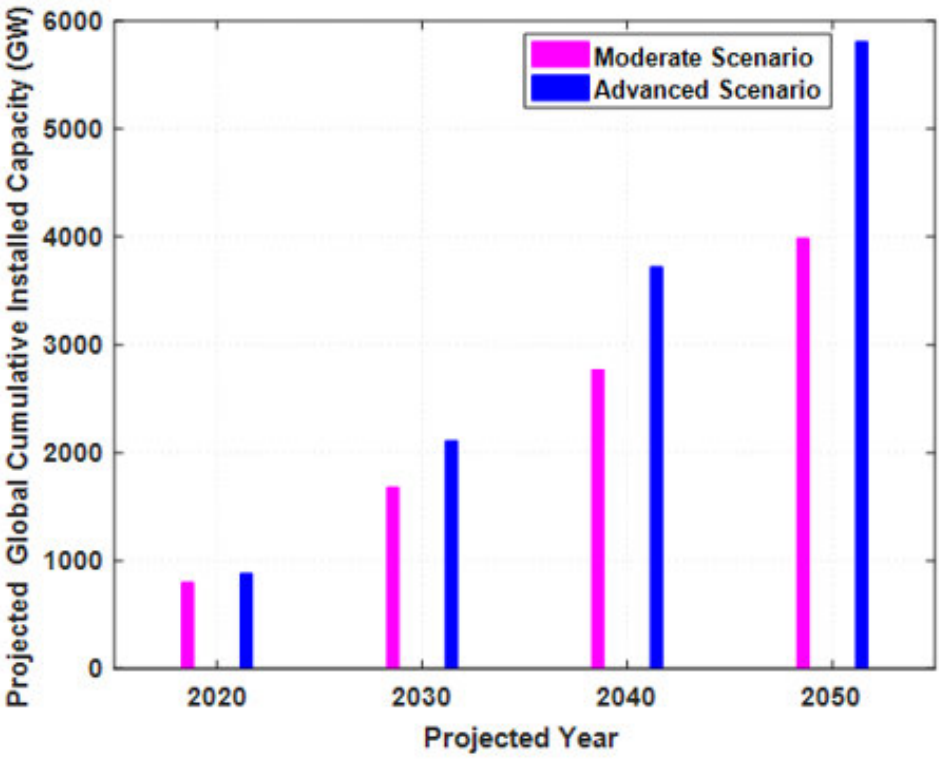

Figure 2.4: Projected Global Cumulative Installed Capacity of Wind Energy 2020-2030

The authors in [16] predicted the global cumulative wind energy generation based on two different scenarios: moderate and advanced. The global wind energy conversion (GWEC) based on a moderate scenario projected that by 2020 the total installed capacity of wind energy globally will be 797 GW and 1,676 GW in 2030 as shown in Fig. 2.4, while the total projections for years 2040 and 2050 are around 2,767 GW and 3,984 GW respectively. Based on an advanced scenario, GWEC projected that the total global wind energy production in 2020 and 2030 would be 879 GW and 2,110 GW respectively, while the projections for the years 2040 and 2050 is 3,721 GW and 5,806 GW respectively [16].

2.3 Wind Energy Conversion Systems

Wind energy conversion is a process of getting kinetic energy from wind and changing it into electrical energy. Fig. 2.5 shows the general process of wind energy conversion.

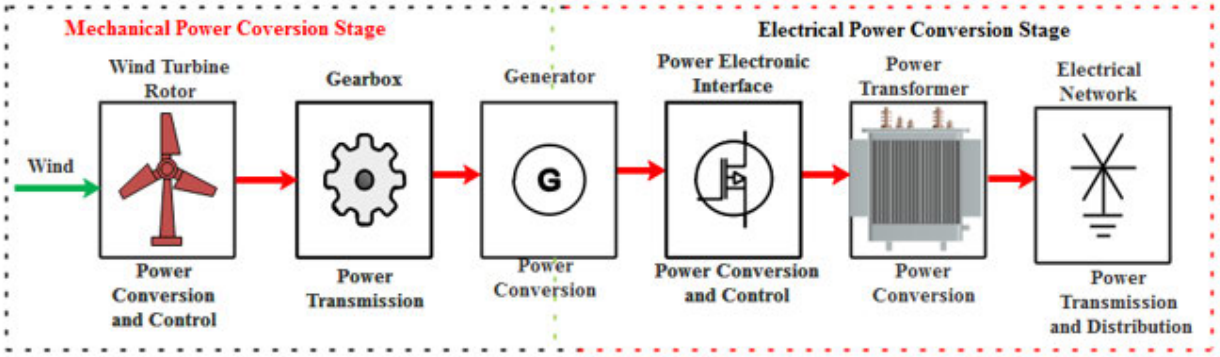

Figure 2.5: Wind Energy Conversion System

2.3.1 Wind Turbine Technology and Application

The transformation of wind energy into electrical energy is achieved using a wind turbine. The basic configuration of a typical wind turbine is shown in Fig. 2.6.

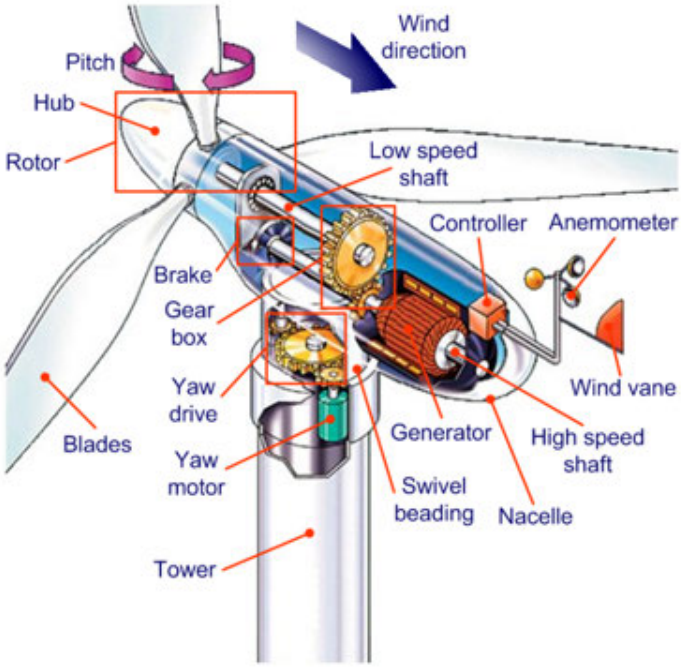

Figure 2.6: Wind Turbine [7]

The major components are: rotor, gearbox, generator and tower. There are turbines that eliminate the gearbox using direct drive generators with high pole number. The rotor consists

of the blade and the hub. The energy in the wind rotates the turbine. The rotor is joined to the main shaft, which rotates the generator to produce electricity. The shape of the rotor blade and the angle of attack relative to the direction of the wind determines the performance and efficiency of the wind turbine. The size of the turbine varies and depends on the manufacturer, nevertheless, most wind turbines are made up of three glass reinforced plastic blades. Other materials that can be used for rotor blade are metals such as aluminium and steel alloys and synthetic composites which consist of an polyester or epoxy matrix that is reinforced with glass fibres. Wind turbine rotors can be operate either upwind or downwind. In an upwind arrangement, the turbine faces the wind with the nacelle and tower behind it (downwind) so that it is unaffected by the tower to any great extent. In a downwind arrangement, the tower and nacelle are in front of the turbine. Virtually all wind turbines are upwind turbines. The two shafts (low-speed shaft and high-speed shaft) are joined by a gearbox which increases the rotational speed to the required speed by the generator to generate electricity. The tower is usually tubular steel, concrete or steel lattice. Tall towers enable turbines to capture more wind and generate more electricity than short towers because wind speed increases with altitude [7].

2.3.2 Applications of Wind Turbines

- **Onshore Wind Energy Technology**

  Onshore wind is one of the most developed renewable energy technology and presently plays a growing role in global energy production. Onshore wind farms are an economical technology. They are easier to maintain then offshore wind turbines. Onshore wind has the highest installed global capacity [17].

- **Offshore Wind Energy Technology**

  There is increasing installation of offshore wind. This is because offshore wind is normally stronger and more uniform compared to onshore wind. Offshore wind energy accounts for a small amount of the total installed wind power capacity across the globe. The growth of offshore wind farms has primarily been in Europe and Asia. The amount of electricity produced by a wind turbine is determined by the wind turbine capacity, wind speed as well as the arrangement of the turbine. Offshore wind turbines produce more energy per hour than onshore wind turbines due to their larger size and higher mean wind speeds. They are still not widely installed because of higher costs of installation and operation, and inaccessibility in poor weather. Limited locations for offshore wind farms have also contributed to the slow growth in their installation. The mode of operation of offshore and onshore wind turbines is the same; however, the power generated by offshore turbines

is transmitted through sub-sea cables to shore [17].

2.4 Impacts of High Penetration of Wind Energy on Power Grid

In traditional power networks the flow of power is unidirectional. The generated power at a centralised power station is transmitted directly to distribution networks via long distance transmission lines. However, introduction of renewable energy sources may cause a change in the direction of power flow on grid. One of the impacts of high penetration of renewable energy sources such as wind energy is reverse power flow (RPF), which generally occurs when the generation from the wind energy source exceeds the local load demand, causing power to flow in the opposite direction to the normal power flow [18]. The introduction of RPF may impact electricity networks negatively. Therefore, this section presents a general overview of RPF issues.

2.5 Reverse Power Flow and Mitigation Strategies

According to [19] and [20], renewable energy sources can have positive impacts on distribution system voltage profile, power quality and they can reduce power losses on distribution networks due to their proximity to end-users. However, high penetration can expose the grid to some challenges. RPF is one of the problems of high penetration of RES. Recently, RPF has been seen as a serious threat to electric power networks globally. Voltage rise is one of the consequences of RPF on the grid. RPF can lead to excessive power losses and cause malfunction of protection systems and grid instability.

2.5.1 Definition and Causes of Reverse Power Flow

Reverse power flow (RPF), is a situation whereby the power generated by the integrated renewable energy sources exceeds the local load demand, causing power to flow back to the substation and could feed power back into the transmission system [18], [21]. RPF can impede the normal operation of the grid and thus causes damage to the connected elements of the system such as transformers and conductors [22]. Reverse power flow causes over-voltage on the distribution feeder, increased short-circuit currents, protection desensitization, and potential breach of protection coordination and irregular operation of control equipment. Overproduction or excess power generation usually occurs during peak periods of generation and off-peak periods

of consumption. These periods vary from one renewable energy source to another. In wind energy, even with lower energy due to lower wind resource, there is more excess energy due to low demand.

2.6 Overview of Excess Power Generated From Renewable Energy Sources

This section presents an overview of excess power generated from different combinations of renewable energy sources. A hybrid renewable energy source (HRES) is the combination of different renewable energy sources. Various reported systems are briefly described below.

- For a HRES reported in [23], the excess power generated from solar PV and wind was 3839.54 kWh/yr which is about 64.2 % of the total power generated. This is even with battery storage.
- For the system reported in [24], which had solar, wind and diesel generation, the excess was 1163.8 kWh/year, which is about 3.3 % of the total power generated.
- The excess power generated by the HRES reported in [25] was 4519.3 kWh/y which was about 7 % of the total power generated. This consisted of PV and diesel generation together with battery storage.
- In [26], the excess power generated by a system with a wind turbine, PV and a small-scale hydro station was 7022.12 kWh/yr which is about 70 % of the total power generated.
- According to [27] and [28], about 33 % of the total power generated from a HRES consisting of solar PV, wind turbines and diesel generators, together with battery storage in a remote location in Palestine remained unused.
- According to [29], about 56.4 % of the total power generated from standalone a reported HRES consisting of PV panels and wind turbines without energy storage devices was unused.
- The authors in [30], show that about 14 % of the total power generated by a HRES comprising of PV and diesel generators, with battery banks, in remote houses in Langkawi Island (Malaysia) is not used.

These examples show that there is a pattern of excess power that needs to be utilized.

2.7 Impacts of Reverse Power Flow on the Grid

The introduction of RPF has a direct impact on the entire power system network. Some of these impacts are discussed below.

2.7.1 Reverse Power Flow and Voltage Profile

One of the parameters that determines the stability and effectiveness of the power system network is the voltage profile. High penetration of wind energy into the grid may alter the voltage profile of the network. RPF is accompanied by over-voltage or voltage rise on the grid [31]. Voltage rise is a situation whereby the voltage on the end-user side of the network is greater than the voltage on the supply side of the network. The situation becomes more critical during off-peak periods when the energy demand is low and the generation is high. RPF has problems in keeping the voltage within operational limits, thus leading to voltage rises on the grid. In general, over-voltage can increase power system vulnerability to voltage instability if not properly managed and controlled. This situation may be aggravated and eventually lead to voltage collapse on the grid and consequently system breakdown [32],[33].

2.7.2 Reverse Power Flow and Grid Protection

RPF on the grid makes protection and control more complex and difficult for system operators. At any point in time, a grid protection system must be able to effectively perform two basic functions: it must be able to recognise and pickup fault areas on the grid [34][35]. In order to ensure adequate security and reliability of a power network diverse protection schemes are put in place. The most common protection systems are over-current and over-voltage protection systems. All these systems are effective in conventional power systems because current flows only in one direction; however, RPF makes the system more complex. RPF leads to changes in the fault current level of the system and therefore imposes problems on the over-current protection system [36].

An over-current protection system (OPS) uses over-current protection relays. This is a device that differentiates between the incoming grid current and the predefined over-current relay current setting. They operate when the incoming grid current (phase current) is above the predefined pick up current of the relay by tripping the connected circuit breaker [37]. However, the presence of RPF greatly impedes the performance and effectiveness of the protection system.

According to [2], [34], [38], [39], and [40], the following protection issues may occur due to RPF on the grid: false tripping, blinding of protection, loss of fuse recloser coordination,

unsynchronized reclosing, and prohibition of automatic reclosing. False tripping is the most common problem associated with RPF on the grid. An increase in grid phase current is one of the effects of RPF. RPF causes the grid phase current to be higher than the predefined pick-up current in the over-current protective relay. In this case, the relay senses it as a fault and quickly reacts in order to mitigate the effect on the grid. False tripping can cause unintentional islanding. In addition, RPF can interfere with the voltage control system of the grid since it increases the voltage magnitude above the standard limit value thus causing the implementation of voltage control to be complex and difficult. This is because the control systems are designed based on a unidirectional power flow so cannot handle reversal of power on the grid.

2.7.3 Reverse Power Flow and Grid Loading

RPF has significant impact on grid connecting elements such as transformers, conductors and the connected loads. Transformers and conductors have a specific power ratings called thermal capacity. This determines the loading capacity. RPR causes overloading of these elements, which leads to violation of their thermal capacity rating [41],[42]. Also, RPF may cause damage to the connected loads due to excess current flow through. Aside from the overloading of these elements, RPF also leads to losses on the grid, consequently reducing the efficiency and the performance of the elements. The transformer winding loss is the sum of all the losses on both sides of the transformer and is given as:

$$T_{Los} = \sum I_{L,H}^2 R_{L,H} \tag{2.1}$$

where, $I_{L,H}^2$ and $R_{L,H}$ are the currents at the low and high voltage side and resistances of the transformer respectively. Conductor losses are determined using

$$C_{Los} = \frac{P^2 R}{V^2} \tag{2.2}$$

where, C_{Los} is the conductor or line losses, P is power flowing through the conductor, R is the resistance of the conductor in Ohms and V is the voltage of the conductor in V. This assumes that there is unity power factor.

2.7.4 Reverse Power Flow and Grid Congestion

Power system congestion occurs when the power flowing through the connecting elements exceed their thermal capacity ratings. The intermittent nature of wind energy makes it difficult to predict the power output generation; consequently, grid operators may find it difficult to develop

effective control strategies for the system. This can result in unanticipated congestion on the power system through overloading [42].

2.7.5 Reverse Power Flow and Power Losses

RPF incurs losses on all systems of power networks from transmission systems to secondary distribution systems. As the RPF increases active power losses also increase [42]. The active power loss in a line in the system under investigation is given by

$$P_{\text{Loss}} = I^2 R \tag{2.3}$$

where, I and R are the current and resistance of the line. The absorbed reactive power is

$$Q_{Abs} = I^2 X \tag{2.4}$$

where, I and X are the current and inductive reactance of the line. This assumes the short line power line model represented by a series resistance and inductance. Smart grids do tend to be at distribution levels over a limited area. Obviously if they are larger systems then power line can be represented by T or Π models that includes capacitance which will generate reactive power.

The total active power losses and absorbed reactive power in the network under investigation are calculated using

$$P_{\text{TLoss}} = \sum_{i=1}^{N} P_{\text{Los}} \tag{2.5}$$

$$Q_{Abs} = \sum_{i=1}^{N} Q_{Abs} \tag{2.6}$$

where, N is the total number of lines in the network under investigation. Power and reactive power balance can be used. All power generated has to equal the sum of all loads and losses and likewise all reactive power generated has to balance with the reactive power absorbed. By convention, assuming a sinusoidal system, reactive power is absorbed by inductive components while capacitive components generate reactive power. Power electronic devices such as STATCOMs, and synchronous generators, can be used to control the reactive power.

2.7.6 Reverse Power Flow and Power Quality

Power quality is concerned with the reliability of power supply which is associated with parameters such as voltage, current and frequency. The voltage variation as a result of RPF may

negatively affect power quality. In addition, over-voltage, and difficulty in voltage control due to RPF power may deteriorate the grid power quality [43][44].

2.7.7 Reverse Power Flow and Grid Stability

Due to the complexity of the protection and control systems of the grid during RPF, the stability of the system is at high risk. In addition, the high voltage profile of the grid during reverse power flow also contributes to the high level of instability on the grid. Furthermore, the reliability of the system will be greatly affected due to the fact that the protection devices will be trying to react and mitigate the effect of the unwanted situations such as over-voltage and over-current due to RPF and consequently the system will become unstable [44].

2.7.8 Reverse Power Flow and Islanding

This is a situation on a power network where a certain portion of the network is out of service for some period of time. Islanding can be intentional and unintentional. Intentional islanding is where the system operator deliberately shuts down certain portions of the system due to some circumstances. Unintentional islanding is a situation where a certain portion of the system is suddenly broken down. The sudden breakdown of a certain portion or the entire system may occur due to RPF and violation of the thermal rating of connecting elements such as transformers and conductors through overloading. The breakdown of the power grid due to RPF has diverse negative effects on all energy stakeholders [45][46].

2.7.9 Reverse Power Flow and Total Harmonic Distortion

High penetration of renewable energy source introduces harmonics into the grid. According to [47], the integration of distribution generation into the power grid is likely to introduce harmonic problems in the power system. These come from inverters and some synchronous machines. [48] illustrates that the converter-inverter system used in wind farms produces harmonic emissions, which may result in power quality problems within the wind farm and the grid connected to it. The authors in [49] show that most power utilities within Southern Africa are faced with the challenges of harmonic distortion due to the high penetration of renewable energy sources (RES) and the use of electronic devices. There is an excessive total harmonic distortion (THD) measured at the point of common coupling (PCC).

In [50], the harmonic emission measured at the connection point from the wind turbine to the medium-voltage collection grid was investigated. This was relatively high; however, the high emission was attributed to strong variations in active power flow (fundamental current) and not caused by the power electronics.

According to [51], the generation unit characteristics and their daily generation profiles, network configuration characteristics, and load profiles, as well as the grid codes, are some of the factors that determine the amount of distributed generation integrated into a particular power grid. High penetration of RESs in the DNs (medium voltage networks) may cause reverse active power flows, voltage rise and increase in voltage distortion due to the large use of power-electronic converters where the generation interfaces with the grid. According to [52], harmonics have some negative effects on power system connecting elements and loads. Harmonics cause an increase in thermal capacity of the connecting devices such as transformers and conductors, and therefore cause overheating. Aside from the overheating of the elements, harmonics cause malfunctioning of the protection systems such as irregular circuit breaker operation.

In order to prevent harmonics and ensure safety in the performance of the power grid and the connected loads, international standard limits have been instituted regarding the total harmonic generation in a power system. According to [53], IEEE 519-1992 is one of most widely used international standards for harmonics restriction on the grid. Standard limits are set for both voltage and current distortion and IEEE 519-1992 proposes to limit the harmonics generation based on the obtained value of the short circuit level at the PCC and the magnitude of connected loads. Even though the total voltage harmonics distortion restrictions are encountered at the PCC, they can feed down to the connected loads. Since the total voltage harmonic distortion is independent of the total harmonic of current flowing through the grid impedance, the total voltage distortion will be higher downstream because of the high harmonic currents generated and high impedance. Based on IEEE 519-1992, Table 2.2 shows the proposed standard harmonic voltage limits. The limits are intended to be applied at the PCC.

Table 2.2: IEEE Standard 519-1992 Harmonic Voltage Distortion Limits

Bus Voltage at PCC	Individual Voltage Distortion (%)	Total Voltage Distortion (%)
69 kV and Below	3	5
69 kV to 161 kV	1.5	2.5
161 kV and Above	1	1.5

2.8 Mathematical Analysis of Reverse Power Flow and Voltage Rise on the Grid

RPF occurs during low demand and high generation which strongly depend on the type and nature of the RESs. The simple power network in Fig. 2.7 is considered for mathematical analysis of RPF and voltage rise (VR) issues.

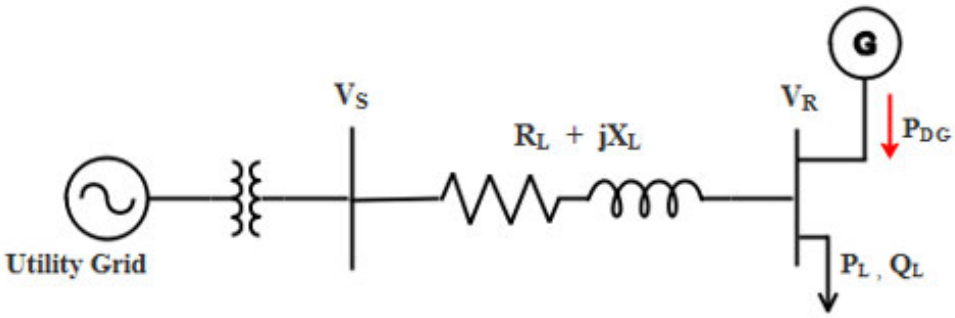

Figure 2.7: Two-Bus System with Wind Energy Source Connected

Considering Fig. 2.7, RPF and VR will occur if the total power generated (P_{DG}) by the connected wind energy source (G) is greater than the total power demanded by the connected load (P_L). The receiving end voltage is given as:

$$V_R = V_S - I\left(R_L + jX_L\right) \tag{2.7}$$

where the current I is a function of the receiving end power P_L, reactive power Q_L (neglecting the renewable generation) and voltage V_R::

$$I = \frac{P_L + jQ_L}{V_R} \tag{2.8}$$

By substituting (2.8) into (2.7) then the receiving end voltage is obtained:

$$V_R = V_S - \left[\frac{P_L + jQ_L}{V_R}\right] \times \left(R_L + jX_L\right) \tag{2.9}$$

Expanding (2.9) gives:

$$V_R = V_S - \left[\frac{P_L \times R_L + Q_L \times X_L}{V_R}\right] + j\left[\frac{Q_L \times R_L - P_L X_L}{V_R}\right] \tag{2.10}$$

which can be simplified to:

$$V_R = V_S - \left[\frac{P_L R_L + Q_L X_L}{V_R}\right] \tag{2.11}$$

By considering the connected renewable energy source, the receiving end voltage can be re-written as:

$$V_R = V_S - \left[\frac{\left(P_L - P_{DG}\right) \times R_L + Q_L\left(X_L\right)}{V_R}\right] \tag{2.12}$$

where the renewable generation is contributing PDG but not contributing any reactive power to the system. From this equation, it can be seen that voltage at the receiving end will increase

depending on the degree of the RPF, and the line resistance.

By considering a larger power network, the voltage variation at the PCC is

$$\Delta V_{ji} = \frac{R_{ij}\left(P_{Gj} - P_{Lj}\right)}{V_j} + X_{ij}\left(\pm Q_{Gj} - Q_{lj}\right) \tag{2.13}$$

where, ΔV_{ji} is the change in voltage level at the PCC, P_{G_j} and Q_{Gj} are the active and reactive power of the connected RES to j^{th} bus, P_{Lj} and Q_{Lj} are the active and reactive power of the load connected to j^{th} bus respectively. R_{ij} and X_{ij} are the resistance and reactance of the connected lines. In order to effectively compute and compare the level of RPF on the grid, an energy balance and feeding index is used. The energy balance index is defined as the difference between the total power generated on the grid and the total load demand on the grid. The energy balance index (EBI) is:

$$\text{EBI} = TA_g - TL_d \tag{2.14}$$

where, TA_g and TL_d are the total active power generated by the connected renewable energy and total load demand on the grid. The feeding index (FI) is defined as:

$$\text{FI} = PL_M\left(\frac{TA_g}{S_L}\right) \tag{2.15}$$

where PL_M is the maximum penetration level of the renewable energy source, and is the apparent power of the connected load. For effective comparison and identification of normal loading from overloading on the grid, the EBI can be grouped into three conditions: the normal loading condition, critical loading condition and overloading condition. The normal grid loading condition is a situation where the EBI is less than zero (EBI < 0), critical loading is when EBI is equal to zero (EBI $= 0$) and grid overloading is a situation where EBI is greater than zero (EBI > 0), at this point, excess power is being generated on the grid. During this period, the voltage at the PCC rises within an acceptable range, since RPF is accompanied by voltage rise as described in (2.12). In a large network, the cumulative overloading power is obtained from

$$P_{TG} = \sum\left(TA_g i - TL_{di}\right) = \sum \text{EBI}_i \tag{2.16}$$

where, $\sum \text{EBI}_i$ is the aggregate excess power generated when considering the worst case on the grid; that is maximum generation and minimum load demand. RPF depends on the voltage level at the PCC. If the voltage at the PCC is greater than 5 % of the grid nominal voltage, then voltage rise will occur which causes RPF onto the grid. The voltage rise or over-voltage

on the grid depends on the penetration level of the connected renewable energy.

2.8.1 Penetration Level

According to [54], wind energy penetration level can be defined in several ways.

1. Wind energy penetration can be defined as the percentage of demand covered by wind energy in a certain region, usually on annual basis:

$$\text{Wind energy penetration (PL) (\%)} = \frac{\text{Total amount of wind energy produced (TWh)}}{\text{Gross annual electricity demand (TWh)}}$$

2. The wind power penetration level can be defined as the total installed wind power in a certain region in relation to peak load in the region over a certain period:

$$\text{Wind power penetration (PL) (\%)} = \frac{\text{Installed wind power capacity (MW)}}{\text{Peak load (MW)}}$$

In the work described here, the second definition will be used to determine the wind penetration level on the investigated network, i.e., the wind power penetration, thus the wind penetration level is defined as:

$$\text{Wind power penetration (PL) (\%)} = \frac{\text{Installed wind power capacity (MW)}}{\text{Feeder load (MW)}}$$

The wind farm will be connected to zone A of the network and the load connected to feeder B7 is considered as the feeder load.

2.9 Reverse Power Flow Mitigation Strategies

RPF is a serious challenge for utility companies globally and many strategies have been developed in order control the situation. In this section, some of those strategies are reviewed. For the purpose of this thesis, the strategies reviewed are grouped into two categories. The first category is the energy management system (EMS) approach and the second category is the voltage rise (VR) mitigation approach.

2.9.1 Energy Management Approach

In this approach, different strategies have been used for monitoring and controlling the performance of electric power network under RPF.

The main type of energy management employed is demand-side management (DSM). According to [55], DSM refers to a system of managing consumers' energy usage so as to yield the desired changes in load profile. DSM is a means of reducing total energy consumption in the residential sector, and is more effective when accompanied with incentives for the participants. The main type of DMS deployed in handling RPF is the demand response (DR) approach. Originally, DR was aimed at encouraging the consumers' to adjust their energy consumption in accordance with electricity pricing by giving the participant incentives. However, due to the advancement in technology, the system was used to manage RPF in conjunction with ESSs. The technology employed in DR is a load shifting approach. This approach involves shifting the use of any domestic appliance from peak to off-peak when there is excess power generation based on the type of renewable energy used. One of the major domestic appliances used for this purpose is a water heater. In many cases, this approach has been combined with the use of ESSs such as batteries. According to [56], [57], [58] and [59], the performance and effectiveness of the approach has been proven to yield good results; however, there are some weaknesses in this approach, including the high cost of the energy storage devices involved. The capacity of the storage system to store large quantities of electricity places a restriction on the use of this approach. Furthermore, the method of shifting energy consumption may pose an inconvenience to the customer, especially where an incentive is not provided. This approach may not be effective where the control method is manual and installed at the consumers' premises due to the fact that the occupants may not be available to switch on the control system when there is excess generated power, especially during the day when they are away at work. Thus, this approach can only work effectively for stand-alone renewable energy applications because the RPF in stand-alone and rooftop applications is minimal.

2.9.2 Voltage Rise (VR) Control Approach

Voltage rise is one of the problems of RPF [60], [61], [62]. Different approaches have been deployed to control and normalize the effect of voltage rise on the grid. According to [63],[64],[65], some of these approaches are

- Line impedance reduction;
- Reactive power compensation;
- Voltage control by using on-load tap changer transformer (OLTC); and
- Generation curtailment.

The level of voltage rise on the grid depends on the resistance of the conductor. The higher the resistance of the conductor the higher the voltage rise on the grid. In this case, the effect of resistance on the voltage rise can be mitigated by increasing the size of the conductor via conductor reinforcement. The reactive power compensation method uses flexible AC transmission system (FACTS) devices such as static var compensation (SVC), static synchronous compensation (STATCOM) and shunt capacitor bank to control and regulate voltage as well as other aspects of the distribution network system. FACTS devices yield good results. The OLTCs are used to maintain constant voltage supply to end users within the specified voltage limits; transformers are provided with automatic voltage control (AVC) relays to monitor and control the voltage.

According to the literature, all these voltage control techniques have proven to be effective in controlling voltage rises on the grid, however, there are some drawbacks to the use of these approaches. According to [34], they need a high level of communication within the grid components, therefore there is a high cost of implementation. In addition, some of these techniques, such as OLTC and reactive power compensation, are known to decentralize the voltage control technique, thus do not provide a solution for the entire grid. Line resistance reduction needs excessive finance since the conductor need to be upgraded and this can only be achieved by replacing all the conductors in the grid. Also, reactive power methods incur high losses on the grid, and require high component thermal rating. The OLTC approach is restricted by its tapping capability.

Generation curtailment is a method used to control the total output active power generated by the connected renewable energy in accordance with the grid demand. Curtailment in wind energy is the situation where the output of wind plants is reduced to a level below its maximum generation capacity. Curtailment can be implemented if the transmission system is overloaded in a certain region, when supply exceeds demand, and the grid operator may need to back down local generation to maintain system stability; it can occur during low price periods where the grid manager decides to curtail high-cost wind or solar in order to keep lower priced resources on-line. Curtailment can be implemented if the owner needs to carry out maintenance [66].

Other approaches for controlling voltage rise on the grid include computational intelligence approaches such as genetic algorithms (GA), artificial neural networks (ANN) and fuzzy logic (FL). Optimal sizing of renewable energy sources on the grid has been employed to control voltage rise. These approaches work in accordance with the varying conditions and grid demand. However, the implementation of these techniques requires a high level of programming and a high level of input data which makes the system more complex.

Another approach is reverse power relay [67]. The principle of a reverse power relay is similar to a normal over-voltage relay, the major difference being that reverse power relay is directional. The relay monitors the power flow from the utility grid running in parallel with the connected renewable energy sources. The reverse power relay prevents a reversal power by disconnecting the connected renewable energy sources from the distribution network when a fault occurs. It estimates the reverse power and proposes corresponding adjustment values to provide solutions to protect the distribution network according to the relay settings and situation on the grid. The major drawback of the approach is the disconnection of the renewable energy sources which may not be agreeable to the independent power producer (IPP) because it will affect their financial planning.

In addition to the above utilization methods, other means of RPF utilization methods such as the use of lump loads are presented in [68].

2.10 Recent Research Work on Reverse Power Flow Utilisation and Control Strategies

Some of the recently proposed control measure deployed to control RPF are now summarized.

The authors of [58] proposed energy management by means of a Supply and Demand Interface (SDI). The aim of the proposed method is to reduce RPF at the customer end and prevent RPF from the distribution network propagating into the transmission system. They show that the maximum RPF at the customer end was reduced by 19 % when using heat pump water heaters (HPWH) with storage battery. The major drawback to this method is the stochastic nature of photovoltaic (PV) power which means that the output generation of the PV cannot be predicted. The degree of RPF and storage battery capacity is another issue that restricts the use of the proposed method.

A method for energy management was put forward in [69]. This was through the use of DR. The authors proposed the use of HPWHs during the daytime for using the excess power generated from the rooftop PV. The use of HPWH in the daytime reduced RPF as well as energy consumption. However, aside from the inconvenience the method imposes on the end-user from shifting the use of the water heater from morning to afternoon, the level and duration of RPF imposes restrictions on the proposed method.

The authors in [70] propose an optimal sizing and location method for PV systems on the power system network in order to avoid RPF on the grid. The process works for maximum line energy losses, with the anticipation of RPF, using a simple optimization technique. The

highest disparities between the feeder load curve and the PV output generation curve are used in this technique. When there is a discrepancy, the PV system will not generate at its maximum capacity at the time the feeder meets its peak demand. The method is repeated at all the nodes on the feeder in the upstream direction commencing from the far end node. At the end of the iteration process, the node and the corresponding location where the maximum generation occurs is selected as the best solution. Apart from avoiding RPF, the method reduces power loses during the day. Nevertheless, the technique is a lengthy process and the generated capacity of the PV is restricted, therefore, the method may not be viable.

An optimal management planning method was proposed in [59] for using the excess power generated from the rooftop PV. The method uses HPWHs in conjunction with ESSs. The proposed method is based on the DR principle. According to the authors, when the maximum permissible RPF was 60 % of the entire energy consumed by the HPWH, its usage was changed to a period with limited production. The authors state that the proposed method reduces the average daily RPF from 9.0 kWh per day to 7.5 kWh per day. However, the change in the use of the water heater poses an inconvenience to the user. In addition, the unpredictable output generation of PV impedes the effectiveness of the method.

The effects of PV on low voltage distribution networks was investigated in [71]. This work developed a mitigation strategy to control the output generation using distributed ESSs. The proposed technique can reduce the influence of unexpected change in the total power generated due to unpredictable weather conditions by setting the ESS into a temporary discharge mode. Nevertheless, the capacity of the storage devices in comparison with the level of excess power generated is a challenge to the proposed method.

Authors in [72] propose the use of EV battery as an ESS for excess power produced by rooftop PV. The method aims to reduce RPF and reliance on the utility power system for charging EV batteries. According to the authors, the investigation demonstrates that using the rooftop PV to charge the EV battery at home will reduce the aggregate sum of power purchased from the utility and furthermore control the degree of RPF on the grid. The major challenge and drawback of the method is the capacity of the EV battery to store the excess power generated.

A new automatic distribution system was proposed in [73] that can accommodate a large PV capacity using smart metering data. The system can monitor the voltage performance of the grid and perform automatic disconnection of some PV systems when the predefined grid voltage is about to be violated. There is a high cost in building a new automatic power distribution system, and there is consumer inconvenience during PV disconnection.

The authors in [74] proposed a method of incorporating a directional over-current (DOC) protection scheme into grid transformers for improving on the existing schemes by setting RPF constraints to accommodate integration of DG into the distribution networks. The setting of the protection system determines the maximum amount of power that can flow through the transformer. However, the costs of upgrading existing traditional line transformers and the time frame of deployment is a drawback to the proposed method.

An index-based assessment method of controlling VR and RPF under high penetration of PV was developed in [75]. The authors determined the suitable range of the proposed indices and safe border, which they contrasted with the basic active power curtailment technique without constraints. This was to prevent VR. The proposed method performed better than the basic active power curtailment method. The proposed method can be used in combination with other voltage control strategies such as reactive power control to enhance voltage control when there is RPF due to high penetration of PV. This makes the scheme less effective and more complex to implement. However, the method needs modification before it can be used in a larger power system networks with high integration of PV. Therefore, the research work proposed a method for using RPF due to excess power generation from a wind energy source to supply power to a modern EV charging station using an MPPET. This can connect both AC and DC loads, it can be used for both AC and DC charging and it allows the off-board and on-board charging methods. MPPETs have the capability of voltage regulation, it allows the use of energy storage devices, and supports bidirectional power flow where it can supply power back to the grid. Furthermore, the proposed method is scaleable and flexible in usage therefore it can accommodate new technology.

2.11 The Concept of Power Electronic Transformer and Electric Vehicle Charging Technology

The concept of a PET was first introduced by McMurray in 1970 [76]. Since then it has been explored by many researchers for different purposes. Recent advances in PET technology has challenged the traditional line frequency transformer (LFT) in relation to its heavy weight and its harmful effect on the environment due to the use of oil for cooling among other reasons. In addition, the emerging technology of the smart grid and the use of RESs in generating electric power has encouraged the use PETs. A PET can transform power system voltages from one form to another through the use of power electronic converters. Such a system is also known as a solid state transformer (SST), electronic transformer (ET), intelligent universal transformer

(IUT) an

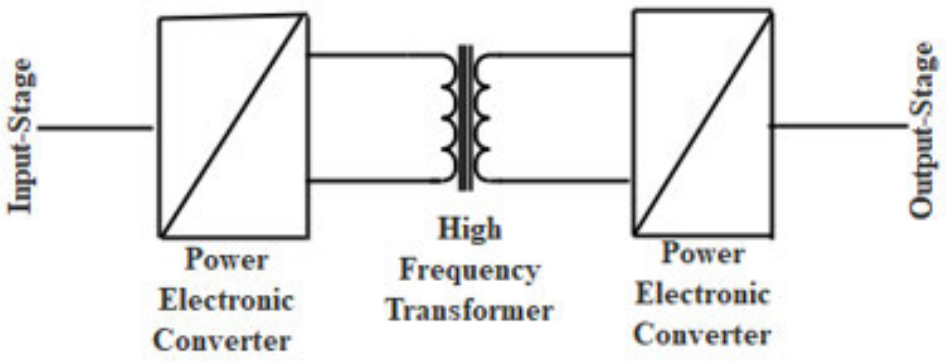

Figure 2.8: Basic Structure of Power Electronic Transformer

A PET consists of power electronic converters on the primary and secondary sides (input and output stages) with a high frequency transformer in the middle. The two power electronic converters perform voltage conversion, voltage regulation and frequency regulation, thereby enhancing bi-directional power flow and reactive power control. The HFT provides electrical isolation and reduction in weight [77].

2.12 Classification and Topology of PET

PETs can be classified into two with different topologies depending on its application as shown in Fig. 2.9.

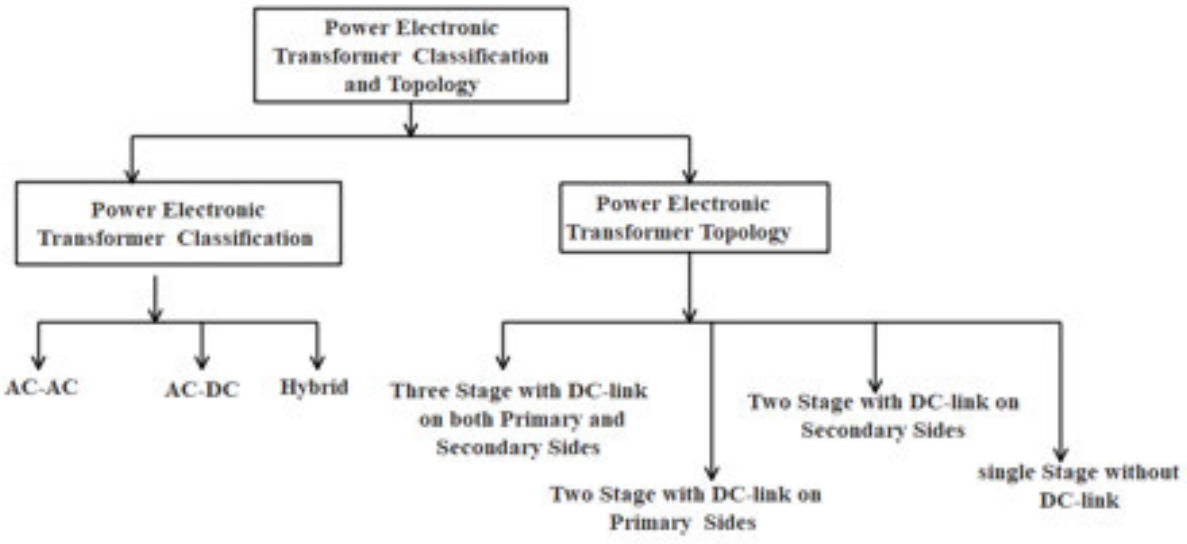

Figure 2.9: Power Electronic Transformer Classification and Topology

2.12.1 Classification of Power Electronic Transformer

- **AC-AC Based Power Electronic Transformer**

  AC-AC conversion is usually done using back-to-back inverters with a DC link. It possible to do AC-AC without a DC link. The first generation of DC-link-less AC-AC PETs utilized mainly of cycloconverters. Recently, matrix converters (MC) have taken over due to advances in technology and the advantages of MCs over cycloconverters. The PET, when utilizing AC-AC matrix converters on the input (frequency step-up) and output (frequency step-down) performs grid-frequency AC-AC power conversion with some voltage regulation and isolation. It offers advantages such as no DC-link capacitor, high efficiency, compact circuit design and regeneration capability. The AC-AC PET allows bi-directional power flow ability and power factor correction without an ESS. The HFT provides electrical isolation along with voltage transformation. However, it imposes high stress on the semiconductor devices due its inability to provide fast voltage regulation and voltage sag compensation due to the absence of an ESS [78],[79],[80]. These devices still require some investigation.

- **AC-DC Based Power Electronic Transformer**

  AC to DC PET transforms alternating current (AC) input into direct current (DC) output. It has bi-directional power flow capabilities which makes it suitable for motor drive application and battery charging/discharging in plug-hybrid EVs. This topology combines all the advantages of an AC-DC converter and an HFT, thus making it more efficient and effective. An AC-DC PET can also serve as an interface between micro-grids and the utility grids.

- **Hybrid Power Electronic Transformer**

  Hybrid AC-DC-AC PET performs multi-stage voltage conversion. It combines the characteristics of AC –DC and DC to AC converters with a high frequency transformer for its effectiveness. It allows the use of ESS due to the DC link. The PET can realize the input power factor correction and can suppress the harmonics and allow bidirectional power flow.

2.12.2 Power Electronic Transformer Topology

The PET can be grouped into four different topologies as described in Fig. 2.9 [81], [82].

- **Single-stage without DC-link**

  This topology makes use of direct MCs. The major advantage of the topology is the

limited number of switches required and reduced losses. However, absence of a DC-link restricts the utilisation and hence restricts the usefulness in terms of power factor compensation (PFC), and integration of RESs and ESSs. The absence of an ESS reduces the grid ride-through capability of the topology. The general structure of the topology is shown in Fig. 2.10.

The HFT can be single or three phase which will lead to the need for either single or three phase matrix converters. A single phase matrix converter is shown in Fig. 2.11. This has six bi-directional switches - these switches are a characteristic of matrix converters. It will operate in a similar manner to an inverter except the supply is not DC, but an AC supply of a different frequency. If the HFT is three phase then a three-phase to three-phase matrix converter is required. These can have several topologies but the two basic direct and indirect matrix converters are shown in Fig. 2.12. Again, bi-directional switches are used and the most simple converter is the direct converter with nine bi-directional switches as shown in Fig. 2.12(a) [83]. The indirect matrix converter in Fig. 2.12(b) allows some understanding of the matrix converter with a virtual DC link V_{pn}. The switching patterns can be used to map to the switches in the direct converter. The operation is described in [84].

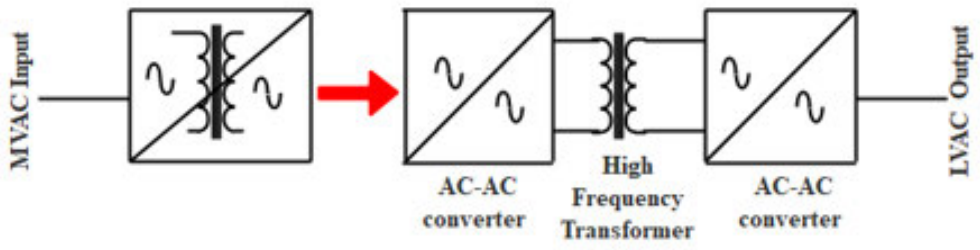

Figure 2.10: Single-Stage without DC link

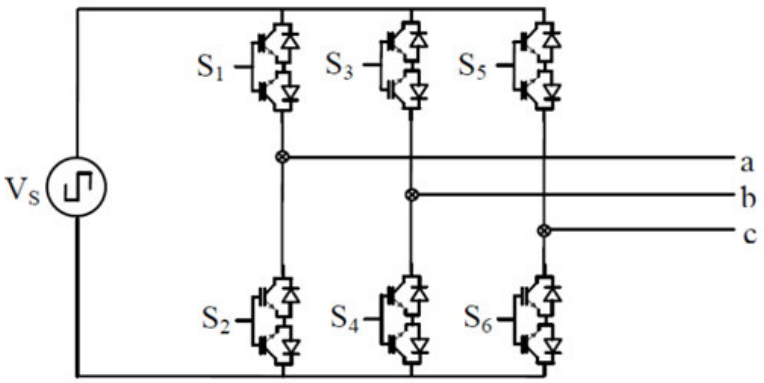

Figure 2.11: Single-phase to 3-phase matrix inverter [78]

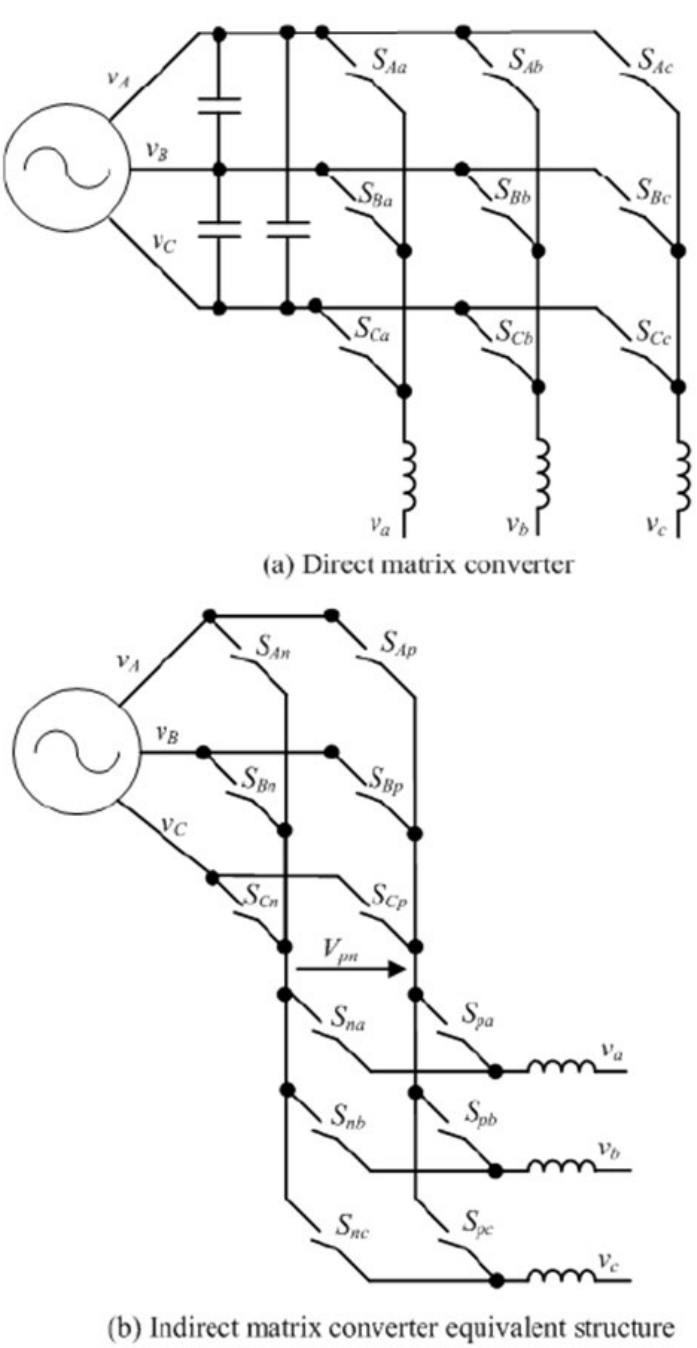

Figure 2.12: 3-phase to 3-phase matrix inverters - direct and indirect [84]

- **Single-stage with DC-link on the Secondary side**

  The single stage topology with a secondary DC-link is shown in Fig. 2.13 [85].

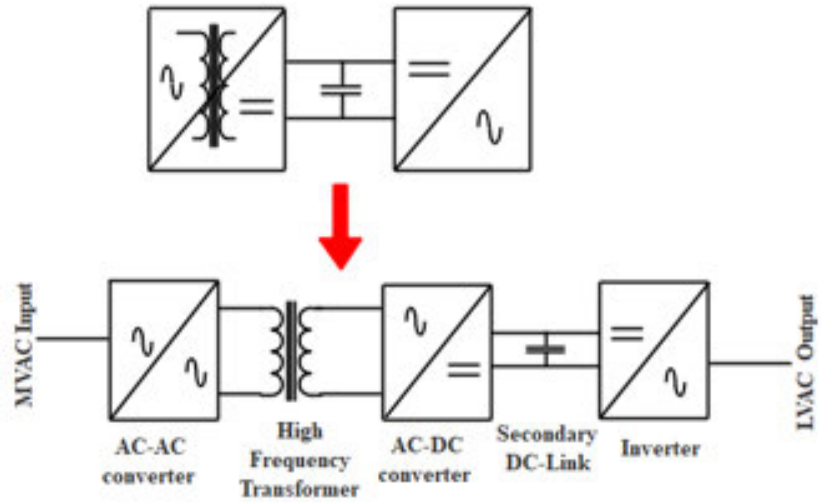

Figure 2.13: Structure of Two Stages PET with DC-link on the Secondary Side

- **Single-stage with DC-link on the primary side**

  Fig. 2.14 shows the structure with DC link on the primary side

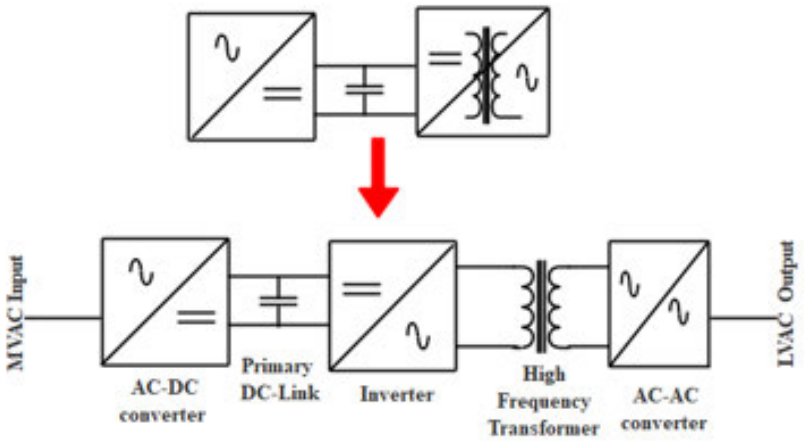

Figure 2.14: Structure of Two Stages PET with DC-link on the Primary Side

Fig. 2.13 and Fig. 2.14 have similar features, the only difference being the placement of the DC-links. The topology with a DC-link on the secondary side has the capability of regulating the output voltage, output reactive PFC and the ability to supply three-phase power from a single-phase system. However, the topology does not allow integration of RESs and ESSs due to the absence of a DC-link at the primary side.

The topology with a DC-link on the primary side lacks the reactive power compensation on the secondary side due to the absence of a DC-link on the secondary side. In addition, this topology has high ripple, since the input ripple cannot be absorbed in the secondary DC-link. However, the presence of the DC-link on the primary side enhances primary

converter output power quality and allows integration of RESs and ESSs. Due to this feature, this topology is considered to be one of the best PET topologies.

- **Three-stage topology with DC link on both the primary and secondary side**

  The basic structure of this topology is shown in Fig. 2.15.

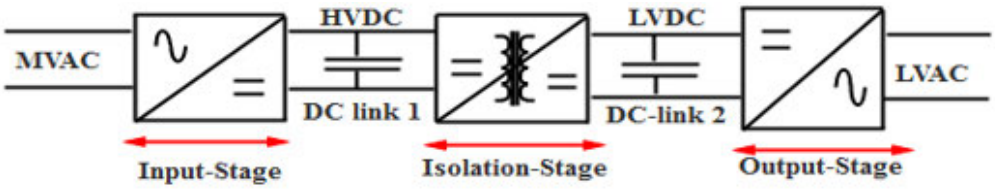

Figure 2.15: Three Stage PET with DC-Link on both Secondary and Primary Sides

The topology comprises of three stages: the input stage, isolation stage and output stage. The input stage consists of a rectifier that converts AC voltage to DC voltage. Hence, the stage is referred to as the rectification stage. The isolation stage is also called the DC-DC conversion stage. This stage is further grouped into three stages as shown in Fig. 2.16: DC–AC conversion stage, isolation stage (high frequency transformer) and AC- DC conversion stage. The isolation stage performs the same task as the normal isolation stage in the PET, it provides electrical isolation, and is also responsible for the general performance of the system. The last stage in the three stage topology is the DC-AC conversion stage which converts alternating current voltage to direct current voltage [86],[87],[88].

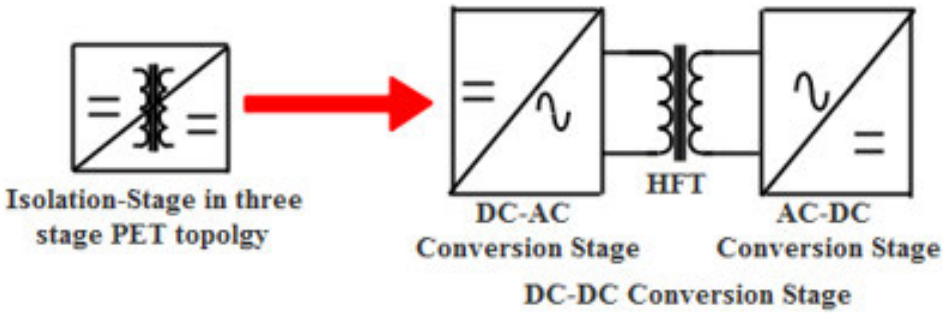

Figure 2.16: DC-DC Conversion Stage

One of the principal benefits of this topology is that each stage can be controlled independently. Voltage and current can also be independently controlled at each stage. The topology encourages mass integration of RESs and ESSs due to the DC-links on both sides. High voltage direct current (HVDC) and LV DC-links improve the ride-through capacity and permit power quality enhancement in the input and in the output. In ad-

dition, multilevel converter can also be used at each stage and therefore improve high voltage usage of the system.

2.13 Features of a Power Electronic Transformer (PET)

According to [89],[90],[91] Table 2.3 summarises some of the main features of a PET.

Table 2.3: Features of a Power Electronic Transformer

Characteristics	Description
Reduced weight and size	The use of a high frequency transformer, instead of heavy core winding transformer, reduces the size and and weight of the transformer. Generally, the value of the frequency determines the transformer size. The higher the frequency, the more compact the transformer.
Fault detection and isolation	A PET provides quick response to fault and prevents the spread of the fault from one section to another.
Power factor and correction	A PET ensures unity power factor within its power and also provides reactive power compensation.
Voltage regulation	A PET is capable of maintaining constant output voltage. It is not affected by voltage sag and swell due to DC-link.
Harmonic isolation	A PET maintains clean input and output current and voltage.
DC input or output	In addition to 120/240 V AC voltage, PET also operates at 400 V- to -480 V DC output, which allows integration of distributed generation and electric vehicle charging.

2.14 Comparison between a Power Electronic Transformer and a Traditional Line Frequency Transformer

Some of the comparisons that can be made between a power electronic transformer and a traditional line frequency transformer are shown in Table 2.4 [92], [93], [94], [95], [96],[97] and [98].

Table 2.4: Comparisons between Power Electronic Transformer and Traditional Line Frequency Transformer

Characteristics	**PET**	**TLFT**
Design Components	Power electronic components	Metals and coils
Power flow direction	Allows bi-directional power flow	Allows bi-directional power flow
Energy storage ability	High energy storage ability and allow any ESSs	Does not allow any ESSs
Response to situations on the grid	Quick and automatic response	Slow and manual response
Load connection	Allows any type of electrical load (AC and DC loads)	Allows connection of only AC load
Size and weight	Portable and reduced weight	Bulky size and heavy weight
Pollution	Environmentally -friendly	Not environmentally -friendly
Voltage control	High voltage control ability	No or low voltage control
Fault propagation	It does not allow propagation of fault from high voltage side to low voltage side	It allows propagation of fault from high voltage side to low voltage side
Losses	High losses	Reduced losses

2.15 Functions and Applications of a PET

A PET offers diverse functionalities and can be deployed in different areas. This section describes some of the functionalities and application areas.

2.15.1 Functions of Power Electronic Transformer

- **Power Flow Management**

  Effective power flow control within the electric power network is one of the promising functionalities of a PET. PETs have the capability to regulate active and reactive power and also provide efficient power factor improvement. When implemented in a smart grid, it can control power flow between the main grid and micro-grids [99],[100],[101].

- **Improving Reliability and Stability**

  A PET improves system reliability and stability by quickly adjusting to situations on the grid. In addition, it reduces losses on the grid and enhances usage of different types of ESSs.

- **Voltage and Current Control**

  Effective implementation of PET can reduce the effect of voltage fluctuation and excess current flow, which are the major causes of RPF on the grid. In addition, PETs can reduce harmonics and mitigate the issue of voltage and current unbalance on the grid, hence improve power quality [102],[103],[103].

- **Enhance Inter-Connectivity of Different Renewable Energy Sources**

  PETs allow inter-connectivity of different RESs and different types of electrical loads, either AC or DC. For instance, PV cell arrays could be coupled directly via DC ports with maximum power point (MPP) tracking capacities. A PET enhances inter-connectivity of different electrical phases such as AC single-phase, three-phase to the main grid [77],[104],[105].

2.15.2 Applications of Power Electronics Transformers

The applications of a PET can be categorised into:

- General applications
- Grid applications.

1. **General Application of Power Electronic Transformer**

   Recently, the deployment of PETs are found to be more attractive in certain areas compared to TLFT due to its outstanding performance. Some of theses areas are discussed below [106],[107].

- **Locomotive and Traction System Application**

  In modern train design, traction equipment is spread along the length of the train and suspended under the train has been the challenge due to the weight and size of the traction transformer. The PET has been the most prominent solution due to its light weight and compact size. In modern train systems, the PET enhances efficiency and reduces harmonics and acoustic emissions [108]. Fig. 2.17 shows the structure of a PET used in a traction system. It is grouped into three stages: the rectification stage (input stage), isolation stage (DC-DC conversion stage) and the output stage (inverter stage). The rectification stage, which is directly connected to the medium voltage catenary, converts AC-DC. The rectifier is electrically connected to a DC-DC conversion stage. With the help of a high frequency transformer, the DC-DC conversion stage provides voltage step down and separation of the primary and secondary sides. This makes it possible to reduce the traction size and weight. It provides a low voltage DC-link to the three-phase traction drive inverters [109].

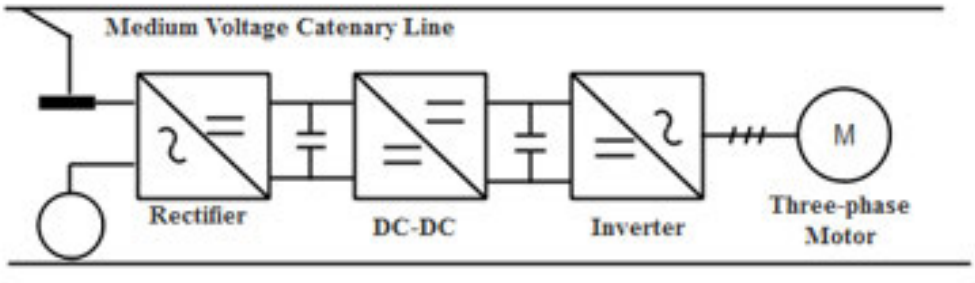

Figure 2.17: Traction Locomotive Application of a PET

- **Renewable Energy Application**

  PETs in wind farms improve frequency, voltage control, active and reactive power control and allow for rapid response to variability in the power system due to the intermittent nature of wind energy. High voltage direct current (HVDC) transmission in conjunction with PETs can enhance long distance offshore wind farms. In this system, low voltage AC from the wind farm is converted to HVDC using a PET. The DC power is transmitted to the onshore system where it is converted to AC through the DC-AC conversion stage. Wind energy conversion via a PET is shown in Fig. 2.18 [110].

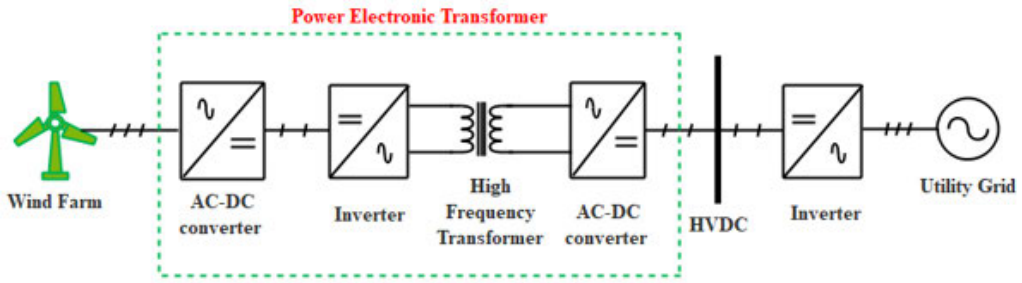

Figure 2.18: Power Electronic Transformer in Wind Energy Conversion

- **Smart Grid Application**

  PETs play significant roles in effective implementation and energy management systems in a smart grid. PETs allow successful integration of RESs into the grid. They provide effective control and management of energy consumption and power flow on the grid. They also help in effective voltage control on the grid. They effectively connect DC and AC loads simultaneously to the grid. Fig. 2.19 shows the application of PETs in a smart grid system.

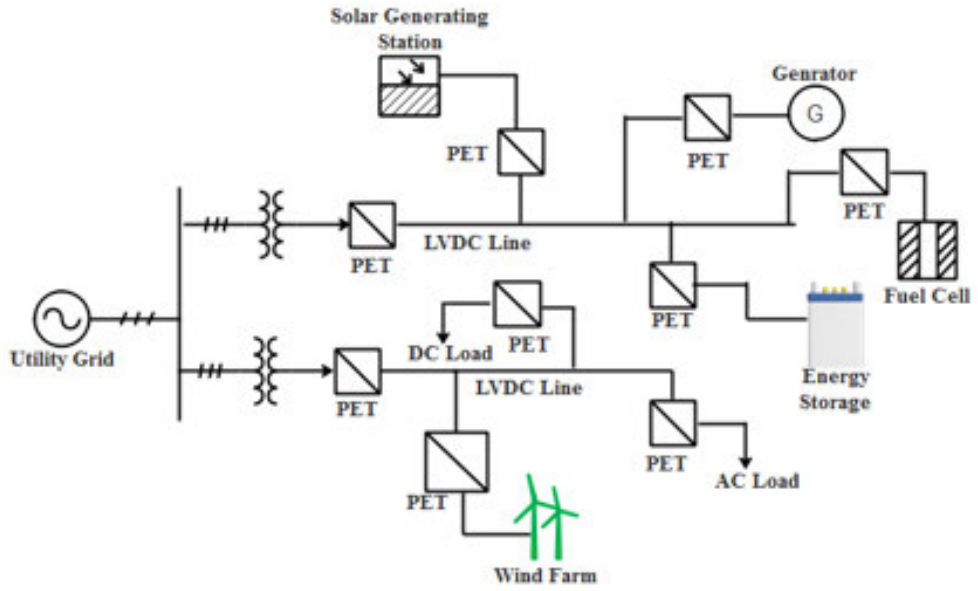

Figure 2.19: Power Electronic Transformer and Smart Grid System

The low voltage direct current (LVDC) link provides effective integration of RESs into the grid. RPF is bound to occur on the grid due to high integration of renewable energy sources, in this condition, PETs provide an effective means of utilising the excess power generated. They can provide a means of utilising the excess directly by connecting directly to a micro grid or through ESSs and then later send it back to the grid. PETs enhance the use of direct current, both in medium and low voltage application. It also aids the process of charging EV batteries on the grid [111].

2. **Grid Applications of Power Electronic Transformer**

   This section presents some of the grid applications of PETs. According to [112], some of these applications are:

   - **Interconnection of power generation sources and load or distribution grid**
     PETs allow transmission of energy between the generation source and load or grid at unity power factor. This situation enhances performance and utilization of transmission lines and thus increases active power flow. They improve system damping during the transient state. Furthermore, PETs allow constant voltage and frequency output even when the input voltage and frequency are interrupted.
   - **Interconnection of two different distribution power networks**
     One of the principal qualities of PETs is that they allow synchronous operation between two or more different distribution networks with different voltage and frequency levels, therefore can regulate active power flow between the two distribution networks as well as provide reactive power compensation on the grid.
   - **Interconnection of medium voltage and low voltage networks**
     Compared to TLFTs, PETs can adequately and effectively regulate the actual amount of active power flowing from medium-voltage networks to low-voltage networks. This scenario plays a critical role when a distributed generation source is integrated with a low-voltage network. The PETs can effectively regulate the amount of energy flow within the grid to avoid overloading of the connecting elements and thus RPF.
   - **Interconnection of medium voltage network and loads**
     Low-voltage loads are always characterised with unbalance which causes harmonic disturbances on the grid. Distribution network operators (DNOs) use a neutral wire to get rid of the disturbances in order to realize a balanced voltage. However, this method may not work when the imbalance is large or the network consists of various non-linear loads. In this situation, PETs provide adequate solutions to voltage unbalance on the grid.
   - **Interface for distributed generation and smart grid**
     PETs allow integration of various RESs with different voltage levels into the utility grid. A major concern of this research work is the interconnection of medium voltage to low voltage networks with the integration of renewable energy source (wind energy) and also interconnection of distribution network to the loads.

2.16 Adoption of Power Electronic Transformers

Despite the numerous applications and functionalities of PET, the technology is still facing some challenges which jeopardize its adoption. Some of the setbacks for its acceptance are summarised in Table 2.5 [85].

Table 2.5: Challenges of Power Electronic Transformer

Challenges	Description
Cost of implementation	PET is expensive to implement and build. However, reduction in the cost of semiconductors, will alleviate this challenge in the near future.
Complexity	Structural design and control of PET is complex.
Efficiency and Reliability	Recently, TLFT is rating better than PET, but in terms of harmonic reduction and unity power factor, PET has good performance. PET reliability will be increasing as the technology grows.

2.17 PET and EV Charging Technology

PETs provide a good platform for integrating EVs to the grid for charging and discharging via bi-directional DC-DC converters, and provide a platform for both AC EV charging and fast DC charging. An EV with vehicle-to-grid (V2G) capability can be charged when there is excess power generation and can be connected to the grid as a storage system and later used as standby power for a home, spinning reserves for the grid, or for peak load shaving [113],[114].

2.17.1 Electric Vehicle and Charging Technology

EVs are not a new technology; the first was in 1832 in Germany powered by a Karl Benz motor. Early EVs used non-rechargeable batteries. As a result of design improvements in 1881, EV development continued into the late nineteenth century. France and Great Britain were the first countries to see the widespread use of electric cars, followed by the United States. Since then, the technology has had intermittent development [115]. However, the persistent issues, such as increases in oil prices and prediction of global oil depletion in the near future, and environmental concerns, have brought EVs into the vogue. EVs are noise free, and this

enhances their usage in environments like warehouses, inside buildings and in environments where pollution and noise are forbidden [116]. The latest developments in rechargeable battery technology contribute to the recent interest in EVs. The size and weight of batteries used in twenty-first century EVs are more portable and lighter than the first generation EVs.

Integration of EVs into the electric power grid can provide ancillary services such as active and reactive power support and load-demand balancing. The major technical challenge in mass deployment of EVs can be attributed to the battery issue. The availability of adequate electricity to recharge in some parts of developing and even developed countries is a challenge. In addition, where there is adequate availability of electrical power, the minimum time to recharge is an issue as it takes several hours to fully charge a battery. However, the recharging duration of some battery models has reduced. In this research work more emphasis will be placed on EV battery charging.

2.17.2 Types of Electric Vehicle

There are three categories of EV: hybrid EV, battery EV and plug-in hybrid EV.

Hybrid electric vehicles (HEV) make use of both electric motors and internal combustion engines. These complement each other; the on-board batteries and drive motors help the internal combustion engine while the internal combustion engine helps in recharging the battery. Hence they are not externally charged.

Battery electric vehicles (BEVs) are powered solely by batteries.

Plug-in hybrids electric vehicles (PHEVs) can operate on both electricity and petrol or diesel, depending on the vehicle configuration and power needs. BEVs can use an on-board charging system for charging battery.

The major concern of this research work is the battery electric vehicle (BEV).

2.17.3 Electric Vehicle Battery and Charging Technology

The battery is considered to be the power-house of the EV, thus an accurate and effective selection of battery for an EV is essential. The key parameters for effective selection of batteries for maximum performance include the following: energy density, power density, life span, volume, energy efficiency and self-discharge. The most commonly used battery in EVs include: lead acid battery (PbA) (early veihicles), nickel metal hybrid battery (NiMH), lithium ion battery (Li-ion) and sodium nickel chloride battery (NaNiCl2). Table 2.6 summarises some of the commonly used battery types [117],[118].

Table 2.6: Characteristics of Various Electric Vehicle Battery

Battery Characteristics	**Electric Vehicle Battery Technology**			
	pbA	**NiMH**	**Li-ion**	**NaNiCl2**
Energy density (Wh/kg)	35	70-95	118-250	90-120
Specific power (W/kg)	180	200-300	200-430	155
Life cycle (%)	1000	1000	2000	1000
Self-discharge (%/Month)	Less than 5	Less than 20	Less than 5	Less than 5
Operating temperature (°C)	-15 to +50	-20 to+60	-20 to +60	234 to 350

Considering the characteristic in the Table 2.6, the lithium ion battery is considered to be the most promising battery for EVs in the near future. It has high energy density and specific power, has high efficiency, and a long lifespan. However, they are expensive.

According to [117] and [118], there are different types of lithium-ion battery for EV. Lithium-ion polymer, lithium-ion phosphate, lithium-sulphur, and lithium-air are the commonly used ones. Lithium-ion polymer has an energy density of about 132 Wh/kg to 225 Wh/kg, specific power of 200 W/kg to 430 W/kg, self-discharge ability of less than 5% per month, and life cycle of 2000 at 80 % depth discharge . Lithium-ion phosphate, has a life span of 2000 at 80 % depth discharge, energy density and specific power of 120 Wh/kg and 2000 W/kg to 4500 W/kg respectively, the operating temperature is $-45°C$ to $70°C$. Lithium-sulphur energy density is 350 Wh/kg to 650 Wh/kg, the life cycle is around 300 at 80 % depth discharge, while the monthly self-discharge is 8 % to 15 %, temperature of operation is $-60°C$ to $690°C$. Lithium-air has an energy density of 1300 Wh/kg to 2000 Wh/kg and life cycle 100, with $-10°C$ to $70°C$ operating temperature.

2.17.4 Electric Vehicle Charging Technology

EV charging is a means of getting a battery energised by passing the required voltage and current into the battery. EV charging technology can be approached in two different ways as shown in Fig. 2.20.

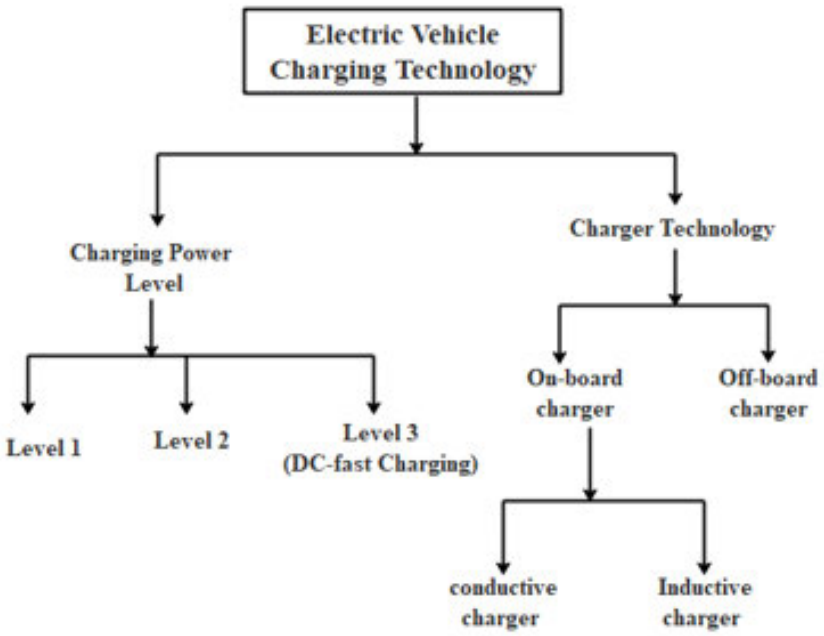

Figure 2.20: Electric Vehicle Charging Technology

2.17.5 Electric Vehicle Charging Power Level

According to some international standard bodies such as the Society of Automotive Engineers (SAE), International Electromechanical Commission (IEC) and CHAdeMO, standards for EV charging power levels can be grouped into three different levels: level 1, level 2 and level 3 [119],[120].

- **Level 1**

  This charging technology uses 120V AC, and up 20 A for charging. It can be used in standard residential or commercial socket-outlets. The system uses up to 1.4 kW to 1.9 kW energy when charging. It takes almost 10 h to 15 h before fully charging a battery. The advantage of this technology includes low cost of installation and low impact on the electricity network. It has a low impact on residential electricity consumption and billing. However, the rate of charging is slow. The technology is designed mainly augment on-board charging.

- **Level 2**

  Level 2 charging technologies need 208 V / 240 V AC power. Residential or commercial buildings with this voltage level can use the level 2 charging technology. Level 2 charging takes 3 h to 7 h before fully charging a battery; however, an EV with a smaller battery capacity may be fully charged with less hours. The system uses up to 30 A for 3.3 kW

to 6.6 kW when charging. The charging period is shorter than level 1. The drawback to this technology includes higher cost of installation and it has a greater impact on the power network.

- **Level 3**

  Level 3 is called DC fast charging. The technology uses DC fast charging to deliver high power directly to the EV battery. It can charge battery up to 80 % charge within 30 minutes or less. The system is designed mainly for public charging systems and for off-board charging. The system can supply 200 to 600 V DC for 90 KW to 250 kW. However, the cost of installation is high, it has potential for increasing peak energy demand from power utilities, and weather conditions have a significant impact on it. Cold weather may lengthen the charging period.

2.18 Electric Vehicle Charger Technology

Battery chargers play a significant role in effective management and durability of EV batteries. An EV charger must be effective and reliable, have high power density, and must be cost effective. EV chargers can be grouped into two: on-board and off-board chargers.

- **On-Board Charger**

  An on-board charger is an inbuilt charger that enables EV owners to charge their cars at their own will and convenient time. The on-board charger is characterised by heavy weight, high cost and requires a larger space. It can only be used with level 1 and 2 charging technologies, however, it requires less energy for charging. On-board chargers can be grouped into conductive and inductive chargers. Conductive chargers use cables to connect directly to the charge socket. Conductive chargers are light, compact and support dual power flow. Inductive chargers transfer power magnetically. This form of charger has been used for Levels 1 and 2 power level. The advantage of contactless charging makes it more convenient for the users. Instead of deep-cycling the battery, when parked at home or at work, shopping and even at traffic lights, the vehicle battery can be frequently charged. This removes the use of cables and cords. Furthermore, galvanic isolation is provided by inductive chargers. Charging strips can be built on highways which enable charging while driving. Inductive charging could therefore significantly reduce the need for a fast charging infrastructure. Nevertheless, it has low efficiency and power density, and the car requires a special design (electrical and mechanical) to use inductive charging [117],[121].

- **Off-Board Charger**

  An off-board charger is placed outside the vehicle and provide a DC output on its terminals that is directly connected to an EV battery. Off-board chargers are lighter than on-board chargers since the charger is used outside the vehicle. It supports higher energy transfer, and has the capability of fully charging a battery in a short time and it can be used with DC fast charging systems with high voltage levels. However, it is not cost effective for private use [122],[123]. A comparison between off-board charging and on-board charging methods is shown in Table 2.7.

Table 2.7: Comparison between Off-board and On-board Charging Technology

Features	**On-board**	**Off-board**
Energy transfer	Less energy transfer	Higher energy transfer
Weight	Heavy weight	Light weigh
Charging rate	Slow charging	Fast charging
Power level	Low power level	High power level
Accessibility	Charge at any electrical power outlet	Electrical power outlet restriction
Power flow direction	Unidirectional only	Unidirectional and bidirectional
Cost of implementation	Low cost	High cost

Table 2.8 summarises EV battery DC fast charging methods, based on power levels, types of charger location, maximum power required, charging current level and total time of charging [120],[124].

Table 2.8: Summary of DC Fast Charging Methods

DC voltage level (V)	**Charger type**	**Power level (kW)**	**Current (A)**	**Charging Time (min)**
Level 1 200-450	Off-board	36	80	22
Level 2 200-450	Off-board	90	200	10
Level 3 200-600	Off-board	240	400	Less than 10

2.18.1 Electric Vehicle Charger Connectors

This section presents some of the standard connectors recommended by international bodies for efficacy of EV charger according to [125], [126].

(i) SAEJ1772 (IEC Type1) connector or J-plug is recommended by the Society of Automotive Engineers (SAE). It is a single-phase EV coupler.

(ii) (IEC62196-2) connector type 2 is another type of connector recommended by European standards for EV charging. It is designed for both single-phase and three-phase. The connector can charge batteries up to 16 A and 3.5 kW power when used in single-phase and up to 63 A, 45 kW for three phase.

(iii) Combo 2 connector (IEC-62196-3) is a hybrid of type 2 AC connector and a two pin DC connector. It can supply AC power up to 43 kW. When in DC mode, it can supply power up to 50 kW. It is implemented in Europe for direct current charging.

(iv) Connector type 3 is recommended by the EV Plug Alliance. This connector is of two types: 3 A and 3 C. 3 A can supply single-phase charging up to 16 A while 3 C can supply both single-phase and three-phase up to 32 A. Type 3 connectors can supply a maximum of 22 kW power.

(v) A type 4 connector is designed mainly for DC fast charging. It supplies up to 63 kW, 125 A by 500 V. It is commonly used in Japan and Europe.

2.19 Electric Vehicle Charger Topologies

An EV charger is a combination of two or more power electronic devices. An EV charger must ensure low distortion of the utility current in order to minimize the impact of the power quality and high power factor in order to maximize the real power available from the utility outlet. In order to achieve this, different charger topologies are used with different control techniques. The control algorithm may be implemented via microcontrollers or integrated circuits depending on the rating, cost, and the types of power electronic devices. The two most popular electric vehicle charger topologies are [124]:

(i) AC/DC/DC-DC converter topology

(ii) AC/AC/ AC/DC converter topology

2.19.1 AC/DC and DC-DC Converter Topologies

This is the most used topology. The front AC-DC converter can perform a rectification function by transforming the grid AC voltage to DC voltage. The rectification stage is responsible for active and reactive power control, and the DC-link voltage is responsible for unity power factor correction, reactive power compensation and current harmonic reduction. Some of the commonly used control methods are direct-power control, direct current control and voltage control. The DC-DC conversion stage is responsible for direct battery charging. The DC/DC converter reduces electrical and thermal stress, while the interleaved converter topology can minimise current fluctuations. Buck or boost converters can be used in the DC/DC conversion stage. This type of charger is referred to as a bi-directional charger.

2.19.2 AC/AC and AC/DC Converter Topologies

This is another widely used charger topology. The AC/AC converter converts the input AC supply to the required AC level before the rectification stage. The rectification stage consists of an AC/DC converter for charging the battery. The AC/AC stage can be exemplified by a three-phase transformer and Z-source network topology. Apart from converting the input voltage to the required voltage level, the three-phase transformer can also provide galvanic isolation between the input and EV. The Z-source network serves as a standby transformer capable of reducing harmonic current and inrush current. In the rectification stage, three-phase inverters or uncontrolled diode bridge rectifiers can be used. The inverter permits bi-directional power flow that can be used to setup the V2G EV application and to regulate the

grid frequency and voltage. It can be used to obtain unity power factor and to provide fast charging. An unregulated rectifier (diode bridge) provides a simple rectification process without active control features.

2.20 EV Charging Control Techniques

EV battery charging control techniques can be grouped into three [127]:

(i) Constant current control (CCC);

(ii) Constant voltage control (CVC); and

(iii) Advanced control technology (ACT).

2.20.1 Constant Current Control

Constant Current control (CCC) is a charging control strategy whereby constant current is supplied to the battery by changing the voltage level until is fully charged. A block diagram for constant current is shown in Fig. 2.21.

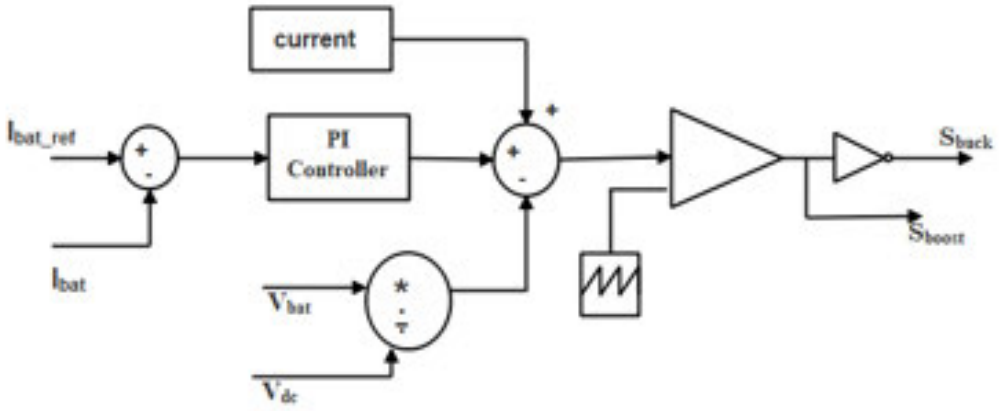

Figure 2.21: Constant Current Control Method

2.20.2 Constant Voltage Control

Constant voltage control (CVC) is a way of controlling the charging level of the battery by supplying constant voltage to the battery. CVC can be used for any type of EV battery and is the simplest charging method available. The current charging of the battery changes while the battery is charging. The initial charging current is higher and gradually decreases along the charging process until it reaches zero when the battery is fully charged. Both constant current and constant voltage make use of PI controller methods for obtaining good tracking of current and voltage references. The CVC control scheme is shown in Fig. 2.22.

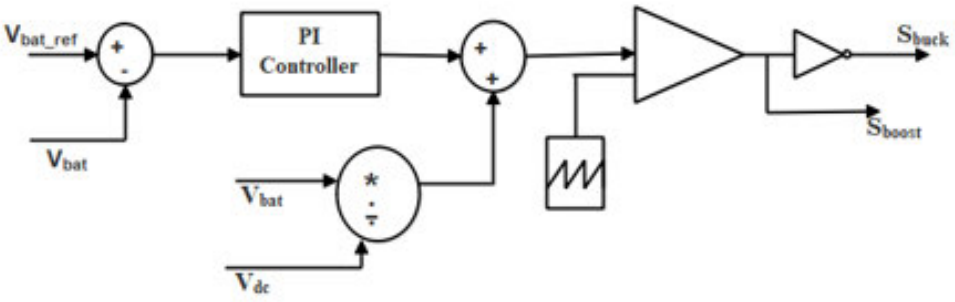

Figure 2.22: Constant Voltage Control Method

2.20.3 Advanced Control Technique (ACT)

Advanced control technique (ACT) combines one or more of the aforementioned methods. One of the most commonly used advanced methods is the constant-current/constant voltage (CC/CV) method. The principle of operation of this method is that constant current charges the battery until the charging capacity reaches the pre-set value. After this, the constant voltage method takes over automatically and during this process the battery is charged with constant voltage at a reduced current. This method is the most used method for DC fast charging. However, the charging period is almost the same as that of constant current charging time, due to decrease in the charging current. Fig. 2.23 shows the charging technique [128],[129].

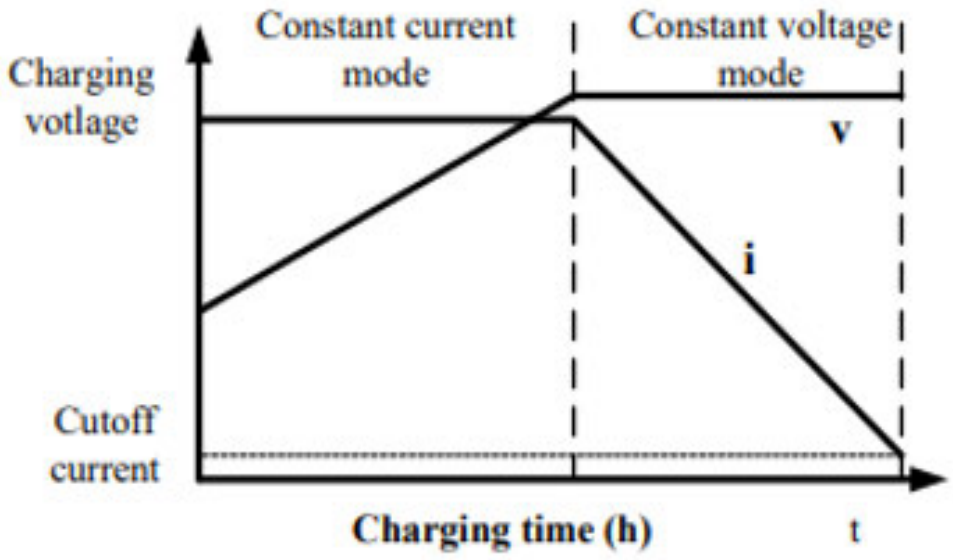

Figure 2.23: Advanced Charging Method

2.21 Impacts of EV Charging on Electric Power Grid

Some of the technical impacts of EV charging on power system networks are described in this section.

2.21.1 Electric Vehicle Charging and Load Profile

An EV battery connected to the grid is considered to be a load on the power system network. The charging load corresponding to all the EV batteries connected to the grid depends on the charging strategies. The charging of EV batteries during peak period will increase the load on the grid; as a group, charging with an uncontrolled method where EV owners charge their cars as they wish to also increases the grid load [118].

2.21.2 Electric Vehicle Charging and Grid Connecting Elements

Higher penetration of EV battery chargers on the grid can incur a negative impact on the power system loading. High integration of EV into the grid may overload conductors and distribution transformers above their thermal rating capacity. Level 1 and level 2 charging strategies have a serious negative impact on the conductors and transformers [130],[131],[132],[133].

2.21.3 Electric Vehicle Charging and System Losses

A high penetration of EV chargers into the grid can incur losses in the system. According to [134], a high penetration on a Danish distribution network incurred additional losses; at a penetration level of 50 %, the total losses on the grid rose to 40 % in an uncontrolled mode.

2.21.4 Electric Vehicle Charging and Grid Stability

A high penetration of EV charging causes voltage issues, such as voltage rise and voltage drop on the grid depending on the period of charging. According to [125] and [135], a high penetration causes significant grid instability; it increases the sensitive of the grid to disturbance and makes the grid less stable. EV charging reduces the steady-state voltage stability of the power grid and high penetration can lead to phase unbalance when using single-phase AC charging [118].

2.22 Electric Vehicle Battery Charging Stations

A charging stationis a geographical location set aside for supplying power for charging EV batteries. Siting EV charging station depends on factors such as the type of charging, vehicle

usage, and availability of land and electricity. According to [126], [131] and [136], EV charging stations can be grouped into:

(i) Residential charging stations;

(ii) Private charge stations; and

(iii) Public charging stations.

2.22.1 Residential Charging Stations

Residential charging stations are also called domestic charging points. They make use of level 1 and 2 charging power levels and special connectors. Residential charging points have no user verification, they only require special wiring circuits for the cars. This type of charging station makes use of an on-board charging technique. Residential charging increases household energy consumption, thereby increasing the monthly electricity bill. If the owner is not using regulated charging techniques, the battery can be overcharged and this reduces the life span of the battery. It can cause a fire hazard in case of overcharging or fault especially in a poorly electrified house. Therefore these systems need to supply the on-board charging correctly.

2.22.2 Private Charging Stations

Private or commercial charging points are located in public places such as malls, garages or working places. Such a charging point allows employees to charge their cars for longer hours while at work. However, space availability poses a restriction on their usage. System security is a challenge; it adds to the load profile of the area and thus has a directly impact on the distribution transformers and conductors connecting the area.

2.22.3 Public Charging Station

Such charging stations are located in areas away from residential or commercial places. They are monitored and controlled charging stations with all facilities complying with international standards for EV charging. Such charging points make use of level 3 (DC fast charging). The stations combine both off-board and on-board charging technologies. The major disadvantages are the charging slot availability and regular power supply to the charging station.

2.23 Summary

The chapter started with a general review of electrical power grids with and without integration of RESs. The market strength of wind energy considering the total global installed capacity and predicted future statuses was reviewed. Wind energy conversion systems, and applications

of wind energy both onshore and offshore, were reviewed. The chapter reviewed the impact of wind energy sources on the grid, focusing mainly on the impact of RPF. Overviews of the excess power generated from different hybrid renewable energy sources, causes, impacts, mathematical analysis of RPF, and VR issues on the grid were put forward. Different mitigation strategies for RPF that have been used by different researchers and their drawbacks were reviewed. The concept of a PET and EV charging technology were presented. Different PET topologies, functionalities, applications and differences between a TLFT and a PET were described. The chapter discussed different EV charger topologies, charging methods, on-board and off-board charging systems, and the impact of an EV charging on power network. Different types of charging power levels were presented. Different types of EV, battery, different battery control technologies were reviewed. The chapter described different EV charging stations.

Chapter 3

Investigation and Analysis of Reverse Power Flow Conditions of High Penetration of Wind Energy Source on Power System Network

3.1 Introduction

A comprehensive investigation, assessment and analysis of RPF on a power system network with high penetration of wind energy sources is considered in this chapter. The investigation was carried out to evaluate the potential impacts of RPF on power system networks. The effect of RPF on power system connecting elements (transformers and conductors) and power system losses are some of the impacts considered in this chapter.

3.2 System Description and Modelling

Fig. 3.1 shows a single-line diagram of the power system network under investigation. The system consists of an external grid (utility grid) and connected wind farm. A 120 MVA, 22/220 kV step-up transformer, which feeds the primary and secondary systems respectively, through a connected sub-transmission system transformer of 220/33 kV. There are two sub-system transformers in the system with 47 MVA and 40 MVA power ratings respectively. The two primary distribution system transformers ratings are 60 MVA and 30 MVA respectively, the secondary distribution system consists of two 500 kVA transformers TR4 and TR7 as shown in Fig. 3.1. The system consists of transmission, sub-transmission and distribution lines. The transmission lines transmit 220 kV, the sub-transmission lines transmit 33 kV, while distribution lines transmit 11 kV and 0.4 kV respectively. Aside from the normal grouping of power system networks (transmission and distribution), the system is grouped into zone A and zone B for effective analysis and understanding of the impact of RPF on the network due to the connected wind farm. Zone A represents the part of the grid that is directly connected to the wind farm, while zone B is the other part of grid that is far from the wind farm. The analysis is mainly based on zone A which is the zone that is directly connected to the wind

farm. There are seven power transformers and six loads in the system with total active power of 120.45 MW. The network was modelled and simulated using MATLAB/Simulink software. The technical parameters of the loads and the transformers are given in Table 3.1, while Table 3.2 shows the line parameters of the network.

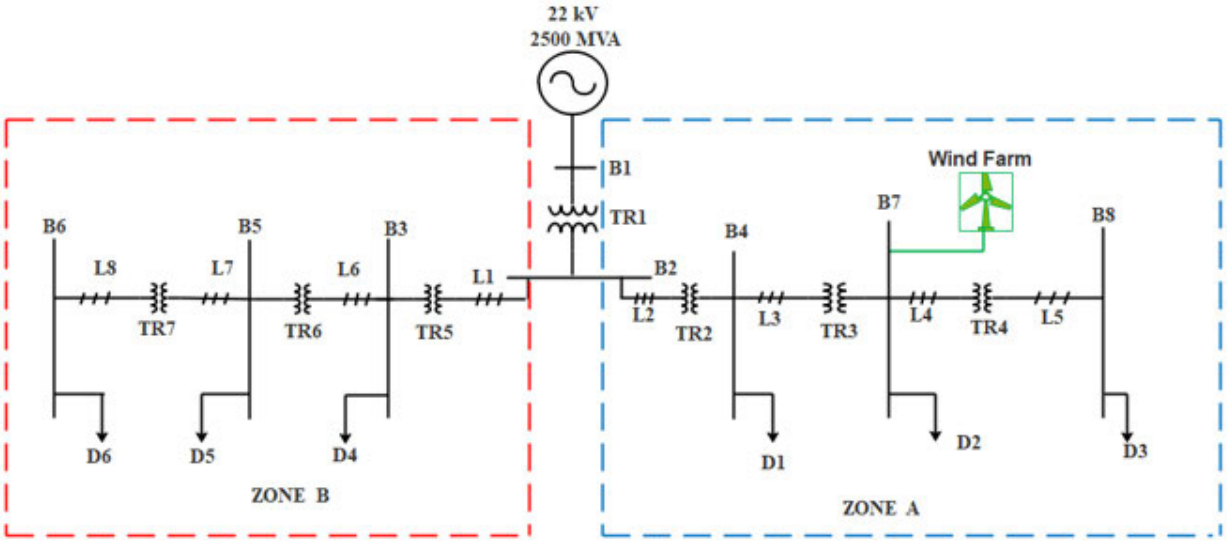

Figure 3.1: Single-Line Diagram of the Power System Network under Investigation

Table 3.1: Network under Investigation Parameters

LOAD PARAMETERS

Load	Active Power (MW)	Reactive Power (MVAr)	Power Factor
D1	30	5	1
D2	45	8	1
D3	0.2	0.002	1
D4	25	3	1
D5	20	4	1
D6	0.25	0.002	1

TRANSFORMER PARAMETERS

Transformer	Primary Voltage (kV)	Secondary Voltage (kV)	Nominal Power (MVA)
TR1	22	220	120
TR2	220	33	47
TR3	33	11	60
TR4	11	0.4	0.5
TR5	220	33	40
TR6	33	11	30
TR7	11	0.4	0.5

3.2.1 Conductors

The conductors used in the network are predominantly aluminium conductor steel reinforcement (ACSR) British standard size types. The conductor design parameters for the simulation are resistance, inductance and capacitance.

3.2.2 Resistance

The voltage profile and power losses in any power network depend strictly on the resistance of the line. The resistance determines the size of the conductor which in turn determines the thermal capacity of the conductor. The resistance of the line conductors is

$$R = \frac{\rho L}{A} \tag{3.1}$$

where R is the resistance of the conductor at a specified temperature, ρ is the resistivity of the conductor, L is the length of the conductor (km), and A is the area of the conductor (m^2).

3.2.3 Line Inductance

The line inductance with three phases and three lines with an equal phase spacing conductor is used. The line inductance is given as:

$$L = 2 \times 10^{-7} \left(\ln \frac{D}{r!} \right) \tag{3.2}$$

where, $r^! = 0.7788 r_x$ and r_x is the radius of the conductor in m. D is the space between each strand of the conductor and is given by:

$$\sqrt[3]{(D_{ab})\,(D_{bc})\,(D_{ac})} \tag{3.3}$$

The values of D vary from the transmission system to the distribution system. For the purpose of this work, 3.7 m and 0.66 m values are used for transmission and distribution lines respectively.

3.2.4 Line Capacitance

The line capacitance with three-phase and three lines with equal phase spacing conductor is considered. The line capacitance is

$$C = \frac{2\pi\varepsilon}{\ln\left(\frac{D}{r!}\right)} \tag{3.4}$$

where ε is the permitivity of free space given as 8.854×10^{-12} F/m, D is the space between each strand of the conductor in m and is given as $r^{!} = 0.7788 r_x$ where r_x is the radius of the conductor.

Table 3.2: Line Parameters

Lines	**Length (km)**	**Resistance** (Ω)	**Inductance** (μ**H**)	**Capacitance (pF)**
L1	10	1.0933	3.242	3.432
L2	10	1.0933	3.242	3.432
L3	5	0.1828	3.054	3.644
L4	5	0.115	1.055	11.33
L5	5	0.0026	2.465	4.514
L6	5	0.1363	3.024	3.679
L7	5	0.0788	2.522	4.412
L8	5	0.0026	2.0625	4.514

3.2.5 Wind Turbine and Wind Farm

The wind turbine used was doubly-fed induction generator (DFIG). This is a wound rotor induction generator with an in-built AC/DC/AC IGBT-based PWM converter. The stator winding is connected directly to the 50 Hz grid while the rotor was fed at variable frequency through the AC/DC/AC converter. The DFIG allows maximum extraction of wind energy from the wind for low wind speeds by optimizing the turbine speed while alleviating mechanical stress on the turbine during high wind speed. The output power generation of a wind turbine depends on the interaction between the wind turbine rotor and the wind speed. The output power of the turbine is obtained from

$$P_{\text{Wind}} = \frac{1}{2}\rho\pi r^2 C_P(\lambda, \theta)V^3 \tag{3.5}$$

where P_{Wind} is the mechanical power extracted from the wind, ρ is the air density in kg/m^3, r is the turbine radius in m, V is the wind speed in m/s, and C_P is the wind turbine power coefficient. C_P is a function of the tip speed ratio λ and blade pitch angle θ. The tip speed ratio (λ) is:

$$\lambda = \frac{r\omega}{V} \tag{3.6}$$

where ω is the wind turbine rotor speed in rad/s. The action of the tip ratio depends on the wind turbine rotor speed and the wind speed. At constant rotor speed, a slight change in the will speed will change the tip-speed ratio, therefore change the power coefficient and the output power generated from the turbine. However, if the rotor speed is adjusted according to the wind speed variation, the tip-speed ratio can be maintained at an optimal point and the wind turbine will produce the maximum power output. The mechanical output power of the

wind turbine is given by:

$$P_m = P_{\text{Wind}} = K_\omega \omega^3 \tag{3.7}$$

where K_ω is the power gain is

$$K_\omega = \frac{1}{2} C_P \rho \pi \frac{R^5}{\lambda^3} \tag{3.8}$$

The wind turbine characteristics with the output power plotted against the rotor speed of the turbine are shown in Fig. 3.2. The turbine mechanical power as a function of turbine speed is displayed for wind speeds ranging from 4 m/s to 10 m/s. C_p typically has a maximum value of 0.45 to 0.5 and this is due to the Betz constant.

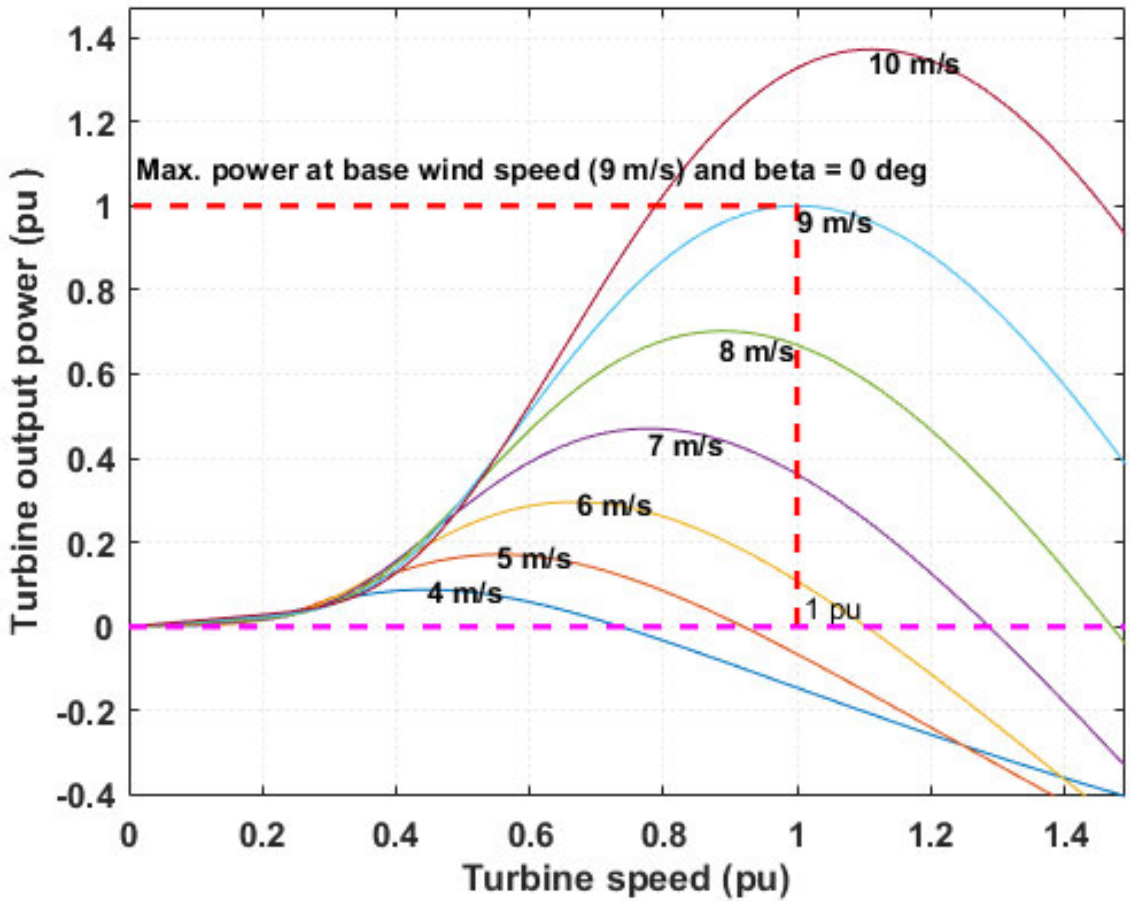

Figure 3.2: Wind turbine characteristic

A wind farm is a collection of wind turbines (WTs) that operate as a single power station. It consists of a substation where the outputs of the WTs are combined and fed to the transmission grid. In this work, the wind farm modeled compromises of forty identical wind turbines with a nominal rating of 1.5 MW each connected to make up of 60 MW. The wind farm was connected at distribution feeder (B7) of a 11 kV distribution network through transformer TR4 as shown in Fig. 3.1. The layout of the wind farm is shown in Fig. 3.4, while Table 3.3 summarises the

wind turbine and wind farm parameters. The turbine parameters are typical for a wind turbine and used in the embedded Matlab model. However, they were checked against typical values as found in [137].

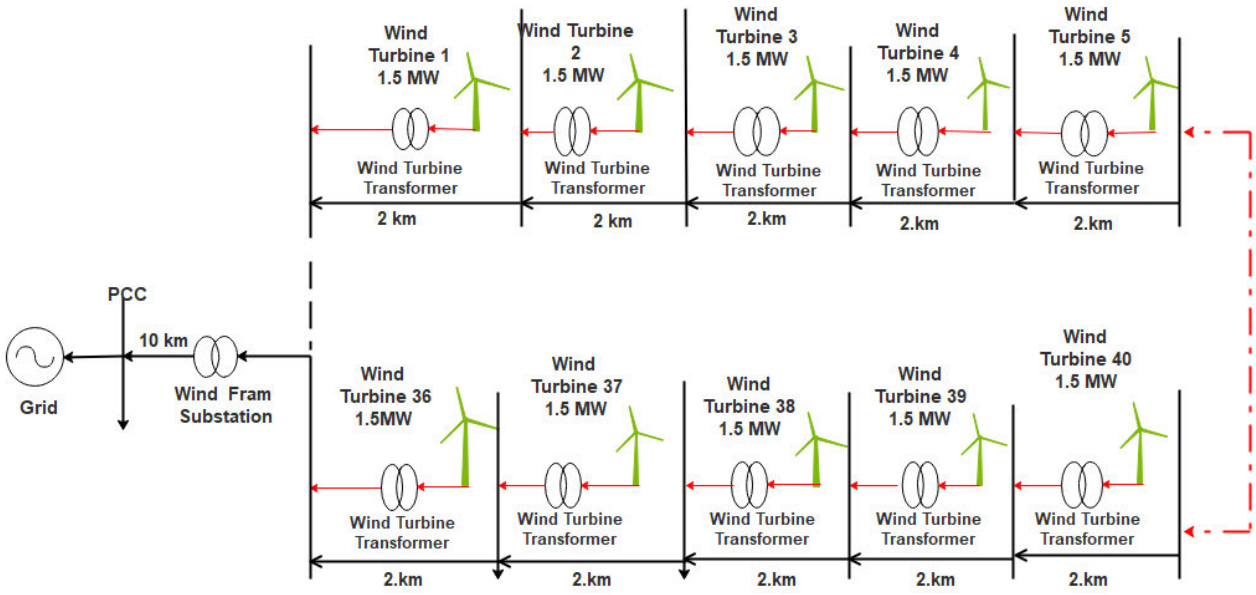

Figure 3.3: Wind farm layout

Table 3.3: Wind Turbine Parameters

Description	Symbol	Value	Unit
Power Rating	P_{WT}	1.5	MW
Rated Voltage	V_R	575	V
Stator Resistance	R_s	0.004843	pu
Stator Inductance	L_s	0.1248	pu
Rotor Resistance	R_L	0.004377	pu
Rotor Inductance	L_r	0.1791	pu
Magnetizing Inductance	L_M	6.77	pu
Friction Factor	F_f	0.01	pu
Base Wind Speed	B_{WS}	9	m/s
Cut-in Wind Speed	$V_{WS_{cin}}$	4	m/s
Maximum Pitch Angle	$\theta_{M\pi x}$	45	°
Generator Pole Pairs	P	3	
Power Coefficient	C_P	0.48	
Wind Farm Rating	P_{WF}	60	MW

3.3 Simulation Scenarios

- **Scenario 1:** The design of the conductor was based on the ampacity which determines the maximum current carrying capacity of the conductor. In this research, for comprehensive

assessment and analysis of RPF, after calculating the normal capacity of the conductor, an additional 2 % of the total capacity of the line was added.

- **Scenario 2:** The network under investigation was simulated without the wind turbines connected. This scenario is called the base case. The purpose of base case is to ascertain that the network under investigation works and complies with the standard range of voltage limit. The standard voltage variation from the nominal voltage considered in this work was ±5% of the nominal voltage.

- **Scenario 3:** This simulation of the power system network is with the wind farm connected. Different penetration levels of the wind farm are considered. The scenario helps in identifying the wind energy penetration levels that cause RPF on the grid.

- **Scenario 4:** For effective investigation and analysis of RPF, balancing between the load demand and the generation is crucial. There are three cases normally considered while trying to investigate the impact of generation and load balancing on the grid. Minimum loading and maximum power production, maximum loading and minimum power production and maximum loading and maximum power production can be considered. However, for the purpose of this research work, only minimum loading and maximum power production was considered.

- **Scenario 5:** Aside from the normal grouping of the power system network, the system is grouped into zone A and zone B as shown in Fig. 3.1. However, the analysis is mainly based on zone A, which is the zone that is directly connected to the wind farm.

3.4 Simulation Results Analysis and Discussions

The simulation results analysis of the power system network without and with integration of wind farm are presented in this section.

3.4.1 Voltage Profile Analysis

- **Voltage Profile Analysis without Wind Farm Connected**

  Figs. 3.4 to 3.7 show the scope display of all the buses, while Table 3.4 presents the per unit voltage analysis of the buses. The graphical representation of the bus voltage is shown in Fig. 3.8.

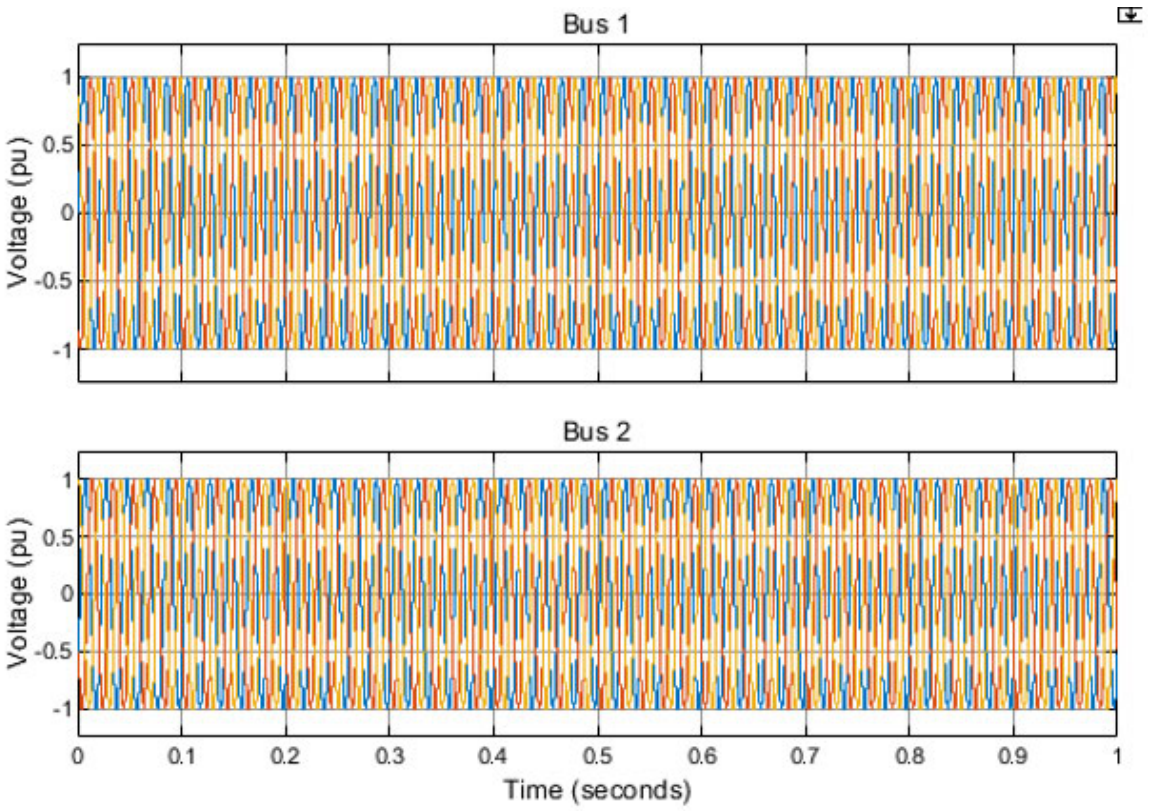

Figure 3.4: Scope Display of the Network without Wind Farm Connected

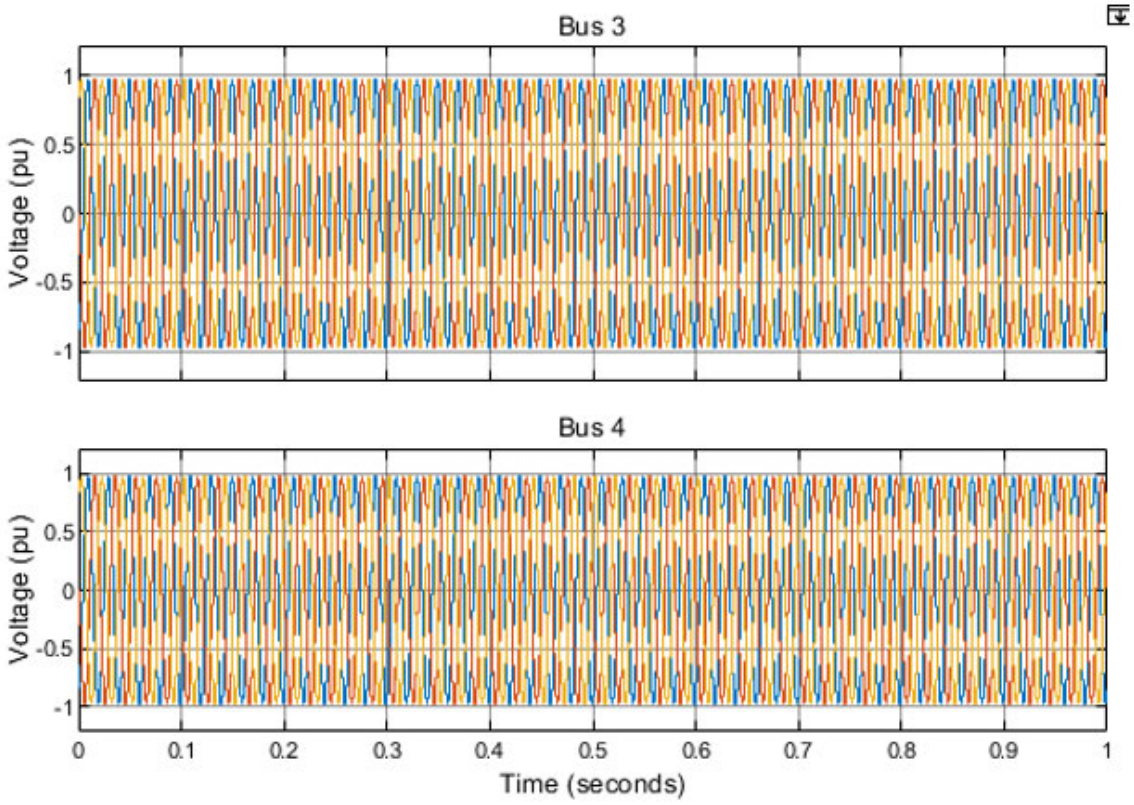

Figure 3.5: Scope Display of the Network without Wind Farm Connected

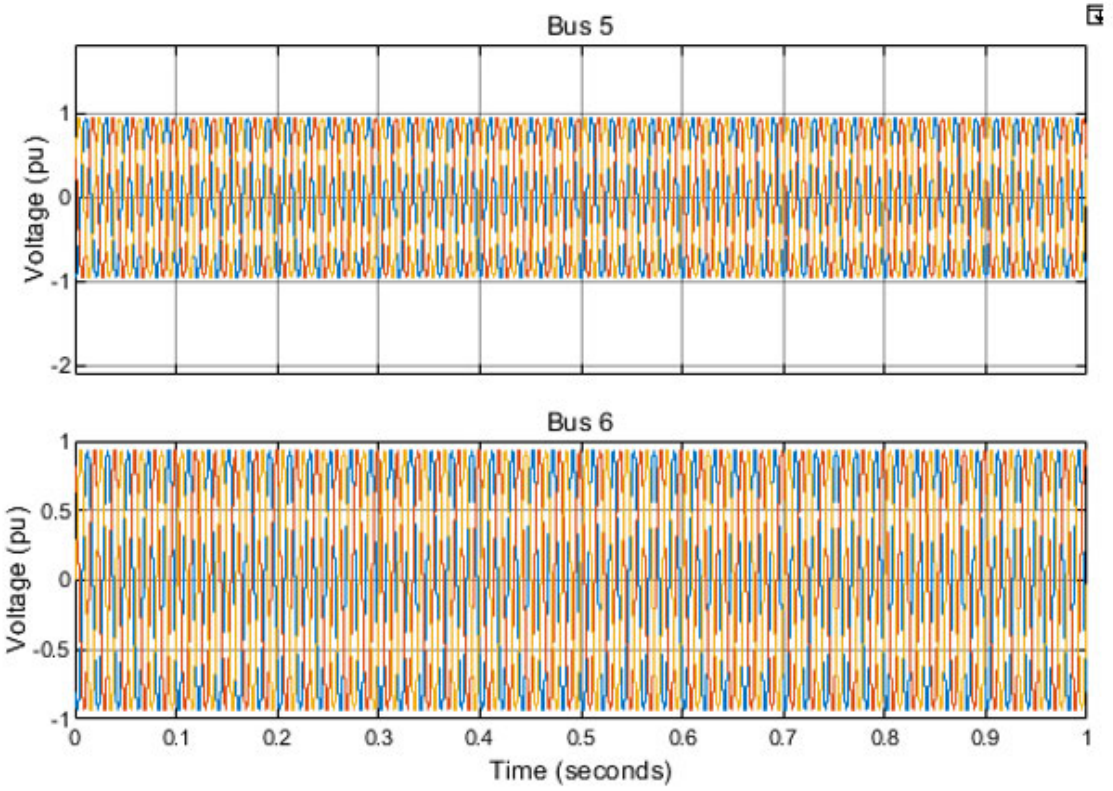

Figure 3.6: Scope Display of the Network without Wind Farm Connected

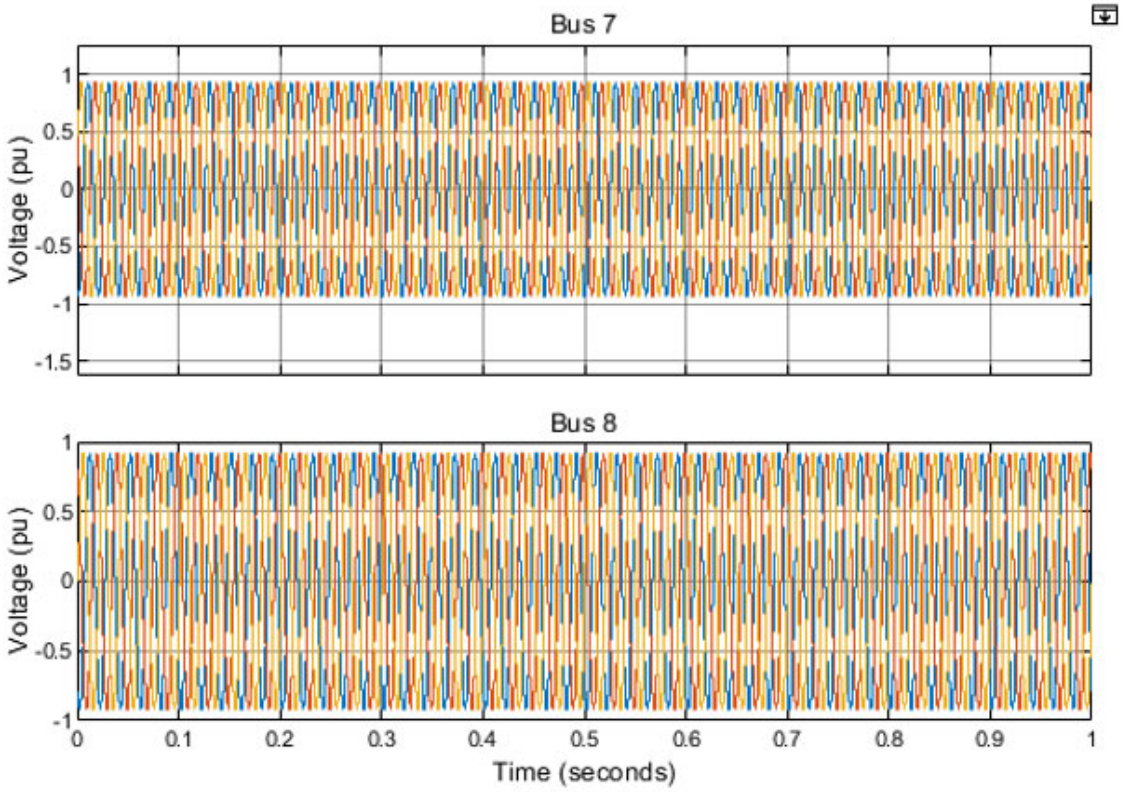

Figure 3.7: Scope Display of the Network under Investigation without Integration of Wind Farm

Table 3.4: Per-unit Voltage Analysis of the Grid without Wind Farm Integration

Bus bar	Voltage (pu)
B1	1.000
B2	0.9934
B3	0.9757
B4	0.9672
B5	0.9575
B6	0.9498
B7	0.9313
B8	0.9280

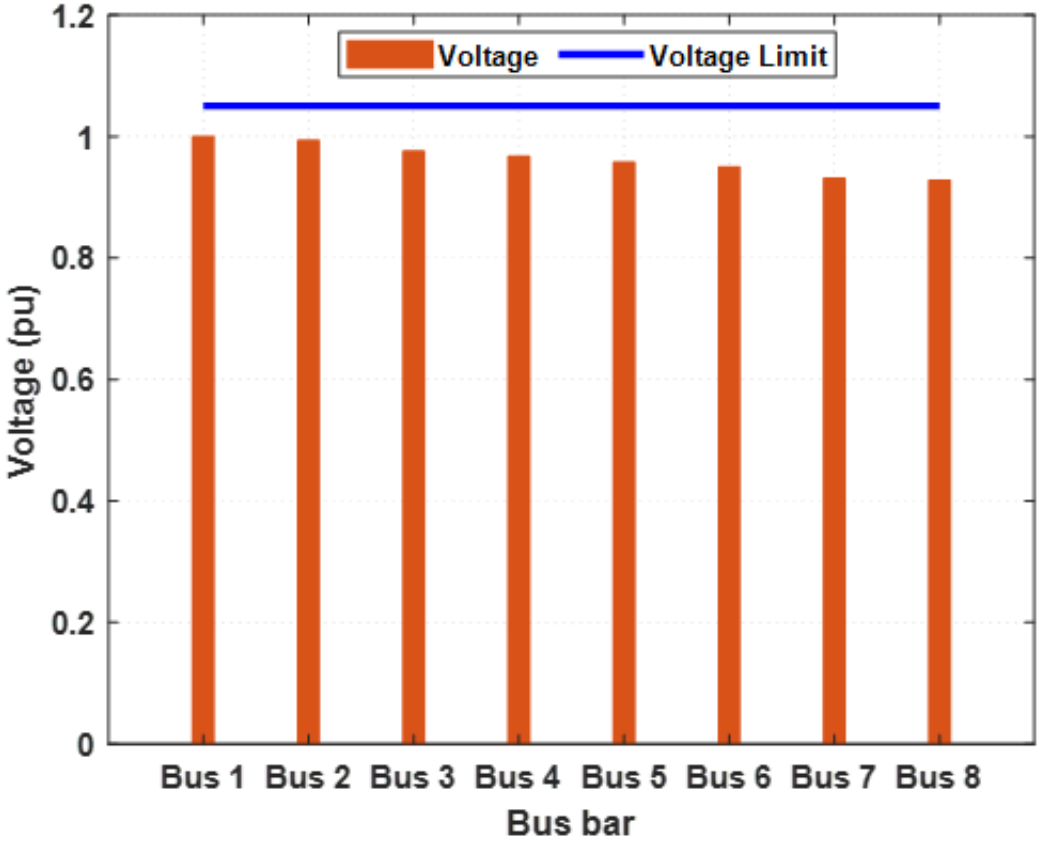

Figure 3.8: Voltage Profile Analysis without Wind Farm

For the purpose of power quality delivery to the end-users, it is essential that the grid works within the acceptable voltage limit. The permissible voltage variation considered in this research was 1.05 pu. As it can be seen in Fig. 3.8, the grid under investigation worked within the acceptable voltage range of 1.05 pu.

- **Voltage Profile Analysis with Wind Turbine Connected**

  The wind farm was integrated into 11 kV distribution network, different wind farm penetration level was carried out to determine the impacts on the power system network under investigation. Table 3.5 shows the per unit voltage analysis of all the buses with the wind farm connected with different penetration levels (PL), while Fig. 3.9 presents

the graphical representation of the per unit analysis.

Table 3.5: Bus Voltage Analysis with Wind Turbine Connected in per unit

PL (%)	**0.1**	**0.2**	**0.3**	**0.4**	**0.5**	**0. 6**	**0.7**	**0.8**	**1.0**	**1.1**	**1.2**
Bus	**Voltage (pu)**										
B1	1.000	1.000	1.000	1.000	1.000	1.000	1.000	1.000	1.000	1.000	1.000
B2	0.933	0.993	0.993	0.993	0.993	0.993	0.993	0.993	0.993	0.993	0.993
B3	0.976	0.976	0.976	0.976	0.976	0.976	0.976	0.976	0.975	0.975	0.975
B4	0.967	0.967	0.967	0.967	0.966	0.966	0.966	0.966	0.966	0.966	0.966
B5	0.958	0.958	0.958	0.957	0.957	0.957	0.957	0.957	0.957	0.957	0.957
B6	0.950	0.950	0.950	0.950	0.950	0.950	0.950	0.950	0.950	0.950	0.950
B7	0.916	0.933	0.972	1.030	1.105	1.192	1.290	1.395	1.507	1.624	1.745
B8	0.928	0.929	0.968	1.026	1.011	1.188	1.285	1.39	1.502	1.617	1.739

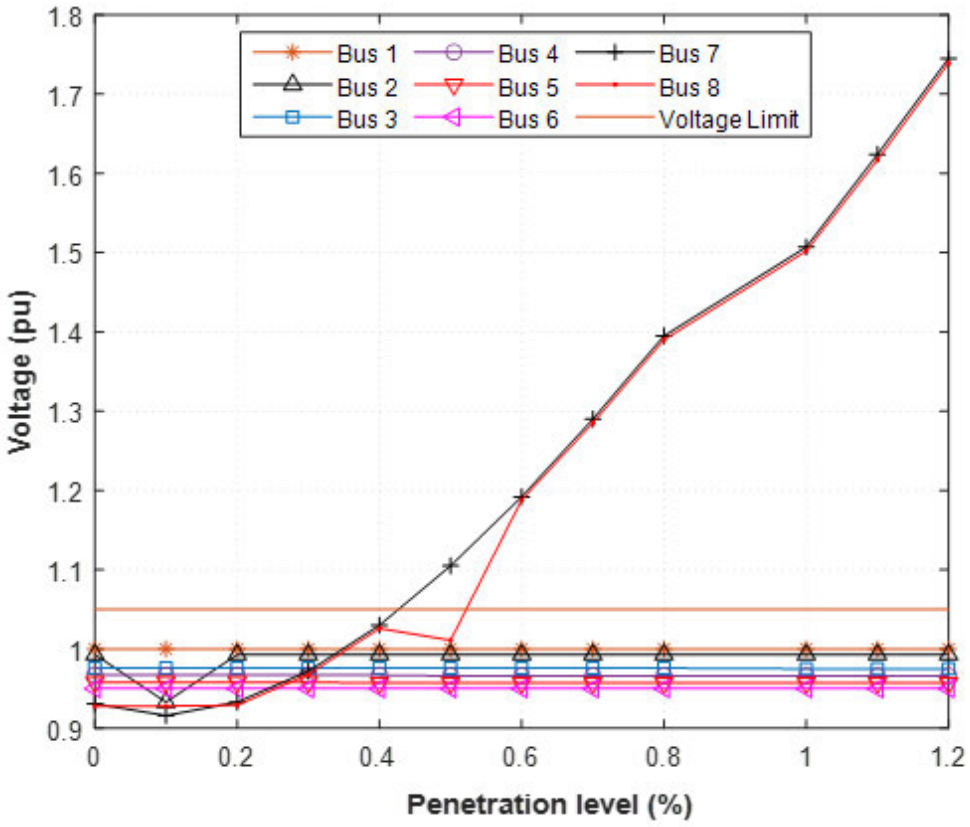

Figure 3.9: Penetration Effect of Wind Farm on Voltage Profile

From the analysis, the voltage at the PCC increases with increase in wind energy penetration level. The bus 7 voltage (PCC) increased to 1.745 pu and the feeder voltage close to the PCC (B8) increased to 1.739 pu at 1.2 % penetration level respectively. Based on this observation, the voltage on the two bus bars violate the standard voltage limit of 1.05 pu that is ±5 % of the nominal voltage.

3.5 Network Loading and Reverse Power Flow Analysis

As stated in the previous section, reverse power flow has a direct impact on the network loading system. The two major elements that are concerned with power system network loading are transformers and conductors. RPF causes overloading of these elements, thus violating their thermal rating capacity. This section presents the analysis of the impact of reverse power flow on these elements. The analysis is based on zone A of the network which is directly connected to the wind farm.

3.5.1 Transformer Loading

There are three different transformers in zone A; TR2, TR3, and TR4. The wind farm is connected to the grid via transformer TR4. Table 3.6 shows the transformer loading analysis, while the graphical analysis are shown in Figs. 3.10 to 3.12.

Table 3.6: Transformer Loading

Penetration Level (%)	**TR2 (33/11 kV, 47 MVA) Maximum Loading Capacity 36 MW**	**TR3 (33/11 kV, 60 MVA) Maximum Loading Capacity 48 MW**	**TR4 (11/0.4 kV, 500 kVA) Maximum Loading Capacity 0.4 MW**
NO WT	14.79	21.24	0.227
0.1	15.345	22.643	0.228
0.2	15.513	23.215	0.233
0.3	15.714	23.95	0.245
0.4	15.949	24.831	0.263
0.5	16.215	25.844	0.271
0.6	16.511	26.973	0.281
0.7	16.834	28.202	0.289
0.8	17.182	45.821	0.301
1.0	17.556	49.26	0.329
1.1	17.953	50. 981	0.357
1.2	18.369	51.502	0.385

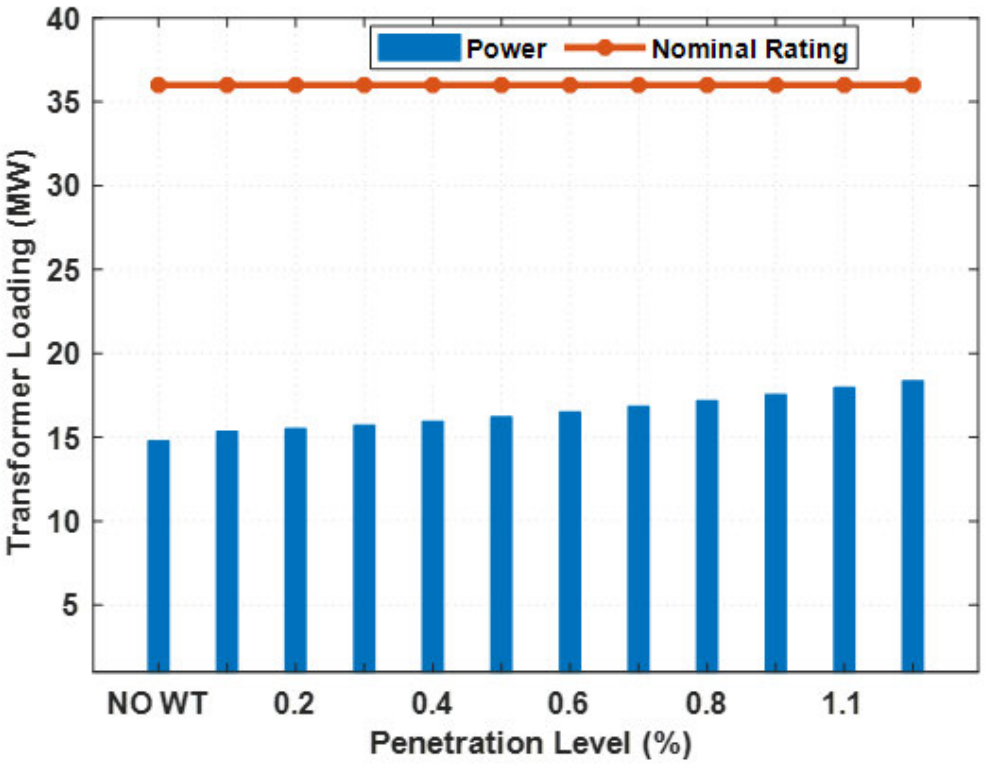

Figure 3.10: Power Flow Through TR2

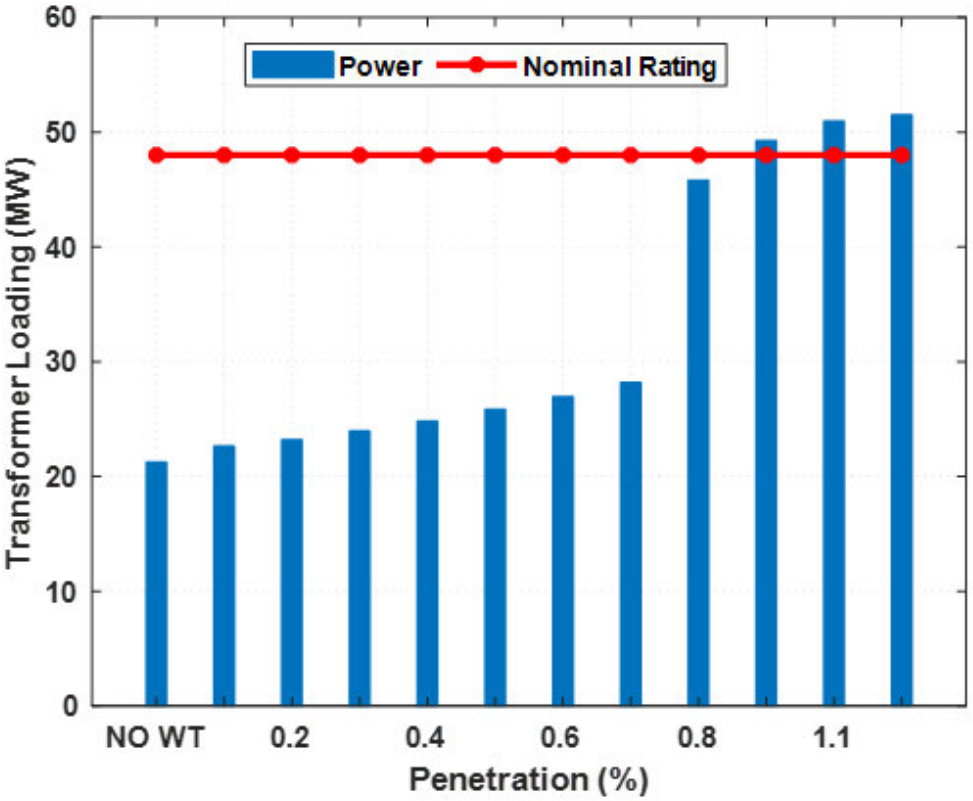

Figure 3.11: Power Flow Through TR3

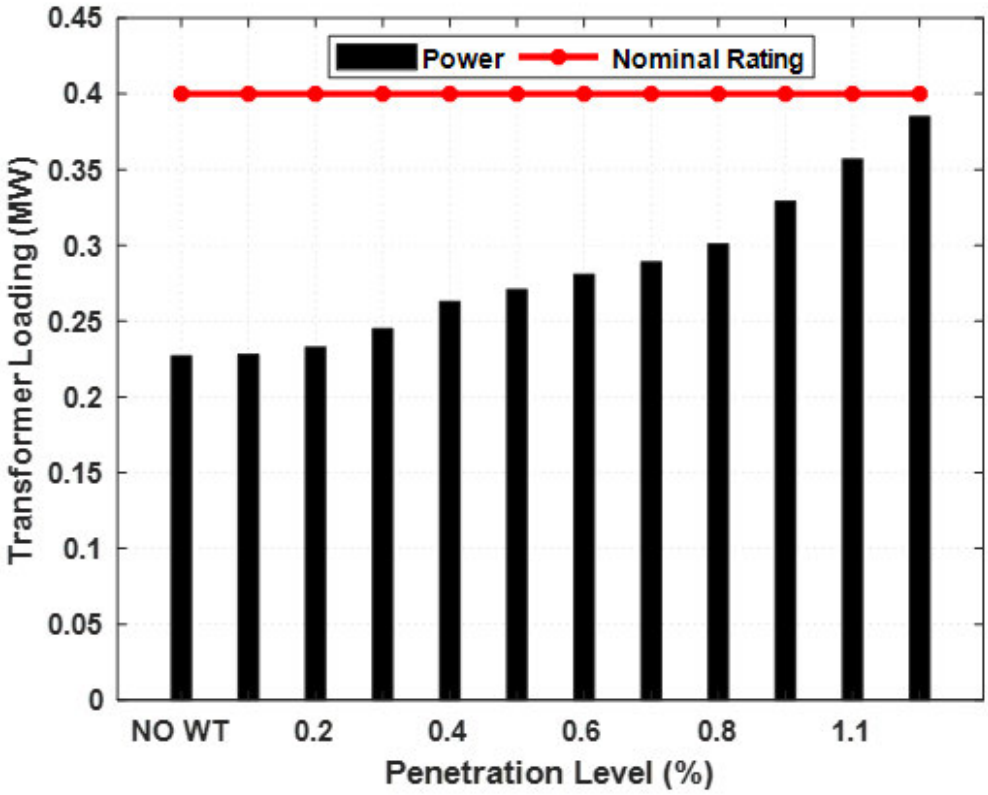

Figure 3.12: Power Flow Through TR4

From the analysis, it was observed that the loading of the three transformers increases with an increase in penetration level. However, transformer TR2, TR4 work within the acceptable capacity as shown in Fig. 3.10 and Fig. 3.12 respectively. Transformer TR4 experiences overloading as shown in Fig. 3.11. With the penetration level of 0.8 %, the transformer loading was 45.82 MW. A further increase in the penetration level from 1.0 % t0 1.2 %, the loading increase to 49.26 MW, 50.98 MW, and 51.50 MW respectively. With the penetration level of 1.0 % the transformer was overloaded by 1.26 MW, which represents a percentage increase of 12.48 % of the transformer loading. At penetration levels of 1.1 % and 1.2 %, the transformer was overloaded by 2.98 MW and 3.503 MW respectively. This represents an increase of 106.21 % and 107.30 % respectively. RPF was observed at penetration level of 1.0%. From the analysis, the RPF contributes 38.45 % of the total loading of the transformer and this may have a detrimental effect on the transformer efficiency and performance.

3.6 Reverse Power Flow Analysis

This section presents the reverse power flow analysis. From the simulation, it was observed that reverse power flow occurs at transformer TR3 in zone A of the network at the penetration level of 1.1 %. From the observation the reverse power flow occurred when the power generated

from the wind farm exceeds the local load at the low distribution system. The reverse power flow through transformer TR3 at different penetration levels are shown in Figs. 3.15 and 3.16 where it is shown that the active power flow in the negative direction. The power flow analysis is in per unit of the nominal rating of transformer TR3 as measure from the transformer during simulation.

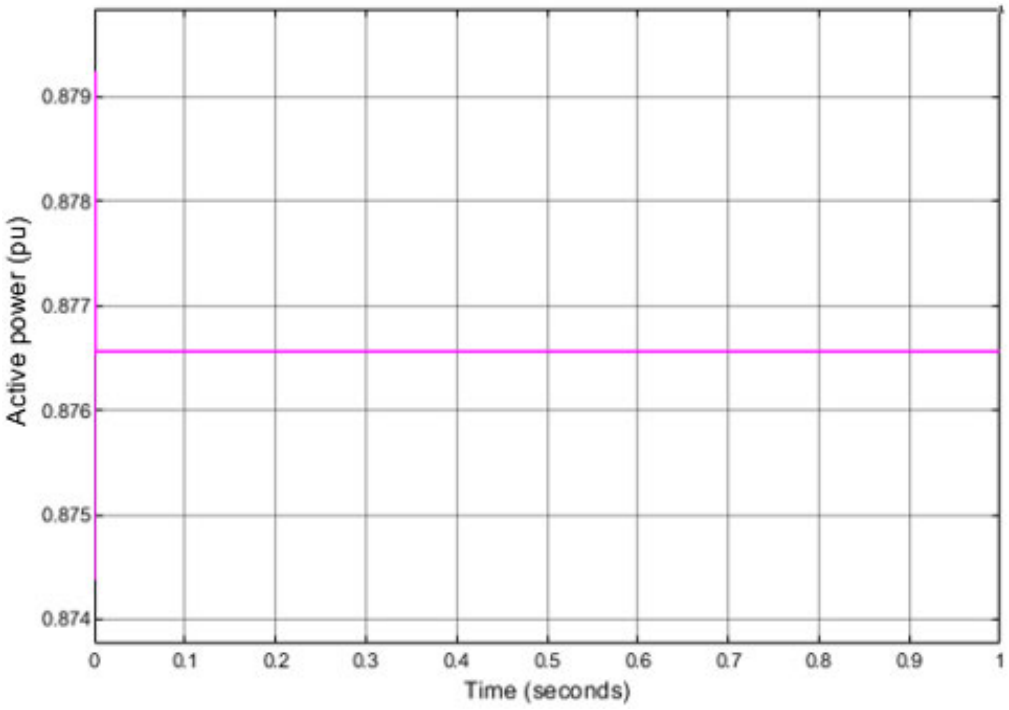

Figure 3.13: Active power flow without integration of wind farm

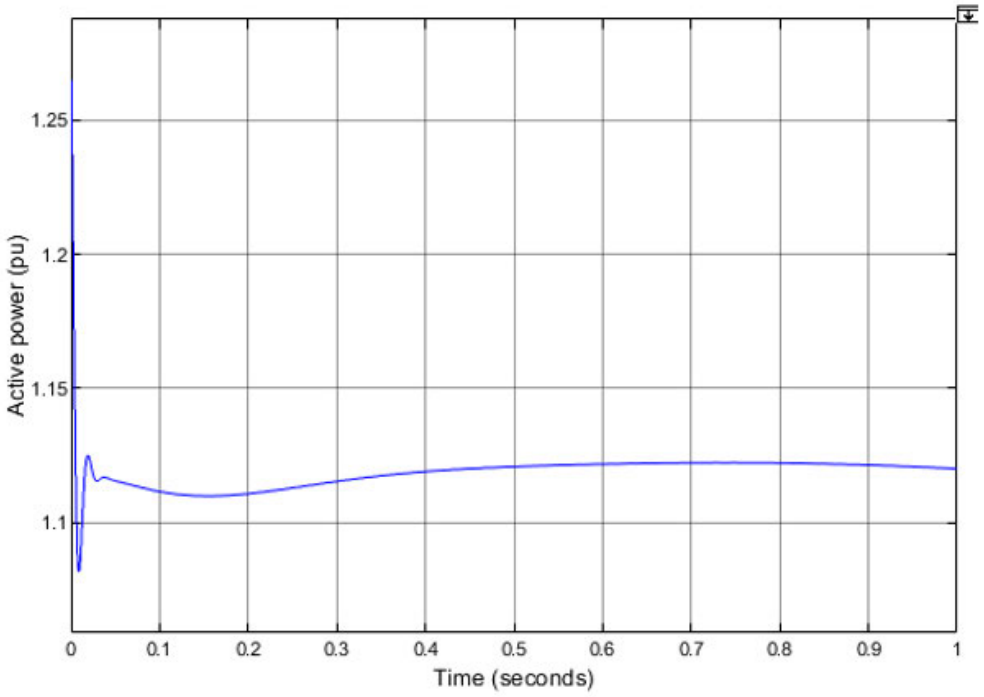

Figure 3.14: Reverse active power flow with 1.0 % penetration at transformer TR3

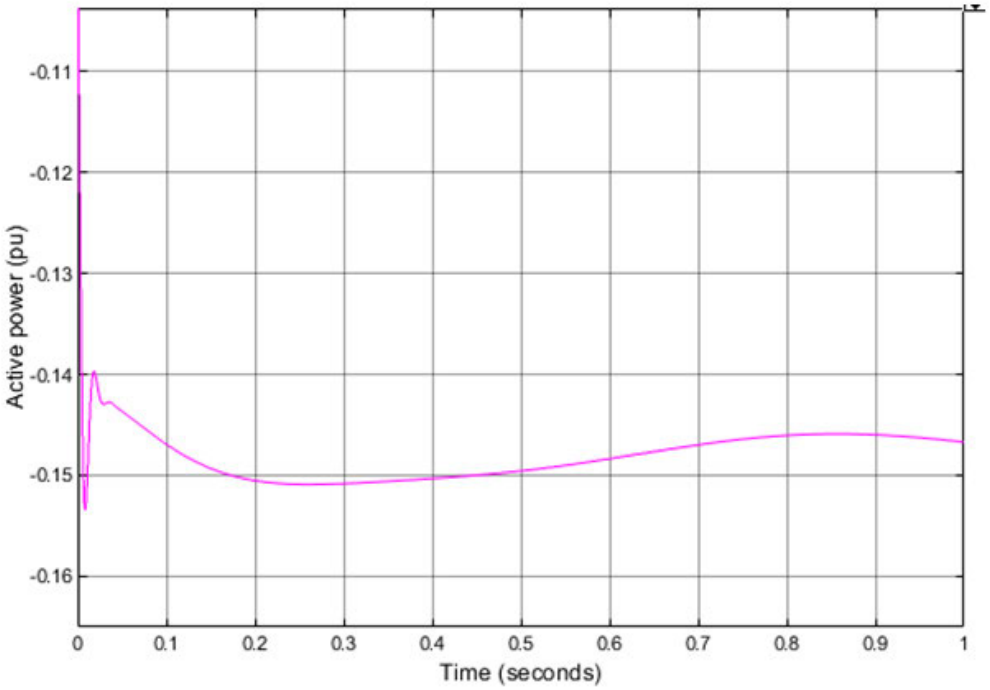

Figure 3.15: Reverse active power flow with 1.1 % penetration at transformer TR3

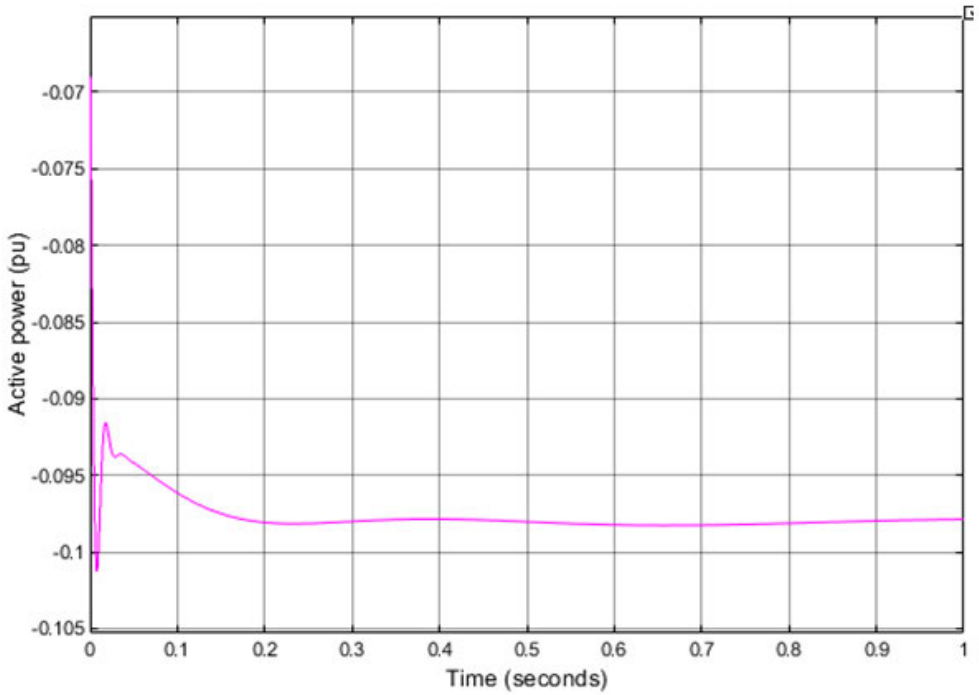

Figure 3.16: Reverse active power flow with 1.2 % penetration at transformer TR3

From the simulation results, the active power flow without the wind farm connected is shown in Fig. 3.13. However, with high penetration of wind farm, reverse power flow was observed as shown in Figs. 3.16 and 3.17 respectively. With an increase in penetration level to 1.1 %, a reverse active power of 0.145 pu was observed. A further increase in the penetration level from 1.1 % to 1.2 %, led to a reverse active power increase from 0.145 pu to 0.0975 pu. As

discussed in the previous chapter, the phenomenon of reverse power flow fundamentally changes the operation of the grid and it may have a negative effect on the network loading and losses; therefore, the next section discusses the impact of RPF on the transformer losses.

3.6.1 Transformer Losses Analysis

The transformer losses analysis is presented in this section. Table 3.7 shows the simulation analysis while the graphical presentation is shown in Fig. 3.17

Table 3.7: Transformer Losses Analysis

Penetration Level (%)	**TR2 (kW)**	**TR3 K(W)**	**TR4 (W)**
NO WT	1.653	1.726	4.152
0.1	1.675	1.726	4.085
0.2	1.702	1.867	4.203
0.3	1.733	2.058	4.502
0.4	1.769	2.23	4.985
0.5	1.807	2.592	5.649
0.6	1.851	2.933	6.493
0.7	1.899	3.325	7.516
0.8	1.951	3.764	8.714
1.0	2.008	4.253	10.091
1.1	2.068	4.791	11.641
1.2	2.133	5.377	13.363

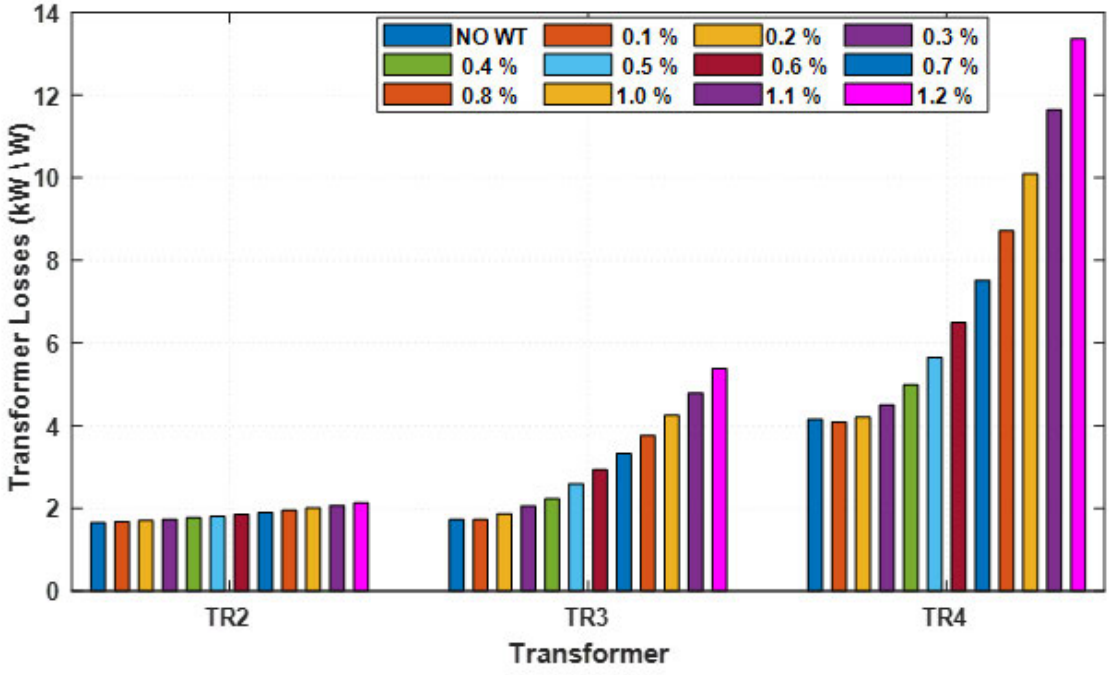

Figure 3.17: Transformer Losses at Different Penetration Level

From the analysis, the three transformers in the zone experience losses, and the losses increase with an increase in penetration level. However, transformers TR3 and TR4 experience more losses than TR2. Transformer TR 4 experiences RPF at a penetration level of 1.0 %. At this penetration level, the total losses rose from 10.09 W to 13.36 W with a penetration level of 1.2 %. From the analysis, it was also observed that RPF incurs additional losses of 41 % in the transformer.

3.7 Line Loading and Losses Analysis

The line loading and losses analysis in the considering zone A of the network under investigation are presented in this section. There are four lines in the zone. L2, L3, L4, and L5 as shown in Fig. 3.1. The loading analysis and graphical representation of the analysis are shown in Table 3.8 and Fig. 3.18 respectively.

Table 3.8: Line Loading Analysis

	Line Loading (kA)			
Penetration Level (%)	**Line 2 Thermal Capacity 0.371**	**Line 3 Thermal Capacity 0.967**	**Line 4 Thermal Capacity 3.705**	**Line 5 Thermal Capacity 0.849**
NO WT	0.203	0.56	1.674	0.106
0.1	0.2	0.543	1.663	0.106
0.2	0.198	0.526	1.69	0.107
0.3	0.196	0.509	1.754	0.112
0.4	0.193	0.492	1.85	0.115
0.5	0.191	0.475	1.974	0.125
0.6	0.189	0.459	2.12	0.135
0.7	0.186	0.443	2.284	0.145
0.8	0.184	0.427	3.463	0.157
1.0	0.182	0.411	3.853	0.169
1.1	0.18	0.396	3.952	0.181
1.2	0.177	0.381	4.058	0.194

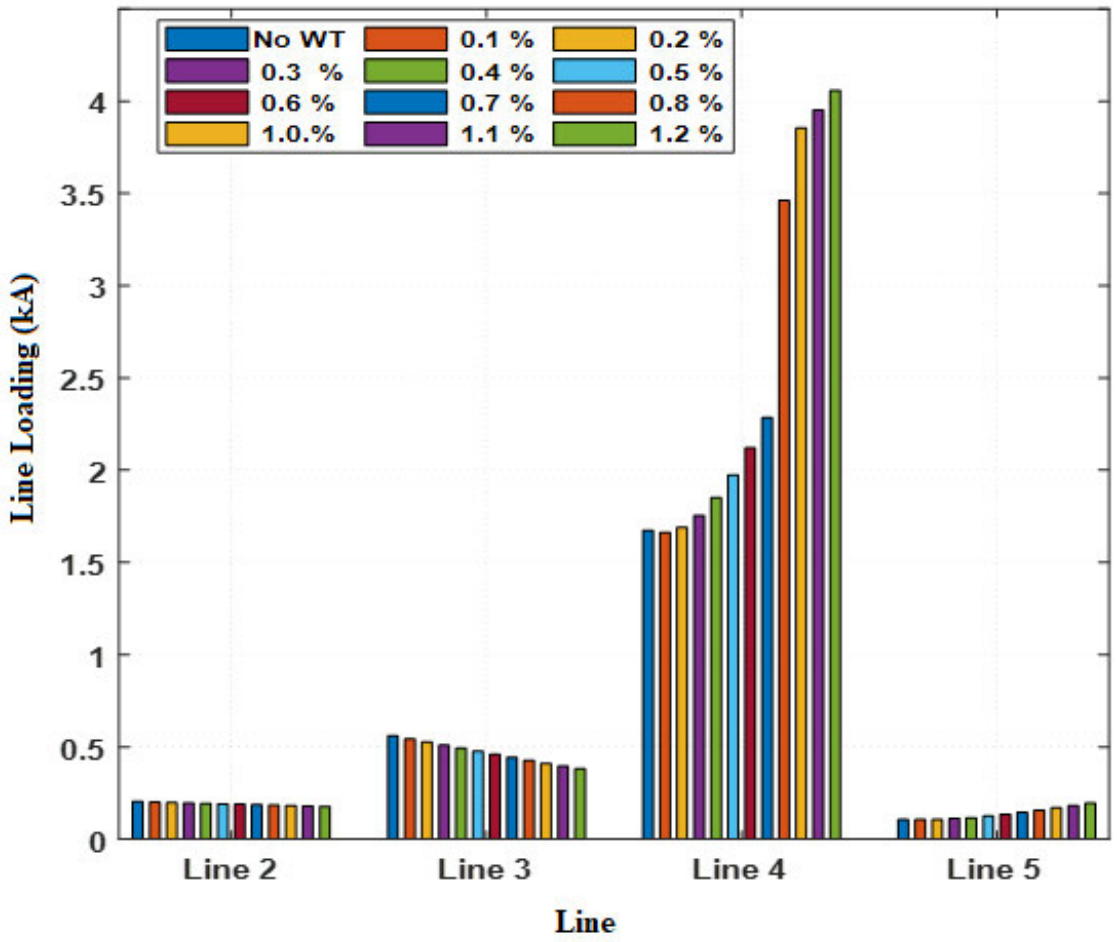

Figure 3.18: Line loading at Different Penetration Levels

From the analysis, it can be observed that the loading in lines 2 and 3 decreases with an increase in penetration level, while lines 4 and 5 that are directly connected to the wind farm experience increase in loading as the penetration level increases. However, only line 4 experiences overloading above its thermal capacity of 3.705 kA as shown in Table 3.8. From the analysis, the line starts to experience overloading and thus reverse current at the penetration level of 1.0 %. The excess current flow increases from 0.148 kA at the penetration level of 1.0 % to 0.353 kA at the penetration level of 1.2 %. From the analysis, the total reverse current in the line was 11.863 kA which contributes about 39 % of the total loading in the line. The line losses analysis is shown in Table 3.9 while Fig. 3.19 presents the graphical analysis of the losses.

Table 3.9: Line Losses Analysis

	Line Losses Analysis			
Penetration Level (%)	**Line 2 (kW)**	**Line 3 (kW)**	**Line 4 (kW)**	**Line 5 (W)**
NO WT	43.1	53.2	5.00	29.2
0.1	43.7	53.9	5.00	29.2
0.2	42.9	50.6	5.10	30.0
0.3	42.0	47.4	5.50	33.0
0.4	40.7	44.2	6.10	34.0
0.5	39.9	41.2	7.00	41.0
0.6	39.1	38.5	8.00	47.0
0.7	37.8	35.9	9.30	55.0
0.8	37.0	33.3	28.58	66.0
1.0	36.2	30.9	30.40	78.0
1.1	35.4	28.7	35.80	85.0
1.2	34.3	26.5	40.30	98.0

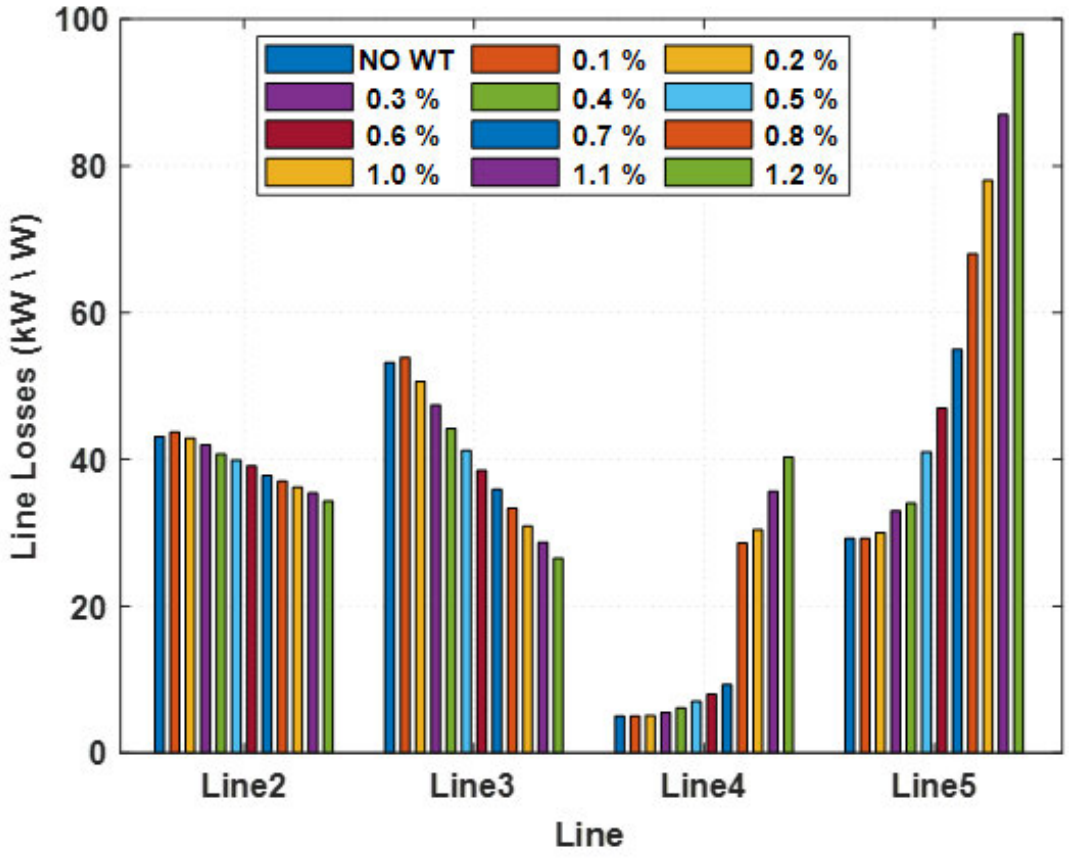

Figure 3.19: Line Losses at Different Penetration Levels

The losses in lines 2 and 3 reduce with increase in penetration level. While lines 4 and 5 that are directly connected with the wind farm experience increase in losses with an increase in penetration level as shown in Fig. 3.19. Lines 4 and 5 experience high losses immediately the reverse power flow occurred. The loss in line 4 rose from 30.40 kW at a penetration level

of 1.0 % to 40.30 % at a penetration level of 1.2 %. The loss in line 5 increases from 78 W at the penetration of 1.0 % to 98 W at a penetration of 1.2%. RPF incurs about 57 % additional loss in line 4. Line 5 did not experience RPF, but about 52 % additional loss was incurred in the line from a penetration increase from 1.0 % to 1.2 % when RPF occurs in the zone.

3.7.1 Total Power Losses

The influence of RESs on the grid losses relate to their impact on the total power flow in the system. This depends on the quantity of injected power and the positioning of the RES in the power system. Where RES is close to the demand, the energy injected is consumed. In this case, the energy losses are reduced compared to the case with no RES. However, grid losses may increase as the penetration level increases on the grid. Losses can also increase at night when demand is low and wind generation is high due to the excess energy produced. The analysis of the total power losses in zone A is shown in Table3.10 while Fig.3.20 shows the graphical analysis of the losses.

Table 3.10: total Power Losses Analysis

Penetration level (%)	**Power Losses (%)**
NO WT	8.838
0.1	8.951
0.2	8.603
0.3	8.28
0.4	7.94
0.5	7.688
0.6	7.47
0.7	7.244
0.8	8.63
1.0	8.685
1.1	8.747
1.2	9.184

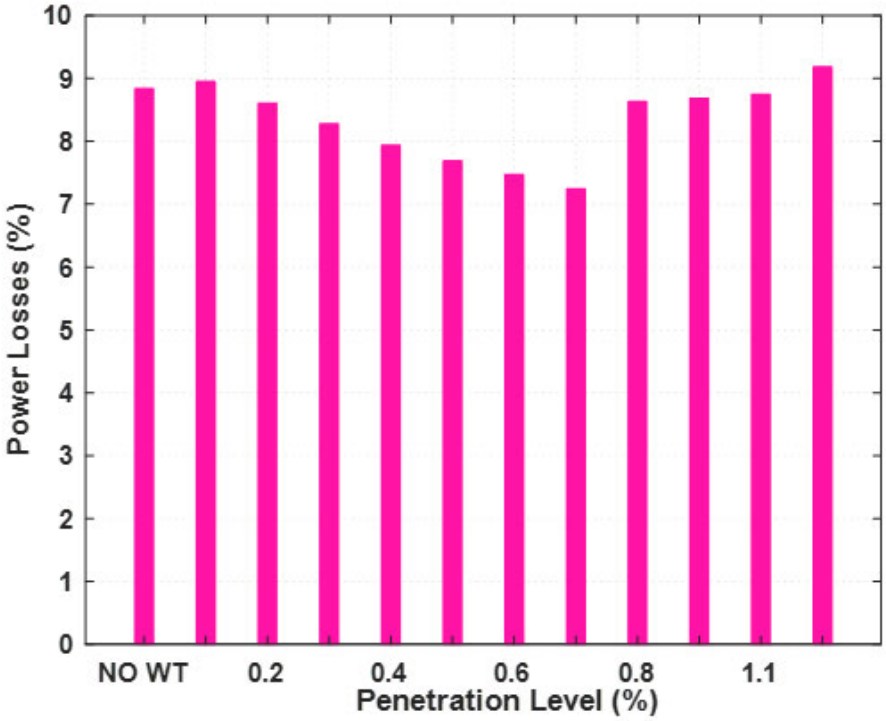

Figure 3.20: Line Losses at Different Penetration Level

From the analysis, can be seen that the total power losses in zone A reduce with an increase in penetration level due to the location of the wind farm; however, the presence of RPF due to excess power injected into the grid from the wind farm leads to grid loss increase as shown in Fig. 3.20. From the figure, it can be observed that the total losses increase from 8.69 % to 9.18 % as the penetration level increases from 1.0 % to 1.2 % when the RPF occurs in the zone.

3.7.2 Voltage Total Harmonic Distortion at Different Penetration Levels

This section presents an analysis of voltage total harmonic distortion (THD) measured at the PCC. Figs. 3.21 to 3.26 show the total harmonic distortion measured at the PCC (11 kV) with different wind farm penetration levels. Table 3.11 shows the analysis of the total harmonic distortion as measured at the PCC while Fig. 3.27 shows the graphical representation of the analysis at different penetration levels.

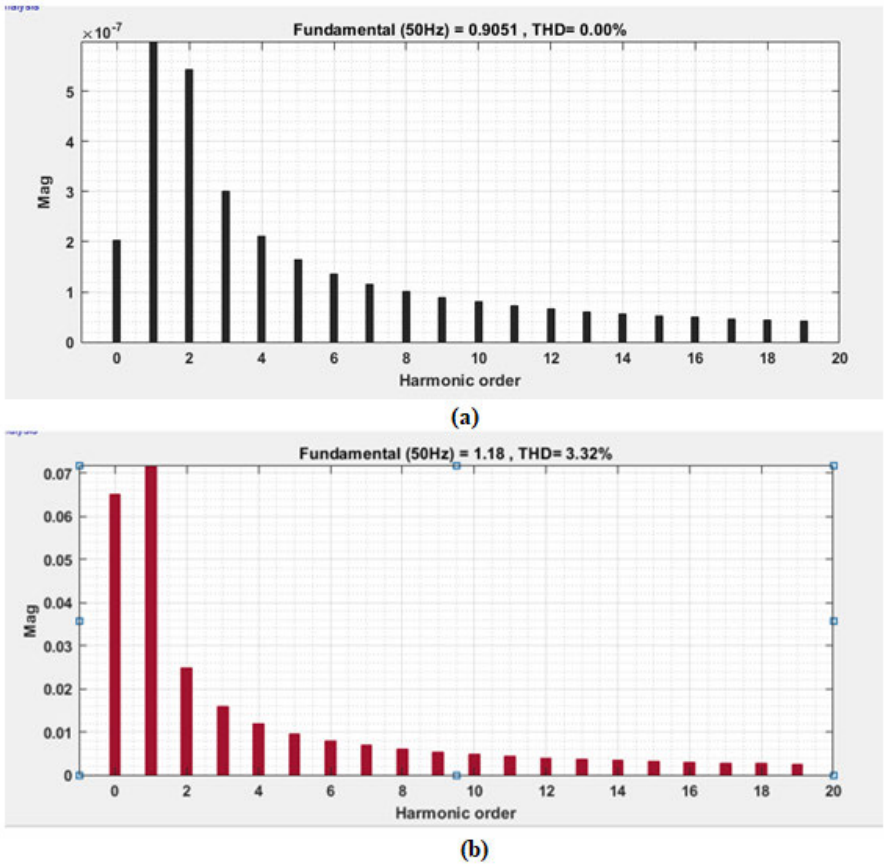

Figure 3.21: Voltage Total Harmonic Distortion at NO WT and 0.1 % Penetration Levels

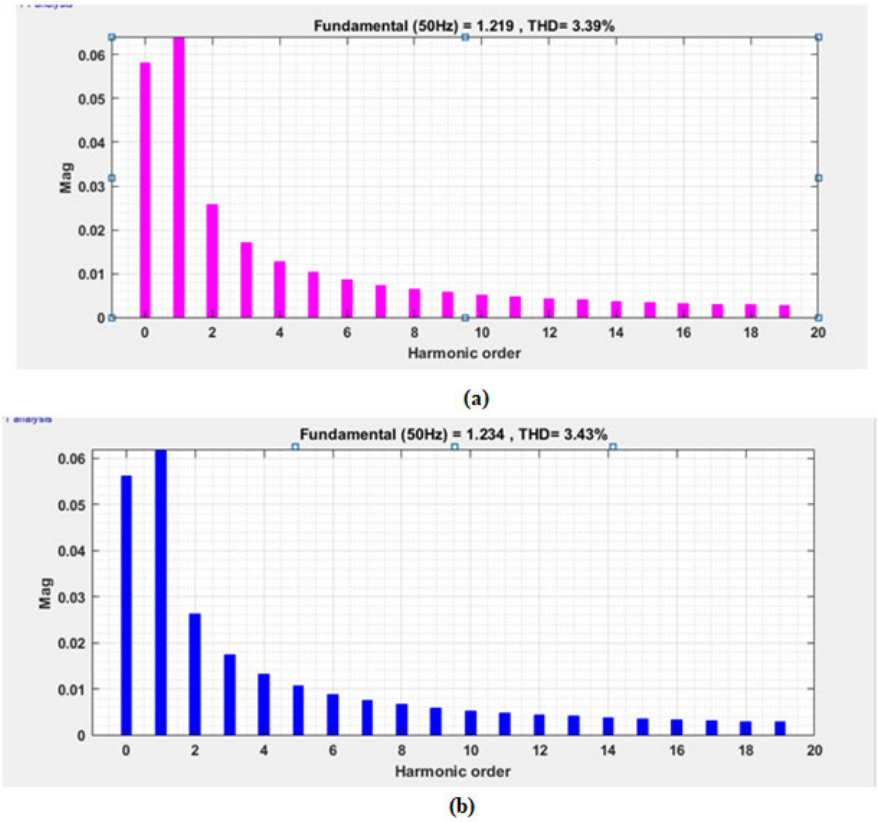

Figure 3.22: Harmonics at 0.2 and 0.3 % Penetration Levels

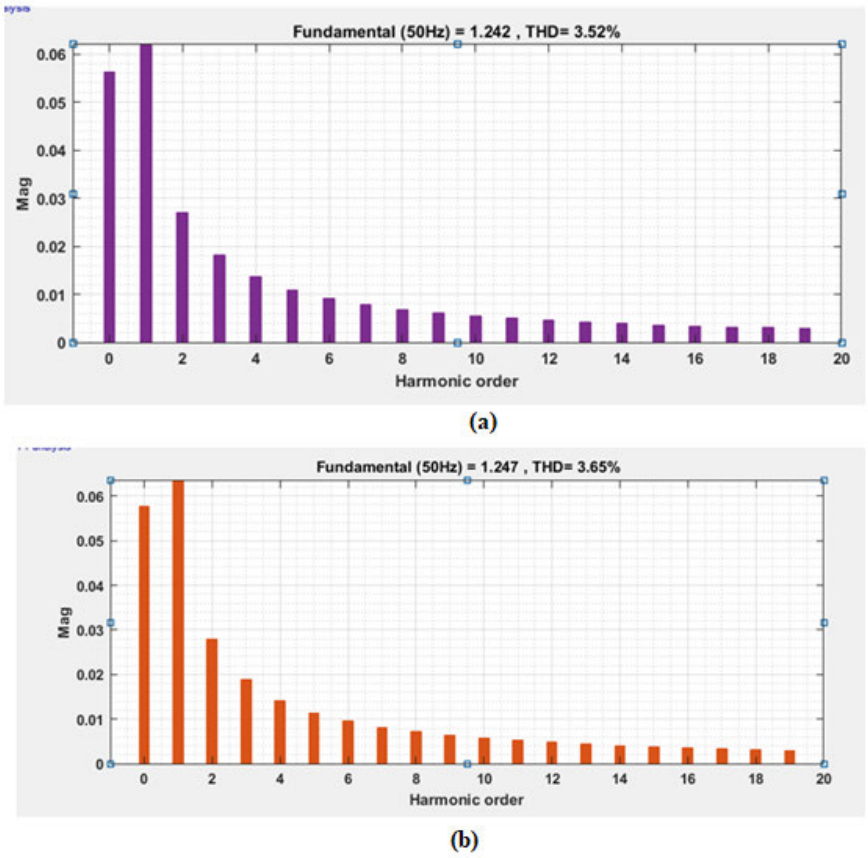

Figure 3.23: Voltage Total Harmonic Distortion at 0.4 and 0.5 % Penetration Levels

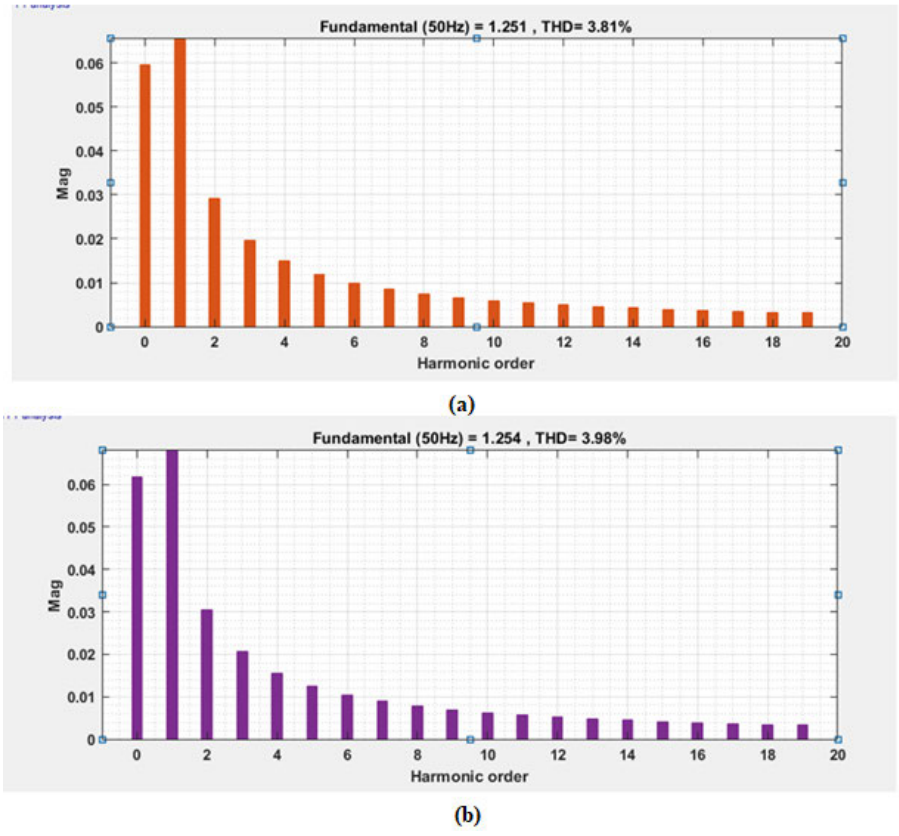

Figure 3.24: Voltage Total Harmonic Distortion at 0.6 and 0.7 % Penetration Levels

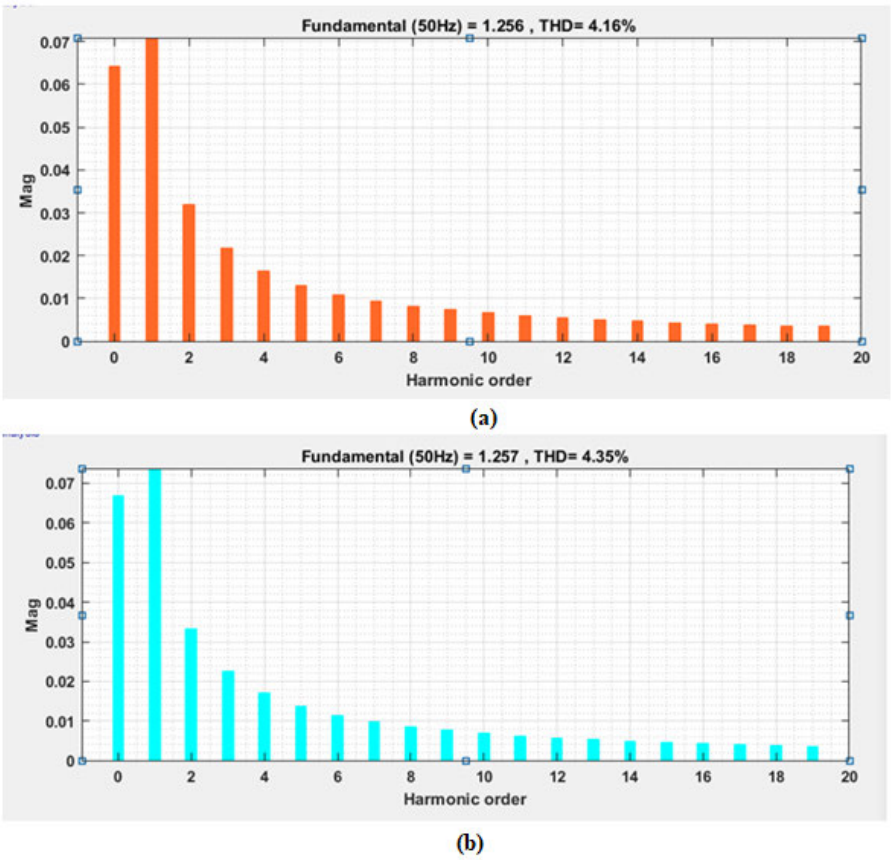

Figure 3.25: Voltage Total Harmonic Distortion at 0.8 and 1.0 % Penetration Levels

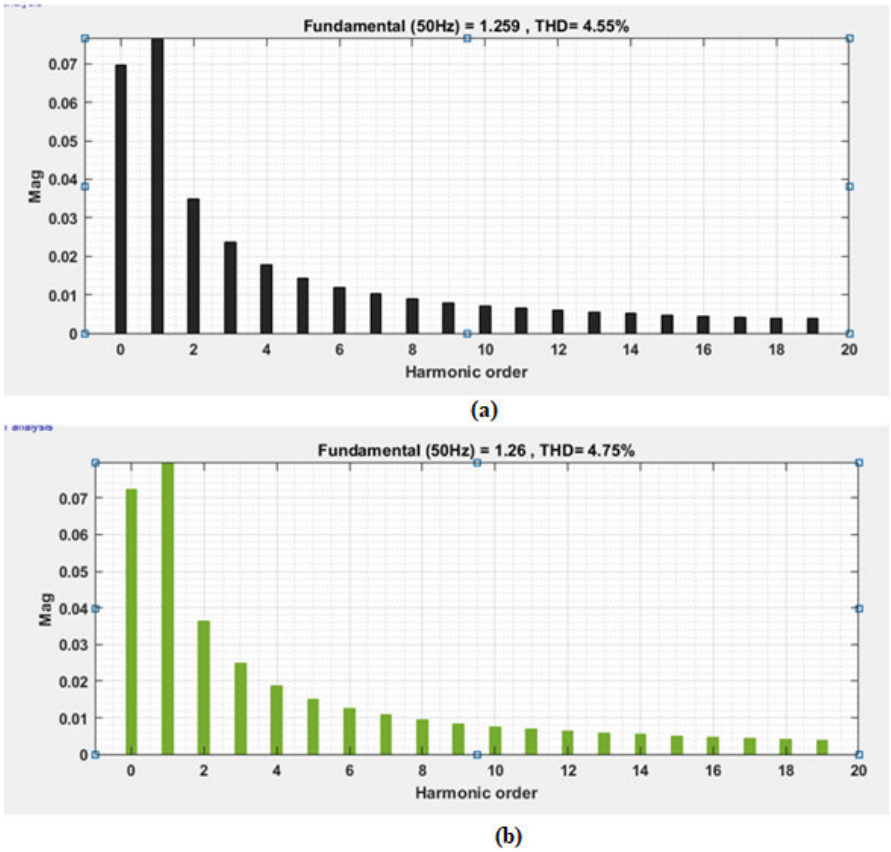

Figure 3.26: Voltage Total Harmonic Distortion at 1.1 and 1.2 % Penetration Levels

Table 3.11: Voltage Total Harmonic Distortion Analysis

Penetration Level (%)	**Voltage Total Harmonic Distortion**
NO WT	0.00
0.1	3.32
0.2	3.39
0.3	3.43
0.4	3.52
0.5	3.65
0.6	3.81
0.7	3.98
0.8	4.16
1.0	4.35
1.1	4.55
1.2	4.75

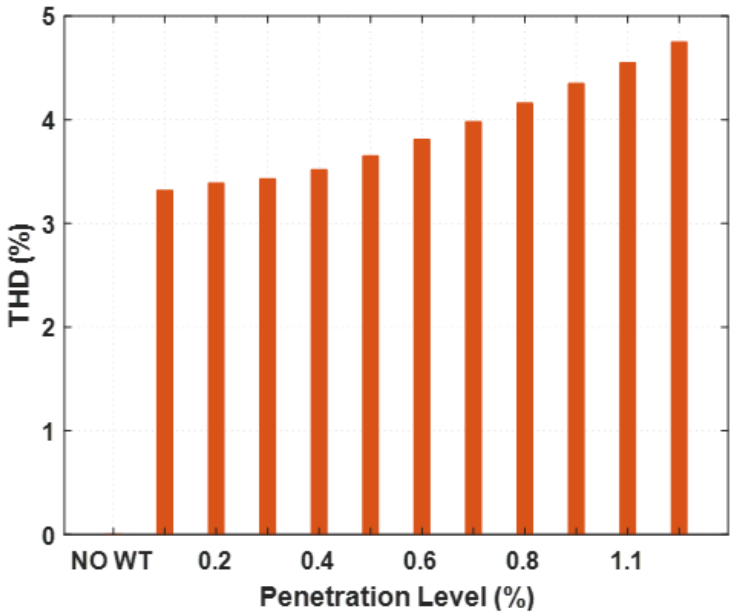

Figure 3.27: Voltage Total Harmonic Distortion (THD %) at the PCC

According to IEEE Standard 5194 requirements, the total harmonic distortion level for voltages less than or equal to 11 kV should be less than 5 %. From the analysis it was observed that the total harmonic distortion increased greatly with an increase in wind farm penetration. The analysis shows that the total harmonic distortion increases exponentially from 4.16 % to 4.75 % at a penetration level of 1.0 % to 1.2 % when RPF occurs on the grid. This is still within the IEEE Standard 5194 requirements as described in Section 2.7.9, Table 2.2. However, any further increase in the wind farm penetration level may violate the standard harmonic limit.

3.8 Summary

The main points in this chapter can summarized as follows:

- RPF increases with an increase in the penetration level of wind energy.
- RPF only affects transformer TR 3 which is the transformer closest to the PCC of the wind farm. This occurs when the generation from the wind farm exceeds the load demand in the distribution network.
- The transformer, line, and total losses on the grid increase with an increase in reverse power flow. RPF incurs additional losses in the system connecting elements (transformers and conductors).
- It was observed that the total harmonic distortion increases with an increase in RPF on the grid; however, the increase is still within the acceptable limit recommended by IEEE Standard 5194.

Chapter 4

Proposed Reverse Power Flow Utilisation Using Power Electronic Transformer

4.1 Introduction

This chapter presents the validity of a PET in reverse power flow utilisation. The concept depends on the association or interaction between the power grid, PET and the connected loads. The proposed PET regulates and converts the power from one voltage level to another. The proposed PET has the ability of voltage-frequency regulation without implementation and installation of any special communication devices on the network. Energy imbalance or grid disturbances such as fault or line disconnection may lead to abnormality in voltage profile which may lead to reverse power flow on the grid.

4.2 Methodology

This section describes the proposed method for RPF utilisation. The proposed method uses a MPPET to supply the excess power generated to an EV charging station. The general structure of the proposed RPF utilisation network is shown in Fig. 4.1.

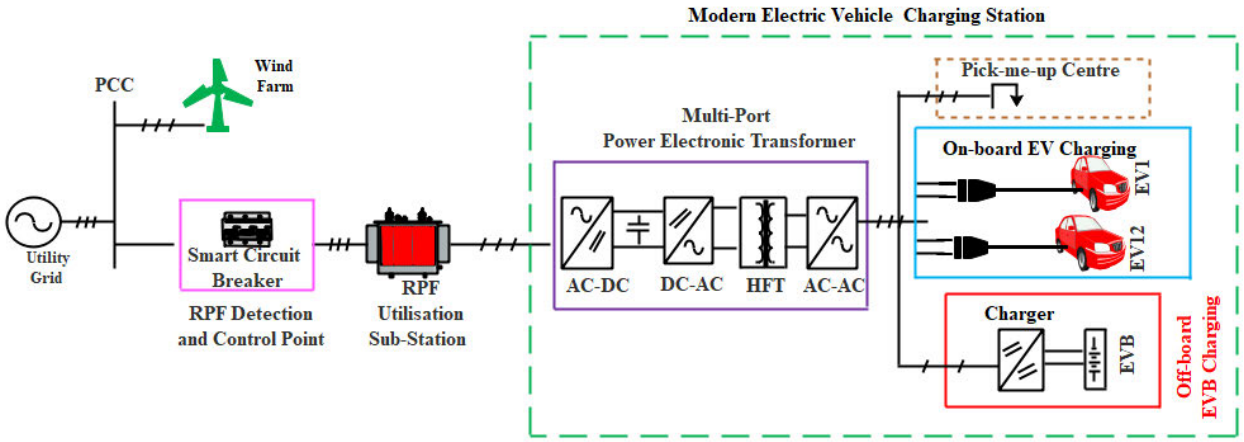

Figure 4.1: Single Line Diagram of the Proposed Method for Reverse Power Flow Utilisation

4.3 Utilisation Procedure

4.3.1 Reverse Power Flow Detection Stage (RPFDS)

This stage consists mainly of a smart circuit breaker which is electrically coupled to the grid at the PCC. RPFDS is a stage that discriminates between the total power generated on the grid and the total load demand and immediately takes automatic action based on the result and the pre-set conditions.

4.3.2 Reverse Power flow Utilisation Substation (RPFUS)

The substation makes use of step-down transformer to change the voltage level of the incoming power to the level required by EV battery charging station. The rating of the substation is 11/0.4kV.

4.3.3 Multi-port Power Electronic Transformer

The block diagram of the proposed PET is shown in Fig. 4.2. As can be seen from the Figure this is a three-stage design that includes an input stage, an isolation stage, and an output stage. The input stage consists of an AC-DC converter which converts the input AC voltage to DC voltage. The second stage consists of a DC-AC converter which is connected to the high frequency transformer (HFT). The third stage is the output stage, which consists of AC-AC (matrix converter). The proposed topology has a reduced number of conversion stages compared to the usual topology. The topology has the capability of sag control and reactive power compensation. Each stage can be controlled separately.

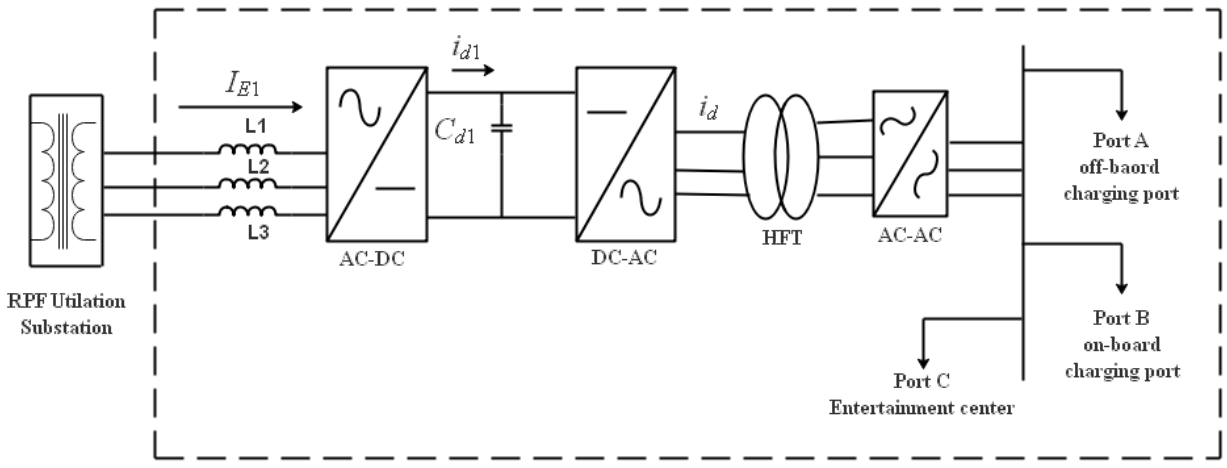

Figure 4.2: Single line Diagram of the Proposed Power Electronic Transformer

The transformer consists of more than one port, thus the name multi-port power electronic transformer. Port A connects the transformer to an off-board EV battery charging station,

while port B connects to the on-board EV battery charging station and port C is connected to the entertainment center

4.3.4 Input Stage (AC-DC Converter)

The input stage is a three-phase AC-DC converter for converting AC voltage to DC voltage. The primary function associated with controlling the rectifier is adjusting the input current, controlling the input power factor, and maintaining the DC-link voltage at the required reference value. A two-level standard inverter when used as the input stage AC-DC, with input inductance is shown in Fig. 4.3.

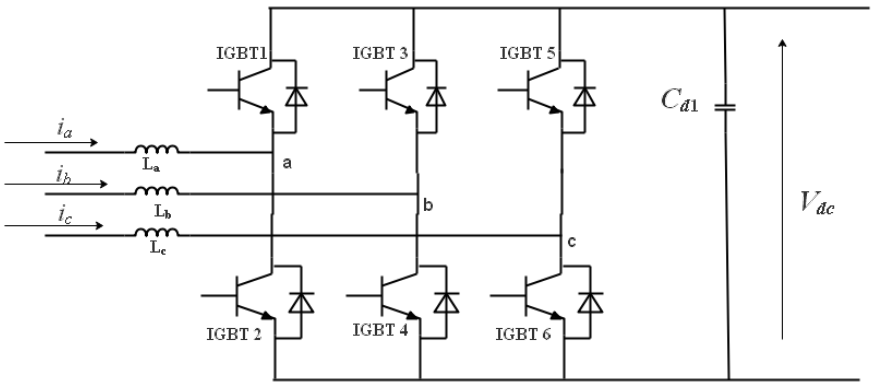

Figure 4.3: Basic Structure of AC-DC Converter with DC-link

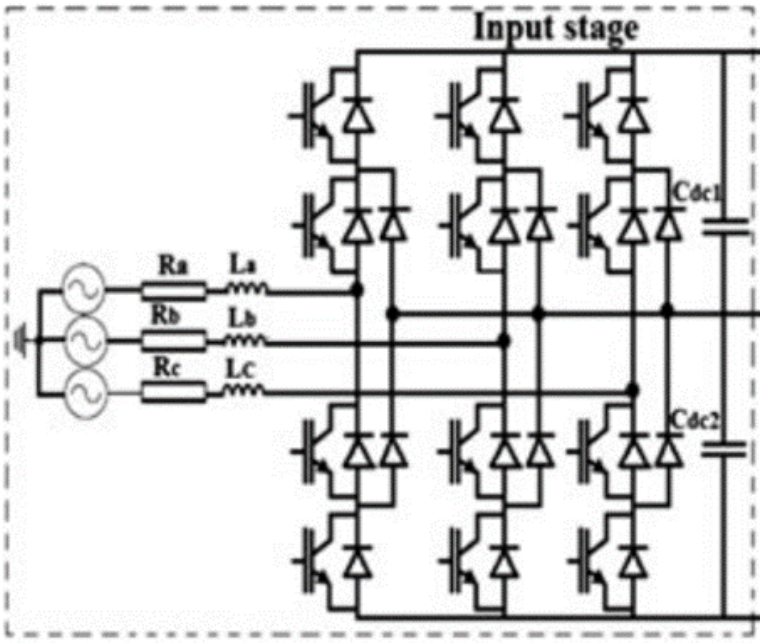

Figure 4.4: Three level converter [138]

It is possible to use a three level inverter as reported in [138] and illustrated in Fig. 4.4.

Fig. 4.5 shows the input stage control diagram. The DC regulator uses a PI controller to regulate the DC voltage while maintaining unity power factor for the AC supply. For the three level converter AC-DC conversion stage [138]:

$$L_{E1}\frac{di_{Eld}}{dt} = \omega L_{E1} i_{E1q} + V_{1d} - V_{E1d} \tag{4.1}$$

$$L_{E1}\frac{di_{Elq}}{dt} = \omega L_{E1} i_{B1d} + V_{1q} - V_{E1q} \tag{4.2}$$

where, L_{E1} is the interface inductance, i_{E1} is the line current in the input side of the converter, V_{E1} is the input voltage and ω is the angular velocity respectively. The three-level PWM of the converter output voltage is controlled using current $I_{\text{dilq_Ref}}$ and I_{d1q} in this regards, the voltage is presumed be constant, therefore V_{Id} and V_{I_q} are given by

$$V_{Id} = -\left(K_{ip} + K_i I/S\right)\left(i_d^* - I_{diq_\text{Ref}}\right) + \omega L_{qs} + V_{dS} \tag{4.3}$$

$$V_{Iq} = -\left(K_{ip} + K_i I/_S\right)\left(i_q^* - I_{diq}\right) + \omega L_{ds} + V_{qS} \tag{4.4}$$

To implement the above functions, in the outer-loop control, the feedback DC voltage is compared to the reference value. The difference is then passed through the PI controller to get the reference value i_d. When the reference value i_q is set to zero, the rectifier can achieve the unity power factor operation. In the inner-loop, three-phase input currents are transformed into i_d and i_q components in the synchronous rotating d-q reference frame. The components are compared with the reference values of i_d and i_q . The difference was formulated to wave signal by the PI controller.If the d axis of the reference frame is aligned to the grid voltage, $V_{\text{inq}} = 0$ [138], [139].

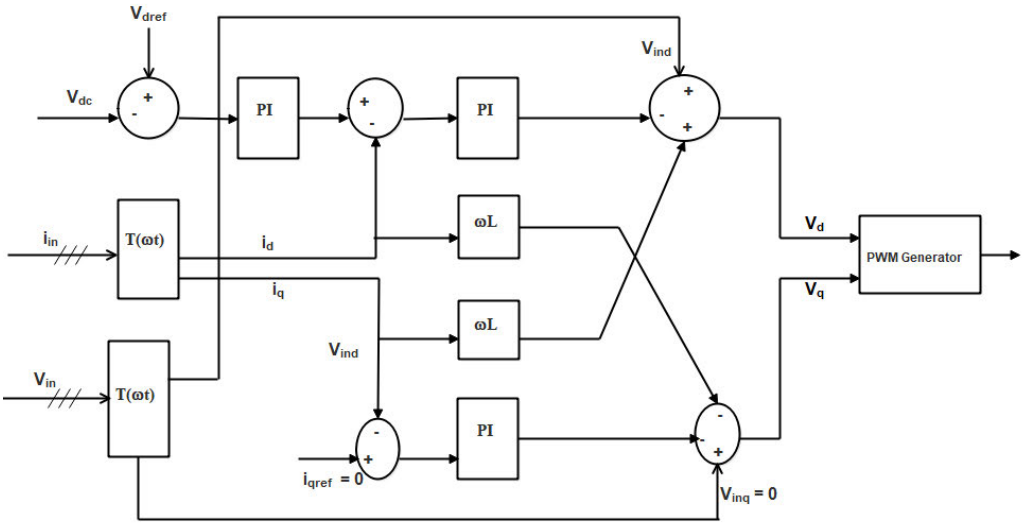

Figure 4.5: Input stage AC-DC control circuit

This converter is used in back-to-back form for AC-DC-AC simulations as illustrated in Section 4.5.2 with the model in Fig. A.8.

4.3.5 DC-AC Conversion Stage

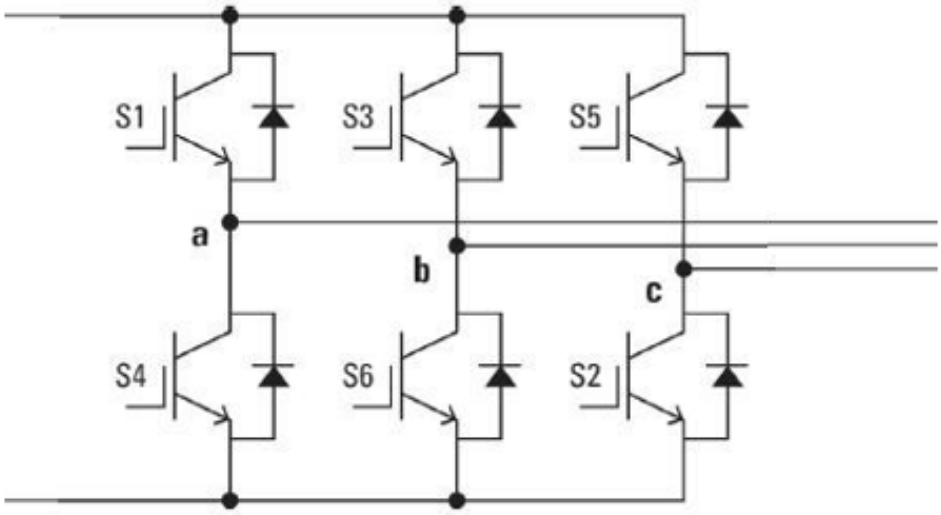

Figure 4.6: Basic Structure of DC-AC Inverter

A two-level DC-AC inverter is shown in Fig. 4.6. This converts DC voltage to AC voltage. The input comes from the output of the previous AC-DC stage. The main purpose this stage is to ensure a constant output AC voltage and frequency to the HFT. A three level converter such as in Fig. 4.4 can also be used if the grid side converter is a three-level converter. The control system consists of external loop, internal current loops and phase lock loop (PLL). The phase lock loop supplies a reference phase angle for the control system. The internal loop tracks the

current reference in the dq frame, and the external loop produces d and q current references for the internal loop. The external loop includes active power control and AC voltage control (or reactive power control). Active current (I_d) reference is the output of the DC voltage external controller. V_d and V_q voltage outputs of the current controller are converted to three modulating signals $V_{abc-ref}$ used by the PWM Generator. The complete control circuit diagram is shown in Fig. 4.7.

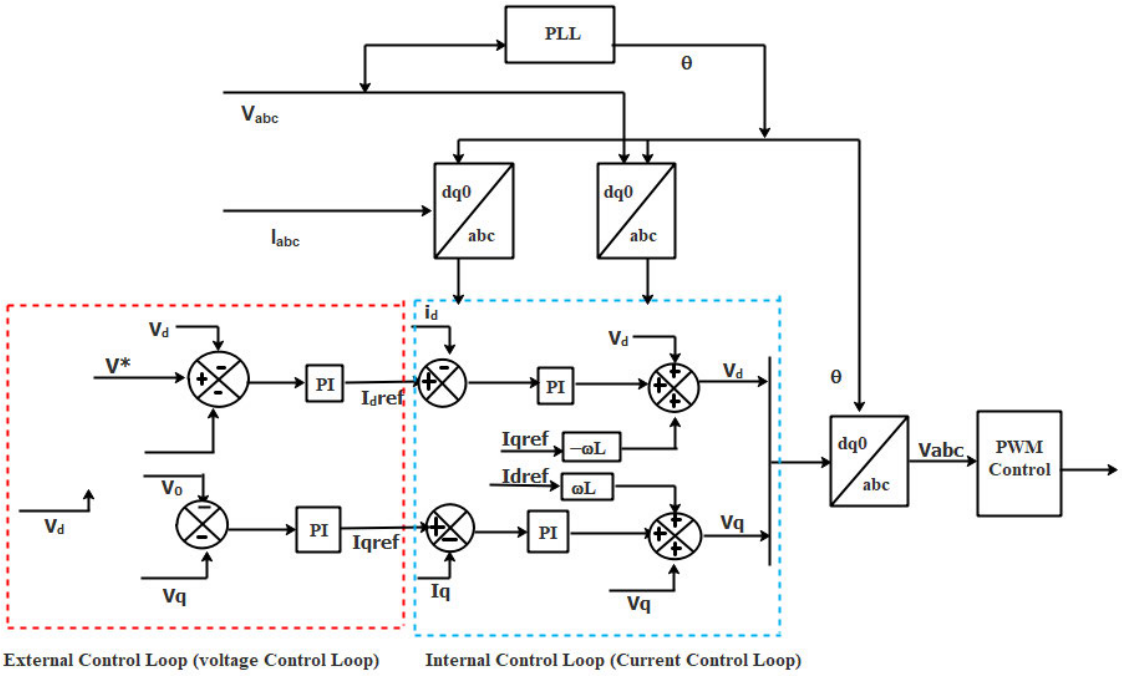

Figure 4.7: Complete Control Circuit for DC-AC PET Conversion Stage

Considering the external control loop, the PI controller outputs I_{dref} and $\dot{I}_{qref}$ are calculated from

$$I_{\dot{\omega}\in f} = \left[K_p + \frac{Ki}{S}\right](V_{ref} - V_d) \tag{4.5}$$

$$I_{qref} = \left[K_p + \frac{Ki}{S}\right](-V_d + V_0) \tag{4.6}$$

V_{rff} is the new voltage reference. I_{dref} and $\dot{I}_{qref}$ are the q-axis actual and reference inverter current components, V_d and V_q are the d-axis and q-axis of the voltage component respectively, while K_p and K_i are the proportional and integrator gain of PI controller. The outputs of the PI controller in the external control loop are given as V_d and V_q in d-q form. These voltages are used as a reference voltage for pulse width modulation (PWM) [138], [139].

4.3.6 High Frequency Transformer

High frequency transformer design is another key parameter be considered when designing a PET. The HFT allows electric power transfer from the input converter to the output converter of the transformer and provides galvanic isolation. The size of the transformer depends on the capacity and operating frequency. Thus, the higher the frequency, the smaller the size of the transformer. Normally, the frequency of operation ranges from 20 kHz to 100 kHz [140]. The basic structure of the high frequency transformer is shown in Fig. 4.8.

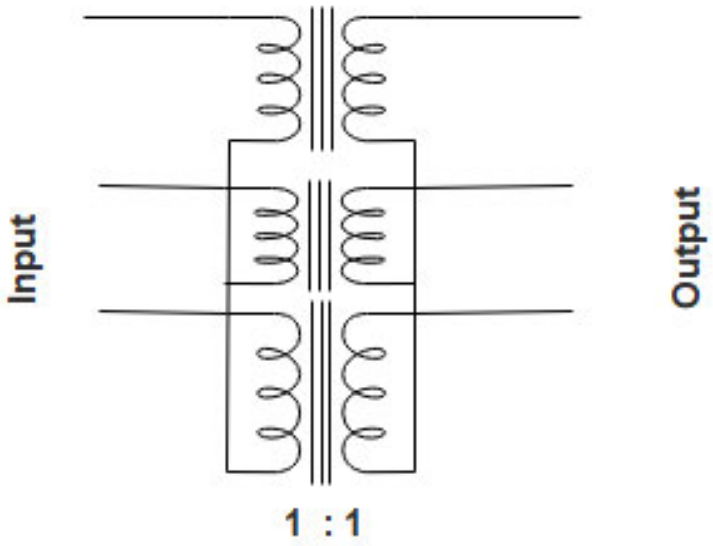

Figure 4.8: Basic Structure of Three-phase High Frequency Transformer

4.3.7 AC-AC Conversion Stage

This stage consists of MC. The converter consists of 18 IGBTs which are arranged in common emitter mode to form nine bidirectional switches. The nine switches were designed to connect any three-phase input to any output phase. Therefore, the voltage at any input terminal can appear at any output terminal, allowing the load to draw current from any of the input supply phases. For each possible connection there must only be one input connected one output via one switch and this is for all three outputs. Hence, for each output phase, the inputs are chopped to reconstruct the output voltage which will be a different frequency from the input voltages. There are many techniques for MC modulation; however, this work uses the indirect space vector modulation technique. The technique allows direct control of the input and output voltage, thereby providing regulation of the source's power factor. The circuit diagram of the proposed three-phase to three-phase MC is shown in Fig. 4.9 [141].

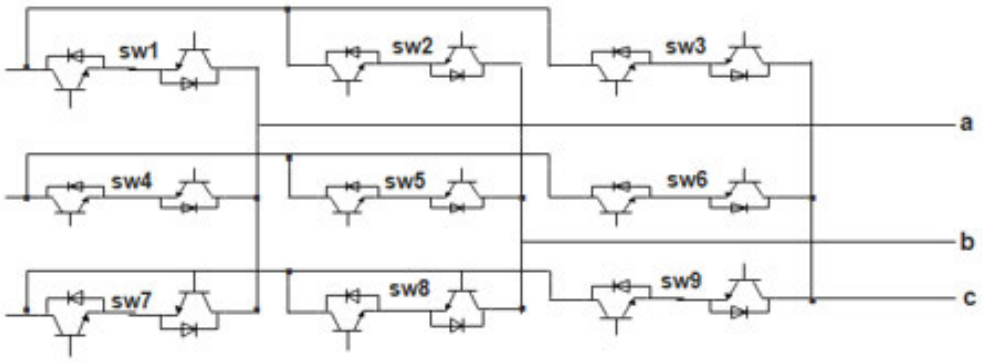

Figure 4.9: Basic Structure of Matrix Converter. v_{ABC} are three phase inputs and v_{abc} are three phase outputs of different frequency and magnitude; sw1 = S_{Aa}, sw2 = S_{Ab}, sw4 = S_{Ba}, etc.

The switching principle of the MC can be represented as:

$$S_{ij} = \begin{cases} 1, & S_{ij} \text{ is closed} \\ 0, & S_{ij} \text{ is open} \end{cases} \tag{4.7}$$

where, i, j are the indexes that represent each switch and are given as $i = (A, B, C), j = (a, b, c)$. When applying different switching states to MC, there are two constraints that must be noted at any switching time. Firstly, the input phases must not be shorted, and secondly, the output phases must not be opened. Thus, the constraints are

$$S_{Aj} + S_{Bj} + S_{Cj} = 1 \tag{4.8}$$

For a balanced the three-phase set, the instantaneous input voltage can be express as:

$$V_i(t) = \begin{bmatrix} v_A(t) \\ v_B(t) \\ v_C(t) \end{bmatrix} = V_M \begin{bmatrix} \cos \omega_i t \\ \cos\left(\omega_i t - 120^\circ\right) \\ \cos\left(\omega_i t + 120^\circ\right) \end{bmatrix} \tag{4.9}$$

The reconstructed PWM output voltage (line-line) is

$$V_0(t) = \begin{bmatrix} V_{ab}(t) \\ V_{ac}(t) \\ V_{ca}(t) \end{bmatrix} = \sqrt{3} V_0 \begin{bmatrix} \cos\left(\omega_0 t - \varphi_0\right) \\ \cos\left(\omega_0 t - \varphi_0 - 120^\circ\right) \\ \cos\left(\omega_0 t - \varphi_0 + 120^\circ\right) \end{bmatrix} \tag{4.10}$$

while the indirect transfer function is

$$[ITF(t)] = M \times \begin{bmatrix} \cos(\omega_0 t - \varphi_0) \\ \cos(\omega_0 t - \varphi_0 - 120^\circ) \\ \cos(\omega_0 t - \varphi_0 + 120^\circ) \end{bmatrix} \begin{bmatrix} \cos \omega_i t \\ \cos(\omega_i t - 120^\circ) \\ \cos(\omega_i t + 120^\circ) \end{bmatrix}^T \tag{4.11}$$

where M is the modulation index which is less or equal to unity, thus, the transfer matrix is given as the product of the two matrices where

$$[ITF(t)] = [ITF_{rs1}(\omega_0)] [ITF_{rsR}(\omega_i)]^T \tag{4.12}$$

where M is incorporated into the first term on the right. A constant virtual DC voltage is obtained by multiplying with the input vector voltage so that:

$$[ITF_{rsR}(\omega_i)]^T (V_M(t)) = \frac{3}{2} (V_M \times \cos(\varphi_i)) = V_{d\varepsilon} \tag{4.13}$$

This equation shows the operation of a voltage source rectifier of the matrix converter. Voltage source inverter (VSI) of the MC is obtained by multiplying (4.13) by $ITF_{VSI}(\omega_0)$ which gives:

$$v_0(t) = [ITF_{VSI}(\omega_0)] \times V_{dc} \tag{4.14}$$

In reality, since the output voltages are pulse trains from PWM then:

$$V_o(t) = [S_{i,j}] V_i(t) \tag{4.15}$$

4.3.8 Modulation Techniques for Matrix Converter

The aim of modulation in a MC is to improve the voltage transfer ratio. The MC is modulated by choosing a suitable array of switching functions to achieve predefined values for output voltages and input currents. The modulation techniques employed by a MC can be grouped into: pulse width modulation (PWM) technique and the scalar modulation technique. The PWM can be sub-grouped into carrier pulse width modulation and space vector pulse width modulation techniques. This research work uses space vector pulse width modulation techniques for the control of the MC [142], [143], [144] and [145].

4.3.9 Space Vector Pulse Modulation Techniques

Due to better harmonic efficiency with different switching strategies, the SVPM technique is one of the commonly used modulation techniques. At any given sample, the output voltage vector and the displacement angle of the input current are referred to as reference parameters. By adjusting the phase angle of the input current vector, the control of the input side can be realized. The space vector modulation principle is used to determine the switch duty cycle that is crucial in the execution of the PWM digital control concept. The two classes of SVPM are: indirect space vector modulation (ISVPM) and direct space vector modulation (DSVPM). The ISVPM technique uses an equivalent circuit, similar to that of the back-to-back converter, which directly transfers the output result of the modulation to the MC. High output voltage and a reduced number of switches are the main advantages of SVPM over conventional PWM technique. It has an intrinsic ability to fully control both the output voltage vector and the displacement angle of the instantaneous input current. The ISVPM technique has been used for the control of a MCs in previous work [142], [145].

4.3.10 Input Filter

The LC input filter is shown in Fig. 4.10.

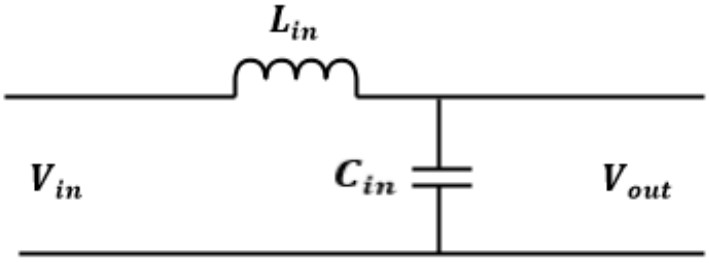

Figure 4.10: Equivalent Circuit of LC Filter

The aim of using an LC filter is to reduce the phase shift between the input current and the output current. The capacitance of the filter is given as:

$$C_{in} = \frac{\sqrt{3} I_{\min} \operatorname{arctg}(Q_{\max})}{\omega V_C} \tag{4.16}$$

where C_{in} is the maximum capacitance of the capacitor, $I_{\min}$ is the minimum current of the PET, $Q_{\max}$ is the maximum possible phase shift between the input current and the output

current, ω is the resonance frequency and V_c is the capacitor voltage. The filter inductor is

$$L_{in} = \frac{1}{\omega_{in}^2 C_{in}} \tag{4.17}$$

where ω_{cin} is the cut-off angular frequency of the filter and C_{in} is the input capacitor.

4.3.11 Output Filter

An LCL filter is used for the output of the PET. The equivalent circuit of the output filter is shown in Fig. 4.11.

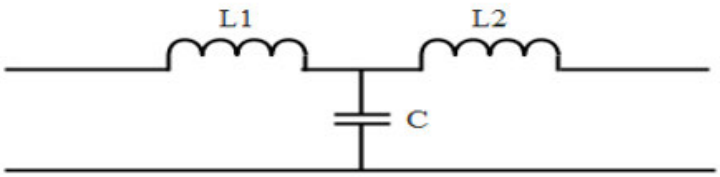

Figure 4.11: Equivalent Circuit of Series LCL Filter

The inverter side inductor and the grid side inductor are:

$$L_1 = \frac{V_{DC}}{6 f_S \Delta I_{L\,\max}} \tag{4.18}$$

$$L_2 = r L_1 \tag{4.19}$$

$$\Delta I_{L\,\max} = 0.1 I_{\Delta xx} \tag{4.20}$$

$$I_{M\alpha x} = \frac{\sqrt{2} P_{rated}}{3 V_{ph}} \tag{4.21}$$

where: V_{DC} is the DC-link voltage, f_S is the switching frequency, $\Delta I_{L\,\max}$ is the maximum peak to peak current ripple, P_{ratad} is the rated active power, while p is the ratio of the inductance at the inverter side to the inductance at the grid sid, and V_{ph} is the phase voltage. The base impedance Z_b and the base capacitance C_b are the parameters used to derive the capacitance of the inverter. The base impedance and the base capacitance are calculated from

$$Z_b = \frac{V_{RMS}}{P_{ramd}} \tag{4.22}$$

$$C_b = \frac{1}{\omega_g Z_b} \tag{4.23}$$

where V_{RMS} is the line-line RMS voltage, and ω_g is the grid angular frequency. The inverter capacitance is:

$$C_f = 0.5 C_b \tag{4.24}$$

4.3.12 Charging Station Arrangement

The charging station comprises of both on-board and off-board EV battery charging sites, as well as the pick-me-up centre. The overall system model is shown in Fig. 4.12.

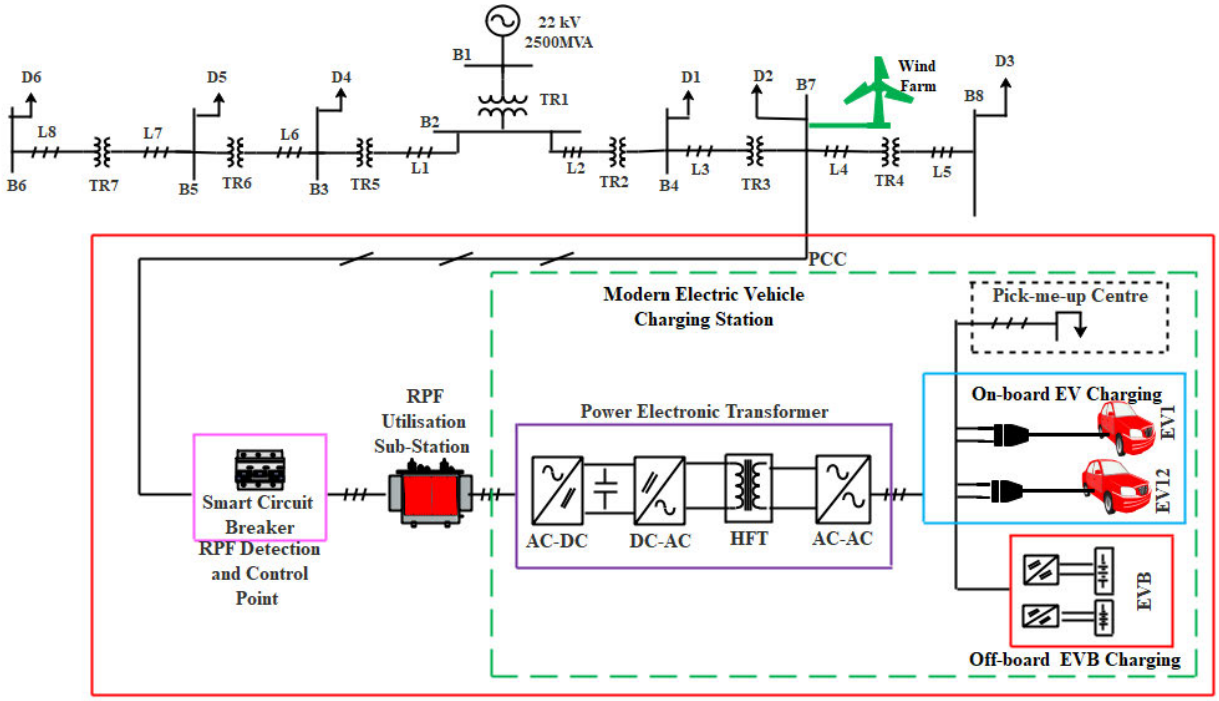

Figure 4.12: Single-Line Diagram of the Overall System Modelling

4.4 Utilisation Algorithm

The flow chart algorithm for the proposed utilisation method is shown in Fig. 4.13.

The algorithm computes the energy balance index (EBI) on the grid and makes comparison with the total grid demand then takes a decision based on the result. As described in Section 2.8, the energy balance index is grouped into three different categories of operation. The grid is under normal loading condition when the energy balance index is less than zero (EBI < 0), it is under critical loading when the energy balance index is equal to zero (EBI $= 0$), and the grid is already overloaded when the energy balance index is greater than zero (EBI >0). The critical loading condition was considered to be the reference point of operation. The algorithm computes the energy balance index and compares it with the total grid demand if the difference is equal to zero, that is EBI $= TA_g - TL_d = 0$. The algorithm takes action by operating the smart break at the PCC to all the excess power generated to flow through for utilisation. TA_g and TL_d are the total active power generated and total load demand on the grid respectively. The design and simulation are carried out using MATLAB/Simulink software. The proposed method ensures grid stability by automatically responding to situations on the grid. The ability

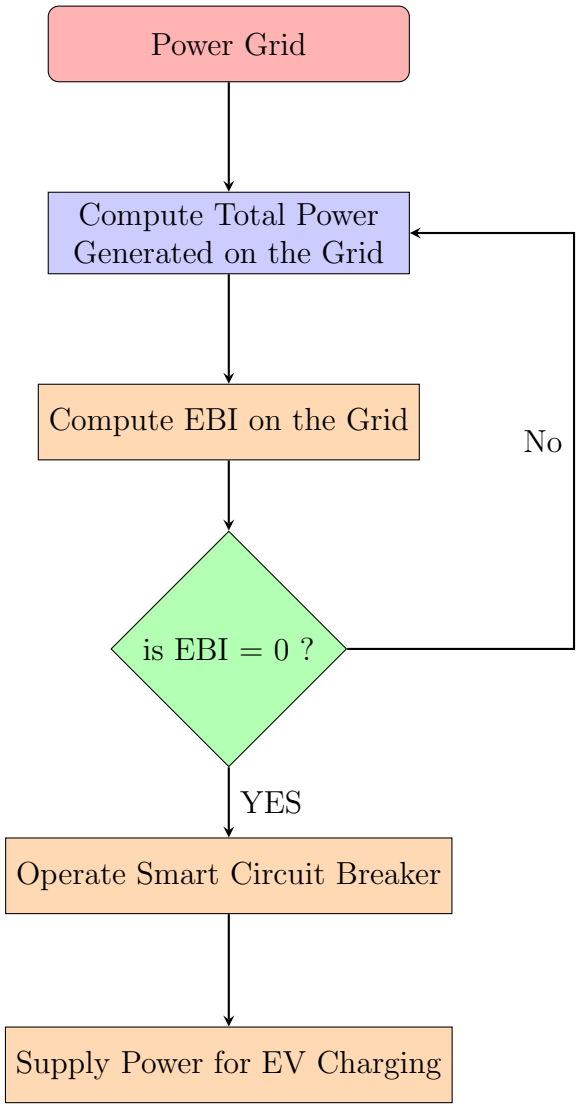

Figure 4.13: Proposed RPF Utilisation Flow Chart Algorithm

of the grid to automatically respond to situations makes the grid reliable and smart during the G2V process. In addition, the proposed method does not make use of an ESS which makes it more cost effective. Furthermore, the proposed method allows different load connection through a MPPET. The method can be used with an ESS to store excess energy during excess generation and later release it, a process called vehicle to grid (V2G) [146]; however, this research work does not consider the process.

4.5 Simulation Scenarios

This section addresses the use in a higher power network as shown in Fig. 4.14. For better understanding and analysis of the effectiveness of a PET in RPF usage the simulation conditions are divided into two sections:

(i) Design and simulation of a PET for effective voltage control; and

(ii) Design and simulation of a MPPET for effective utilisation of RPF.

4.5.1 Design and Simulation of Power Electronic Transformer for Voltage Control

As stated in the previous chapter, RPF is always accompanied by voltage rise on the grid, thus this section presents the simulation of a PET for different conditions on the grid. The network structure consists of a medium voltage network of 11 kV, 100 MVA, the input filter, PET, output filter and the low voltage power network. The basic structure of the PET consists of AC-AD power converter, DC-AC, high frequency 3-phase transformer, AC-AC converter and a micro-generation coupled to the grid via a 11/0.415 kV transformer. The complete simulated system is shown in Fig. 4.14.

The PET is 1 MVA. This size is verified by existing systems reported in the literature sine it is still a developing technology. A 2013 review in [93] reviewed several systems and in 2020, [147] reviewed several more. While most are of only a few kW, larger systems are reported, and a 1 MVA system is described in [148].

The model is implemented in Matlab/Simulink using the parameters listed in Table 4.1. This configuration will be used to evaluate the response of the power electronics transformer to different situations that could cause power flow reversal on the grid.

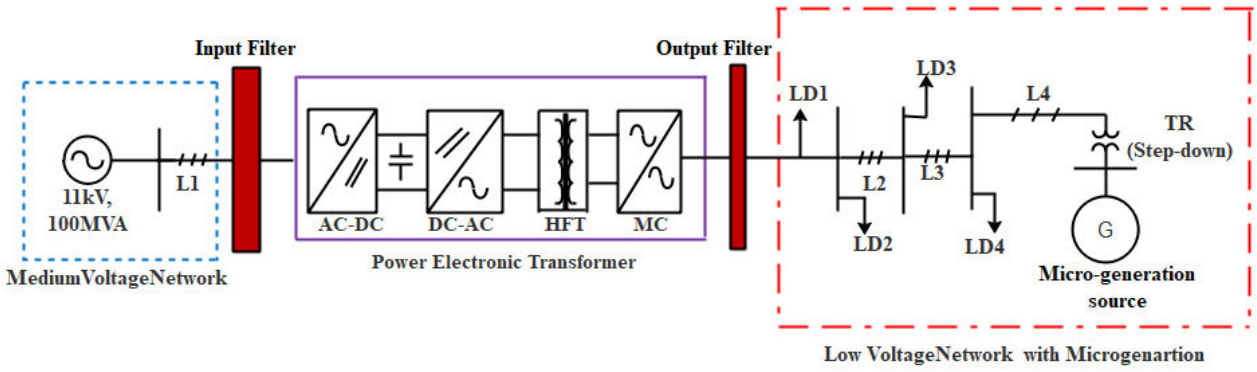

Figure 4.14: Single Line Diagram of Network under Investigations

4.5.2 Simulation Cases

The designed model was used to simulate different power disturbance situations that lead to violation of voltage profiles in a power system network and, consequentially, RPF. For effective investigation and analysis of the performance of PET in voltage rise and RPF issues, different situations on the grid were considered. The situations are:

1. Simulation under normal condition;

2. Simulation under abnormal conditions:
    - Voltage sags; and
    - Voltage swell;
3. Variations in grid loading:
    - Reduction in grid loading system; and
    - Increase in grid loading system; and
4. Variation in output generation of the integrated wind farm.

Table 4.1 and Table 4.2 show the general simulation parameters.

Table 4.1: Power Electronic Transformer and Grid Parameters

Parameters	**Values**	**Units**
Grid frequency	50	Hz
Input filter inductance	0.3	mH
Input filter resistance	0.5	Ω
PET Input resistance	0.2	mΩ
PET input inductance	0.3	mH
PET switching frequency	10	kHz
PET DC voltage	750	V
DC Link Capacitance (C_{dx1})	5000	μF
DC Link Capacitance (C_{dx2})	2200	μF
HFT capacity rating	1.0	MVA
HFT primary voltage	11	kV
HFT secondary voltage	415	V
HFT operating frequency	1	kHz
Output filter inductance	0.9	mH
Output filter capacitance	20	μF
Load (LD1)	0.4	MW
Load (LD2)	0.3	MW
Load (LD3)	0.2	MW
Load (LD4)	0.1	MW
Microgenerator	500	kW peak

Table 4.2: Line Parameters

Line	**Length** (km)	**Resistance** (Ω)	**Inductance μH**	**Capacitance μF**
L1	2	0.0531	0.9337	12.74
L2	1	0.0035	2.4651	4.52
L3	10	0.115	1.0552	11.33

4.6 Simulation Results and Discussion

In this section, simulation results are presented. The model is implemented in Matlab/Simulink assuming the parameters listed in Table 4.1. This configuration will be used to evaluate the response of the PET to different situations that could cause power flow reversal on the grid.

4.6.1 Simulation Under Normal Conditions

In this situation, power system connecting elements are working under normal thermal capacity ratings and they carry normal rated current and voltage, which ensures secure operating conditions of the system. This is for 1 MVA at the grid connections. In this scenario, parameters of the system under investigation remain unaltered. Fig. 4.15 shows the input voltage and current of the system under normal conditions - this sets the power factor to 1. There is no microgeneration. Fig. 4.16 shows the output voltage and current of the system under normal conditions. The primary and secondary line-line voltage of the high frequency transformer is shown in Fig. 4.17 at 1 kHz for the main frequency.

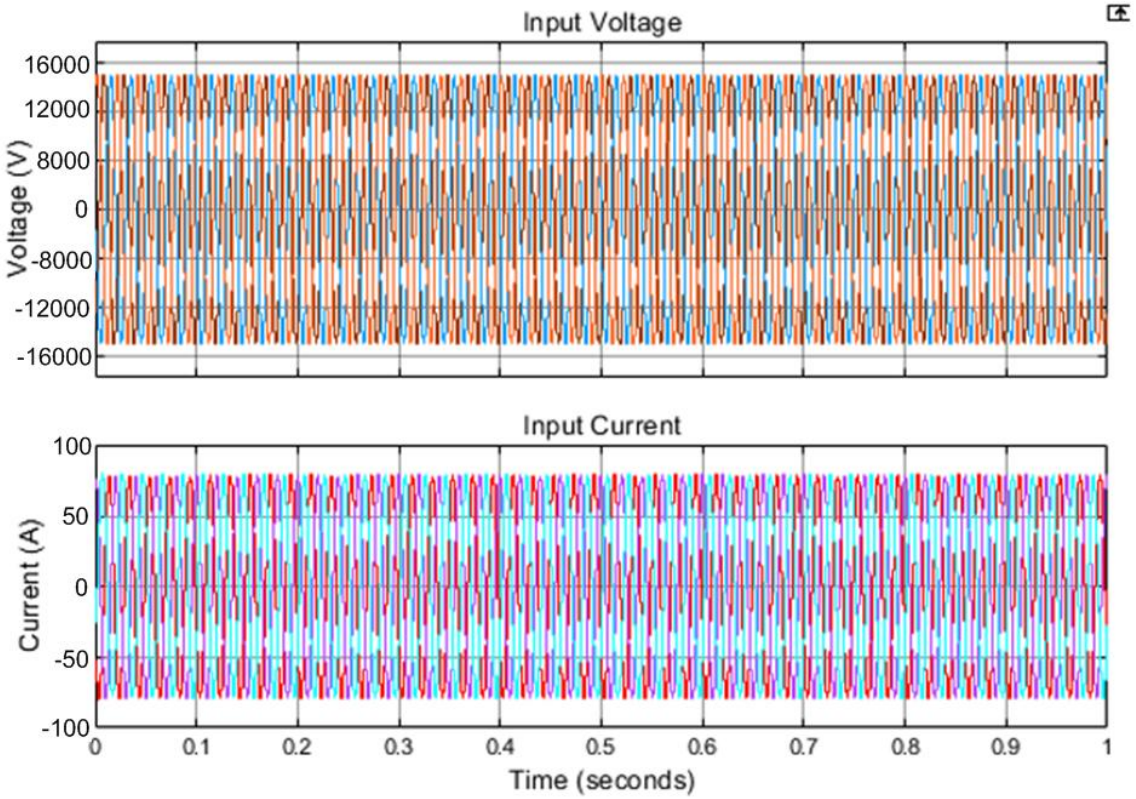

Figure 4.15: PET Input Voltage and Current under Normal Condition

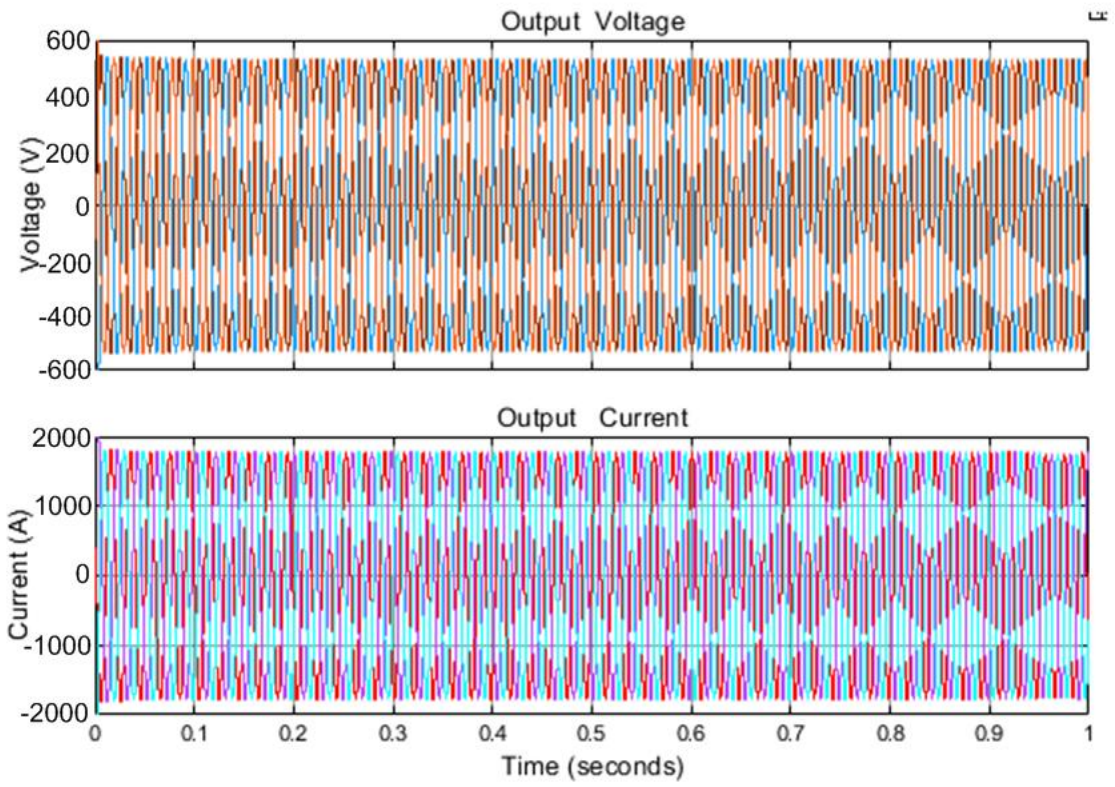

Figure 4.16: PET Output Voltage and Current under Normal Condition

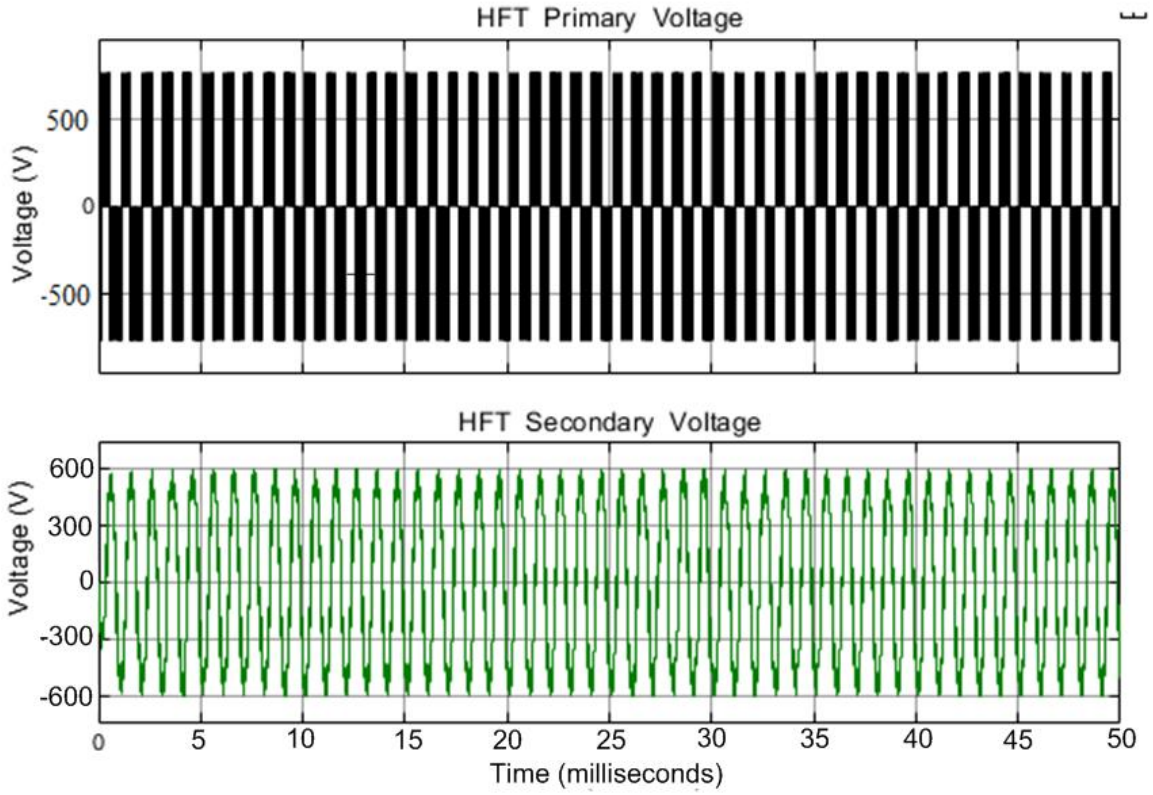

Figure 4.17: HFT Primary and Secondary Voltage

4.7 Simulation Results under Abnormal Conditions

4.7.1 Voltage Sag

Voltage sag is a short period of reduction in grid voltage caused by sudden increases in load such as short circuits or faults. They can also occur as a result of sudden increases in source impedance caused by loss of connectivity. During voltage sag the connected renewable energy sources lose connectivity with the main grid. The instantaneous waveform of the input voltage and current during voltage sag is shown in Fig. 4.18, while Fig. 4.19 shows the output waveform. This is due to a line-to line fault so that two line voltages are reduced and one is zero. Two currents keep flowing but one (blue) is constant. The delivered power is approximately halved.

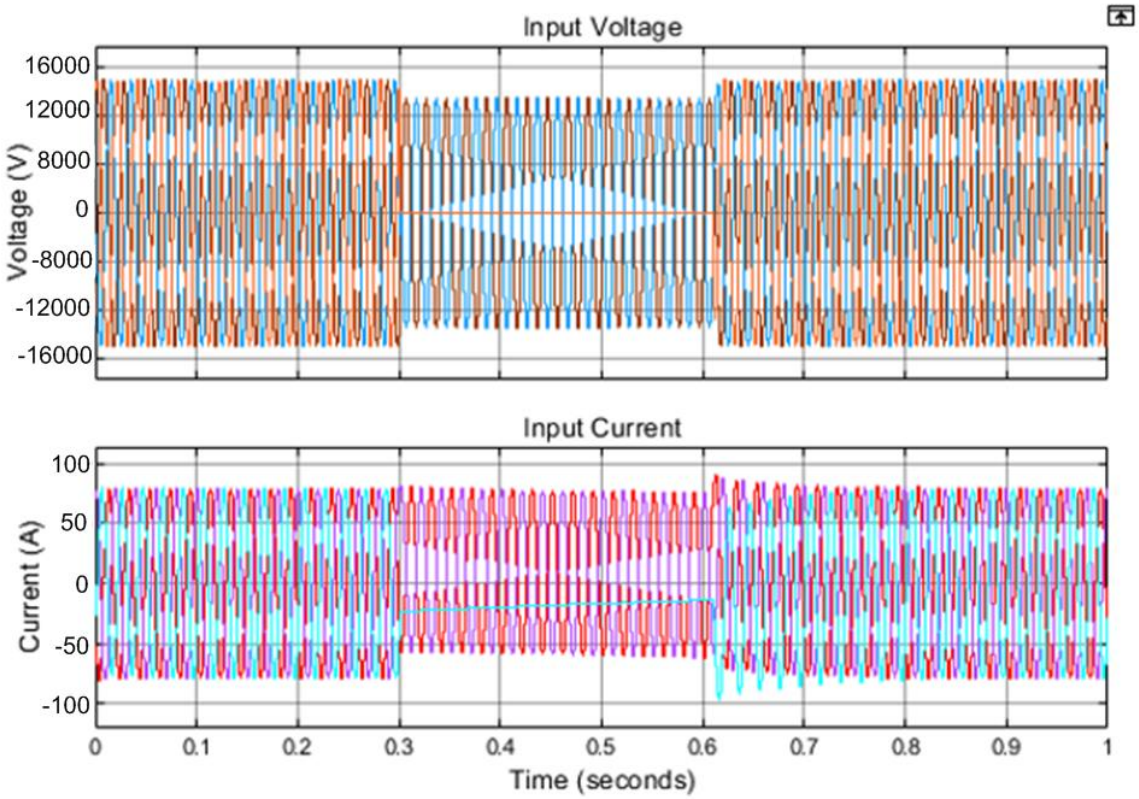

Figure 4.18: PET Input Voltage and Current during Voltage Sag

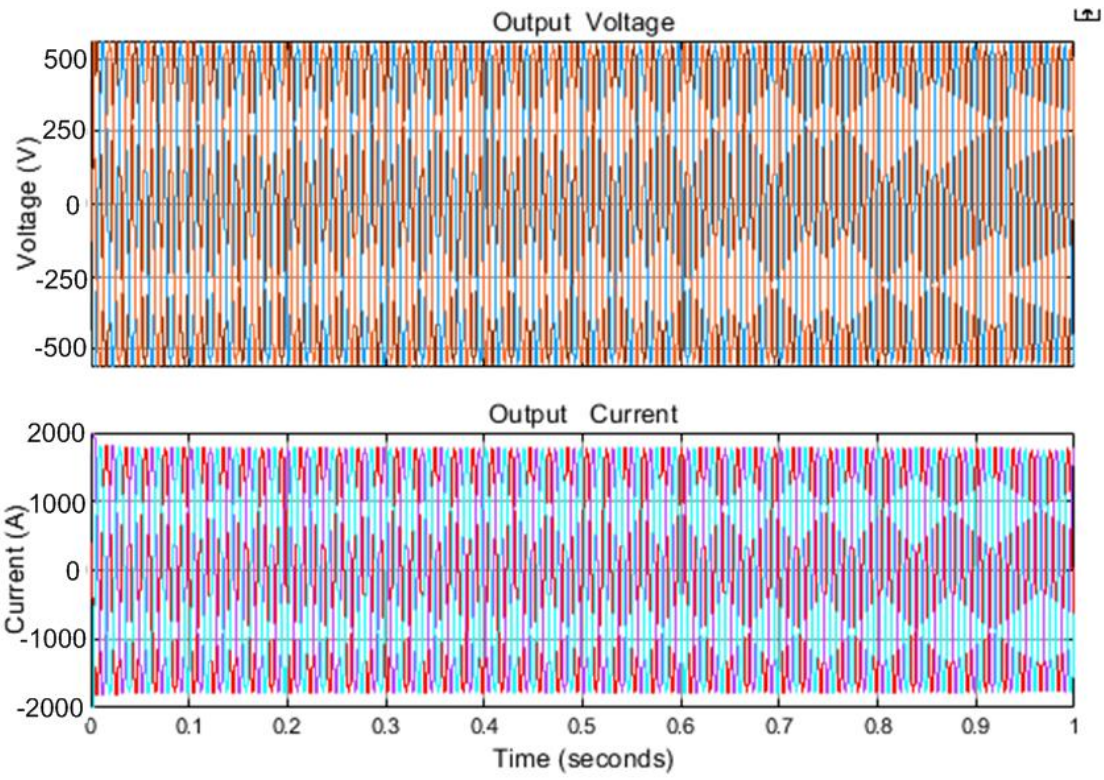

Figure 4.19: PET Output Voltage and Current during Voltage Sags

A voltage sag occurs at the primary side of the transformer between 0.3 and 0.6 s the affected phase experiences a reduction in voltage. As can be seen from Fig. 4.19, the distorted voltages and currents at the primary side of the transformer do not affect the voltages at the secondary side; That is, the voltage sags at the medium voltage side is not propagated to the low voltage side, and the load currents and voltage remain balanced as they were before the sag occurrence. This is due to the stored energy on the DC link. There is a step-down in the AC-DC-AC stage and the DC link voltage can vary and the energy in the capicitors utilized to maintain the power for a limited amount of time. For the capacitors listed in Table 4.1 then a time can be calculated which gives a half drop in DC link voltage from the maximum while supporting half of the load. For an AC voltage of 11 kV, then the maximum DC link voltage is double the peak of the phase voltage so that $V_{DC(MAX)} = 2\sqrt{2} \times 11000 \div \sqrt{3} = 18$ kV. The value of the series DC capacitors 0.005 and 0.0022 F is 0.0015 F. Therefore the approximate time for 500 kW DC link support to the system is $0.5 \times 0.0015 \times (18000^2 - 9000^2) \div 500000 = 0.37$ s. So in this scenario the system can be supported through the sag fault.

4.7.2 Voltage Swell

A voltage swell refers to the case when the RMS voltage increases for a time period before it comes back to its correct value [149], [150]. Line-to-ground faults can cause voltage swell on the system, which leads to voltage rise on the unaffected phase. Voltage swell can also be as a

result of sudden de-energising of a large load on the system. Voltage swell causes a breakdown of power system components due to overheating. In such case, PETs can play a critical role in preventing the impacts of a voltage swell on the grid. The input voltage and current waveforms during a voltage swell are shown in Fig. 4.20, while Fig. 4.21 shows the output waveforms. This is with two phases grounded so that two line voltages increase and are in phase. Again, the system can support the system during the fault.

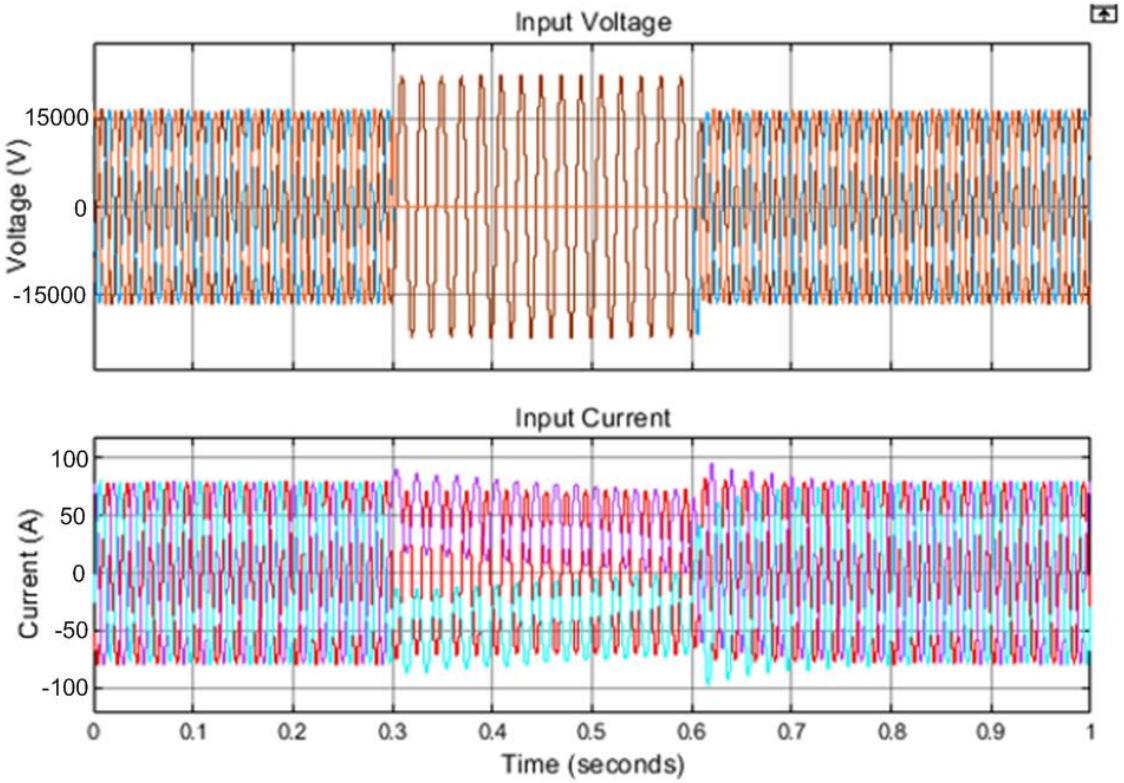

Figure 4.20: PET Input Voltage and Current during Voltage Swell

As can be seen in Fig. 4.20, the voltage swell occurs at the primary side of the transformer between 0.3 and 0.6 s. The two affected phases experience a reduction in voltage to zero. As observed in the figure, the affected phases at the primary side of the transformer do not affect the voltages at the secondary side; That is, the voltage swell at the medium voltage side is not propagated to the low voltage side, and the load currents and voltage remain unaffected as they were before the swell occurrence as seen in Fig. 4.21. The energy in the DC link is able to support this.

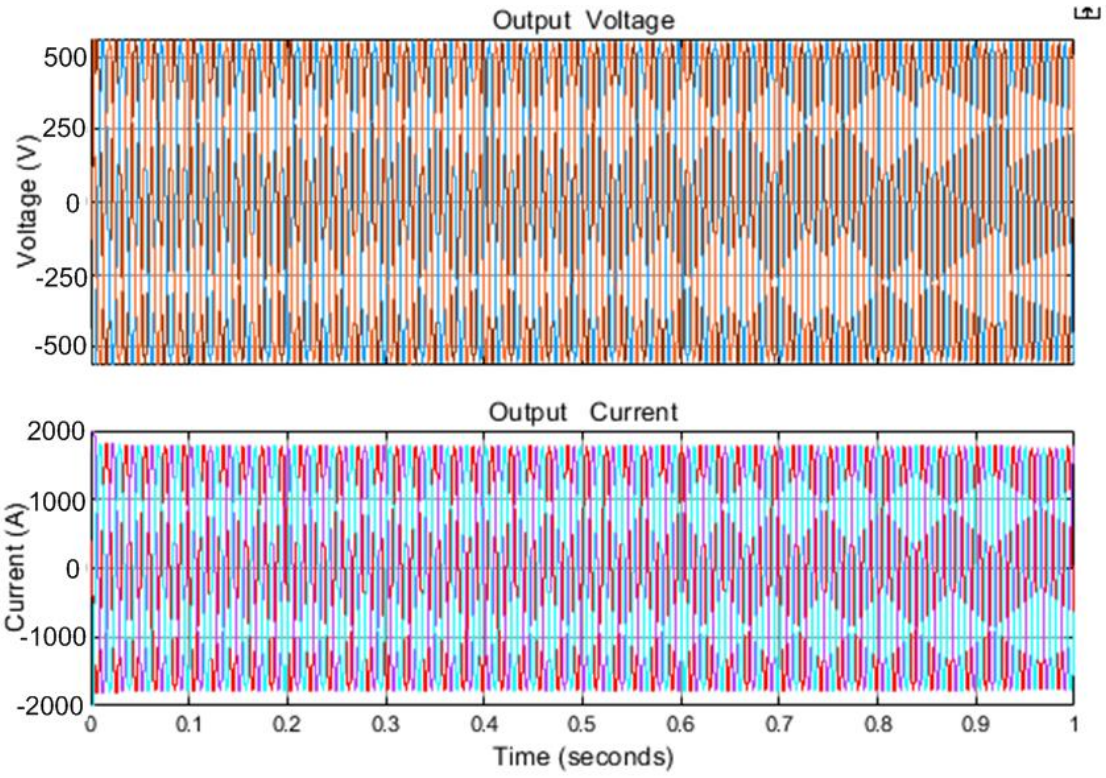

Figure 4.21: PET Output Voltage and Current during Voltage Swell

4.8 Variations in the Grid Loading System

Overvoltage is one of the consequences of RPF. It is not only caused by fault but also by unplanned load variations on the grid. The characteristics of voltage variations depend on the load type and size and the capacity of the power system [151], [152],[153] [154]. Therefore, this section present the response of the PET to load variations on the grid.

4.8.1 Reduction in the Grid Loading System

In this scenario, the total load on the low voltage side of the grid was reduced by 60 %. The output waveforms of the PET during this period are shown in and Fig. 4.22. From the simulation results, it was found that the input voltage and current of the PET were not affected by the load change, the input voltage was controlled to be constant. Fig. 4.22 shows the output voltage and current during reduction in the load. It was observed that the output voltage and current reduces in amplitude.

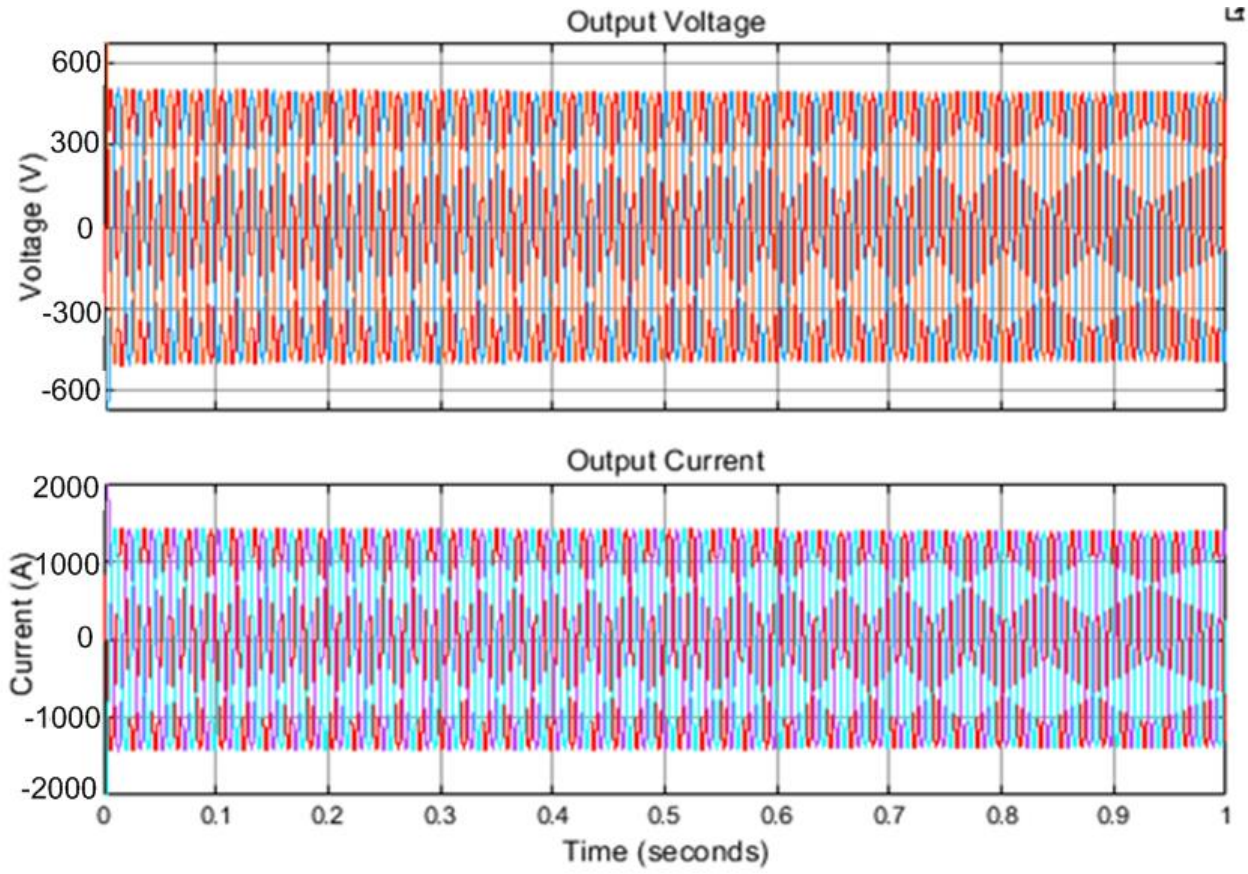

Figure 4.22: PET Output Voltage and Current during Reduction in Load

4.8.2 Increase in the Grid Loading System

Fig. 4.23 shows the PET output results obtained when the total load in the low voltage grid was increased by 20 %. This is a loading that should be able to be dealt with for a short period of time. There is an increase in PET voltage and current.

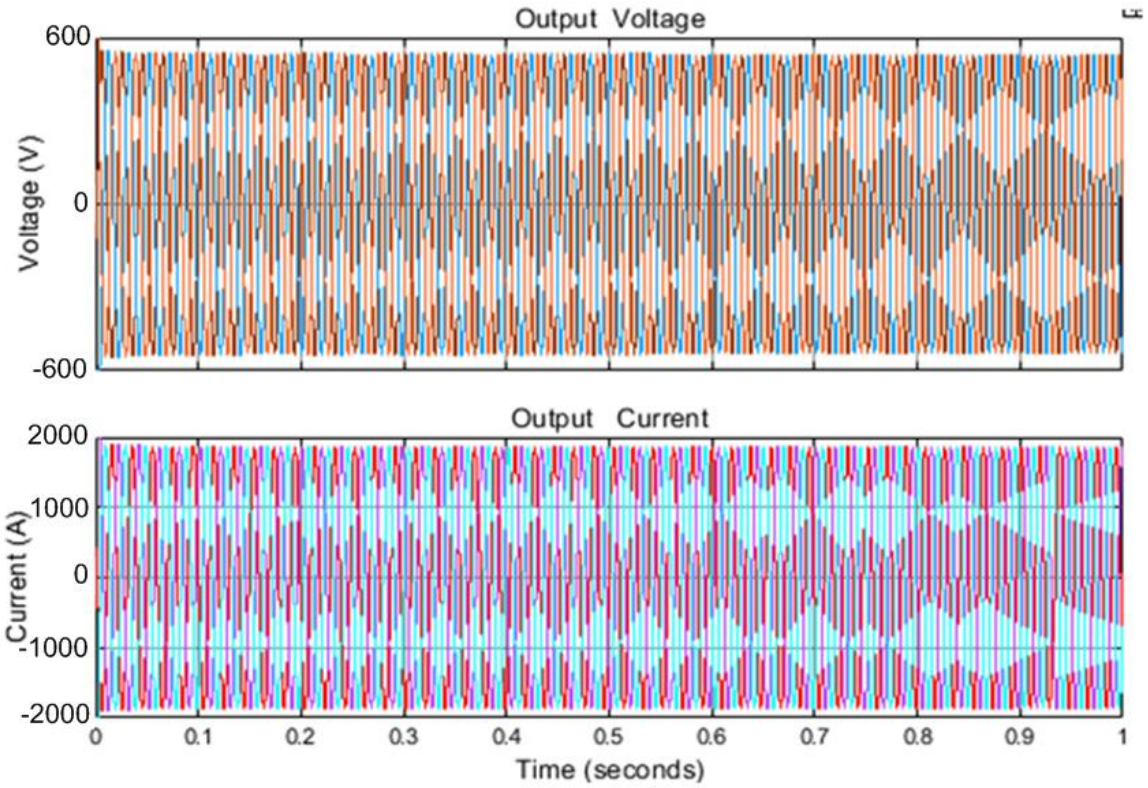

Figure 4.23: PET Output Voltage and Current during Increase in Load

From the simulation results, the primary side of the transformer voltage was controlled to be constant by power and reactive power variation. However, the load variation causes an increment in the output voltage and currents of the transformer.

4.9 Variation in Output of the Micro-generation

Variation in output power generated from the integrated micro generation into the low distribution network has capability to reverse the power flow direction if the penetration is high in particular section of a power system network, therefor, causing bulk power to flow from low to higher power regions of the electricity network [155] This section presents the response of PET to variation in the integrated micro generation into the low distribution network.

Fig. 4.24 shows the PET output voltage and current during high loading with low micro-generation which is similar to the overload in Fig. 4.23. The 500 kW microgenerator is used to reduce the PET loading as shown in Fig. 4.25. It can be seen that the microgenerator significantly reduces the PET loading.

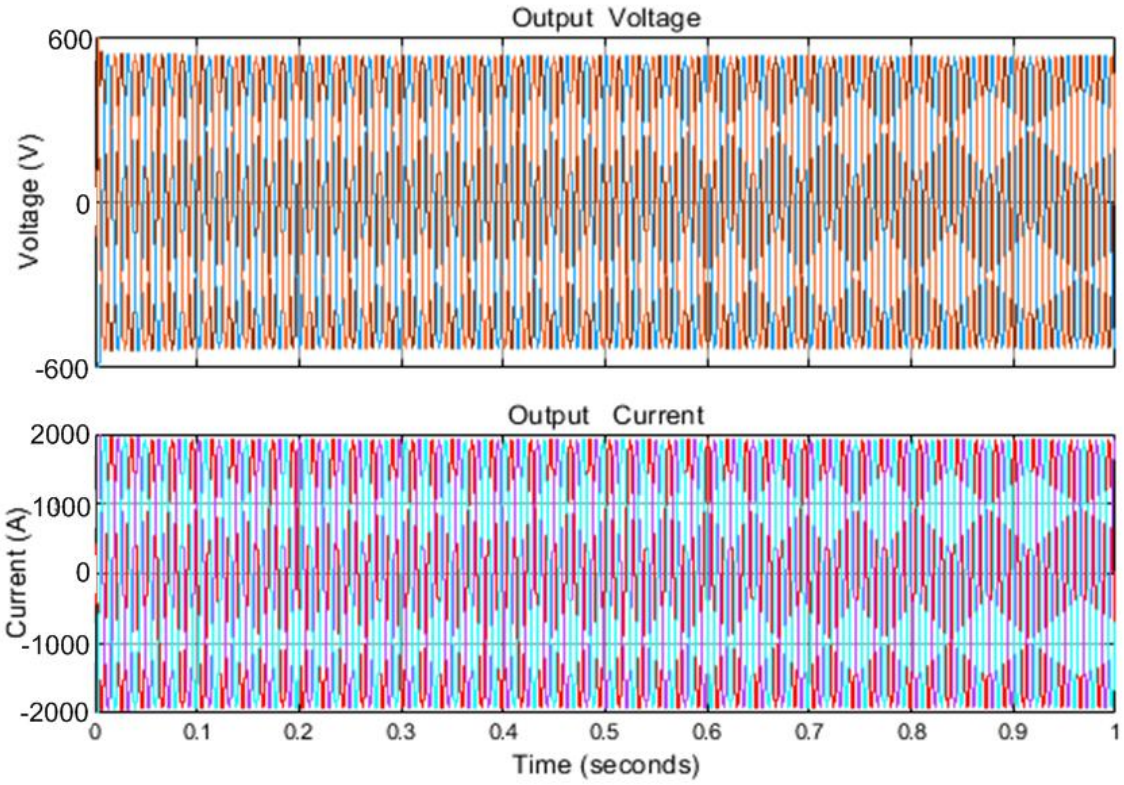

Figure 4.24: PET Output Voltage and Current during Reduction in Output Generation

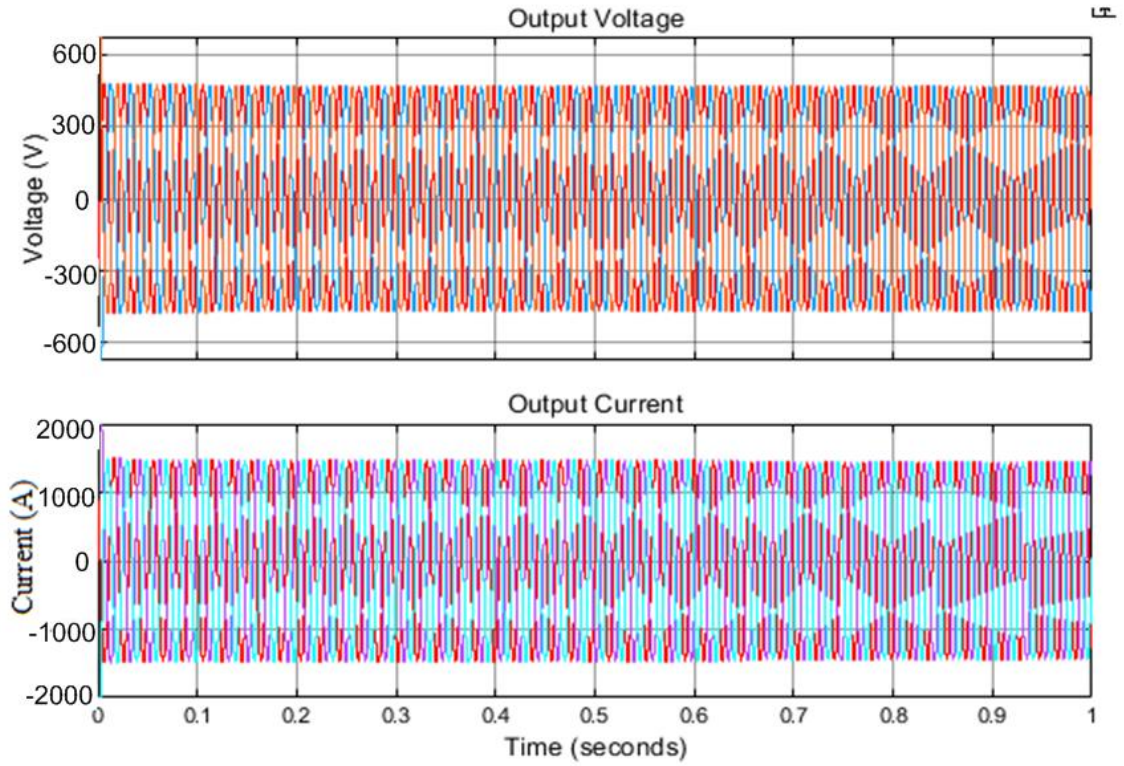

Figure 4.25: PET Output Voltage and Current during Increase in Output Generation

4.10 Modeling and Simulation of the Proposed MPPET for Reverse Power Flow Utilisation

This section presents the simulation of the proposed RPF utilisation using a MPPET. Details of the procedure has been presented in Chapter 3 under methodology. Fig. 4.26 shows the complete one-line schematic diagram of the system model.

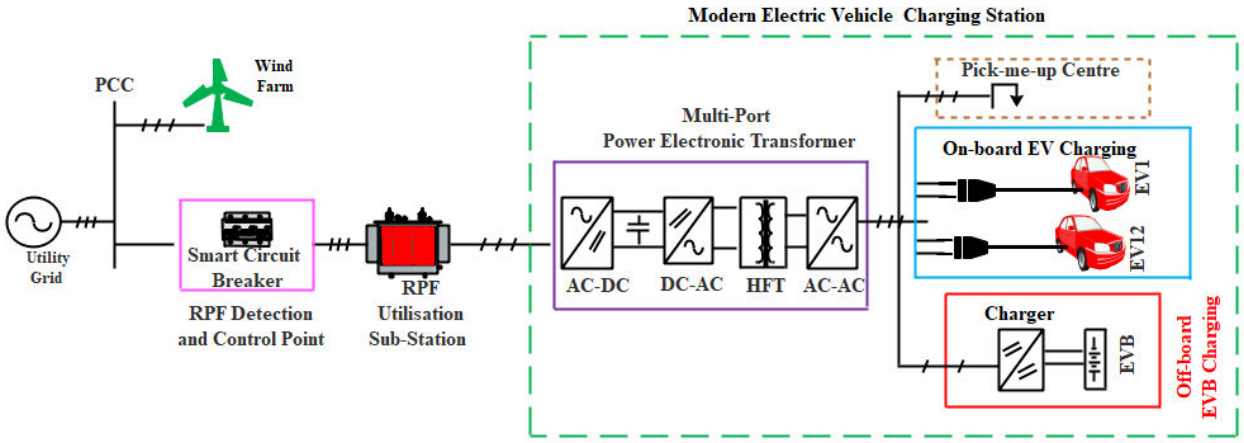

Figure 4.26: Schematic Diagram of the Proposed Utilisation System with Electric Vehicle Charging Station

4.10.1 Electric Vehicle Charging Station Design

The charging station comprises three sections: the off-board charging station, the on-board charging station and the pick-me up center. The MPPET connects the charging station to the grid via an RPF utilization substation which includes a three-phase step-down transformer. This changes the grid voltage to the required voltage by means of the MPPET for the EV battery charging. This work considers an off-board DC fast charging station with power levels of up to 250 kW, voltage ratings ranging from 500 VDC to 600 VDC, and current rating up to 400 A. A DC fast charging station consists of a DC/DC converter which changes the station DC output voltage to an appropriate level suitable for charging the EV battery. The work also considers a 50 kW on-board AC fast charging station with a voltage rating range from 400 V DC to 480 V DC and current rating up to 200 A. The AC fast charging station consists of an AC-DC converter which converts the PET output to DC suitable for charging. A number of factors must be considered when designing an EV charging station. These factors include:

- Availability of charging space, which determines the number of EV or batteries that can be charged at a time;

- Number of charging slots;
- Nominal voltage level and power level at the PCC of the network; and
- Amount of charging power to be supplied to each battery.

The EV charging station capacity can be analyzed using

$$C_{\text{Rated}} = \frac{K_{\text{Load}} N_{\text{Port}} P_{CP}}{\cos\theta} \tag{4.25}$$

where C_{Rated} is the charging station capacity, K_{Load} is the overload factor, N_{Port} is the number of available ports for charging, P_{CP} is battery maximum charging power and $\cos\theta$ is the system power factor.

4.10.2 DC Bus Voltage and Capacitor

The station DC bus voltage is determined by the grid voltage. The integration of the EV into the grid using an MPPET does not restrict the choice of bus voltage from the voltage level of the power system. The battery minimum voltage and the minimum modulation index of the battery impose limitation on the bus voltage. The DC bus voltage is given by:

$$V_{dc} \leq \frac{V_{Min(bat)}}{MI_{Min}} \tag{4.26}$$

where $V_{Min(bat)}$ is the battery minimum voltage and M_{Min} is the charger minimum modulation index. A number of chargers will be connected to the DC bus at every point in time, thus the ripple current can be high. Therefore, a DC capacitor is required to control the DC bus. The DC bus capacitance is calculated using [156], [157]:

$$C_{cd} = \frac{C_{Ratsd} 2nt\Delta P \cos\theta}{V_{dc}^2 \Delta v} \tag{4.27}$$

where, C_{Rated} is the charging station capacity defined in (4.25), t is the period of the AC voltage wave, ΔP is the change in DC power, V_{dx} is the DC voltage defined in (4.26) and Δv is the change in the percentage of DC voltage.

4.10.3 Electric Vehicle Battery Selection and Modeling

There are several types of EV battery but this work uses a Li-ion battery for the EV model. Fig. 4.27 shows the basic equivalent circuit model for a lithium battery pack [158].

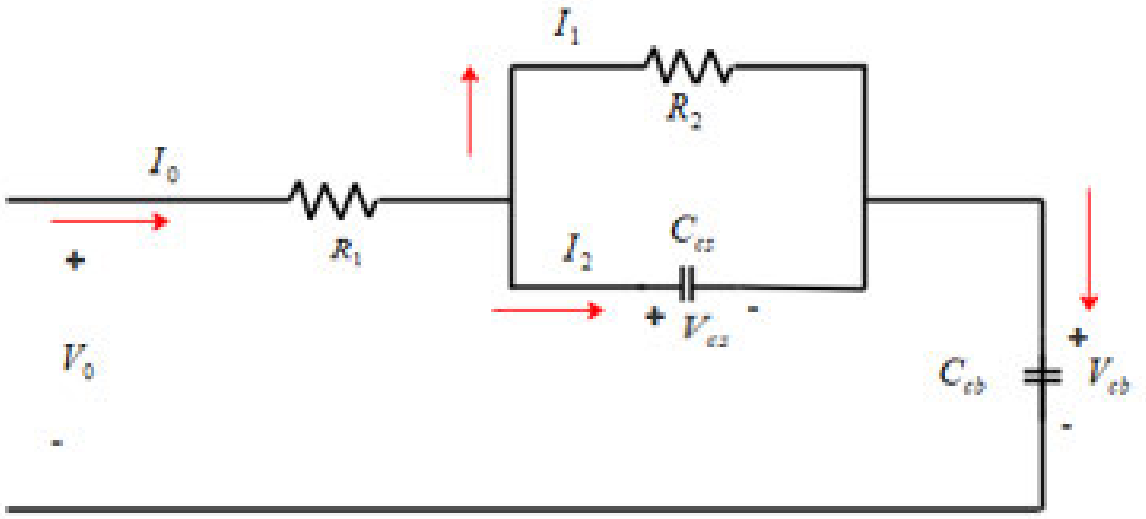

Figure 4.27: Lithium-ion Battery Pack Equivalent Circuit Model

In Fig. 4.27, C_{cb} is the bulk capacitance which represent the charging ability of the battery pack, C_{cs} is the surface capacitance which represent the level of discharge in the battery, and R_1 and R_2 are the internal and polarization resistance of the battery respectively. The voltages across the bulk capacitor and the surface capacitor are represented by V_{cb} and V_{cs}. The terminal voltage and terminal current of the battery pack are denoted by V_0 and I_0. The voltage equations can be derived as [158]:

$$V_0 = V_{cb} + V_{cs} + I_0 R_1 \tag{4.28}$$

$$\dot{V}_{cs} = \frac{I_0}{R_2 C_{cs}} V_{cs} + \frac{I_0}{C_{cs}} \tag{4.29}$$

$$\dot{V}_{cs} = \frac{I_0}{C_{cs}} \tag{4.30}$$

The interaction between the battery open circuit voltage (V_0) and state of charge of the battery is linear. Thus V_{cb} is given as:

$$V_{cb} = K S_{oc} + d \tag{4.31}$$

where the coefficients K and d depends on the battery State of Charge (SOC or S_{oc}) and the ambient temperature. The differential of the S_{oc} can be obtained from

$$\dot{S}_{oc} = \frac{I}{K C_{cb}} \tag{4.32}$$

Some of the important features to be considered when making a choice of EV battery have been discussed in Chapter 2. However, for the purpose of this work, Table 4.3 shows the EV

fast charging stations and EV battery pack parameters.

Table 4.3: Electric Vehicle Charging Station and Battery Parameters

Electric Vehicle Charging Station Parameters		
Characteristics	**Off-board**	**On-board**
Voltage level (V)	600	480
K_{load}	1.1	1.1
Charging current (A)	60	80
Power factor	0.95	0.95
Grid frequency (Hz)	50	50
Electric Vehicle Battery Pack and Charger Parameters		
Battery Characteristics	**DC Charger**	**AC Charger**
Battery nominal voltage (V)	500	400
Rated capacity (Ah)	120	100
Fully charged voltage (V)	600	480
Cut-off voltage (V)	270	270
Nominal discharge current (A)	200	80
Battery internal resistance (R)	12	0.012
Fully charged current (A)	400	250
Battery state of charge (SOC) (%)	80	70
Battery time of response (S)	20	15
Charger inductance (H)	6	5
Charger series resistance (Ω)	2	2
Charger capacitance (μF)	800	750

4.11 Proposed EV Charger and Control

As seen in Fig. 4.26, the proposed charging station comprises of on-board and off-board charging systems. Because the charging station is designed purposely for public use, this work proposes a fast charging system (level 3) for both on-board and off-board charging stations. On-board chargers are usually small in size and have low power ratings, while off-board chargers are built at dedicated locations to provide a fast charging service. The off-board charger uses a DC-DC converter. A DC-DC charger allows effective control during the charging process by interfacing the DC bus voltage with the EV battery. The proposed DC fast charger unit uses a DC-DC buck converter to connect the DC fast charging station (off-board) directly to the grid. The on-board charger uses a AC-DC converter. In this work, an AC-DC charger unit makes use of the three-phase universal AC-DC converter. This transforms the AC power into DC power and forms a DC bus for connecting the EV to the grid. The control system provides smooth transfer of voltage or current from the grid to vehicle (G2V) or from vehicle to grid (V2G); however, here, only G2V is considered which is the charging process.

4.11.1 Proposed DC-DC Charger and Control System

The off-board charger system utilise a DC-DC buck converter to supply a suitable power level to the battery. Fig. 4.28 shows the basic circuit of the buck converter.

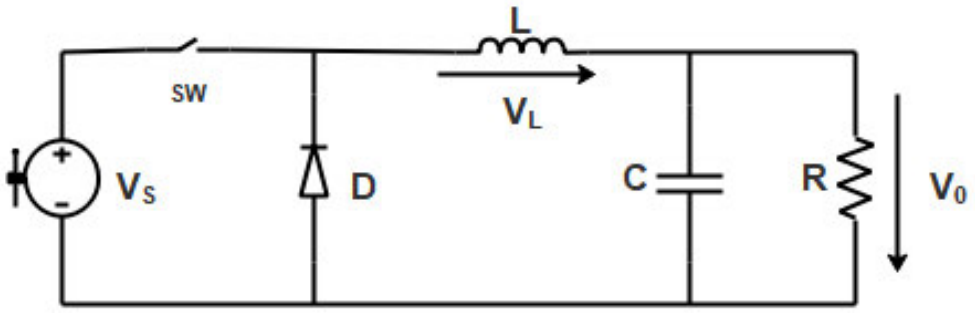

Figure 4.28: Basic Diagram of Buck Converter Circuit

The converter consists of DC input voltage source, control switch, diode, filter inductor, capacitor, and load resistance. The process of generating the desired low output voltage depends on the duty cycle of the converter, which is the ratio of output voltage to input voltage. The duty cycle is determined using:

$$D = \frac{V_0}{V_S} \tag{4.33}$$

The output current in term of duty cycle is given as:

$$I_0 = \frac{I_S}{D} \tag{4.34}$$

$$L_{Min} = \frac{V_0\,(V_S - V_0)}{\Delta I_L f_S V_S} \tag{4.35}$$

$$C = \frac{\Delta I_L}{8 f_S \Delta V_0} \tag{4.36}$$

where, ΔI_L is the inductor current ripple, f_S is the switching frequency, and ΔV_0 is the output voltage ripple. V_S and V_0 are the input and output voltages respectively. Fig. 4.29 shows the dynamic control system used between the buck converter and EV battery.

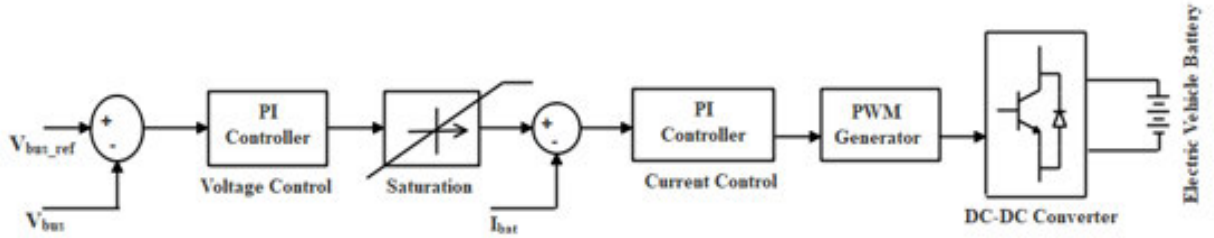

Figure 4.29: Proposed DC-DC Charger Control Circuit

In order to ensure constant voltage supply to the EV battery, the measured battery voltage (V_{EIB}) is compared with the reference voltage (V_{rj}). The reference voltage is used as a linear loop of the buck converter for the dynamic limitation of the EV current and also to determine the SOC of the battery. The control system works by using the difference between the actual and reference voltage in order to feed the appropriate signal value to the pulse width modulator (PWM). The PWM signal then controls the switching process of the buck converter in order to supply the desired voltage to the battery.

4.11.2 Proposed AC-DC Charger and Control System

The on-board charger utilises universe AC-DC converter to supply a suitable power level to the battery. Fig. 4.30 shows the basic AC-DC charger topology.

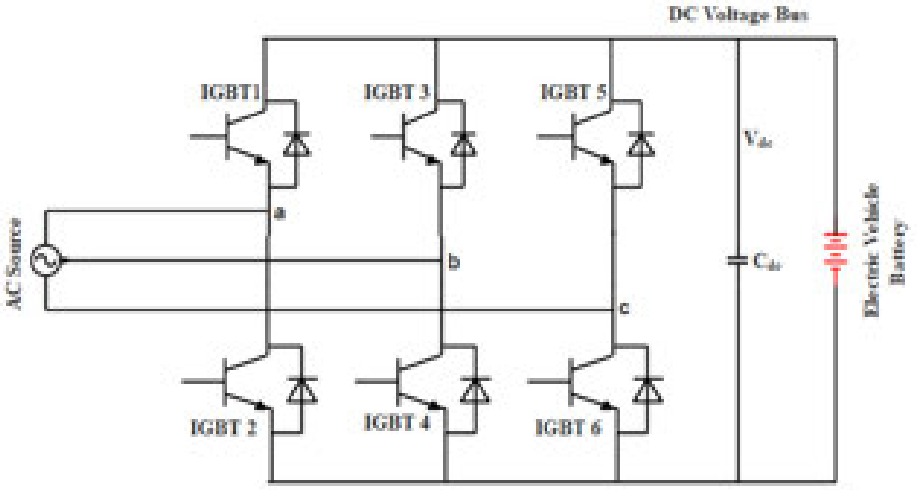

Figure 4.30: Proposed AC-DC Charger Topology

The universal AC-DC converter used in this research, worked as a rectifier since only G2V of the EV battery is considered. The AC-DC converter controller for G2V mode is shown in Fig. 4.31.

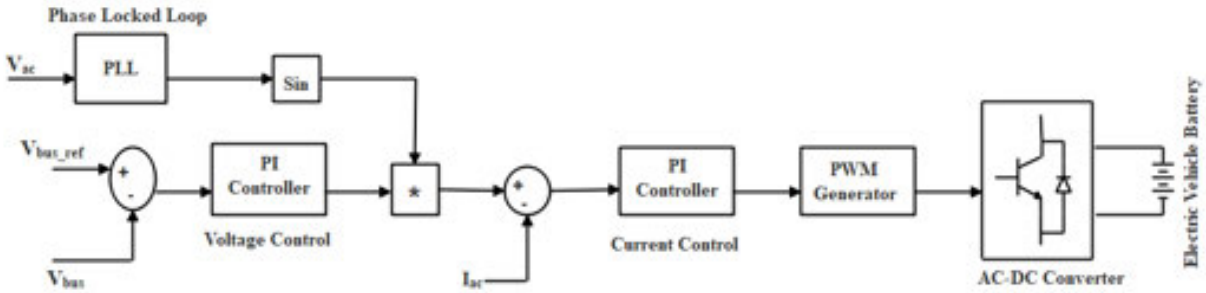

Figure 4.31: Proposed AC-DC Charger Control in Grid-to-Vehicle Operation Mode

The proposed control uses two PI controllers; one for DC bus voltage control and the other for AC current control. Three-phase locked loop (PLL) is used for AC current reference.

4.12 Proposed EV Charging Station Control

As described in Chapter 2, three basic methods are normally used for the charging control of an EV battery. These are constant current control (CCC), constant voltage control (CVC), and advanced charging methods. This work uses the constant voltage control (CVC) battery charging technique. This method is proposed because of its simplicity, ease of implementation, cost effectiveness and suitability for all types of EV batteries. During the charging process, the proposed constant-voltage control (CVC) charging method supplies the same input voltage to the battery regardless of its SOC. The proposed EV charging control system is shown in Fig. 4.32.

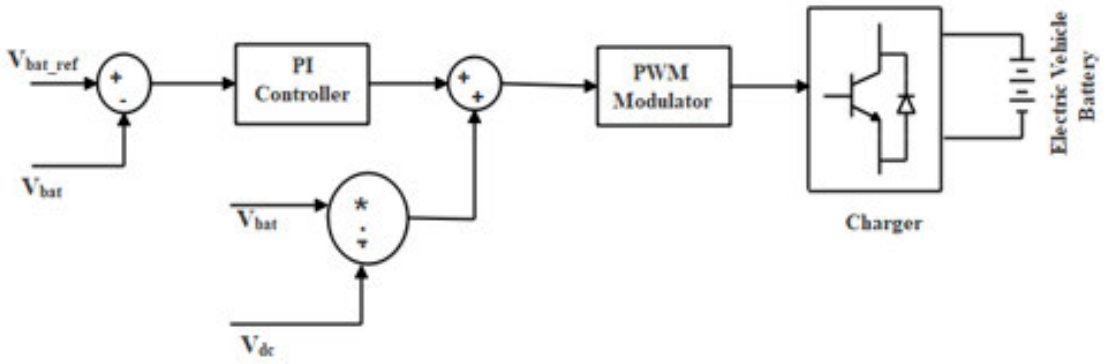

Figure 4.32: Proposed Constant Voltage Electric Vehicle Battery Control

The CVC method has a higher voltage variation between the battery and the charger which causes the initial current to be high and later decreases to zero at the completion of the processes. In order to produce the required output voltage the PI controller regulates the charger output and generates a PWM signal of suitable duty-cycle for the charger. The controller aims to control the switching process of the system resulting from any change in voltage and current references, thus stabilising the output of the system with little error. A PI controller comprises of a proportional constant (K_p) and integral constant (K_i). The proportional constant reduces the overall errors in the control system with time, while the integral constant completely reduces the error. The PI controller transfer function is

$$\frac{U(S)}{E(S)} = K_p + \frac{K_i}{S} = K_p\left(1 + \frac{K_i}{K_P S}\right) = K_p\left(1 + \frac{1}{T_i S}\right) \tag{4.37}$$

$$T_i = \frac{K_p}{K_i} \tag{4.38}$$

The block diagram for the PI controller transfer function is given in Fig. 4.33.

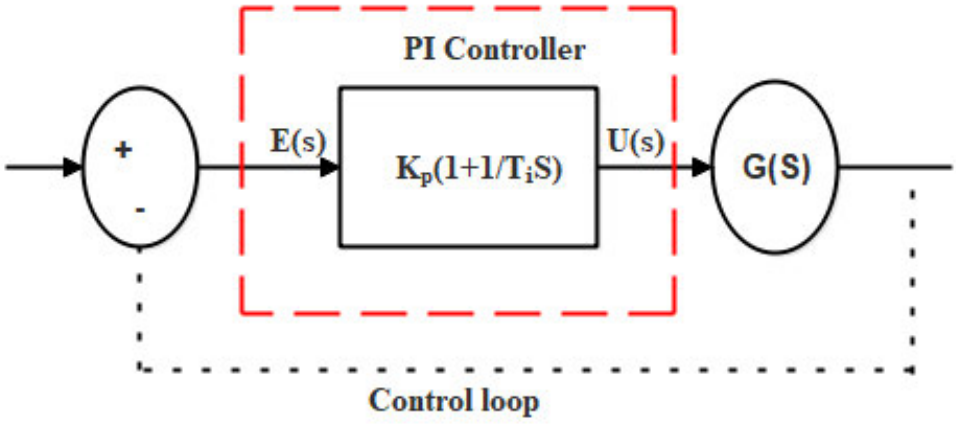

Figure 4.33: PI Controller Transfer Function Control Loop

4.13 Simulation Results Analysis and Discussion

4.13.1 Impacts of the Proposed PET on RPF at Different Penetration Levels of Wind Energy Source

From the investigation and analysis in Section 3.5, it was found that RPF occurs at the penetration level of 1.0 % as shown in Fig. 3.15. However, this section presents the impact of the proposed MPPET on reverse power flow utilisation. It was observed that the smart circuit breaker at the input of the utilisation section responds to mitigate the impact of RPF on the grid. Fig. 4.34 shows the normalise power flow at transformer TR3.

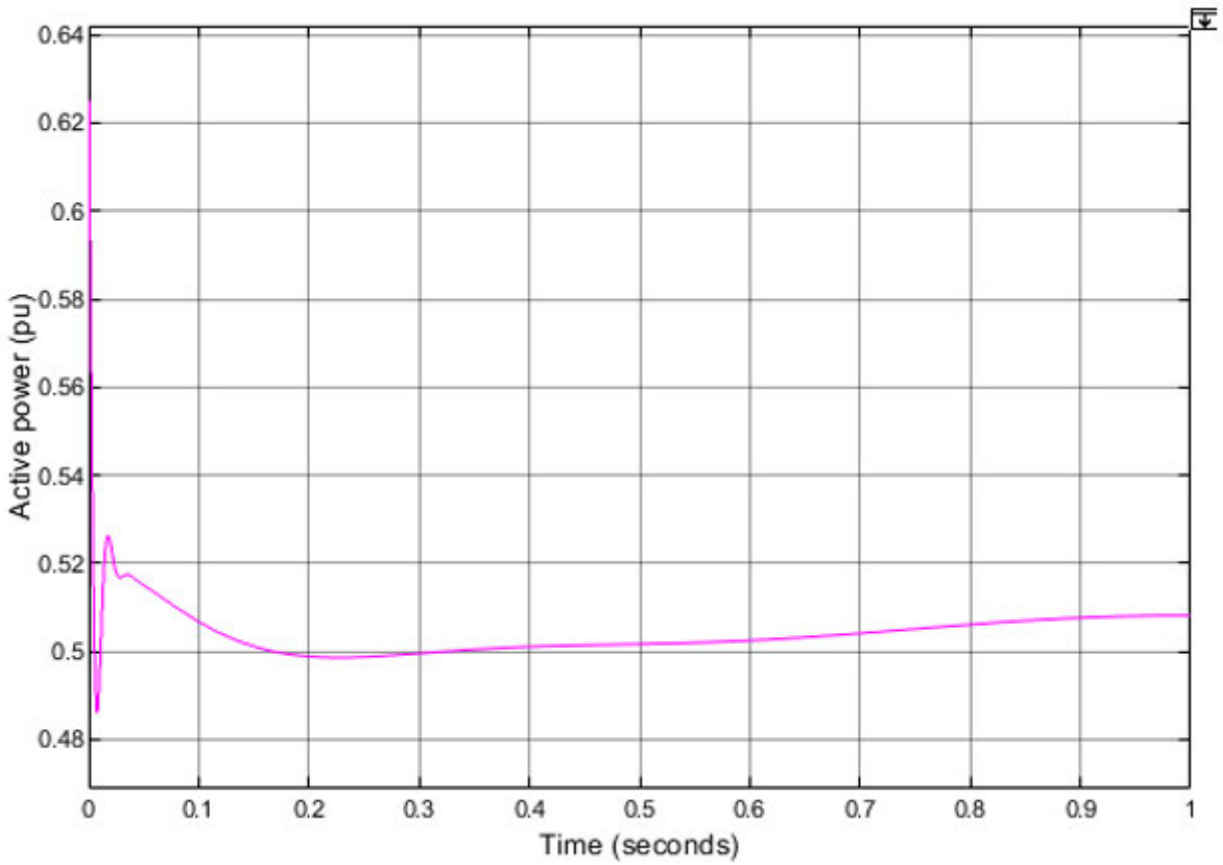

Figure 4.34: Active power flow at 1.1 % penetration after utilization

As proposed in the method, the utilisation aims to supply the excess power generated (RPF) to an EV charging station through an MPPET, Fig. 4.35 shows the DC fast charging EV characteristics during the RPF utilisation process, while Fig. 4.36 shows the AC fast charging characteristics.

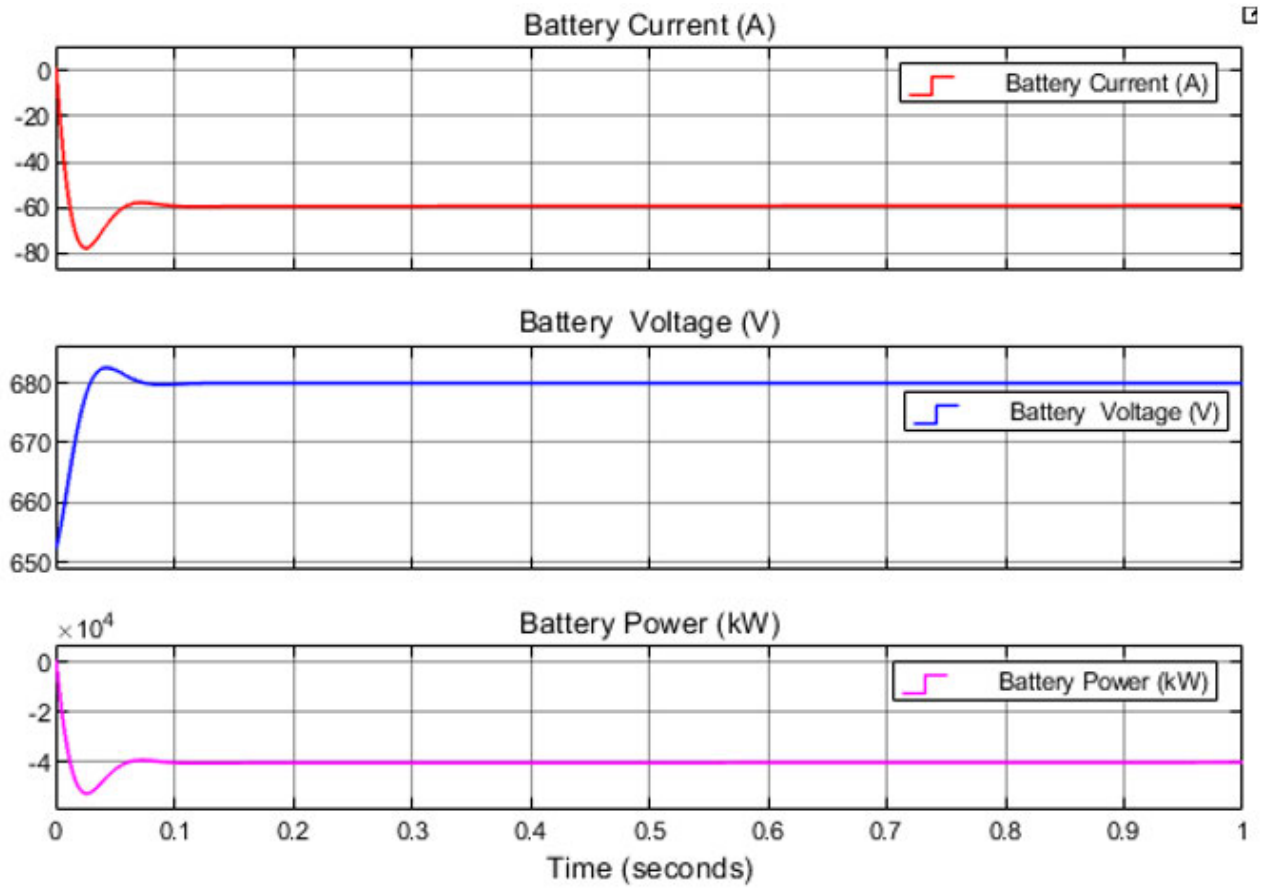

Figure 4.35: DC Fast Charging Characteristics

Fig. 4.35 shows the EV battery wave forms (current, voltage and power) during DC fast charging in constant current charging mode. From the results it can be seen that the current maintains a constant changing mode while the voltage increases from the nominal value of 600 V until it reaches a constant voltage where the charging takes place. The battery voltage remains constant at 680 V at a point throughout the charging process while the battery current was 60 A. Similarly, Fig. 4.36 shows the AC fast charging characteristics. It was observed that the simulation results followed the same trend as DC fast charging. The battery charging current was set to 70 A which was constant throughout the charging process. The battery SOC for both DC and AC charging process are shown in Fig. 4.37 and Fig. 4.38.

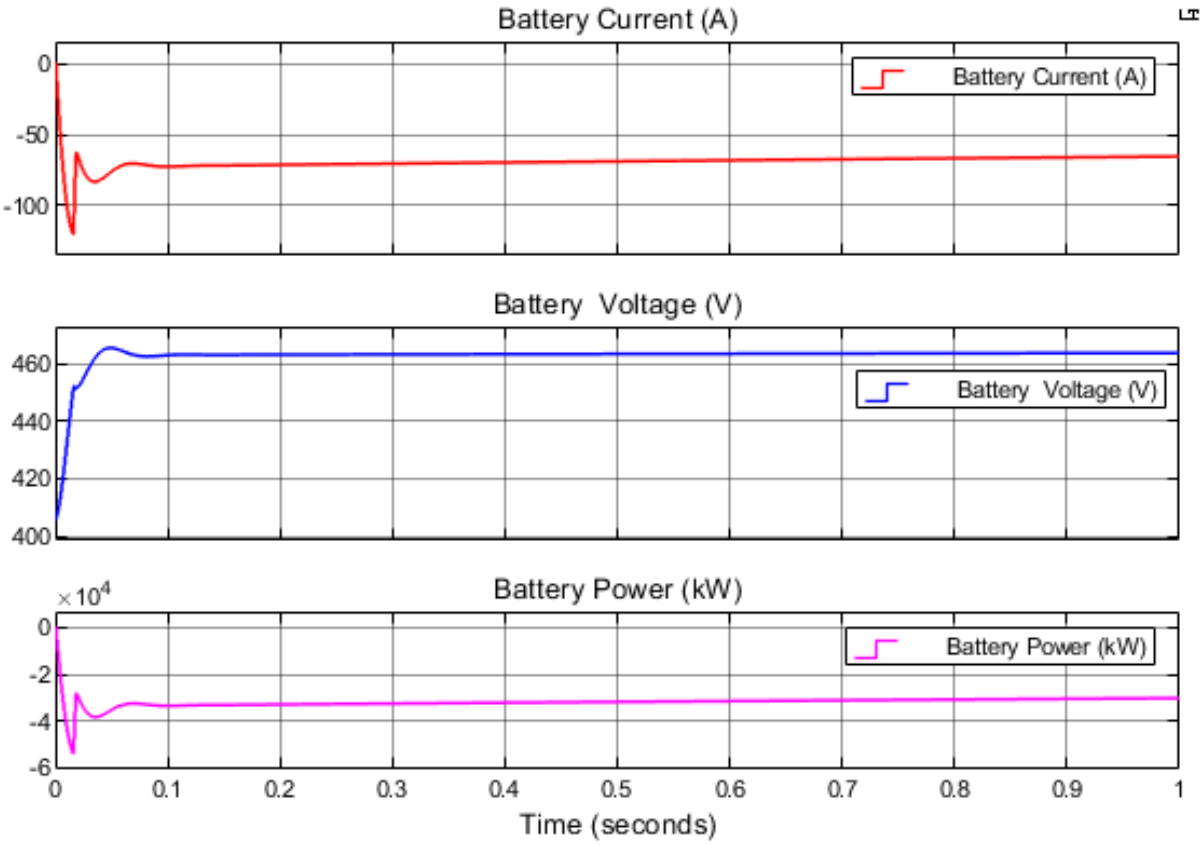

Figure 4.36: AC Fast Charging Characteristics

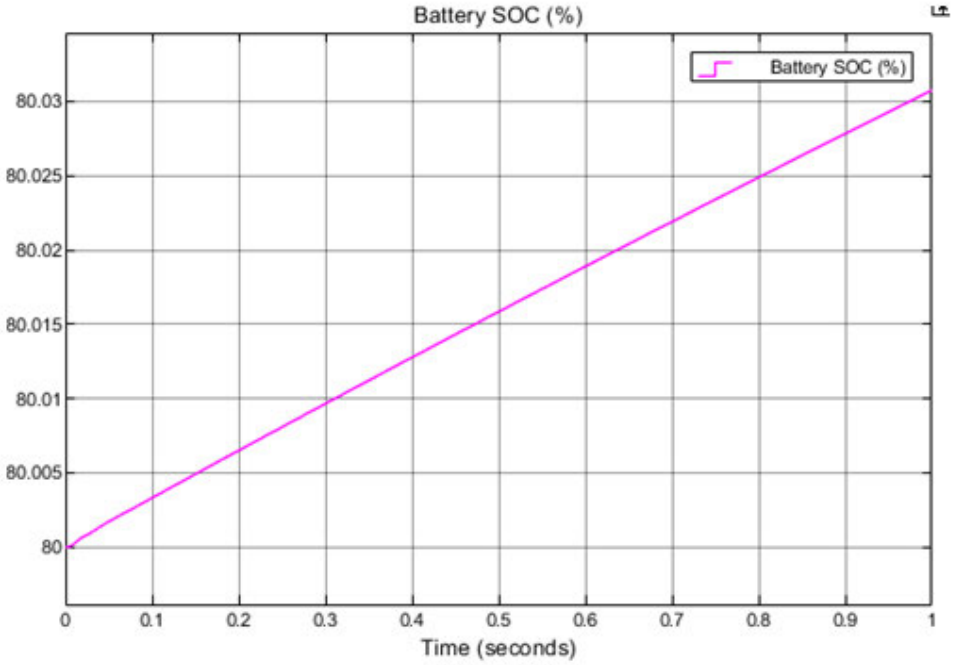

Figure 4.37: Battery SOC during Fast Charging DC Charging

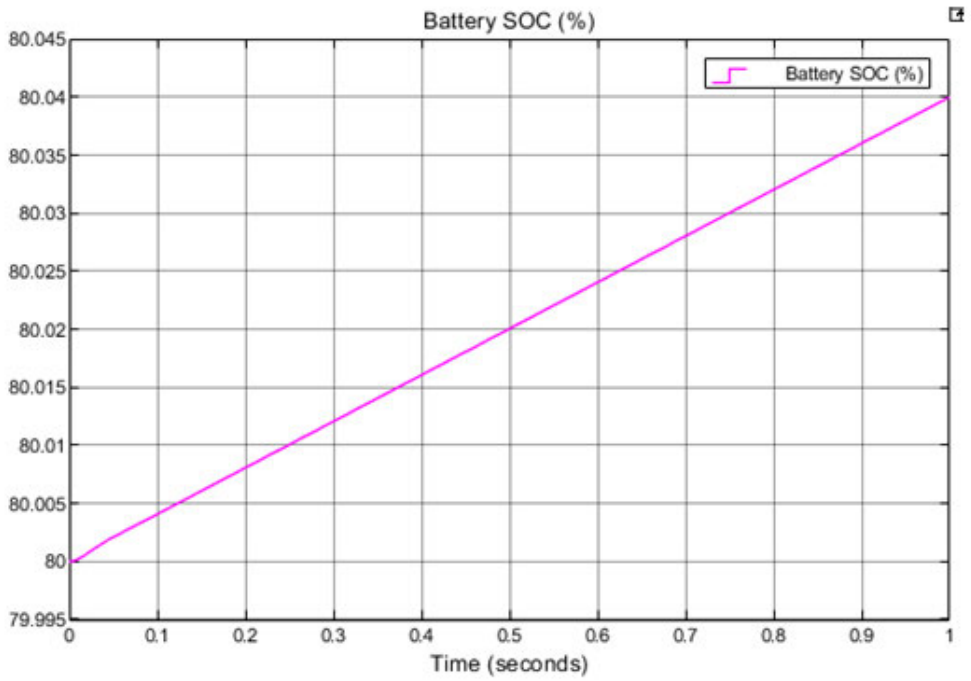

Figure 4.38: Battery SOC during Fast Charging AC Charging

4.14 Summary

This chapter presented the utilisation and analysis of the proposed methodology. The first section of the chapter presented the design and simulation of a PET for effective voltage rise mitigation. The responses of power PET to different situations on the grid was analysed. The results from the various scenarios showed that the PET is effective in mitigating voltage rise on the grid and did not allow disturbances on one side of the transformer to propagate to the other side during short faults. The second section demonstrated the use of an MPPET in RPF utilisation. From analysis of the results, it can be seen that the PET proved effective in both voltage rise mitigation and RPF utilisation.

Chapter 5

Implementation and Testing of the Proposed MPPET

5.1 Background

In this chapter, the design, implementation and testing of the proposed three-phase, 3 kVA MPPET transformer prototype is outlined. The operation of the MPPET transformer during tests was limited to a much lower level for safety reasons.

The prototype is a unidirectional model consisting of an input diode rectifier, a DC-AC inverter, a high frequency transformer and an AC-AC direct matrix converter. It should be noted that for bi-directional power flow, which will give more flexibility, the diode bridge rectifier can be replaced with an inverter as illustrated in Chapter 4. Unidirectional operation simplifies the experimental work so that the HFT can be focused upon.

Each conversion stage was controlled independently. The designed prototype was used to evaluate the behavior of the PET model under different operating conditions. Before the prototype was assembled, testing of each conversion stage/block was done to evaluate the continuity of power flow and synchronization of the response time. The block diagram of the proposed prototype is presented in Fig. 5.1. Detailed explanations of the functionality of each conversion stage/block were given in Chapter 4.

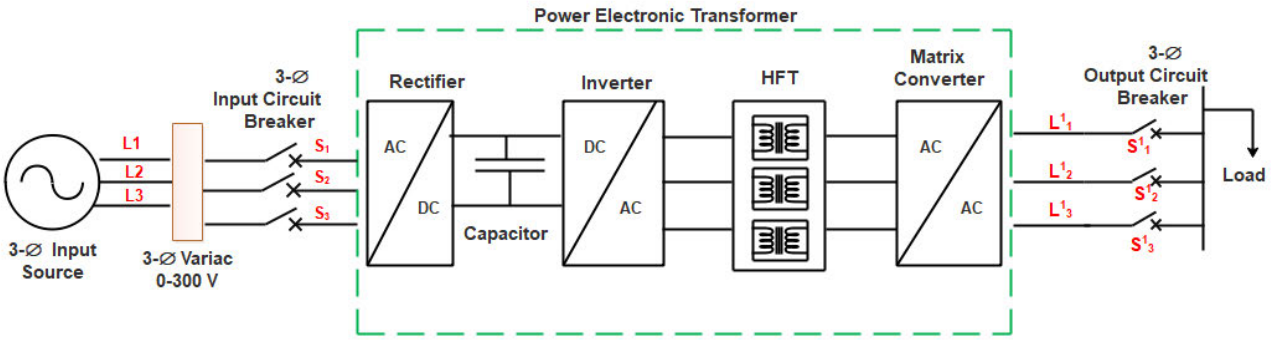

Figure 5.1: Complete block diagram of the implementation prototype

5.2 Design Procedure

An eight-staged design procedure was formulated and used to prototype the MPPET transformer in this work as shown in Fig. 5.2.

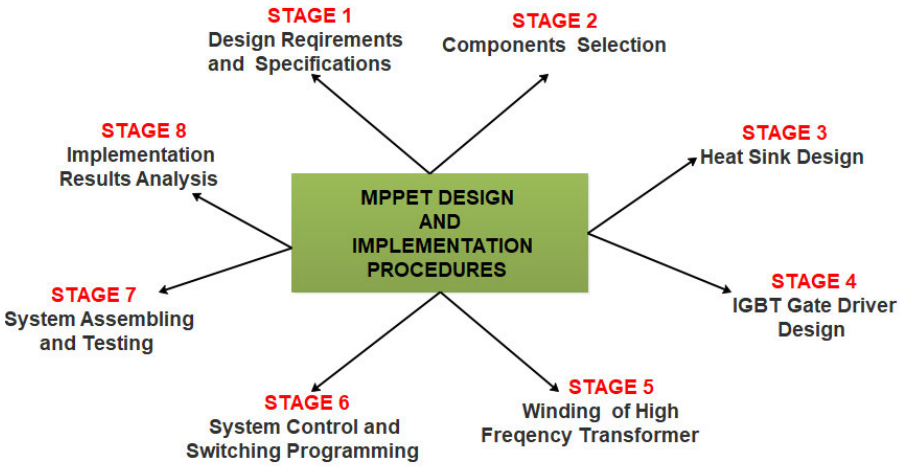

Figure 5.2: MPPET Design and Implementation Procedures

The design stages are elaborated on in the following subsections.

5.2.1 System Requirements and Specifications

The general requirement of the designed transformer was that it should be able to respond to conditions such as voltage sag, load variation and faults. Here, the general transformer specifications are: operating line voltage of 156 V, grid frequency of 50 Hz, switching frequency 5 kHz and rated power of 3 kVA.

5.2.2 Components Selection

The selection of components was based on the system design requirements and specifications. The major components in the design include: diodes, capacitors, control switches, wires and transformer. The rectification of the input AC voltage to DC of the design consisted of diodes whose selection depends on the operating voltage and current range of the design. D-FR 607 Fast Recovery Diode with voltage and current capacity rating of 1000 V and 6.0 A respectively were used. This selected diode has a low forward voltage drop, high current capability, high reliability and high surge current capacity. Table 5.1 shows some of the electrical characteristics of the selected diode.

Table 5.1: Electrical Characteristics of the Selected Diode @$T_A = 25^O$C

Rating	**Symbol**	**Value**	**Unit**
Maximum peak reverse voltage	V_{RRM}	1000	V
Maximum RMS reverse voltage	$V_{R(RMS)}$	700	V
Maximum DC blocking voltage	V_{DC}	1000	V
Average rectifier output current @$T_A = 55^O$**C**	I_O	6	A
Forward voltage @$I_F = 6.0$A	V_{FM}	1.2	V
Peak reverse current at rated DC blocking voltage @$T_A = (25 - 100)^0$**C**	I_{FM}	10 - 200	μA
Recovery time	t_{rv}	500	nS
Operating temperature	T_j	-65 to 125	^{O}C

A sizable capacitor was used for the DC to allow for some energy storage to allow fault ride through as discussed in Section 4.7. Switch selection is the most crucial aspect since it determines the appropriate range of operating frequency and the system losses. The selection of switches depends on the input voltage and output current. Supply voltage should be less than maximum collector to emitter voltage (VCE) of the selected switch. The output current of the device can be calculated using:

$$I_{out} = \frac{P_{out}}{V_{out} \cos\theta} \tag{5.1}$$

where, I_{out} is the output current, P_{out} is output power and V_{out} is the output voltage, while $\cos\theta$ is the power factor.

There are many switching devices, but insulated-gate bipolar transistor (IGBT) are used here. The selected IGBT is STGW20NC60VD N-CHANNEL 30 A - 600 V TO-247 Very Fast Power MESH^{TM} IGBT. The IGBT has off losses, tail current, high current capability, high frequency operating range and very soft ultra-fast recovery anti-parallel diode. Table 5.2 shows some of the features of the selected switching device as specified in manufacturer data sheet.

Table 5.2: IGBT Absolute Maximum Rating

Parameters	**Maximum Value**	**Units**
Collector-emitter voltage (V_{CES})	600	V
Gate emitter voltage (V_{GE})	± 20	V
Gate threshold voltage ($V_{GE}(th)$)	5.75	V
Continuous collector current @ 25°C	60	A
Continuous collector current @ 0°C	30	A
Turn-on delay time	31	nS
Turn-on delay time	100	nS
Operating junction temperature	-55 to 150	^{O}C

- **IGBT Switching Power Losses**

  According to [159], switching losses directly depend on anti-parallel diode, circuit inductance, snubber, junction temperature, operating voltage, and current. The IGBT switching power losses is given as:

$$P_{SW} = f_{SW} \times E_{SW} \tag{5.2}$$

  where, P_{SW} is the switching power losses, f_{SW} is the switching frequency and E_{SW} is the total energy losses. The average IGBT total energy losses during both turn-on and turn-off can be obtained from

$$E_{SW} = E_{SW(on)} + E_{SW(off)} \tag{5.3}$$

  $E_{SW(on)}$ is the energy losses during IGBT turn on where

$$E_{SW(on)} = \frac{1}{2} V_{CE} I_C \left(t_{on}\right) \tag{5.4}$$

and $E_{SW(off)}$ is the energy losses during IGBT turn off so that

$$E_{SW(off)} = \frac{1}{2} V_{CE} \left(I_C \times t_{off} \right) \tag{5.5}$$

The total power dissipated during turn-on and turn-off are given in (5.6) and (5.7) respectively:

$$P_{SW(on)} = \frac{1}{2} V_{CE} I_C f_{SW} t_{on} \tag{5.6}$$

$$P_{SW(off)} = \frac{1}{2} \times V_{CE} \times f_{SW} \times I_C \times t_{off} \times I_{c-tail} \tag{5.7}$$

where I_{c-tail} is the collector current tail.

5.2.3 Heat Sink Design and Analysis

Appropriate heat sink design is one of the prerequisites for effective performance of semiconductor devices. A heat sink maintains the maximum allowable temperature of a semiconductor device for maximum performance, and minimizing the thermal resistance between the junction and ambient temperature of the component in order to prevent the junction temperature from exceeding the highest allowable values specified by the manufacturer. In designing a heat sink, adequate knowledge of the power dissipated is critical. IGBT switching frequency ability depends on the power dissipation during the switching operation. The IGBT junction temperature during normal operation is given by:

$$T_j = T_C + P_{tot} \times \theta_{JC} \tag{5.8}$$

while the heat sink to ambient thermal resistance used to design an efficient heat sink to keep the desired junction temperature is

$$R_{SA} = \frac{\Delta T}{P_{tot}} - \theta_{JC} - \theta_{CS} \tag{5.9}$$

where, R_{SA} is the heat sink to ambient thermal resistance, θ_{JC} is the junction-to-case thermal resistance, θ_{CS} is the case to heat sink thermal resistance, P_{tot} is the total power dissipation and T_c is the case temperature. The heat sink selection is determined by the value of the heat sink-to-ambient thermal resistance. The maximum amount of power dissipated depends on the maximum junction to case thermal resistance. The total power dissipated is

$$P_{tot} = \frac{\Delta T}{\theta_{JC}} \tag{5.10}$$

The collector-emitter saturation voltage of IGBT determines the total power dissipated, and this depends on the junction temperature, collector current and gate emitter voltage. Therefore, the power dissipated can be expressed as:

$$P_{tot} = I_{CE(ave)} \times V_{CE(sat)} \tag{5.11}$$

where ΔT is the difference between junction temperature and case temperature given as $T_j - T_C$, $I_{CE(\text{ave})}$ is the collector current and $V_{CE(sat)}$ is the collector-emitter saturation voltage.

5.2.4 IGBT Gate Driver Design

The purpose of a gate-driver is to generate a current output to energize the IGBT switches. The first parameter to consider while designing a gate driver is the minimum output current. A critical prerequisite for an IGBT gate driver optocoupler is to provide the lowest or minimum gate current to switch the IGBT to the low impedance state. The gate current is desirable when the gate drive optocoupler is energizing the IGBT gate. In this situation, the output voltage is said to be low, thus,the load draws maximum current. A simple circuit for delivering the gate current to drive IGBT is shown in Fig. 5.3.

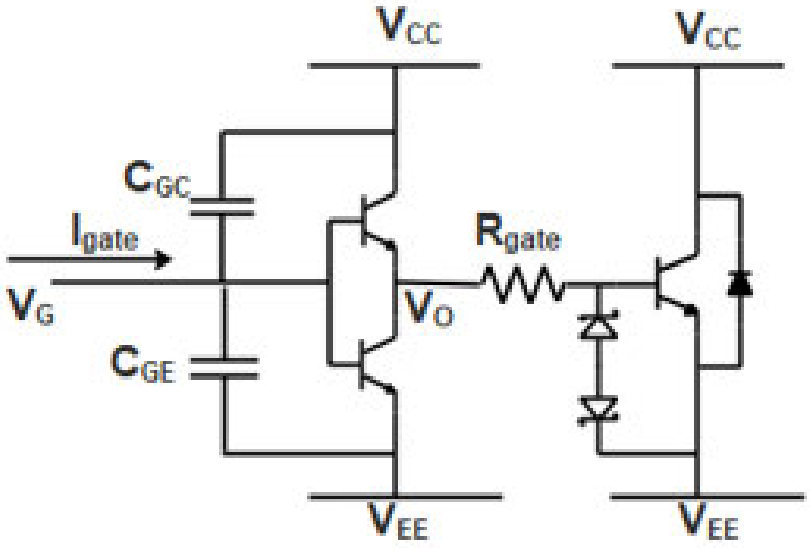

Figure 5.3: IGBT Gate Driver

The required gate current to energize the IGBT can be calculated from

$$I_{\text{gate}} = I_{GC} + I_{GE} \tag{5.12}$$

where I_{GC} and I_{GE} are the current through C_{GC} and C_{GE} respectively. Equation (5.12) can be re-written as:

$$I_{gate} = \frac{V_{GE}C_{GE} + V_{GC}C_{GC}}{t_{SW}} \tag{5.13}$$

where t_{Sw} is the switching time. The gate resistor guarantees that the highest peak output current rating of the gate driver optocoupler is not surpassed; therefore the gate resistor is given by:

$$R_{gate} = \frac{V_{CC} - V_{EE} - V_{OL}}{I_{OL(\text{peak})}} \tag{5.14}$$

where V_{OL} and $I_{OL(peak)}$ are the low level output voltage of the drive optocoupler and output peak current respectively. Designing a more efficient driver for IGBT requires correct layout and power supply bypassing in order to avoid undesirable voltage spikes, oscillation and false turn-on. Power dissipated in the IGBT driver is another critical element to look into when designing a driver for IGBT, since the component has some losses. Thus, the total power dissipated in the IGBT driver is

$$P_{\text{driver}(tot)} = P_O + P_E + P_I \tag{5.15}$$

where, P_0 is the output power, P_E is the emitter power and P_I is the internal power. The emitter power is the power dissipated at the input of the driver so that

$$P_E = I_F \times V_F \times D \tag{5.16}$$

where I_F, V_F and D are the forward input current, forward input voltage and duty cycle respectively.

5.2.5 High Frequency Transformer Design

A high frequency transformer (HFT) is another important component to be considered in the design of a PET. Fig. 5.4 shows the stages involve in HFT design and implementation.

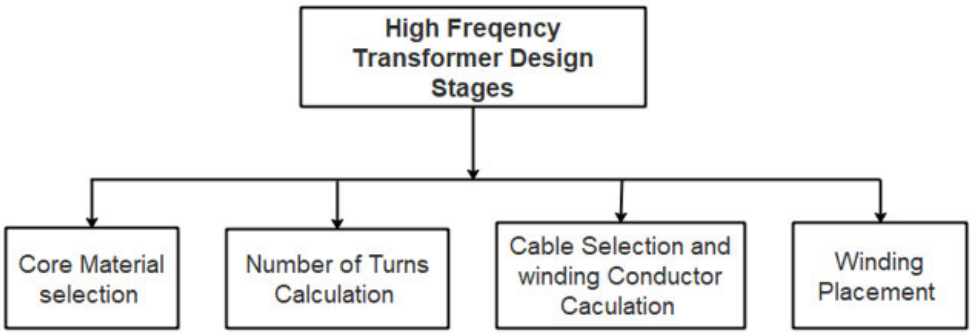

Figure 5.4: HFT Design and Implementation stages

1. **Core Material Selection**

   Core material selection and core design are the first steps in HFT design. According to [160], [93], the size of the transformer, power density, power losses and the frequency range of the transformer depends on the material of the core. The commonly used materials for HFT core design are amorphous, silicon steel, nanocrystalline and ferrite. According to [93], [161], silicon steel has the advantage of relatively high saturation flux density and permeability. However, high core losses due to the high frequency restrict its usage. Ferrite is readily available in various shapes and sizes, is cheap and it has low power losses at high frequency. However, it has relatively low saturation flux density and thus increases the weight of the transformer. Amorphous material has higher saturation flux density than ferrite, is cheaper and easy to obtain, but high power losses for high power applications restrict its usage. Nanocrystalline has moderate saturation flux density in the high frequency operation and low losses in medium frequency operation. However, its high cost, scarcity in diverse shapes and sizes restrict its usage, and it has high core losses for frequencies of operation higher than 35 kHz. The saturation flux density is relatively lower than other materials, it has high switching frequency of up to 100 kHz, and is readily available in various shapes and sizes. These features make its usage in high frequency transformer design appropriate.

   This work made use of ferrite for the design of the high frequency transformer core. The transformer is designed using the area-product method. According to Faraday's law the design of a transformer is constrained by:

$$V_p = K_f N_1 B_{\max} A_c f_S \tag{5.17}$$

$$V_s = K_f N_2 B_{\max} A_c f_S \tag{5.18}$$

where V_p and V_s are the primary and secondary voltages of the transformer, and N_1 and N_2 are the number of turns on primary and secondary side of the transformer. $B_{\max}$ is the maximum flux density and A_c is the cross section of the core. K_f, is the constant depending on whether the HFT is sine or square wave fed; for sine wave it is 4.44. f_S is the transformer frequency. The type of material used for the transformer core design determines the maximum value of the flux density, while the core determines the cross sectional area. The area product is:

$$A_w A_c = \frac{nV_{in}}{K_f B_{\max} f K_w J}[\sqrt{2}+1]I_{sec(rms)} \tag{5.19}$$

2. **Number of Turns Calculation**

Selection of both primary and secondary number of turns influences the magnetic flux density within the core of the transformer. Variation in flux density of the transformer depends on the operating frequency and the number of turns on the primary side of the transformer. The greater the operating frequency and the number of primary turns, the smaller the change in the flux density of the transformer. Thus, change in flux density of the transformer is given by

$$\Delta B = \frac{V_p\left(\frac{1}{2}T\right)}{N_p A_{\min}} \tag{5.20}$$

where V_p is the primary voltage, N_p is the number of turns on the primary side of the transformer, $A_{\min}$ is the minimum cross sectional area of the core and T is the period of operation. From (5.17). The number of turns in the primary side of the transformer is

$$N_P = \frac{V_p\left(\frac{1}{2}T\right)}{\Delta B\,(A_{\min})} \tag{5.21}$$

3. **Cable and Winding Calculation**

The flow of high frequency current along the surface of a conductor is referred to as skin effect. Magnetic flux pushes the current to the conductor surface at high frequency. It increases alternating current resistance in the conductor which gives rise to high transformer losses. According to [162], [163], Litz-wire alleviates the impact of skin effects on conductor resistance. Litz wire uses fine strands in a random form with insulation to prevent skin effect [164]. For a high-frequency operation, the thinner the wire strands the better the performance. In order to attain an acceptable resistance performance in a

high frequency transformer with frequency and voltage range of up to 100 kHz and 0.6 kV, Litz copper wire size 47 gauge which approximates to 28 AWG, 2.5 mm^2 is used. The current RMS value determines the diameter of a conductor. The RMS current in relation to power is given as the ratio of output power to the input voltage as shown in:

$$I_{RMS} = \frac{P_{out}}{V_{in}} \tag{5.22}$$

where, I_{RMS} is RMS current, P_{out} is output power and V_{in} is the input voltage. The cross sectional area and the diameter of the wire are determined using

$$A_{\text{wire}} = \frac{I_{RMS}}{S} \tag{5.23}$$

and

$$d_{wire} = \sqrt{I_{RMS}\frac{4}{S\pi}} \tag{5.24}$$

where, A_{wire} is the cross-section of the wire, d_{wire} is the diameter of the wire and S is the current carrying capacity of the cable.

4. **Winding and Transformer Configuration**

A high-frequency transformer has the same principles of operation as the normal standard transformers. The major difference is the range of frequency of operation. A high frequency transformer operates at a higher frequency than a normal standard transformer. High-frequency transformers can operate at a high frequency up to 1 MHz, while a normal standard frequency only operates at 50 Hz or 60 Hz. Transformer losses and efficiency directly depend on the winding configuration and placement in the core. The configuration used here connects three single-phase transformers to form a three-phase transformer bank. Depending on the specific purpose of application, the transformer input and output can be connected in three different ways: star, delta and interconnected star. In this work, the primary low voltage side was connected in delta while the secondary high voltage side was connected in star. The secondary side of the transformer is connected to the the output converter. This type of connection is referred to as a delta-wye configuration or a delta-star configuration which steps up the voltage. This is capable of supplying three-phase and single-phase load, creating common output when no neutral exists in the line. The three single phase transformer bank is easy maintenance because each unit in the bank may be replaced; however, a three-phase transformer wound on a common core is lighter, smaller and cheaper than the bank of three single-phase transformers [165],

[166]. Table 5.3 shows the HFT design parameters, while Fig. 5.5 shows the complete high transformer winding.

Table 5.3: HFT Design Parameters

HFT Characteristics	**Value**	**Unit**
Rated power	3	kVA
Input winding connection	Δ	
Output winding connection	Y	
Turn ratio	1:1	
Number of primary and secondary turns	39	turns

Figure 5.5: High Frequency Transformer Winding

The measurements for each of the three-single phase transformer bank is shown in Table 5.4.

This shows that the linkage in the transformer is good. Further tests showed good regulation under load. This was done at low voltage.

Table 5.4: HFT Measurement

	OPEN CIRCUIT ON SECONDARY		
Parameter	**TR1 (V)**	**TR2 (V)**	**TR3 (V)**
Primary Voltage	5.48	5.49	5.51
Secondary Voltage	5.05	5.34	5.38

5.2.6 System Control and Switching Programming

The principal aim of a control system is to facilitate effective power flow control from the input stage to the loads and also to regulate voltage, current and the frequency during various faults on the grid. Fig. 5.6 shows the block diagram of the proposed prototype with the control systems.

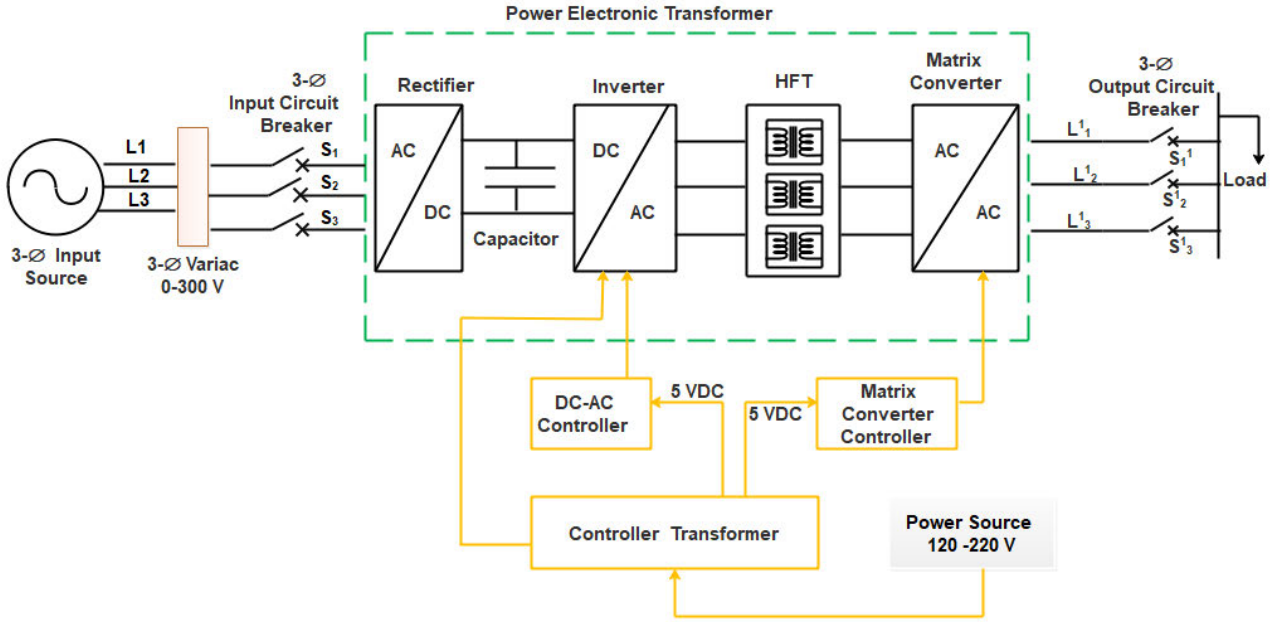

Figure 5.6: Block diagram of the proposed PET with control blocks

To improve control flexibility and independence, each conversion stage/block in the design is controlled independently. For rectification from AC to DC voltage, a three-phase full-wave uncontrolled rectifier is implemented using 24 diodes connected in the form of a full-wave bridge configuration - four diodes were connected in parallel to form one device with higher current capacity. The three-phase uncontrolled rectifier used diodes to generate a fixed average output voltage depending of the value of the input voltage. With no load on the DC link the DC rail voltage will charge the capacitor to $2 \times \left(\sqrt{2} \div \sqrt{3}\right) \times V_{L(RMS)}$. With a load this will decrease

to the average output voltage so that

$$V_{DC} = \frac{2\sqrt{2}\sqrt{3}}{\pi} V_{L(RMS)} \tag{5.25}$$

where $V_{L(RMS)}$ is line-line rms voltage. In order to generate the required output voltage in DC-AC conversion stage, the IGBT switches are triggered at a proper switching time and sequence. In this stage, all the IGBTs switches are controlled using a simple coded PIC18F46K20 micro-controller. The PIC18F46K20 code is written in C language. Switching frequency of 5 kHz at a duty cycle of about 50 % with a delay or dead-time of 100 μs was used. The designed printed circuit board (PCB) of the IGBT gate driver with micro-controller is shown in Fig. 5.10, while Appendix B shows the programming code.

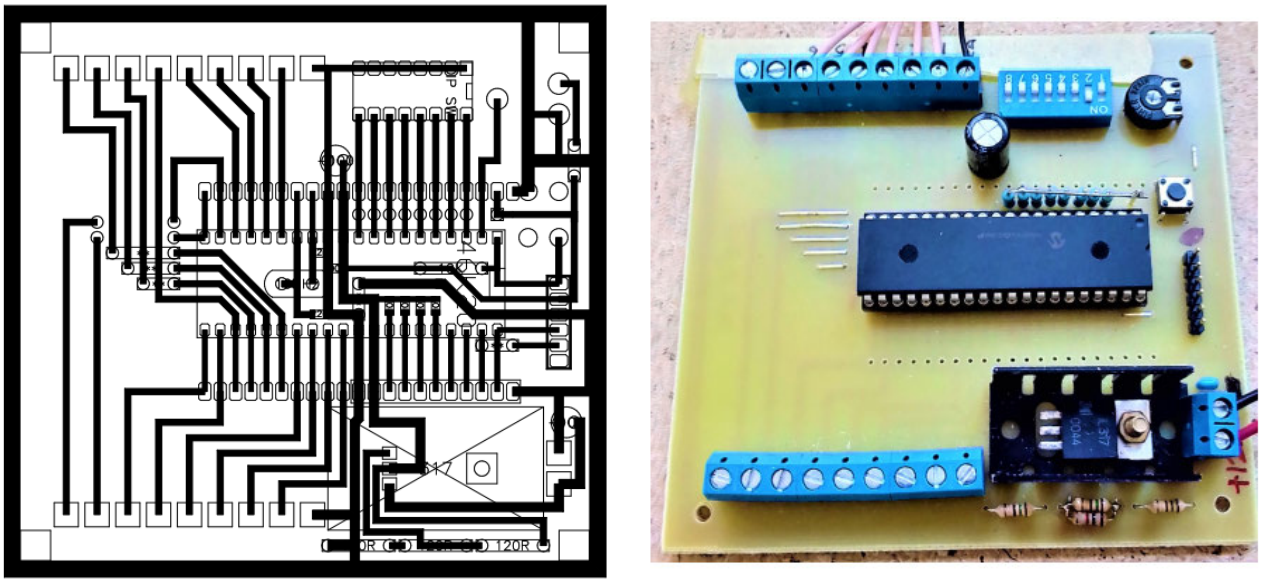

(a) Controller PCB

(b) Controller Prototype Module

Figure 5.7: Controller Printed Circuit Board and Design Prototype Module

Finally, the output stage of the transformer consists of MC. Compared to AC-DC-AC converters, MC simplify direct conversion from AC-AC, enhance power quality issues such as voltage sag and swell regulation and reactive power reimbursement. A chipKITMax32 micro-controller board based on the Microchip PIC32MX795F512L was used for the control and switching sequence of MC. Table 5.5 shows some of the operating characteristics of the micro-controller, while Fig. 5.11 shows a picture of the micro-controller.

Table 5.5: Summary of Micro-controller Characteristics

Micro-controller Characteristics	**Values**	**Units**
Operating voltage	3.3	V
Operating frequency	80	MHz
Operating current	90	mA
Input voltage recommended range	7 to 15	V
Input voltage maximum	20	V
Total input \ output pins	80	

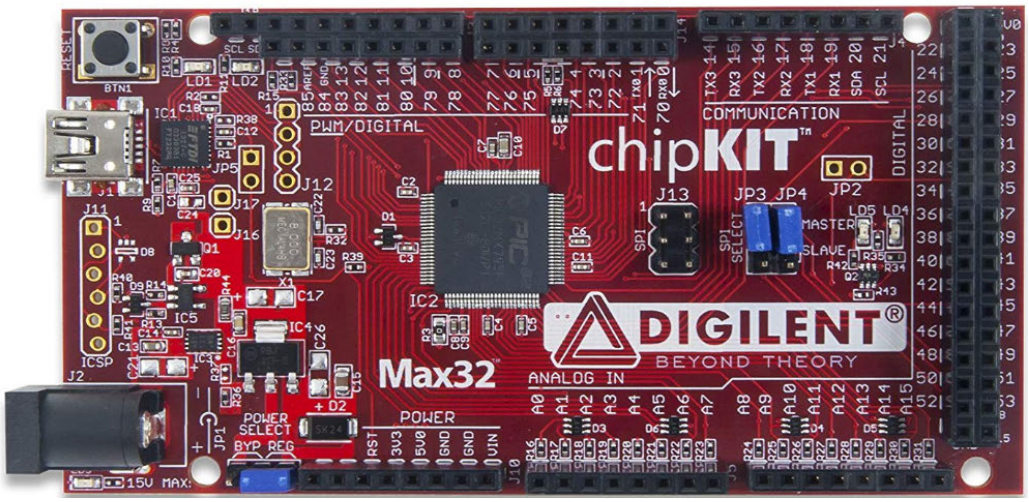

Figure 5.8: ChipKIT Max32 Micro-controller board.

Simple codes written in C language (see Appendix B and C) were used for the switching programming. The codes were developed using the designed controller to program the hardware control board. These generated the gate signals for the IGBTs with appropriate switching sequences and time.

Table 5.6 summaries some of the MPPET design parameters.

Table 5.6: MPPET Prototype Design Parameters

Parameter	**Value**	**Unit**
Rated Power	3	kVA
Input Voltage	156	V
Grid Frequency	50	Hz
Input Capacitance	1000	μF
Output Voltage	92	V
Switching Frequency	10	kHz

5.2.7 System Assembling and Testing

This section presents testing and final integration of individual voltage conversion stages/blocks of the proposed transformer prototype. Fig. 5.9 shows the hardware implementation of the input stage which consists AC to DC diode rectifier, while Fig. 5.10 presents a side by side printed

circuit board(PCB) and hardware implementation of DC-DC converter. The AC-AC matrix converter PCB and hardware implementation is presented in Fig. 5.11 while Fig. 5.12 shows the complete assembly of the transformer prototype.

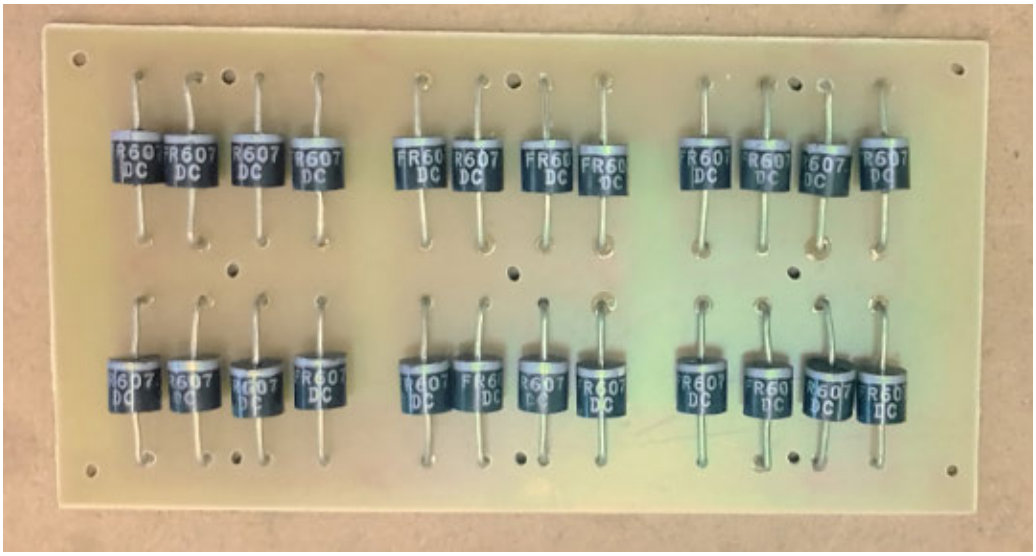

Figure 5.9: Hardware Implementation of Diode Rectifier

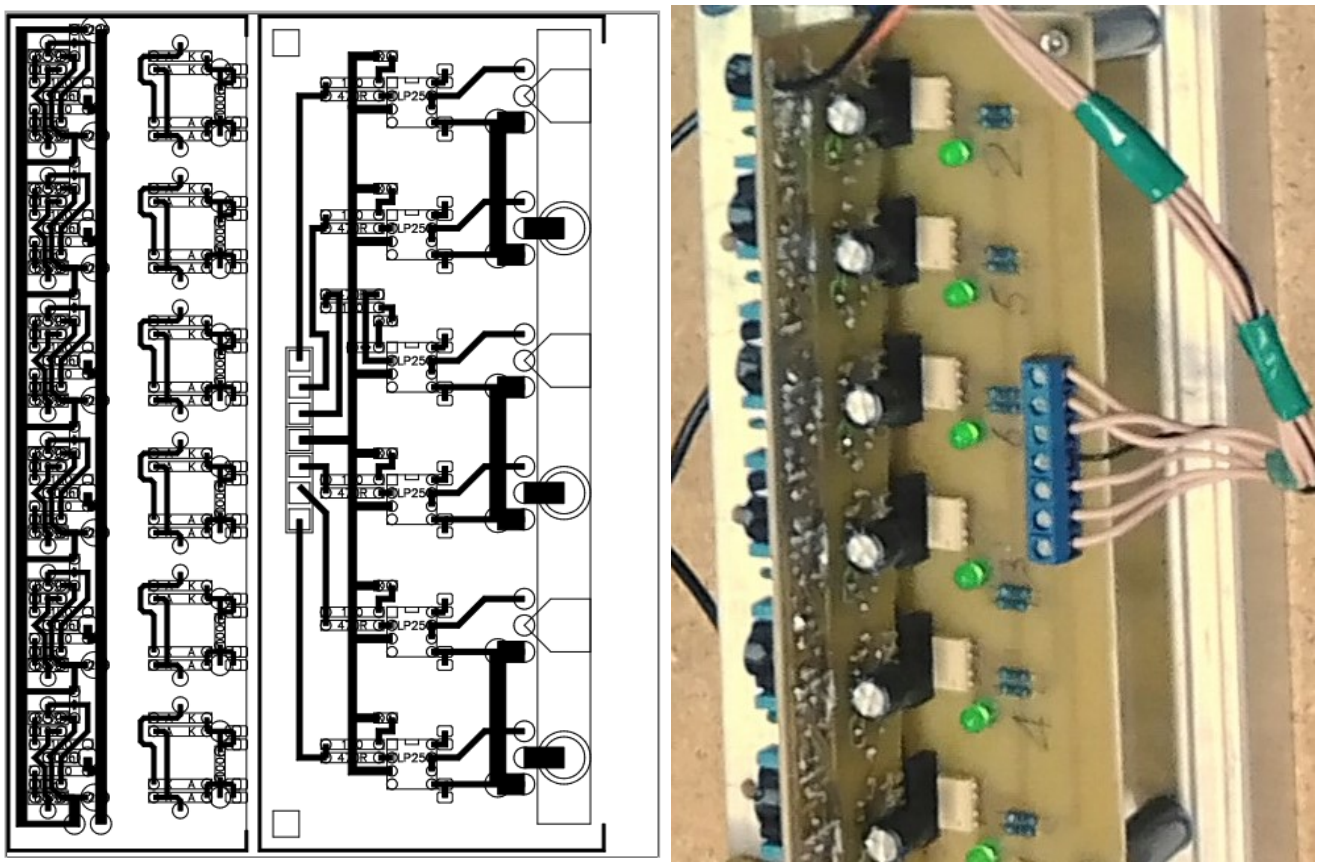

(a) DC-AC Converter PCB

(b) DC-AC Converter Prototype Module

Figure 5.10: Printed Circuit Board and Design Prototype Module of DC-AC Converter

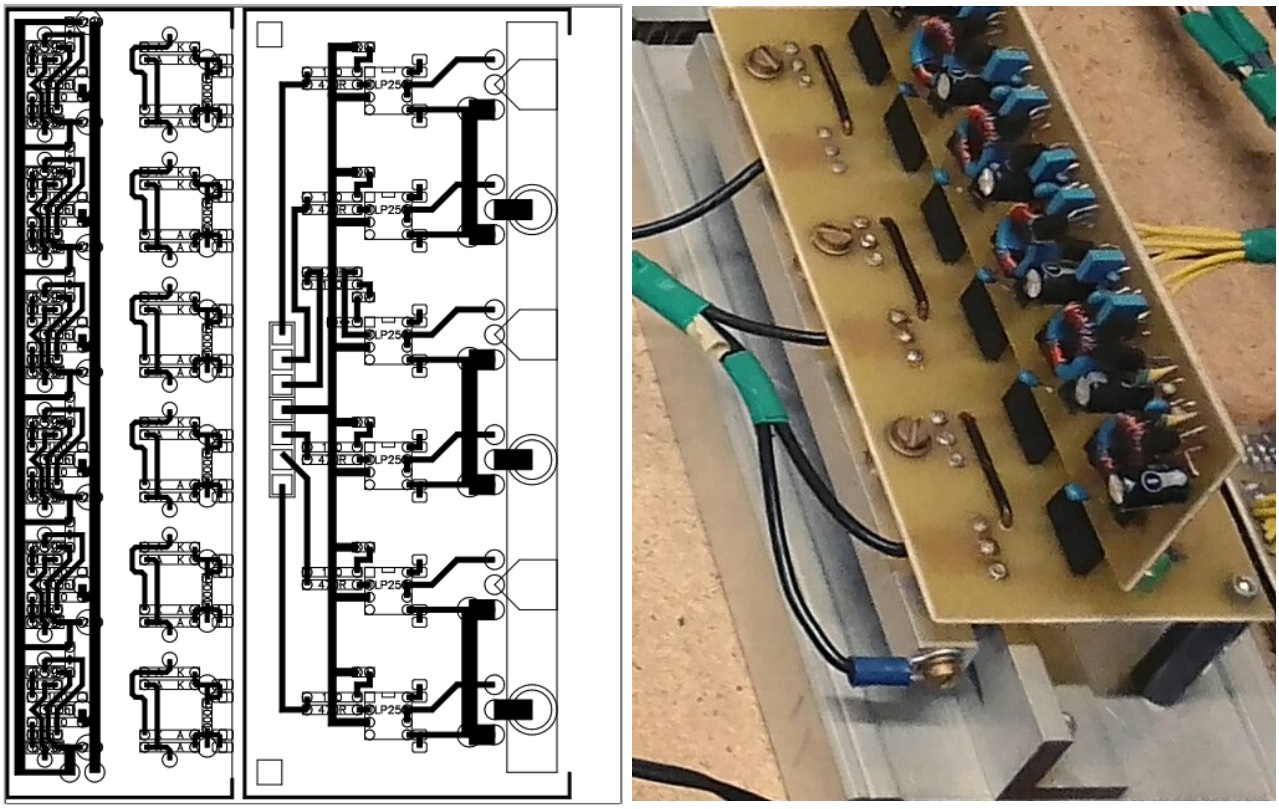

(a) Matrix Converter PCB

(b) Matrix Converter Prototype Module

Figure 5.11: Printed Circuit Board and Design Prototype Module of Matrix Converter

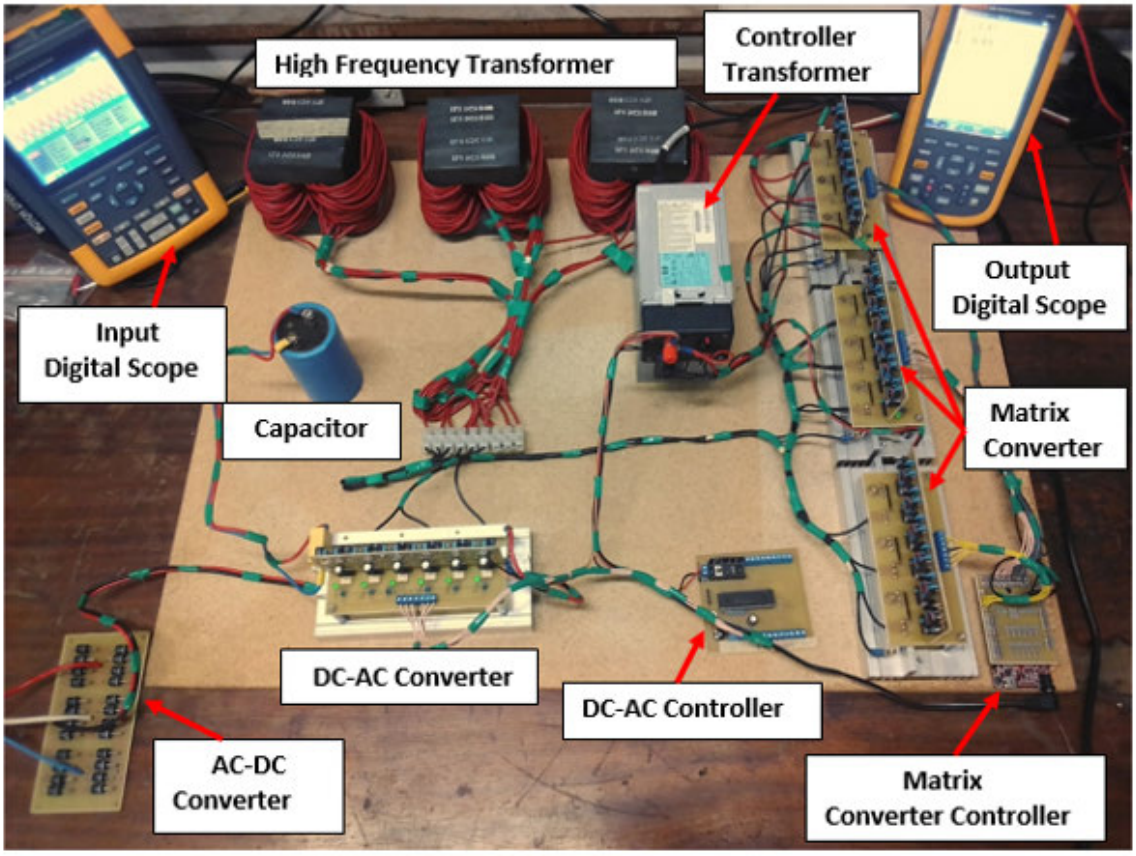

Figure 5.12: Complete Assembly of the Designed Transformer Prototype

5.3 Case Studies and Implementation Results Analysis

Implementation scenarios and results analysis of the designed transformer are presented in this section.

5.3.1 Implementation Scenarios

Case studies were carried out to evaluate the behavior of the designed transformer under different conditions. The normal operating condition refers to a situation where the transformer is running under normal loading and good conditions. While abnormal conditions refer to changes in load.

The variation in grid loading is predominant at the low voltage side due to the variability in load demand. As such, this section presents the reaction of the power electronic transformer to different loading conditions such as increase and decrease in the grid loading. For the purpose of analysis, this work considered a 50 % increase in the system loading.

5.3.2 Experimental Results

The experimental results are presented in this section. Fig. 5.13 presents the HFT prototype under load. In this work, a voltage limit of ±5% of the nominal voltage was considered.

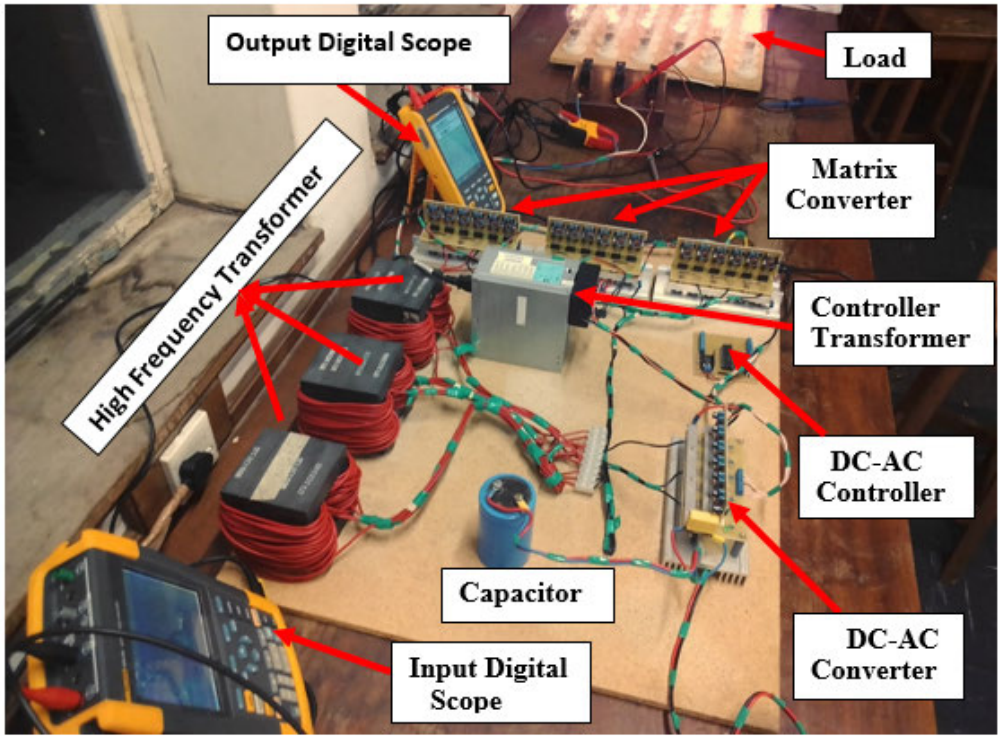

Figure 5.13: Transformer prototype design under Load Condition

- **Case 1: Normal Operating Condition**

  This scenario present the operation of the transformer under normal conditions, when

the transformer was loaded. The grid input voltage and current wave-forms obtained from the implementation of the designed transformer under normal operating condition is shown in Fig. 5.14. Fig. 5.15 shows the output voltage of the inverter to the HFT. This is a 5 kHz nominal square wave though the rise and fall times of the voltage are slow - this shows this system is close to its maximum frequency to the HFT. The normal loading was set to 100 W. Fig. 5.21 shows a matrix converter output after filtering when switched at 10 kHz. Because there is not a large difference between the HFT input and the output then this affects the quality of the sinusoidal waveform. with a higher input voltage to the matrix converter then this can be improved.

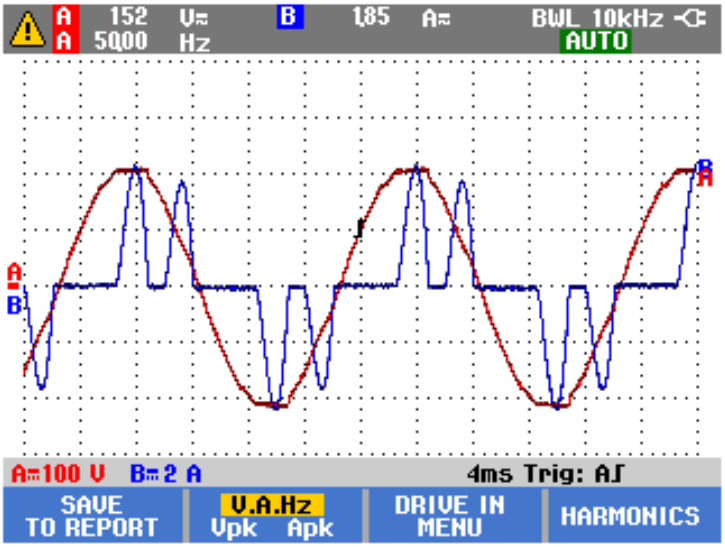

Figure 5.14: Grid input line voltage (red - 100 V/div) and line current (blue - 2 A/div) wave-forms under normal conditions - 50 Hz input

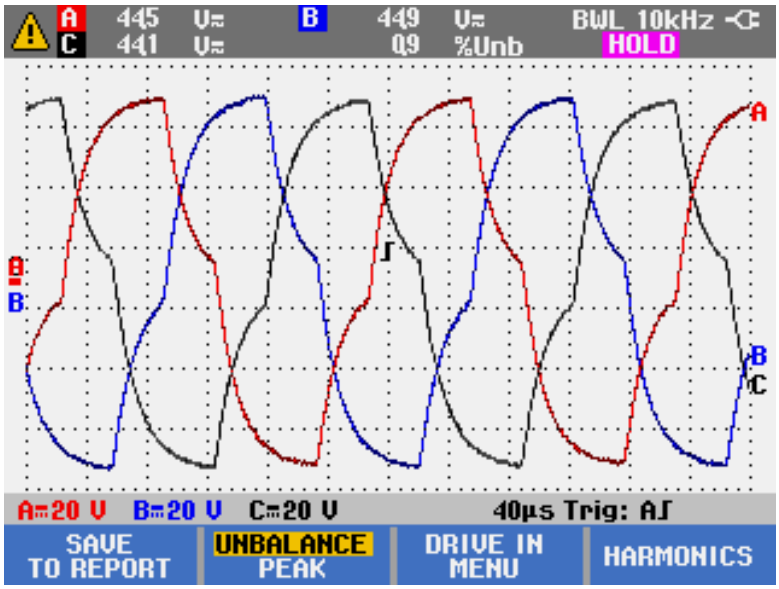

Figure 5.15: Input line-line voltage to HFT under normal conditions - V_{Line} = 44.5 V

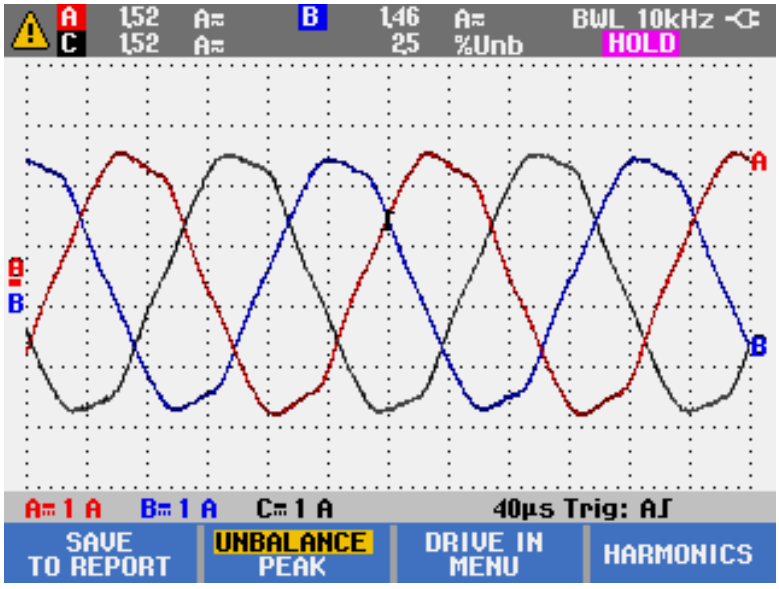

Figure 5.16: Input current to HFT under normal conditions - I_{Line} = 1.5 A

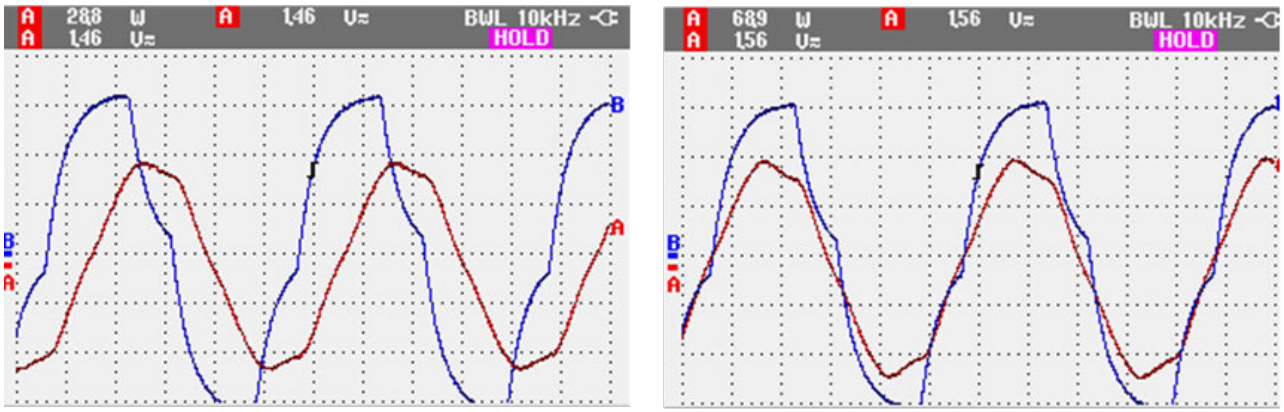

Figure 5.17: Input power using to HFT under normal conditions measured using 2-Wattmeter method - total power = 97.7 W

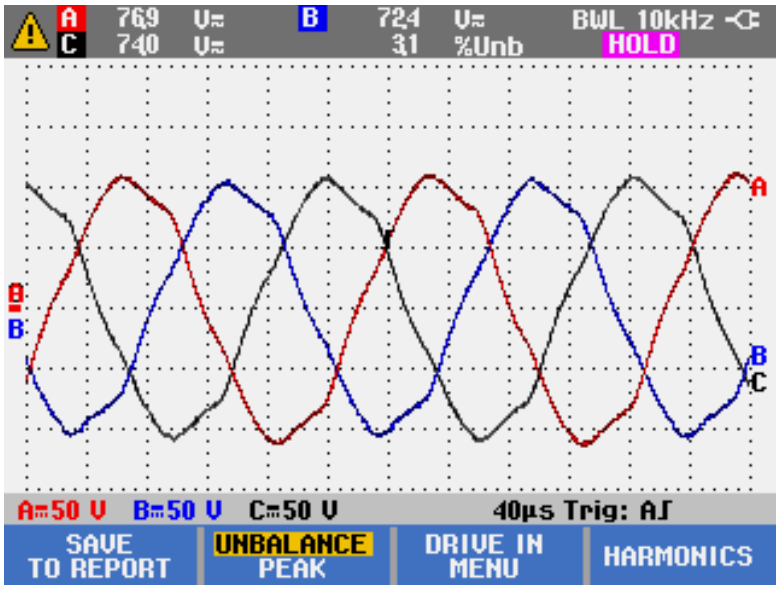

Figure 5.18: Output line-line voltage to HFT under normal conditions - V_{Line} = 44.5 V

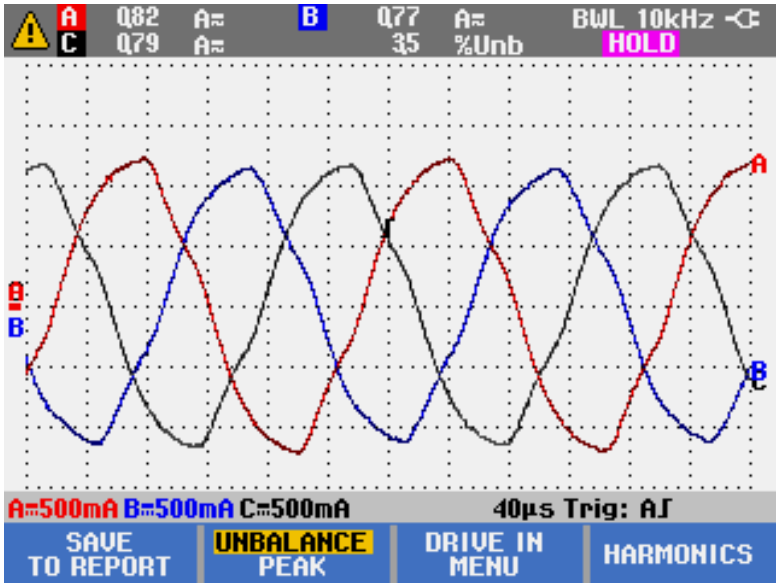

Figure 5.19: Input current to HFT under normal conditions - I_{Line} = 0.883 A

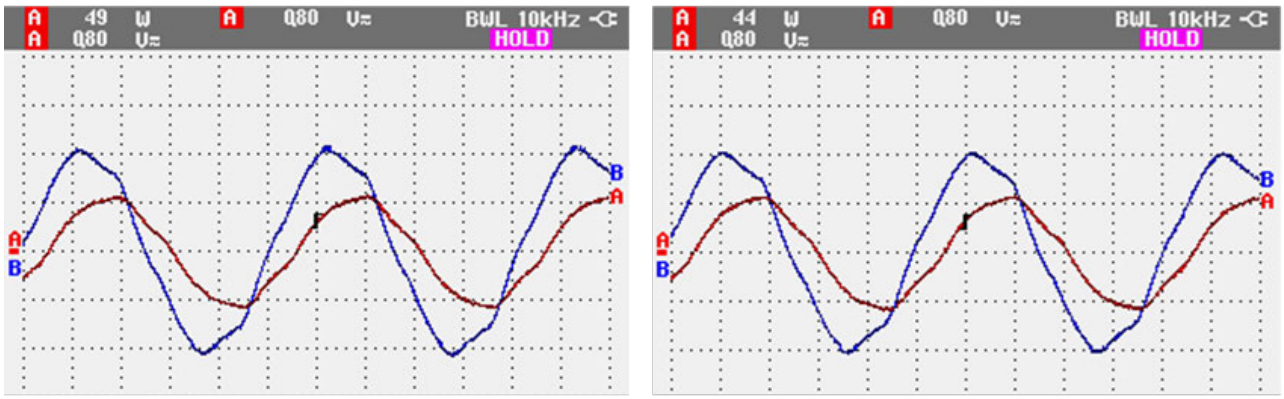

Figure 5.20: Output power using to HFT under normal conditions measured using 2-Wattmeter method - total power = 93 W

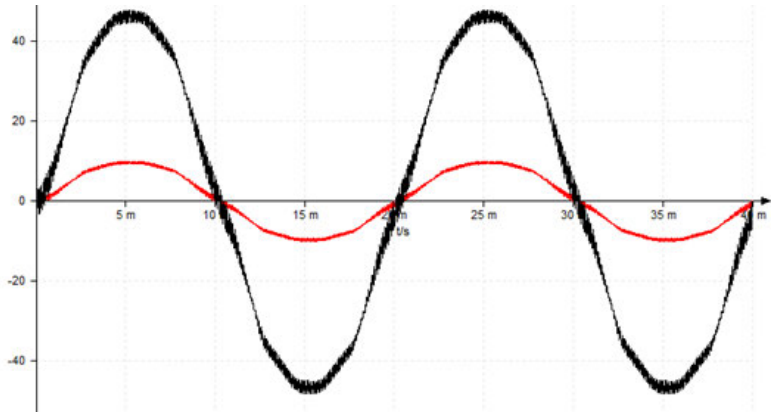

Figure 5.21: Matrix converter output power to resistive load - black is phase voltage (V) and red is current (10 × A)

As can be seen from the Fig. 5.14 to 5.20, the input voltage from the grid is 156 V which feeds the HFT at 44.5 V The output from the HFT is 74 V at 5 kHz. The matrix converter transforms this down to 50 Hz and maintains this voltage. The HFT efficiency, which is possibly the main source of system loss, was measured at $(93.07.7) \times 100 = 95.2$ % which is a good efficiency for a prototype high frequency transformer. The grid input is $\sqrt{3} \times 152 \times 1.85 = 187$ VA. This gives a low power factor of $100 \div 487 = 0.21$ due to the light loading of the diode bridge and the poor form factor. If this was replaced by a PWM inverter this would improve.

- **Case 2: Load Variation - 50 % increase**

  This scenario investigated the response of the transformer during a 50 % load increase on the secondary side of the transformer.

  Fig. 5.22 shows the grid input waveforms for the line voltage and line current. This is $\sqrt{3} \times 156 \times 3.9 = 1093$ VA. Again, it has poor form factor.

  Fig. 5.23 shows the inverter output waveform during load reduction. The red line shows the voltage in V while the blue line shows the current in A. There is good regulation and the output seems consistent with normal conditions. There is some unbalance in the input current but that is not passed through to the output voltage. Table 5.7 shows a comparison of the loading conditions and the efficiency remains high. Any decrease in the HFT voltage due to loading can be addressed in the matrix converter.

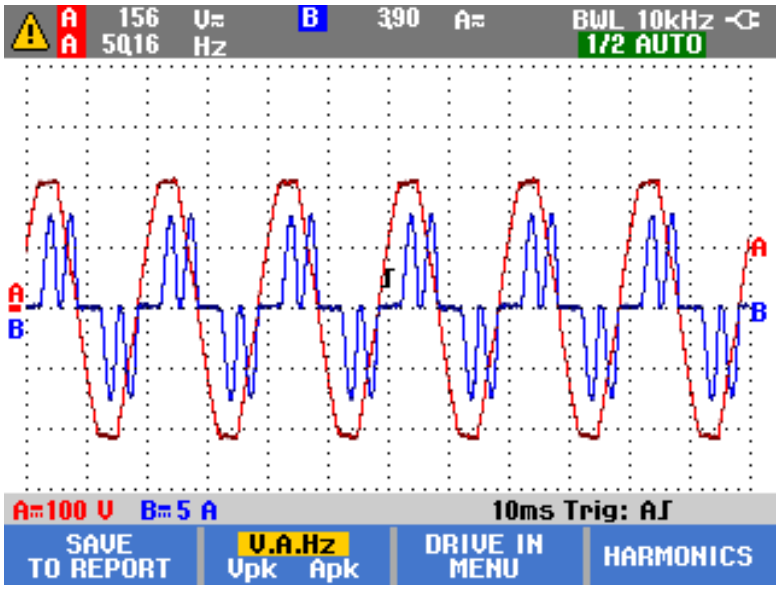

Figure 5.22: Grid input line voltage (red - 100 V/div) and line current (blue - 5 A/div) waveforms under 50 % increased conditions - 50 Hz input

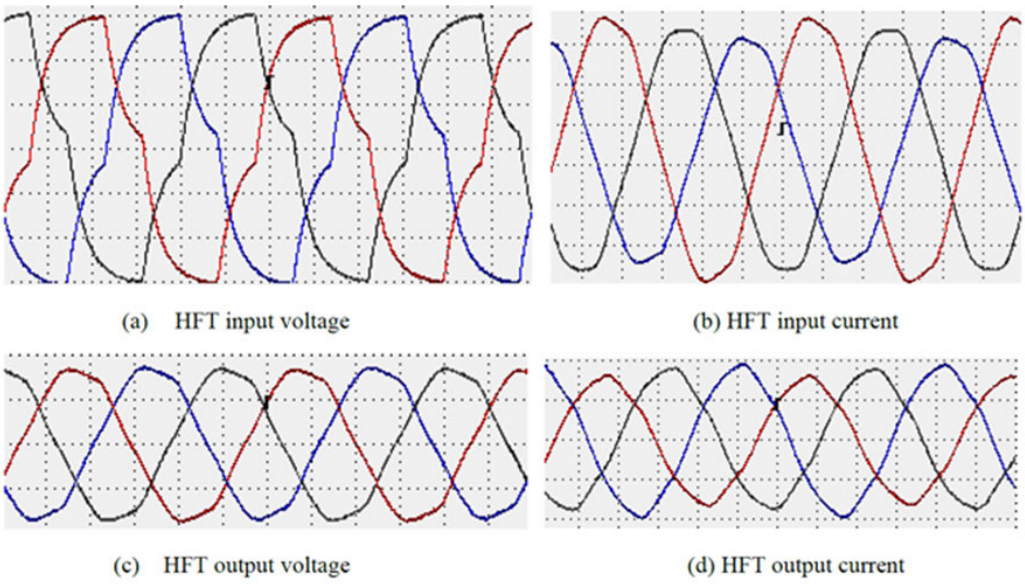

Figure 5.23: Input and output voltage waveforms are 50 % loading

Table 5.7: Comparison of normal and increased loading on HFT

	$V_{Line}[V]$	I_{Line} [A]	VA	Power [W]	p.f.
Normal loading					
Input	45.5	1.52	119.8	97.7	0.82
Output	74.0	0.88	113.3	93.0	0.82
Increased loading					
Input	42.5	2.24	164.9	147.1	0.89
Output	70.2	1.23	149.2	142.3	0.95

5.4 Summary

This chapter demonstrated the concept and implementation of the proposed power electronic transformer. The following points can be observed during different test scenarios carried out on the transformer. It was noted that the transformer was capable of withstanding different situations relating to loading. However, it was observed that the transformer was sensitive to situations such as high noise during increase in voltage, this may have been due to the use of ferrite in the design of the HFT. Air cored HFT may be an issue to investigate further.

Chapter 6

Conclusions and Recommendations for Further Work

6.1 Conclusions

The increase in integration of renewable energy into the power system network may jeopardize the normal operation and efficiency of the power system. One of the issues associated with high integration of renewable energy sources is excess power generation on the grid. Excess power generation and low energy demand reverse the direction of power flow on the grid. This situation is referred to as reverse power flow (RPF). This condition has diverse negative effects on the grid. Thus, the research aimed to investigate, analyze and provide effective technique for utilising the excess power generated due to high penetration of a wind farm. Established on the findings of the investigation and analysis given in Chapter 3 of this thesis, RPF causes high voltage along the grid, high power losses, upsurge of voltage harmonic distortion, overloading of the connecting elements (transformers and conductors) and the connected loads. Based on these findings, the research proposed the utilization of a MPPET for effective usage of RPF by diverting the excess power generated to an EV charging station. The proposed MPPET can effectively accommodate both off-board and on-board charging systems, therefore the name MPPET. The MPPET is active when the set smart circuit breaker at the PCC receives a signal that the energy balance index at the PCC is in critical condition; that is, the energy balance index is equal to zero. The effects of the proposed technique proved to be efficient; the MPPET was able to effectively supplied the surplus power on the grid to both off-board and on-board charging stations thereby reducing the high active power flow at the PCC and on the entire grid. Furthermore, MPPET was able to effectively control situations associated with voltage such as voltage swell on the grid. In addition, the system was able to adjust to variations in the system of loading and output generation of the connected wind farm as presented in Chapter 4 of this thesis. Finally, the scaled-down prototype of the proposed MPPET was designed and implemented in the laboratory and tested under different loadings. The design and implantation process such as system requirements, component selection, heat sink system design, high frequency transformer design, IGBT gate driver design implementation

and system control and switching programming were described. The results proved satisfactory as shown in Chapters 4 and 5 of this thesis. Due to it ability to enhance grid stability due to it ability to control VR and RPF, the proposed utilization technique will be able to enhance higher integration of renewable energy sources in the near future. It can be used to connect different distribution system networks and loads together. However, high power electronics devices involved increase the sensitivity of the proposed transformer and also an increase in the cost of execution. In addition, the control scheme of the proposed utilization technique is complex. However, each level of the design can be controlled independently, therefore, relieve the control complexity.

6.2 Recommendation for Further Work

The proposed method has set the foundation for utilization of reverse power flow using a MPPET. However, the scheme is receptive to improvement in term of topology modification to reduce the number of conversion stages in order to reduce the complexity of the system and also the cost of implementation. Furthermore, future work will improve the switching sequences and response time to situations on the grid. Another crucial area to develop on is the protection system of the proposed transformer. In addition, the transformer will be be upgraded to a bi-directional model for effective utilization of RPF. This model will incorporate the use of energy storage devices which can store excess power and supply the power back to the grid when there is power generation shortage on the grid. An automatic reverse power flow detector and control circuit will be incorporated into the transformer for more effective operation.

Bibliography

[1] J. Kabouris and F. Kanellos, "Impacts of large scale wind penetration on energy supply industry," *Energies*, vol. 2, no. 4, pp. 1031–1041, 2009.

[2] E. J. Coster, J. M. Myrzik, B. Kruimer, and W. L. Kling, "Integration issues of distributed generation in distribution grids," *Proceedings of the IEEE*, vol. 99, no. 1, pp. 28–39, 2010.

[3] T. T. Hashim, A. Mohamed, and H. Shareef, "A review on voltage control methods for active distribution networks," *Przeglad Elektrotechniczny (Electrical Review)*, vol. 88, no. 6, 2012.

[4] R. G. Newell, S. Iler, and D. Raimi, "Global energy outlooks comparison methods: 2018 update," *Resources for the Future, April*, vol. 26, 2018.

[5] Y. Tvehlov, "Energy, electricity, and nuclear power estimates for the period up to 2020; Nuclear power reactors in the world," *Atomnaya Ehnergiya*, vol. 92, no. 4, p. 333, 2002.

[6] S. Wharton and J. Lundquist, "Atmospheric stability affects wind turbine power collection," *Environmental Research Letters*, vol. 7, pp. 1–10, 2012.

[7] M. G. Molina and P. E. Mercado, "Modelling and control design of pitch-controlled variable speed wind turbines," in *Wind turbines*, In Tech, 2011.

[8] A. Fernández-Guillamón, K. Das, N. A. Cutululis, and Á. Molina-Garcıa, "Offshore wind power integration into future power systems: Overview and trends," *Journal of Marine Science and Engineering*, vol. 7, no. 11, p. 399, 2019.

[9] F. Santjer, G. Gerdes, P. Christiansen, and D. Milborrow, *Wind turbine grid connection and interaction*, http://ec.europa.es/energy, 2001.

[10] H. Smail, R. Alkama, and A. Medjdoub, "Optimal design of the electric connection of a wind farm," *Energy*, vol. 165, pp. 972–983, 2018.

[11] G. Shafiullah, A. M. Oo, A. Ali, and A. Stojcevski, "Influences of wind energy integration into the distribution network," *Journal of Wind Energy*, vol. 2013, 2013.

[12] S. Gasnier, V. Debusschere, S. Poullain, and B. François, "Technical and economic assessment tool for offshore wind generation connection scheme: Application to comparing 33 kV and 66 kV AC collector grids authors," in *2016 18th European Conference on Power Electronics and Applications (EPE'16 ECCE Europe)*, IEEE, 2016, pp. 1–8.

[13] M. Pöller, "Grid Integration of Wind Energy in Western Cape - Results of Feasibility Studies," *Gomaringen: DIgSILENT GmbH*, 2009.

[14] GWEC, *Global Wind Report: Annual market update 2015*, `http://gwec.net/global-figures/graphs/`, Accessed: May 18 2017.

[15] A. Whiteman, T. Rinke, J. Esparrago, and S. Elsayed, "Renewable capacity statistics 2016," *IRENA*, vol. 3, p. 29, 2016.

[16] A. Zervos and C. Kjaer, "Pure Power. Wind Energy Scenarios up to 2030," *European Wind Energy Association*, 2006.

[17] T. Ackermann *et al.*, *Wind power in power systems*. Wiley Online Library, 2005, vol. 140.

[18] J. P. Holguin, D. C. Rodriguez, and G. Ramos, "Reverse power flow (RPF) detection and impact on protection coordination of distribution systems," *IEEE Transactions on Industry Applications*, vol. 56, no. 3, pp. 2393–2401, 2020.

[19] W. El-Khattam and M. M. Salama, "Distributed generation technologies, definitions and benefits," *Electric power systems research*, vol. 71, no. 2, pp. 119–128, 2004.

[20] E. S. Elmubarak and A. M. Ali, "Distributed generation: Definitions, benefits, technologies & challenges," *Int. J. Sci. Res.(IJSR)*, vol. 5, no. 7, 2016.

[21] P. Unahalekhaka and P. Sripakarach, "Reduction of Reverse Power Flow using the Appropriate Size and Installation Position of a BESS for a PV Power Plant," *IEEE Access*, 2020.

[22] R. Passey, T. Spooner, M. Watt, J. McDonald, P. McCracken, J. Gordon, and K. Syngellakis, "Addressing grid-interconnection issues in order to maximize the utilization of new and renewable energy sources," *IT Power Pty Ltd, O'Conner, Australia*, 2010.

[23] A. Demiroren and U. Yilmaz, "Analysis of change in electric energy cost with using renewable energy sources in Gökceada, Turkey: An island example," *Renewable and Sustainable Energy Reviews*, vol. 14, no. 1, pp. 323–333, 2010.

[24] J. Barzola, M. Espinoza, and F. Cabrera, "Analysis of hybrid solar/wind/diesel renewable energy system for off-grid rural electrification," *Int. J. Renew. Energy Res*, vol. 6, no. 3, pp. 1146–1152, 2016.

[25] M. S. Ismail, M. Moghavvemi, and T. Mahlia, "Techno-economic analysis of an optimized photovoltaic and diesel generator hybrid power system for remote houses in a tropical climate," *Energy conversion and management*, vol. 69, pp. 163–173, 2013.

[26] O. Hafez and K. Bhattacharya, "Optimal planning and design of a renewable energy based supply system for microgrids," *Renewable Energy*, vol. 45, pp. 7–15, 2012.

[27] A.-K. Daud and M. S. Ismail, "Design of isolated hybrid systems minimizing costs and pollutant emissions," *Renewable energy*, vol. 44, pp. 215–224, 2012.

[28] J. L. Bernal-Agustın, R. Dufo-López, and D. M. Rivas-Ascaso, "Design of isolated hybrid systems minimizing costs and pollutant emissions," *Renewable Energy*, vol. 31, no. 14, pp. 2227–2244, 2006.

[29] D. Ipsakis, S. Voutetakis, P. Seferlis, F. Stergiopoulos, and C. Elmasides, "Power management strategies for a stand-alone power system using renewable energy sources and hydrogen storage," *International journal of hydrogen energy*, vol. 34, no. 16, pp. 7081–7095, 2009.

[30] M. Moghavvemi, M. S. Ismail, B. Murali, S. Yang, A. Attaran, and S. Moghavvemi, "Development and optimization of a PV/diesel hybrid supply system for remote controlled commercial large scale FM transmitters," *Energy Conversion and Management*, vol. 75, pp. 542–551, 2013.

[31] M. Tahir, M. E. Nassar, R. El-Shatshat, and M. Salama, "A review of volt/var control techniques in passive and active power distribution networks," in *2016 IEEE Smart Energy Grid Engineering (SEGE)*, IEEE, 2016, pp. 57–63.

[32] M. A. Eltawil and Z. Zhao, "Grid-connected photovoltaic power systems: Technical and potential problems — A review," *Renewable and sustainable energy reviews*, vol. 14, no. 1, pp. 112–129, 2010.

[33] M. M. Begovic, I. Kim, D. Novosel, J. R. Aguero, and A. Rohatgi, "Integration of photovoltaic distributed generation in the power distribution grid," in *2012 45th Hawaii International Conference on System Sciences*, IEEE, 2012, pp. 1977–1986.

[34] J. Driesen and R. Belmans, "Distributed generation: Challenges and possible solutions," in *2006 IEEE power engineering society general meeting*, IEEE, 2006, 8–pp.

[35] E. Coster, J. Myrzik, and W. Kling, "Effect of distributed generation on protection of medium voltage cable grids," in *CIRED 19th International Conference on Electricity Distribution*, 2007, p. 4.

[36] F. Motabarian, M. A. Golkar, and S. Hajiaghasi, "Surveying the effect of distributed generation (DG) on over current protection in radial distribution systems," in *18th Electric Power Distribution Conference*, IEEE, 2013, pp. 1–6.

[37] A. Khademlahashy, L. Li, J. Every, and J. Zhu, "A review on protection issues in micro-grids embedded with distribution generations," in *2017 12th IEEE Conference on Industrial Electronics and Applications (ICIEA)*, IEEE, 2017, pp. 913–918.

[38] V. A. Papaspiliotopoulos, G. N. Korres, and N. D. Hatziargyriou, "Adverse impact of distributed generation on protection of the hellenic mv network–recommendations for protection scheme upgrade," *CIRED-Open Access Proceedings Journal*, vol. 2017, no. 1, pp. 934–938, 2017.

[39] F. Bastiao, P. Cruz, and R. Fiteiro, "Impact of distributed generation on distribution networks," in *2008 5th International Conference on the European Electricity Market*, IEEE, 2008, pp. 1–6.

[40] J. M. Gers and E. J. Holmes, *Protection of electricity distribution networks*. IET, 2005, vol. 47.

[41] L. Cipcigan and P. Taylor, "Investigation of the reverse power flow requirements of high penetrations of small-scale embedded generation," *IET Renewable Power Generation*, vol. 1, no. 3, pp. 160–166, 2007.

[42] L. Bird, M. Milligan, and D. Lew, "Integrating variable renewable energy: Challenges and solutions," National Renewable Energy Lab.(NREL), Golden, CO (United States), Tech. Rep., 2013.

[43] P. González, E. Romero, V. M. Miñambres, M. A. Guerrero, and E. González, "Grid-connected PV plants. Power quality and technical requirements," in *2014 Electric Power Quality and Supply Reliability Conference (PQ)*, IEEE, 2014, pp. 169–176.

[44] K. I. Sgouras, A. S. Bouhouras, P. A. Gkaidatzis, D. I. Doukas, and D. P. Labridis, "Impact of reverse power flow on the optimal distributed generation placement problem," *IET Generation, Transmission & Distribution*, vol. 11, no. 18, pp. 4626–4632, 2017.

[45] A. Pouryekta, V. K. Ramachandaramurthy, N. Mithulananthan, and A. Arulampalam, "Islanding detection and enhancement of microgrid performance," *IEEE Systems Journal*, vol. 12, no. 4, pp. 3131–3141, 2017.

[46] G. De Carne, G. Buticchi, Z. Zou, and M. Liserre, "Reverse power flow control in a ST-fed distribution grid," *IEEE Transactions on Smart Grid*, vol. 9, no. 4, pp. 3811–3819, 2017.

[47] U. N. Khan, "Distributed generation and power quality," in *International Conference on Environment and Electrical Engineering, Karpacz, Poland*, vol. 145, 2009, pp. 232–235.

[48] Z. Chen, "Issues of connecting wind farms into power systems," in *2005 IEEE/PES Transmission & Distribution Conference & Exposition: Asia and Pacific*, IEEE, 2005, pp. 1–6.

[49] R. Sinvula, K. M. Abo-Al-Ez, and M. T. Kahn, "A Proposed Harmonic Monitoring System for Large Power Users Considering Harmonic Limits," *Energies*, vol. 13, no. 17, p. 4507, 2020.

[50] M. H. Bollen and K. Yang, "Harmonic aspects of wind power integration," *Journal of modern power systems and clean energy*, vol. 1, no. 1, pp. 14–21, 2013.

[51] C. A. Pereira, J. A. P. Lopes, and M. A. Matos, "Assessment of the Distributed Generation Hosting Capacity Incorporating Harmonic Distortion Limits," in *2018 International Conference on Smart Energy Systems and Technologies (SEST)*, IEEE, 2018, pp. 1–6.

[52] G. Eduful, E. A. Jackson, and J. E. Cole, "Harmonic emission limits and selecting PCC location based on the type of distribution system," in *Proceedings of the World Congress on Engineering*, vol. 1, 2014.

[53] T. M. Blooming and D. J. Carnovale, "Application of IEEE Std 519-1992 harmonic limits," in *Conference Record of 2006 Annual Pulp and Paper Industry Technical Conference*, IEEE, 2006, pp. 1–9.

[54] P. Morthorst, H. Auer, A. Garrad, and I. Blanco, *Wind Energy — The Facts; Part-II: Grid Integration*, `https://iopscience.iop.org/article/10.1088/1757-899X/353/1/012014/pdf`, European Wind Energy Association, Brussels, Belgium, 2009.

[55] H. Hussain, N. Javaid, S. Iqbal, Q. Hasan, K. Aurangzeb, and M. Alhussein, "An efficient demand side management system with a new optimized home energy management controller in smart grid," *Energies*, vol. 11, no. 1, p. 190, 2018.

[56] H. Hatta, W. Shima, T. Kawakami, H. Kobayashi, N. Sueyoshi, H. Nakama, Y. Oshiro, and M. Toguchi, "Demonstration test of PV output reduction method using battery energy storage system and customer equipment," in *IEEE PES ISGT Europe 2013*, IEEE, 2013, pp. 1–5.

[57] H. Hatta and H. Kobayashi, "Utilization of Surplus Electric Power of Photovoltaic Systems by Heat Pump Water Heaters: A Planning Method and Its Effect in an Autonomous Demand Area Power System," *Electrical Engineering in Japan*, vol. 185, no. 2, pp. 12–20, 2013.

[58] H. Hatta, M. Asari, and H. Kobayashi, "Study of energy management for decreasing reverse power flow from photovoltaic power systems," in *2009 IEEE PES/IAS Conference on Sustainable Alternative Energy (SAE)*, IEEE, 2009, pp. 1–5.

[59] M. Asari and H. Kobayashi, "Method of controlling reverse power flow of PV system with heat pump water heater," in *2012 3rd IEEE PES Innovative Smart Grid Technologies Europe (ISGT Europe)*, IEEE, 2012, pp. 1–6.

[60] P. J. P. Eloja, N. A. F. Jorda, and M. A. A. Pedrasa, "Reverse Power Flow Detection Using Optimally Placed μPMUs in a Distribution System," in *International Conference on Sustainable Energy for Smart Cities*, Springer, 2019, pp. 98–109.

[61] Y. Liu, J. Bebic, B. Kroposki, J. De Bedout, and W. Ren, "Distribution system voltage performance analysis for high-penetration PV," in *2008 IEEE Energy 2030 Conference*, IEEE, 2008, pp. 1–8.

[62] R. Seguin, J. Woyak, D. Costyk, J. Hambrick, and B. Mather, "High-penetration PV integration handbook for distribution engineers," National Renewable Energy Lab.(NREL), Golden, CO (United States), Tech. Rep., 2016.

[63] M. A. Mahmud, M. J. Hossain, and H. R. Pota, "Voltage variation on distribution networks with distributed generation: Worst case scenario," *IEEE Systems Journal*, vol. 8, no. 4, pp. 1096–1103, 2013.

[64] D. Gaonkar, G. Pillai, and R. Patel, "Steady state voltage rise and its control in distribution system with distributed generation," *International Energy Journal*, vol. 8, no. 3, 2007.

[65] M. A. Mahmud, M. Hossain, and H. R. Pota, "Analysis of voltage rise effect on distribution network with distributed generation," *IFAC Proceedings Volumes*, vol. 44, no. 1, pp. 14 796–14 801, 2011.

[66] L. Bird, D. Lew, M. Milligan, E. M. Carlini, A. Estanqueiro, D. Flynn, E. Gomez-Lazaro, H. Holttinen, N. Menemenlis, A. Orths, *et al.*, "Wind and solar energy curtailment: A review of international experience," *Renewable and Sustainable Energy Reviews*, vol. 65, pp. 577–586, 2016.

[67] P. Sudhakar, S. Malaji, and B. Sarvesh, "Reducing the impact of DG on distribution networks protection with reverse power relay," *Materials Today: Proceedings*, vol. 5, no. 1, pp. 51–57, 2018.

[68] M. S. Ismail, M. Moghavvemi, T. Mahlia, K. M. Muttaqi, and S. Moghavvemi, "Effective utilization of excess energy in standalone hybrid renewable energy systems for improving comfort ability and reducing cost of energy: A review and analysis," *Renewable and Sustainable Energy Reviews*, vol. 42, pp. 726–734, 2015.

[69] K. Inoue and Y. Iwafune, "Operation of heat pump water heaters for restriction of photovoltaic reverse power flow," in *2010 International Conference on Power System Technology*, IEEE, 2010, pp. 1–7.

[70] A. Al-Sabounchi, J. Gow, M. Al-Akaidi, and H. Al-Thani, "Minimizing line energy loss of radial distribution feeder with a PV Distributed Generation unit avoiding reverse power flow," in *2011 2nd International Conference on Electric Power and Energy Conversion Systems (EPECS)*, IEEE, 2011, pp. 1–6.

[71] M. Alam, K. Muttaqi, and D. Sutanto, "Mitigation of rooftop solar PV impacts and evening peak support by managing available capacity of distributed energy storage systems," *IEEE Transactions on Power Systems*, vol. 28, no. 4, pp. 3874–3884, 2013.

[72] M. Aachiq, T. Oozeki, Y. Iwafune, and J. G. Fonseca Jr, "Reduction of PV reverse power flow through the usage of EV's battery with consideration of the demand and solar radiation forecast," in *2013 IEEE International Electric Vehicle Conference (IEVC)*, IEEE, 2013, pp. 1–3.

[73] K. Kuroda, Y. Matsufuji, T. Kashiwagi, T. Ichimura, and R. Yokoyama, "An approach of distribution systems stabilization for a large-scale PV systems installation environment," in *IEEE PES ISGT Europe 2013*, IEEE, 2013, pp. 1–5.

[74] A. Al-Riyami, K. Burt, G. Manhangwe, P. Pretlove, and S. Georgiopoulos, "An investigation into alternatives to directional overcurrent protection on grid transformers to improve the network capacity to accommodate reverse power flow," 2014.

[75] M. Hasheminamin, V. G. Agelidis, V. Salehi, R. Teodorescu, and B. Hredzak, "Index-based assessment of voltage rise and reverse power flow phenomena in a distribution feeder under high pv penetration," *IEEE Journal of Photovoltaics*, vol. 5, no. 4, pp. 1158–1168, 2015.

[76] W. McMurray, *Power Converter Circuits Having a High Frequency Link*, U.S. Patent 3,517,300, 1970.

[77] J. Bian and G. Qiu, "The application of power electronic transformer in distribution power system," in *4th International Conference on Information Technology and Management Innovation*, Atlantis Press, 2015.

[78] B. Kalyan and P. R. Prasad, "Analysis and design of power electronic transformer based power quality improvement," *IOSR J Electr Electron Eng*, vol. 5, pp. 61–69, 2013.

[79] K. Basu, R. K. Gupta, S. Nath, G. F. Castelino, K. K. Mohapatra, and N. Mohan, "Research in matrix-converter based three-phase power-electronic transformers," in *The 2010 International Power Electronics Conference-ECCE ASIA-*, IEEE, 2010, pp. 2799–2803.

[80] R. B. Roy, M. Rokonuzzaman, and M. Hossam-E-Haider, "Design and analysis of the power electronic transformer for power quality improvement," in *2015 International Conference on Electrical Engineering and Information Communication Technology (ICEEICT)*, IEEE, 2015, pp. 1–5.

[81] S. Falcones, X. Mao, and R. Ayyanar, "Topology comparison for solid state transformer implementation," in *Power and Energy Society General Meeting, 2010 IEEE*, Citeseer, 2010, pp. 1–8.

[82] I. Roasto, E. Romero-Cadaval, J. Martins, and R. Smolenski, "State of the art of active power electronic transformers for smart grids," in *IECON 2012-38th Annual Conference on IEEE Industrial Electronics Society*, IEEE, 2012, pp. 5241–5246.

[83] N. W. Basri, H. Daniyal, and M. S. Bakar, "MATRIX CONVERTER: A REVIEW," *ARPN Journal of Engineering and Applied Sciences*, vol. 10, no. 22, pp. 17 070–12 077, 2015.

[84] D. G. Dorrell, "Understanding and Modeling of Matrix Converters for Application in Renewable Energy and Micro Grid Applications," in *IEEE International Industrial Electronics Conference (IECON)*, IEEE, 2014, pp. 1–6.

[85] J. Van Der Merwe and H. d. T. Mouton, "The solid-state transformer concept: A new era in power distribution," in *AFRICON 2009*, IEEE, 2009, pp. 1–6.

[86] C. Ling, B. Ge, D. Bi, and Q. Ma, "An effective power electronic transformer applied to distribution system," in *2011 International Conference on Electrical Machines and Systems*, IEEE, 2011, pp. 1–6.

[87] H. Fan and H. Li, "High frequency high efficiency bidirectional dc-dc converter module design for 10 kva solid state transformer," in *2010 Twenty-Fifth Annual IEEE Applied Power Electronics Conference and Exposition (APEC)*, IEEE, 2010, pp. 210–215.

[88] J.-S. Lai, A. Maitra, A. Mansoor, and F. Goodman, "Multilevel intelligent universal transformer for medium voltage applications," in *Fourtieth IAS Annual Meeting. Conference Record of the 2005 Industry Applications Conference, 2005.*, IEEE, vol. 3, 2005, pp. 1893–1899.

[89] T. Kang, S. Essakiappan, P. Enjeti, and S. Choi, "Towards a smart distribution transformer for smart grid," in *2015 9th International Conference on Power Electronics and ECCE Asia (ICPE-ECCE Asia)*, IEEE, 2015, pp. 1997–2003.

[90] S. Bhattacharya, T. Zhao, G. Wang, S. Dutta, S. Baek, Y. Du, B. Parkhideh, X. Zhou, and A. Q. Huang, "Design and development of generation-i silicon based solid state transformer," in *2010 Twenty-Fifth Annual IEEE Applied Power Electronics Conference and Exposition (APEC)*, IEEE, 2010, pp. 1666–1673.

[91] A. Borgaonkar, "Solid state transformers: A review of technology and applications," *Indian Inst. Technol., New Delhi, India, Tech. Rep*, 2015.

[92] Q. Yue, C. Li, Y. Cao, Y. He, B. Cai, Q. Wu, and B. Zhou, "Comprehensive power losses model for electronic power transformer," *Ieee Access*, vol. 6, pp. 14 926–14 934, 2018.

[93] X. She, A. Q. Huang, and R. Burgos, "Review of solid-state transformer technologies and their application in power distribution systems," *IEEE journal of Emerging and Selected Topics in Power Electronics*, vol. 1, no. 3, pp. 186–198, 2013.

[94] P. Tatcho, H. Li, Y. Jiang, and L. Qi, "A novel hierarchical section protection based on the solid state transformer for the future renewable electric energy delivery and management (FREEDM) system," *IEEE Transactions on Smart Grid*, vol. 4, no. 2, pp. 1096–1104, 2012.

[95] X. She, S. Lukic, A. Q. Huang, S. Bhattacharya, and M. Baran, "Performance evaluation of solid state transformer based microgrid in FREEDM systems," in *2011 Twenty-Sixth annual IEEE applied power electronics conference and exposition (APEC)*, IEEE, 2011, pp. 182–188.

[96] H. De Silva, D. Jayamaha, and N. Lidula, "Review on design and control of solid state transformer based microgrids," *AIMS Energy*, vol. 7, no. 6, p. 901, 2019.

[97] R. He, Y. Zhang, D. Zhang, and D. Xie, "An Improvement of Core Losses Estimation Model in Power Electronic Transformer," in *2018 IEEE Student Conference on Electric Machines and Systems*, IEEE, 2018, pp. 1–5.

[98] W. Rodrigues, L. Morais, T. Oliveira, R. Santana, A. Cota, and W. Silva, "Analysis of solid state transformer based microgrid system," in *2016 12th IEEE International Conference on Industry Applications (INDUSCON)*, IEEE, 2016, pp. 1–6.

[99] T. L. Vandoorn, J. D. De Kooning, B. Meersman, J. M. Guerrero, and L. Vandevelde, "Voltage-based control of a smart transformer in a microgrid," *IEEE Transactions on Industrial Electronics*, vol. 60, no. 4, pp. 1291–1305, 2011.

[100] S. Hosseini, M. Sharifian, M. Sabahi, Z. Hooshi, and G. Gharehpetian, "A tri-directional power electronic transformer for photo voltaic based distributed generation application," in *2009 IEEE Power & Energy Society General Meeting*, IEEE, 2009, pp. 1–5.

[101] J. Shah, R. K. Gupta, K. K. Mohapatra, and N. Mohan, "Power management with a dynamic power limit by a power electronic transformer for micro-grid," in *IEEE PES General Meeting*, IEEE, 2010, pp. 1–5.

[102] M. Saghaleini, A. Hekmati, and S. Farhangi, "An advanced distributed power supply for power electronic transformers," in *IECON 2007-33rd Annual Conference of the IEEE Industrial Electronics Society*, IEEE, 2007, pp. 2038–2043.

[103] R. K. Gupta, G. F. Castelino, K. K. Mohapatra, and N. Mohan, "A novel integrated three-phase, switched multi-winding power electronic transformer converter for wind power generation system," in *2009 35th Annual Conference of IEEE Industrial Electronics*, IEEE, 2009, pp. 4481–4486.

[104] P. Kumar, "Application of distribution power electronic transformer for medium voltage," *International Journal of Power Electronics and Drive Systems*, vol. 4, no. 4, p. 547, 2014.

[105] B. Kalyani and G. R. Kumar, "Function of distribution power electronic transformer for medium voltage," *IJCERT*, vol. 1, no. 6, pp. 524–528, 2014.

[106] J. W. Kolar and G. Ortiz, "Intelligent solid state transformers (ssts) a key building block of future smart grid systems," in *Keynote speech at China Power System Society Conference*, vol. 2011, 2011.

[107] J. W. Kolar and G. Ortiz, "Solid state transformer concepts in traction and smart grid applications," *Tutorial*, 2012.

[108] J. Venkat, A. Shukla, and S. Kulkarni, "Power electronic transformers in smart grids," *IEEMA TRAFOTECH*, pp. 1–8, 2014.

[109] J. W. Kolar and G. Ortiz, "Solid-state-transformers: Key components of future traction and smart grid systems," in *International Power Electronics Conference (IPEC), Hiroshima*, 2014.

[110] B. Liu, Y. Zha, T. Zhang, and S. Chen, "Solid state transformer application to grid connected photovoltaic inverters," in *2016 International Conference on Smart Grid and Clean Energy Technologies (ICSGCE)*, IEEE, 2016, pp. 248–251.

[111] M. Morawiec, A. Lewicki, and Z. Krzemiński, "Power electronic transformer for smart grid application," in *2015 First Workshop on Smart Grid and Renewable Energy (SGRE)*, IEEE, 2015, pp. 1–6.

[112] D. Wang, C. Mao, and J. Lu, "Operation and control mode of electronic power transformer," in *2009 IEEE PES/IAS Conference on Sustainable Alternative Energy (SAE)*, IEEE, 2009, pp. 1–5.

[113] S. N. Vaishnav and H. Krishnaswami, "Single-stage isolated bi-directional converter topology using high frequency ac link for charging and v2g applications of phev," in *2011 IEEE Vehicle Power and Propulsion Conference*, IEEE, 2011, pp. 1–4.

[114] T. Yiyun, L. Can, C. Lin, and L. Lin, "Research on vehicle-to-grid technology," in *2011 International Conference on Computer Distributed Control and Intelligent Environmental Monitoring*, IEEE, 2011, pp. 1013–1016.

[115] X. De-jian, "Overview on research in electric vehicles [j]," *Energy Technology and Economics*, vol. 7, 2010.

[116] H. A. Kiehne, *Battery technology handbook*. CRC Press, 2003, vol. 118.

[117] A. M. Andwari, A. Pesiridis, S. Rajoo, R. Martinez-Botas, and V. Esfahanian, "A review of battery electric vehicle technology and readiness levels," *Renewable and Sustainable Energy Reviews*, vol. 78, pp. 414–430, 2017.

[118] J. Y. Yong, V. K. Ramachandaramurthy, K. M. Tan, and N. Mithulananthan, "A review on the state-of-the-art technologies of electric vehicle, its impacts and prospects," *Renewable and Sustainable Energy Reviews*, vol. 49, pp. 365–385, 2015.

[119] S. Habib, M. M. Khan, F. Abbas, and H. Tang, "Assessment of electric vehicles concerning impacts, charging infrastructure with unidirectional and bidirectional chargers, and power flow comparisons," *International Journal of Energy Research*, vol. 42, no. 11, pp. 3416–3441, 2018.

[120] N. Sujitha and S. Krithiga, "Res based ev battery charging system: A review," *Renewable and Sustainable Energy Reviews*, vol. 75, pp. 978–988, 2017.

[121] M. Yilmaz and P. T. Krein, "Review of battery charger topologies, charging power levels, and infrastructure for plug-in electric and hybrid vehicles," *IEEE Transactions on Power Electronics*, vol. 28, no. 5, pp. 2151–2169, 2012.

[122] I. Subotic, N. Bodo, E. Levi, B. Dumnic, D. Milicevic, and V. Katic, "Overview of fast on-board integrated battery chargers for electric vehicles based on multiphase machines and power electronics," *IET Electric Power Applications*, vol. 10, no. 3, pp. 217–229, 2016.

[123] I. Subotic, E. Levi, M. Jones, and D. Graovac, "On-board integrated battery chargers for electric vehicles using nine-phase machines," in *2013 International Electric Machines & Drives Conference*, IEEE, 2013, pp. 226–233.

[124] C. Youssef, E. Fatima, A. Chakib, *et al.*, "A technological review on electric vehicle dc charging stations using photovoltaic sources," in *IOP Conference Series: Materials Science and Engineering*, IOP Publishing, vol. 353, 2018, p. 012 014.

[125] C. Dharmakeerthi, N. Mithulananthan, and T. Saha, "Impact of electric vehicle fast charging on power system voltage stability," *International Journal of Electrical Power & Energy Systems*, vol. 57, pp. 241–249, 2014.

[126] S. Painuli, M. S. Rawat, and D. R. Rayudu, "A comprehensive review on electric vehicles operation, development and grid stability," in *2018 International Conference on Power Energy, Environment and Intelligent Control (PEEIC)*, IEEE, 2018, pp. 807–814.

[127] W. Lynch and Z. Salameh, "Taper charge method for a nickel-cadmium electric vehicle traction battery," in *2007 IEEE Power Engineering Society General Meeting*, IEEE, 2007, pp. 1–5.

[128] S. Ketsingsoi and Y. Kumsuwan, "An off-line battery charger based on buck-boost power factor correction converter for plug-in electric vehicles," *Energy Procedia*, vol. 56, pp. 659–666, 2014.

[129] L. N. Rao, S. Gairola, S. Lavety, and N. Islam, "Design of dc-dc boost converter with negative feedback control for constant current operation," *International Journal of Power Electronics and Drive Systems*, vol. 8, no. 4, p. 1575, 2017.

[130] A. D. Hilshey, P. Rezaei, P. D. Hines, and J. Frolik, "Electric vehicle charging: Transformer impacts and smart, decentralized solutions," in *2012 IEEE Power and Energy Society General Meeting*, IEEE, 2012, pp. 1–8.

[131] G. Razeghi, L. Zhang, T. Brown, and S. Samuelsen, "Impacts of plug-in hybrid electric vehicles on a residential transformer using stochastic and empirical analysis," *Journal of power sources*, vol. 252, pp. 277–285, 2014.

[132] Q. Yan and M. Kezunovic, "Impact analysis of electric vehicle charging on distribution system," in *2012 North American Power Symposium (NAPS)*, IEEE, 2012, pp. 1–6.

[133] R. Romo and O. Micheloud, "Power quality of actual grids with plug-in electric vehicles in presence of renewables and micro-grids," *Renewable and Sustainable Energy Reviews*, vol. 46, pp. 189–200, 2015.

[134] L. P. Fernandez, T. G. San Román, R. Cossent, C. M. Domingo, and P. Frias, "Assessment of the impact of plug-in electric vehicles on distribution networks," *IEEE Transactions on Power Systems*, vol. 26, no. 1, pp. 206–213, 2010.

[135] O. C. Onar and A. Khaligh, "Grid interactions and stability analysis of distribution power network with high penetration of plug-in hybrid electric vehicles," in *2010 Twenty-Fifth Annual IEEE Applied Power Electronics Conference and Exposition (APEC)*, IEEE, 2010, pp. 1755–1762.

[136] A. Ayob, W. M. F. W. Mahmood, A. Mohamed, M. Z. C. Wanik, M. M. Siam, S. Sulaiman, A. H. Azit, and M. A. M. Ali, "Review on electric vehicle, battery charger, charging station and standards," *Research Journal of Applied Sciences, Engineering and Technology*, vol. 7, no. 2, pp. 364–373, 2014.

[137] B. Wu, Y. Lang, N. Zargari, and S. Kouro, *Power Conversion and Control of Wind Energy Systems*. John Wiley Sons, 2011.

[138] K. Ahmed, N. Yahaya, V. Asirvadam, and O. Ibrahim, "Modeling and simulation of power electronic distribution transformer based on a three level converter," in *Applied Mechanics and Materials*, Trans Tech Publ, vol. 785, 2015, pp. 151–155.

[139] S. Subramanya and K. Anjaneyulu, "Modeling and Simulation of AC/AC Matrix Converter Based Power Electronic Transformer for Power Quality Improvement," *International Journal of Engineering Research & Technology (IJERT)*, vol. 1, no. 5, 2012.

[140] D. Wang, Y. Yang, J. Tian, C. Mao, and J. Zhang, "Design and Implementation of 10-kV MW-level Electronic Power Transformer (EPT)," in *2018 IEEE Industry Applications Society Annual Meeting (IAS)*, IEEE, 2018, pp. 1–10.

[141] P. W. Wheeler, J. Rodriguez, J. C. Clare, L. Empringham, and A. Weinstein, "Matrix converters: A technology review," *IEEE Transactions on Industrial Electronics*, vol. 49, no. 2, pp. 276–288, 2002.

[142] J. Karpagam, A. N. Kumar, and V. K. Chinnaiyan, "Comparison of modulation techniques for matrix converter," *International Journal of Engineering and Technology*, vol. 2, no. 2, p. 189, 2010.

[143] J. Vadillo, J. Echeverria, A. Galarza, and L. Fontan, "Modelling and simulation of space vector modulation techniques for matrix converters: Analysis of different switching strategies," in *2008 International Conference on Electrical Machines and Systems*, IEEE, 2008, pp. 1299–1304.

[144] J. Rodriguez, M. Rivera, J. W. Kolar, and P. W. Wheeler, "A review of control and modulation methods for matrix converters," *IEEE Transactions on Industrial Electronics*, vol. 59, no. 1, pp. 58–70, 2011.

[145] H. Karaca and R. Akkaya, "Control of venturini method based matrix converter in input voltage variations," in *Proceedings of the International Multi Conference of Engineers and Computer Scientists IMECS, Hong Kon*, vol. 2, 2009.

[146] A. R. P. Andhra Sridhar, "Bidirectional AC-DC Converter for Vehicle-to-Grid (V2G) Applications," 2015.

[147] M. Hannan, M. Ker P.J. andHossain Lipu, Z. Choi, M. Rahman, K. Muttaqi, and F. Blaabjerg, "State of the Art of Solid-State Transformers: Advanced Topologies, Implementation Issues, Recent Progress and Improvements," *IEEE Accees*, vol. 8, pp. 19 113–19 132, 2020.

[148] J. E. Huber and J. Kolar, "Volume/weight/cost comparison of a 1 MVA 0 kV/400V solid-state against a conventional low-frequency distribution transformer," pp. 4545–4552, 2014.

[149] M. Krarti, *Optimal design and retrofit of energy efficient buildings, communities, and urban centers*. Butterworth-Heinemann, 2018.

[150] S. D. Dhakulkar, V. A. Manwar, S. G. Banole, B. S. Rakhonde, *et al.*, "Inspection of Voltage Sags and Voltage Swells Incident In Power Quality Problems - A Review," *International Research Journal of Engineering and Technology*, vol. 4, no. 1, pp. 1734–1736, 2017.

[151] S. Santoso, M. F. McGranaghan, R. C. Dugan, and H. W. Beaty, *Electrical power systems quality*. McGraw-Hill Education, 2012.

[152] A. Khan, M. Khan, and P. Barendse, "Effects of load variation on a weak grid under unbalanced voltage conditions," in *2014 International Conference on Electrical Machines (ICEM)*, IEEE, 2014, pp. 1711–1716.

[153] J. A. Martinez-Velasco, S. Alepuz, F. González-Molina, and J. Martin-Arnedo, "Dynamic average modeling of a bidirectional solid state transformer for feasibility studies and real-time implementation," *Electric power systems research*, vol. 117, pp. 143–153, 2014.

[154] M. E. Adabi Firouzjaee, "Advanced modeling of solid state transformer," 2018, PhD thesis, Universitat Politècnica de Catalunya.

[155] N. Kelly, M. Sasso, G. Angrisani, and C. Roselli, *Impact of microgeneration systems on the low-voltage electricity grid*, `https://www.researchgate.net/publication/277328405_Impact_of_Microgeneration_Systems_on_the_Low-Voltage_Electricity_Grid`, A Report of Annex 54 "Integration of Micro-Generation and Related Energy Technologies in Buildings"; Energy in Buildings and Communities Programme, 2014.

[156] W. Khan, F. Ahmad, and M. S. Alam, "Fast EV charging station integration with grid ensuring optimal and quality power exchange," *Engineering Science and Technology, an International Journal*, vol. 22, no. 1, pp. 143–152, 2019.

[157] P. Thomas and F. M. Chacko, "Electric vehicle integration to distribution grid ensuring quality power exchange," in *2014 International Conference on Power Signals Control and Computations (EPSCICON)*, IEEE, 2014, pp. 1–6.

[158] M. Murnane and A. Ghazel, *A closer look at state of charge (SOC) and state of health (SOH) estimation techniques for batteries*, `http://www.analog.com/media/en/technical-documentation/technical-articles/A-Closer-Look-at-State-Of-Charge-and-State-Health-Estimation-Techniques-for-batteries.pdf`, 2017.

[159] V. SEMICONDUCTORS, "IGBT/MOSFET Gate Drive Optocoupler," *Retrieved Jul*, vol. 26, pp. 2007–2008, 2011.

[160] D. Shah and M. L. Crow, "Online volt-var control for distribution systems with solid-state transformers," *IEEE Transactions on Power Delivery*, vol. 31, no. 1, pp. 343–350, 2015.

[161] Y. Du, S. Baek, S. Bhattacharya, and A. Q. Huang, "High-voltage high-frequency transformer design for a 7.2 kV to 120V/240V 20kVA solid state transformer," in *IECON 2010-36th Annual Conference on IEEE Industrial Electronics Society*, IEEE, 2010, pp. 493–498.

[162] Y. Yi, U. Buttner, Y. Fan, and I. G. Foulds, "Design and optimization of a 3-coil resonance-based wireless power transfer system for biomedical implants," *International Journal of Circuit Theory and Applications*, vol. 43, no. 10, pp. 1379–1390, 2015.

[163] L. Ke, G. Yan, S. Yan, Z. Wang, and X. Li, "Optimal design of litz wire coils with sandwich structure wirelessly powering an artificial anal sphincter system," *Artificial organs*, vol. 39, no. 7, pp. 615–626, 2015.

[164] M. Rashidi, A. Nasiri, and R. Cuzner, "Application of multi-port solid state transformers for microgrid-based distribution systems," in *2016 IEEE International Conference on Renewable Energy Research and Applications (ICRERA)*, IEEE, 2016, pp. 605–610.

[165] J. C. Olivares-Galván, P. S. Georgilakis, E. Vázquez-Martınez, and J. A. Mendieta-Antúnez, "Comparison of three-phase distribution transformer banks against three-phase distribution transformers," 2010.

[166] J. C. Olivares-Galvan, R. Escarela-Perez, P. S. Georgilakis, and I. Fofana, "Evaluation of distribution transformer banks in electric power systems," *International Transactions on Electrical Energy Systems*, vol. 23, no. 3, pp. 364–379, 2013.

Appendix A

MATLAB/Simulink Models

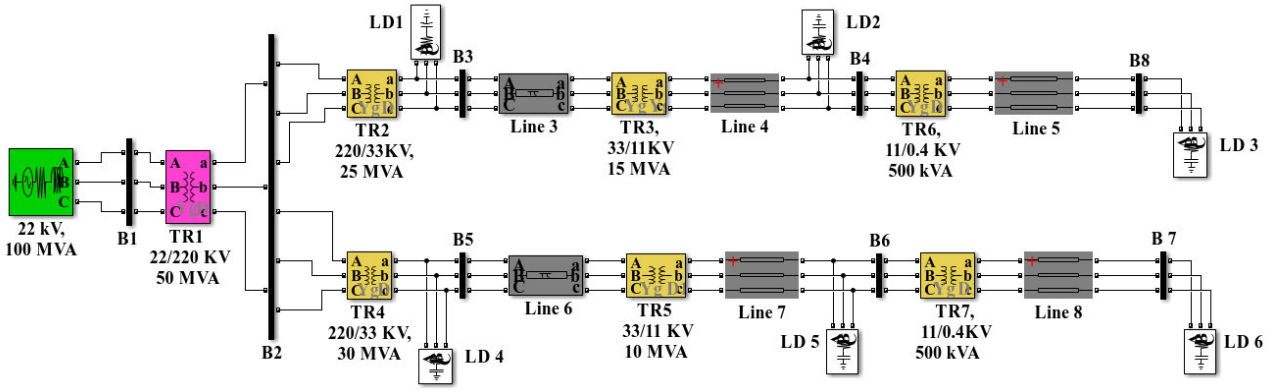

Figure A.1: Network under Investigation Modelled in MATLAB/Simulink

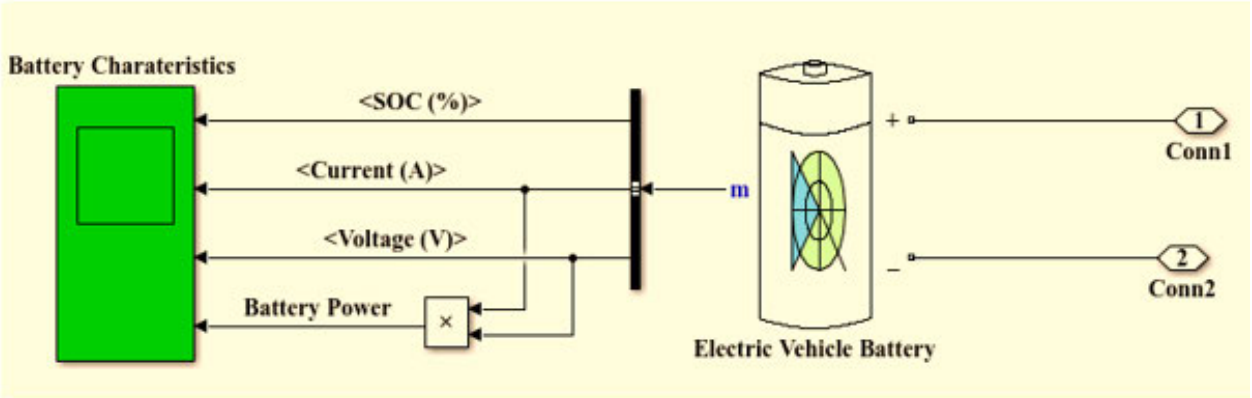

Figure A.2: Battery Equivalent Model in MATLAB/Simulink

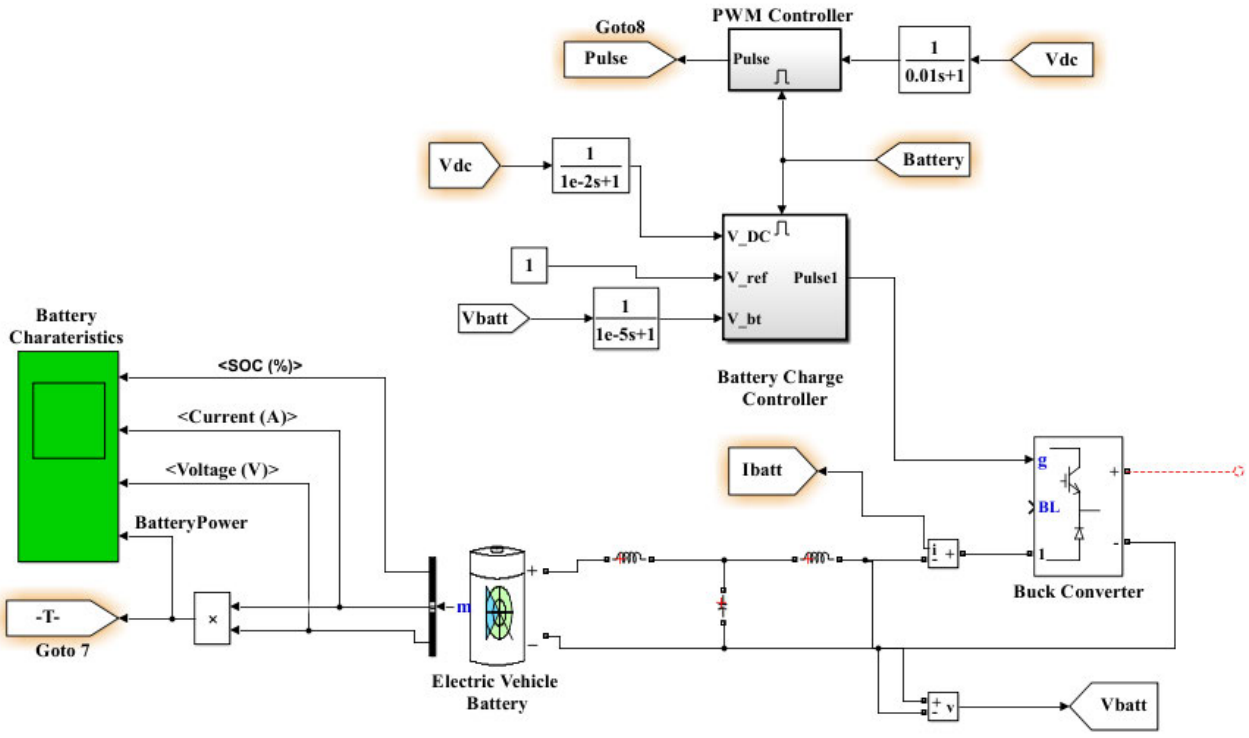

Figure A.3: MATLAB/Simulink Model of Electric Vehicle DC-Fast Charging Station

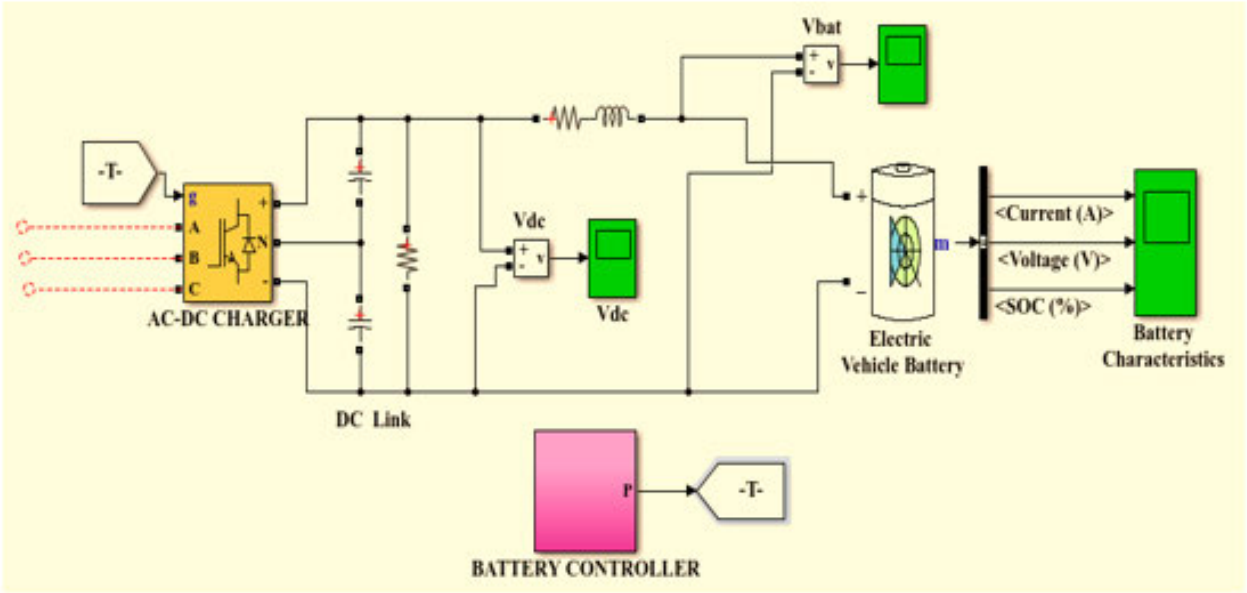

Figure A.4: MATLAB/Simulink Model of Electric Vehicle AC-Fast Charging Station

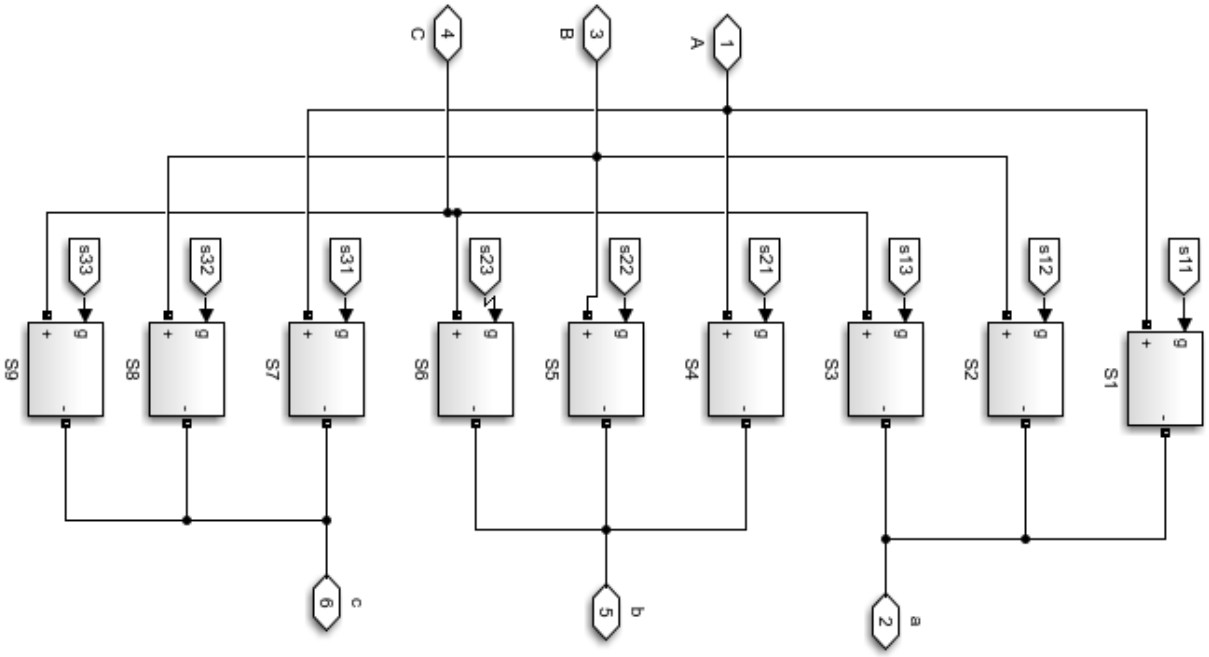

Figure A.5: Block Diagram Internal Structure of Three-Phase MC in MATLAB/Simulink

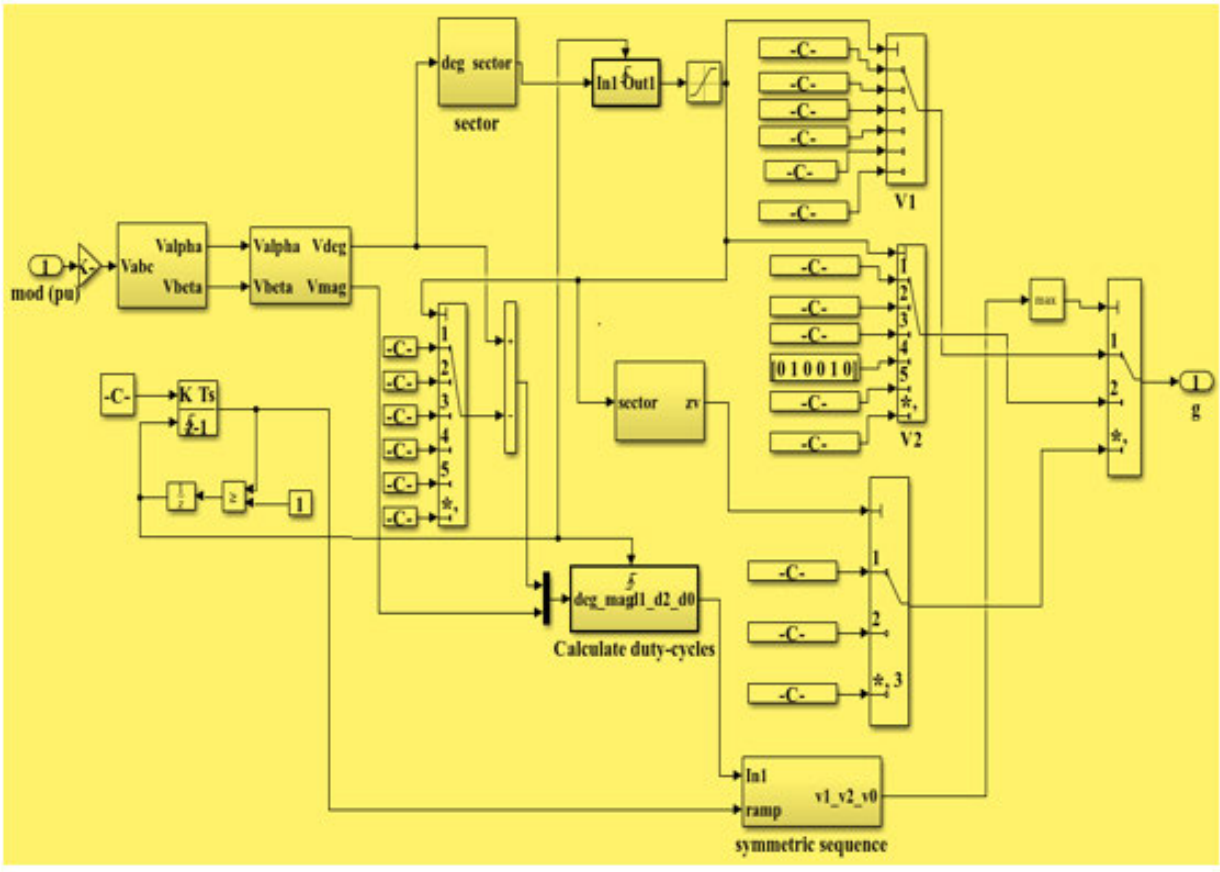

Figure A.6: Internal Structure of MC Input Modulator in MATLAB /Simulink Model

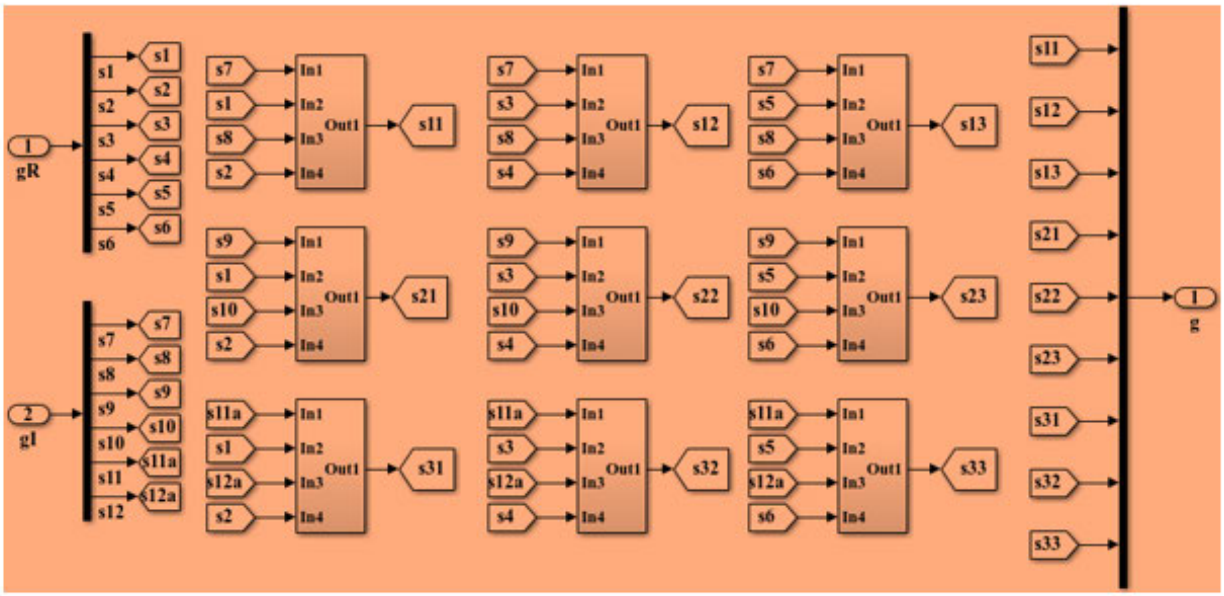

Figure A.7: Internal Structure of MC Switching in MATLAB/Simulink Model

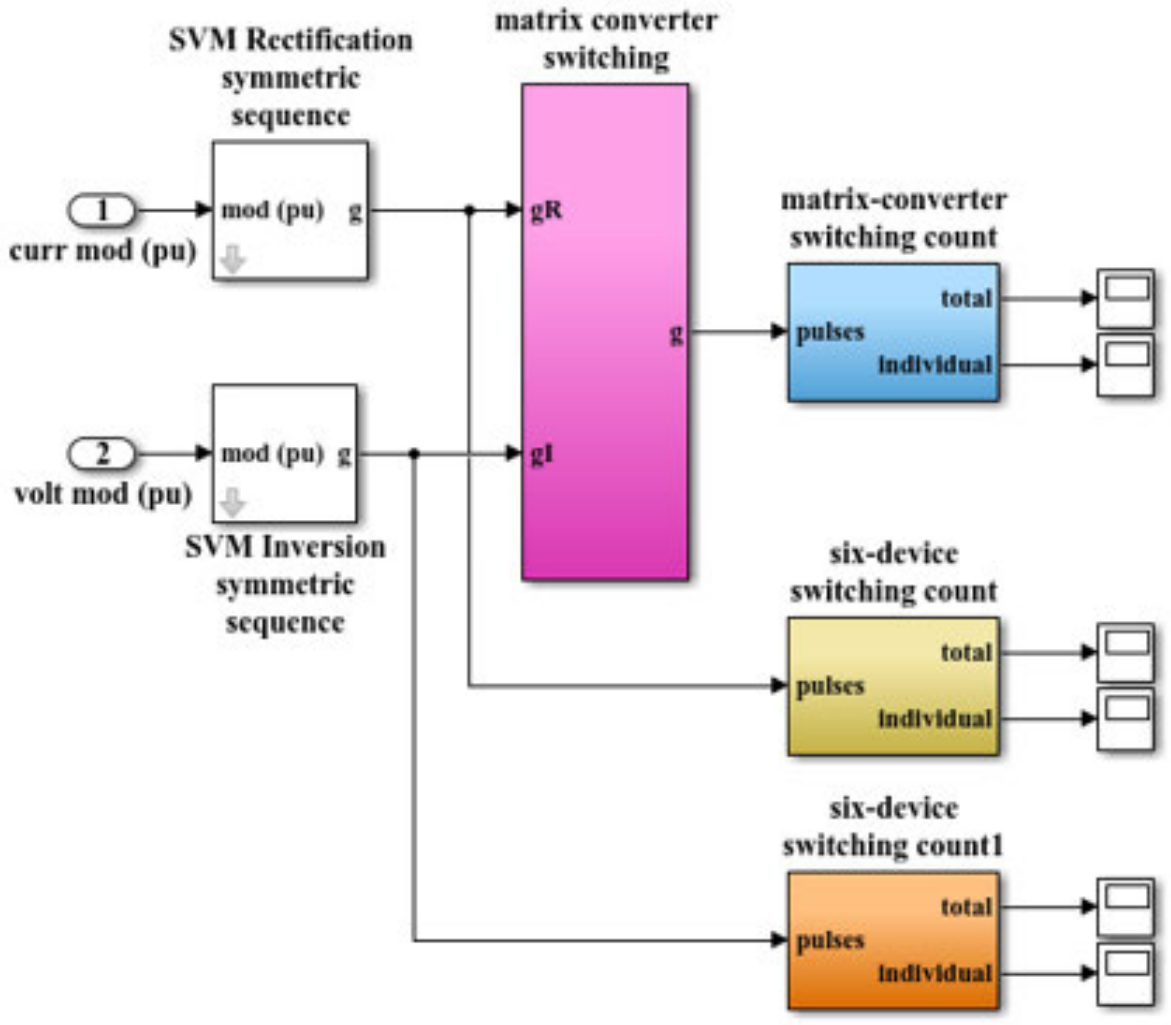

Figure A.8: Complete Structure of MC Switching in MATLAB/Simulink Model

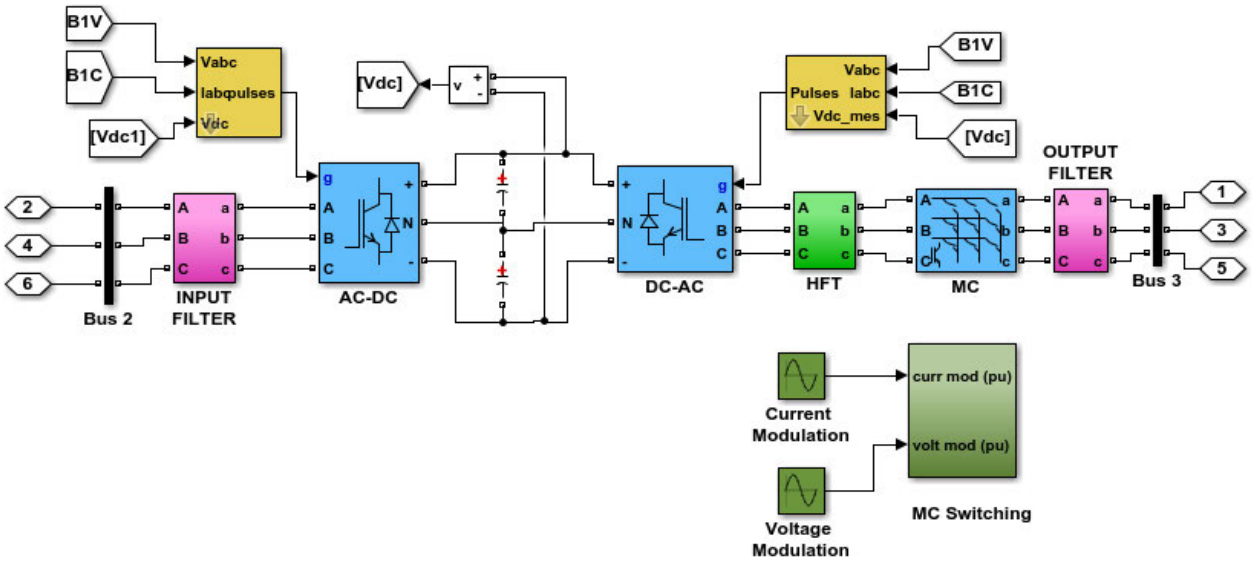

Figure A.9: Complete Model of Power Electronic Transformer in MATLAB/Simulink

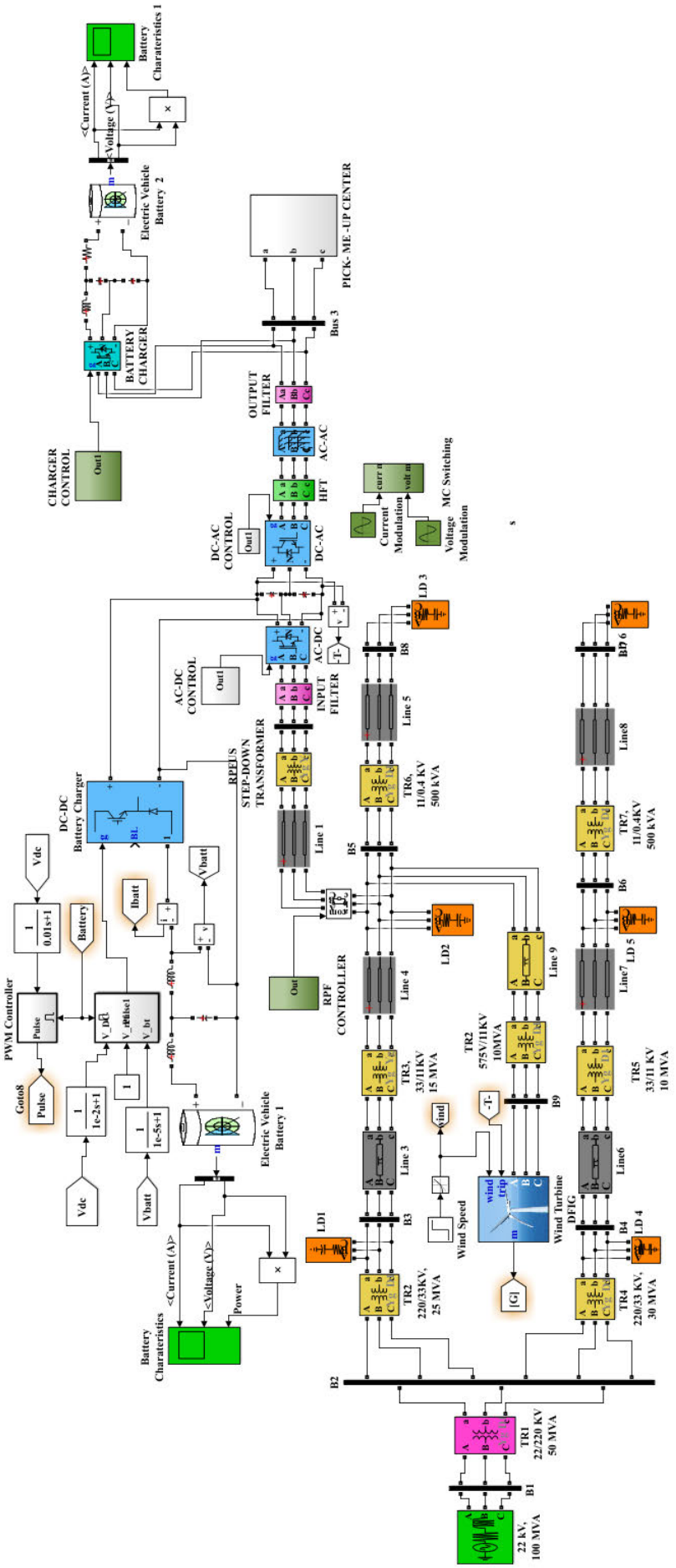

Figure A.10: Complete Model of the Proposed Utilisation Network in MATLAB/Simulink

Appendix B

DC-AC Converter Switching Code

```
/* OLA_3_SW.C
PIC 18F46K20
C18 Compiler
16 MHz External Crystal. 4 PLL Clock
//=====================================================//
//INCLUDES
#include <p18F46K20.h >
#include <stdio.h >
#include <stdlib.h >
#include <delays.h >
#include <timers.h >
#include <adc.h >
//=========================================================// #pragma con-
fig FOSC = HSPLL, FCMEN = OFF, IESO = OFF // CONFIG1H
#pragma config PWRT = OFF, BOREN = SBORDIS, BORV = 30 // CONFIG2L
#pragma config WDTEN = OFF, WDTPS = 32768 // CONFIG2H
#pragma config MCLRE = ON, LPT1OSC = OFF, PBADEN = ON, CCP2MX = PORTC // CONFIG3H
#pragma config STVREN = ON, LVP = OFF, XINST = OFF // CONFIG4L
#pragma config CP0 = OFF, CP1 = OFF, CP2 = OFF, CP3 = OFF // CONFIG5L
#pragma config CPB = OFF, CPD = OFF // CONFIG5H
#pragma config WRT0 = OFF, WRT1 = OFF, WRT2 = OFF, WRT3 = OFF // CONFIG6L
#pragma config WRTB = OFF, WRTC = OFF, WRTD = OFF // CONFIG6H
#pragma config EBTR0 = OFF, EBTR1 = OFF, EBTR2 = OFF, EBTR3 = OFF // CONFIG7L
#pragma config EBTRB = OFF // CONFIG7H
//=====================================================//
 // Variable TYPE definitions
//=====================================================//
signed int TIMESEQ ;
signed int ANALOG_RESULT ;
$#define  SW1$   PORTAbits.RA1$
$#define  SW2$   PORTAbits.RA2$
$#define  SW3$   PORTAbits.RA3$
$#define  SW4$   PORTAbits.RA4$
$#define  SW5$   PORTAbits.RA5$
$#define  SW6$   PORTEbits.RE0$
$#define  SW7$   PORTEbits.RE1$
$#define  SW8$   PORTEbits.RE2$
//=====================================================//
//HIGH PRIORITY interrupt service
//-------------------------------
//#pragma code_HIGH_INTERRUPT_VECTOR = 0x000008 // Pin interrupt
//void_HIGH_ISR (void)
```

```
//{
// INTCONbits.GIEH = 1;
//}
//#pragma code
//-----------------------------------
// LOW PRIORITY interrupt service
//-----------------------------------
/*#pragma code_LOW_INTERRUPT_VECTOR = 0x000018
void_LOW_ISR (void)
{
// possible code here
;
}
#pragma code */ //=======================================
//=======================================
void main(void)
{ // wait for oscillator to stabilise
// while (!OSCCONbits.HFIOFS) {}
PORTA = 0;
PORTB = 0;
PORTC = 0;
PORTD = 0;
PORTE = 0;
LATA = 0;
LATB = 0;
LATC = 0;
LATD = 0;
LATE = 0;
// CM1CON = 7 ;
// CM2CON = 7 ;
// clear interrupt enable register PIE1 = 0x00;
// PIE3 = 0x00;
RCONbits.IPEN = 0; // disable priority interrupts INTCON2bits.RBPU = 0;
ADCON0 = 0b00000000; //
// === PORT-A settings ===
$//             ————RA7$
$//             ———————RA6$
$//             ——————————RA5$
$//             ———————————RA4$
$//             ————————————RA3$
$//             ——————————————RA2$
$//             ———————————————RA1$
$//             ————————————————RA0$
$//              vvvvvvvv$
//
TRISA = 0b00111111;
// === PORT-B settings ===
$//             ————RB7-$
$//             ———————RB6-$
$//             ——————————RB5 =$
```

```
$//          ———————————RB4$
$//          ————————————RB3$
$//          —————————————RB2 =$
$//          ——————————————RB1$
$//          ———————————————RB0-$
$//          vvvvvvvv$
//
TRISB = 0b00000000;
INTCON2bits.RBPU = 0;
WPUB = 0x00;
// === PORT-C settings ===
$//          ————————- RC7-$
$//          ———————RC6-
$ $//          ————————RC5=$
$//          ———————————RC4=$
$//          ————————————RC3=$
$//          —————————————RC2=$
$//          ——————————————RC1 =$
$//          ———————————————RC0 =$
$//          vvvvvvvv$ // IOOOOOOO
TRISC = 0b00000000; TRISD = 0b10000000;
TRISE = 0b00000111;
ANSEL = 0b00000001; //
ANSELH = 0b00000000; //
Open Timer0 (TIMER_INT_OFF
T0_16BIT
T0_SOURCE_INT
T0_PS_1_1);
OpenADC(ADC_FOSC_64
ADC_RIGHT_JUST
ADC_12_TAD,
ADC_CH0
ADC_INT_OFF, 15);
if(!SW1)
{
TIMESEQ = 5220; //500Hz
}
if(!SW2)
{
TIMESEQ = 2400; //1KHz
} if(!SW3){
TIMESEQ = 438; //5KHz
}
if(!SW4){
TIMESEQ = 157; //10KHz
}
if(!SW5){
TIMESEQ = 103; //15KHz
}
if(!SW6){
```

```
TIMESEQ = 66; //20KHz
}
if(!SW7){
OpenTimer0(TIMER_INT_OFF
T0_16BIT
T0_SOURCE_INT
T0_PS_1_256);
TIMESEQ = 60000; //veryslowmodetochecksequence
}
if(!SW8)
{
ConvertADC();
while(BusyADC())
ANALOG_RESULT = ReadADC();
TIMESEQ = ANALOG_RESULT * 4;
OpenTimer0(TIMER_INT_OFF
T0_16BIT
T0_SOURCE_INT
T0_PS_1_1);
}
while(1)
{
LATC = 0b00110001;
WriteTimer0(0); //
while(ReadTimer0() < TIMESEQ)
LATC = 0b00100011;
WriteTimer0(0); //
while(ReadTimer0()<TIMESEQ)
LATC = 0b00000111;
WriteTimer0(0); //
while(ReadTimer0()<TIMESEQ)
LATC = 0b00001110;
WriteTimer0(0); //
while(ReadTimer0()<TIMESEQ)
LATC = 0b00011100;
WriteTimer0(0); //
while(ReadTimer0()<TIMESEQ)
LATC = 0b00111000;
WriteTimer0(0); //
while(ReadTimer0()<TIMESEQ)
} //endwhile1
}
// ========================================
// ========================================
```

Appendix C

Programming Code for Matrix Converter Switching

```
//*****************************************************
{
// PIC32MX795F512L - code for OLA's Project Matrix Convert
// Chipkit Max32 hardware.
//*****************************************************
// Description:
// Oscillator Configuration Bit Settings:
// Oscillator Selection Bits = Primary Osc w/PLL (XT+HS+EC+PLL)
// Primary Oscillator Config = XT osc mode//alteration
// PLL Input Divider = 2x Divider
// PLL Multiplier = 18x Multiplier
//*****************************************************
//*****************************************************
// Rev-1.00
//*****************************************************
#include <plib.h>
#include <p32xxxx.h>
#include<stdint.h>
#include <stdio.h>
#include<stdlib.h>
#include <uart.h>
#include <GenericTypeDefs.h>
// Configuration Bit settings
#pragma config FPLLMUL = MUL_20, FPLLIDIV = DIV_2, FPLLODIV = DIV_1, FWDTEN = OFF
// !!! VERY IMPORTANT TO STOP SOSC and ENABLE RC14 !!!!
#pragma config FSOSCEN = OFF
#pragma config POSCMOD = HS, FNOSC = PRIPLL, FPBDIV = DIV_2
#define SYS_FREQ (80000000L)
// for delay routines
#define Get System Clock((SYS_FREQ)
//-----------------------
// Define INPUTS
//=======================================
// Define OUTPUTS
//-----------------------
$#define          OUT01          LATFbits.LATF13$
$#define          OUT02          LATFbits.LATF12$
$#define          OUT03          LATFbits.LATF5$
$#define          OUT04          LATFbits.LATF4$
$#define          OUT05          LATDbits.LATD15$
$#define          OUT06          LATDbits.LATD14$
$#define          OUT07          LATEbits.LATE6$
$#define          OUT08          LATEbits.LATE4$
$#define          OUT09          LATEbits.LATE2$
$#define          OUT10          LATEbits.LATE0$
```

```
$#define          OUT11          LATDbits.LATD5$
$#define          OUT12          LATBbits.LATB13$
$#define          OUT13          LATGbits.LATG8$
$#define          OUT14          LATFbits.LATF0$
$#define          OUT15          LATDbits.LATD6$
$#define          OUT16          LATDbits.LATD11$
$#define          OUT17          LATGbits.LATG7$
$#define          OUT18          LATGbits.LATG9$
$#define          OUT19          LATEbits.LATE7$
$#define          OUT20          LATEbits.LATE5$
$#define          OUT21          LATEbits.LATE3$
$#define          OUT22          LATEbits.LATE1$
$#define          OUT23          LATDbits.LATD10$
$#define          OUT24          LATBbits.LATB11$
/================================================
//-------------------------------
unsigned char i ;
unsigned char j ;
unsigned char k ;
unsigned char n ;
unsigned char q ;
//-------------------------------
unsigned long TIMESEQ = 643 ; //
//unsigned char
//unsigned char
//unsigned char
//unsigned int
//unsigned int
//unsigned int
//*****************************************
// define the FLAG REGISTER
//*****************************************
union
{
unsigned char FlagRegister;
struct { unsigned Flag0 :1;
unsigned Flag1 :1;
unsigned Flag2 :1;
unsigned Flag3 :1;
unsigned Flag4 :1;
unsigned Flag5 :1;
unsigned Flag6 :1;
unsigned Flag7 :1;
};
} FlagRegisterBits;
//*****************************************
// PROTOTYPES
/*****************************************
// void ( void ) ;
//*****************************************
```

```
// END of PROTOTYPES
//*****************************************
// TMR1 interrupt handler
//*****************************************
void_ISR(_TIMER_1_VECTOR, ipl2) Timer1Handler(void)
{
// clear the interrupt flag
mT1ClearIntFlag();
// .. things to do
}
//*****************************************************
//=============================================================
//*****************************************************
// main loop
//*********************************************************************
int main(void)
{
/
// configure cache, wait states and peripheral bus clock
// configure the device for maximum performance but do not change the PBDIV
// given the options, this function will change the flash wait states, RAM
// wait state and enable prefetch cache but will not change the PBDIV.
// the PBDIV value is already set via the pragma FPBDIV option above..
SYSTEMConfig(SYS_FREQ, SYS_CFG_WAIT_STATES— SYS_CFG_PCACHE);
//
// configure TMR1 using internal clock, 1:1 prescale
// OpenTimer1(T1_ON — T1_SOURCE_INT — T1_PS_1_1, T1_TICK);
// set up the TMR1 interrupt off
// ConfigIntTimer1(T1_INT_OFF — T1_INT_PRIOR_2);
// configure output
// mPORTASetPinsDigitalOut(BIT_3); // change to effect led on max32 tb
//*************************************
// setup PORT pins as I/O's
//************************* AD1PCFG = 0x00001111;// needed to turn OFF all A2D inputs
// disable JTAG port
DDPCONbits.JTAGEN = 0;
// PORTA TRISA = 0b0000000000000000;
TRISB = 0b0000000000000000;
TRISC = 0b0000000000000000;
TRISD = 0b0000000000000000;
TRISE = 0b0000000000000000;
TRISF = 0b0000000000000000;
TRISG = 0b0000000000000000;
//TMR1 single 16 bit
// disable TMR1 interrupts
IFS0bits.T1IF = 0;
IEC0bits.T1IE = 0;
T1CON = 0x8000 ;
T1CONbits.TON = 1; // enabled with 1:1 prescale
// TMR2 and TMR3 concatenated
```

```
// Used for delays. 62.5 uSec to  53 seconds
T2CON = 0x00 ; // Stop any 16/32-bit Timer2 operation
T3CON = 0x00 ; // Stop any 16-bit Timer3 operation
T2CONSET = 0x0008; // Enable 32-bit mode, prescaler 1:1,
// internal peripheral clock source
TMR2 = 0x0; // Clear contents of the TMR2 and TMR3
PR2 = 0xFFFFFFFF; // Load PR2 and PR3 registers with 32-bit value
T2CONSET = 0x8000; // Start Timer2/3
// TMR4 and TMR5 concatenated
// Used for delays. 62.5 uSec to  53 seconds
T4CON = 0x00 ; // Stop any 16/32-bit Timer4 operation
T5CON = 0x00 ; // Stop any 16-bit Timer5 operation
T4CONSET = 0x0008; // Enable 32-bit mode, prescaler 1:1,
// internal peripheral clock source
TMR4 = 0x0; // Clear contents of the TMR4 and TMR5
PR4 = 0xFFFFFFFF; // Load PR4 and PR5 registers with 32-bit value
T4CONSET = 0x8000; // Start Timer4/5
LATA = 0 ;
LATB = 0 ;
LATC = 0 ;
LATD = 0 ;
LATE = 0 ;
LATF = 0 ;
LATG = 0 ;
while ( 1 )
{
OUT20 = 0 ; // S4
OUT21 = 0 ; // S3
OUT24 = 0 ; // S2
OUT22 = 1 ; // S6
OUT23 = 1 ; // S5
OUT19 = 1 ; // S1
TMR4 = 0 ; //stretch clock pulse
while ( TMR4 <TIMESEQ )
OUT20 = 0 ; // S4
OUT23 = 0 ; // S5
OUT21 = 0 ; // S3
OUT19 = 1 ; // S1
OUT22 = 1 ; // S6
OUT24 = 1 ; // S2
TMR4 = 0 ; //stretch clock pulse
while ( TMR4 <TIMESEQ )
OUT20 = 0 ; // S4
OUT22 = 0 ; // S6
OUT23 = 0 ; // S5
OUT21 = 1 ; // S3
OUT19 = 1 ; // S1
OUT24 = 1 ; // S2
TMR4 = 0 ; //stretch clock pulse
while ( TMR4 <TIMESEQ )
```

```
OUT19 = 0 ; // S1
OUT22 = 0 ; // S6
OUT23 = 0 ; // S5
OUT20 = 1 ; // S4
OUT21 = 1 ; // S3
OUT24 = 1 ; // S2
TMR4 = 0 ; //stretch clock pulse
while ( TMR4 <TIMESEQ )
OUT19 = 0 ; // S1
OUT22 = 0 ; // S6
OUT24 = 0 ; // S2
OUT21 = 1 ; // S3
OUT20 = 1 ; // S4
OUT23 = 1 ; // S5
TMR4 = 0 ; //stretch clock pulse
while ( TMR4 <TIMESEQ )
OUT19 = 0 ; // S1
OUT21 = 0 ; // S3
OUT24 = 0 ; // S2
OUT20 = 1 ; // S4
OUT22 = 1 ; // S6
OUT23 = 1 ; // S5
TMR4 = 0 ; //stretch clock pulse
while ( TMR4 <TIMESEQ )
} // end while 1
while ( 1 )
{
OUT01 = 1 ;
OUT02 = 1 ;
OUT03 = 0 ;
OUT04 = 0 ;
OUT05 = 0 ;
OUT06 = 0 ;
OUT07 = 0 ;
OUT08 = 0 ;
OUT09 = 1 ;
OUT10 = 1 ;
OUT11 = 0 ;
OUT12 = 0 ;
OUT13 = 0 ;
OUT14 = 0 ;
OUT15 = 0 ;
OUT16 = 0 ;
OUT17 = 1 ;
OUT18 = 1 ;
TMR4 = 0 ; //stretch clock pulse
while ( TMR4 <TIMESEQ )
OUT01 = 1 ;
OUT02 = 1 ;
OUT03 = 0 ;
```

```
OUT04 = 0 ;
OUT05 = 0 ;
OUT06 = 0 ;
OUT07 = 0 ;
OUT08 = 0 ;
OUT09 = 0 ;
OUT10 = 0 ;
OUT11 = 1 ;
OUT12 = 1 ;
OUT13 = 0 ;
OUT14 = 0 ;
OUT15 = 1 ;
OUT16 = 1 ;
OUT17 = 0 ;
OUT18 = 0 ;
TMR4 = 0 ; //stretch clock pulse
while ( TMR4 <TIMESEQ )
OUT01 = 0 ;
OUT02 = 0 ;
OUT03 = 1 ;
OUT04 = 1 ;
OUT05 = 0 ;
OUT06 = 0 ;
OUT07 = 0 ;
OUT08 = 0 ;
OUT09 = 0 ;
OUT10 = 0 ;
OUT11 = 1 ;
OUT12 = 1 ;
OUT13 = 1 ;
OUT14 = 1 ;
OUT15 = 0 ;
OUT16 = 0 ;
OUT17 = 0 ;
OUT18 = 0 ;
TMR4 = 0 ; //stretch clock pulse
while ( TMR4 <TIMESEQ )
OUT01 = 0 ;
OUT02 = 0 ;
OUT03 = 1 ;
OUT04 = 1 ;
OUT05 = 0 ;
OUT06 = 0 ;
OUT07 = 1 ;
OUT08 = 1 ;
OUT09 = 0 ;
OUT10 = 0 ;
OUT11 = 0 ;
OUT12 = 0 ;
OUT13 = 0 ;
```

```
OUT14 = 0 ;
OUT15 = 0 ;
OUT16 = 0 ;
OUT17 = 1 ;
OUT18 = 1 ;
TMR4 = 0 ; //stretch clock pulse
while ( TMR4 <TIMESEQ )
OUT01 = 0 ;
OUT02 = 0 ;
OUT03 = 0 ;
OUT04 = 0 ;
OUT05 = 1 ;
OUT06 = 1 ;
OUT07 = 1 ;
OUT08 = 1 ;
OUT09 = 0 ;
OUT10 = 0 ;
OUT11 = 0 ;
OUT12 = 0 ;
OUT13 = 0 ;
OUT14 = 0 ;
OUT15 = 1 ;
OUT16 = 1 ;
OUT17 = 0 ;
OUT18 = 0 ;
TMR4 = 0 ; //stretch clock pulse
while ( TMR4 <TIMESEQ )
OUT01 = 0 ;
OUT02 = 0 ;
OUT03 = 0 ;
OUT04 = 0 ;
OUT05 = 1 ;
OUT06 = 1 ;
OUT07 = 0 ;
OUT08 = 0 ;
OUT09 = 1 ;
OUT10 = 1 ;
OUT11 = 0 ;
OUT12 = 0 ;
OUT13 = 1 ;
OUT14 = 1 ;
OUT15 = 0 ;
OUT16 = 0 ;
OUT17 = 0 ;
OUT18 = 0 ;
TMR4 = 0 ; //stretch clock pulse
while ( TMR4 <TIMESEQ )
} // end while 1
// end int main void
}
```